



HAL
open science

Modeling of stable and novel organic materials for high efficiency opv cells

Giovana Aibara Paschoal

► **To cite this version:**

Giovana Aibara Paschoal. Modeling of stable and novel organic materials for high efficiency opv cells. Polymers. Université de Pau et des Pays de l'Adour, 2024. English. NNT : 2024PAUU3026 . tel-04827785

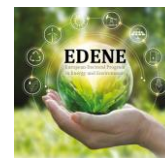
HAL Id: tel-04827785

<https://theses.hal.science/tel-04827785v1>

Submitted on 9 Dec 2024

HAL is a multi-disciplinary open access archive for the deposit and dissemination of scientific research documents, whether they are published or not. The documents may come from teaching and research institutions in France or abroad, or from public or private research centers.

L'archive ouverte pluridisciplinaire **HAL**, est destinée au dépôt et à la diffusion de documents scientifiques de niveau recherche, publiés ou non, émanant des établissements d'enseignement et de recherche français ou étrangers, des laboratoires publics ou privés.



THÈSE

pour obtenir le grade de

Docteur en Chimie polymères

à

l'Université de Pau et des Pays de l'Adour

École Doctorale de Sciences Exactes et de leurs Applications

présentée par

Giovana Miti AIBARA PASCHOAL

Sujet de la thèse:

Modélisation de matériaux organiques stables et nouveaux pour des cellules OPV à haut rendement

Soutenance prévue le 9 septembre 2024

devant la commission d'examen composée de :

JURY

RAPPORTEURS

Lucimara ROMAN

Professeur / Universidade Federal do Paraná, Brésil

Sergey KRASNOSHCHIEKOV

Professeur / Gosudarstvennyj Moskovskij Universitet, Russie

EXAMINATEURS

Laurence VIGNAU

Professeur / Bordeaux-INP, France

Aurélien VITERISI

Enseignant-chercheur HDR / UPPA, France

DIRECTEURS

Didier BÉGUÉ

Professeur / UPPA, France

Roger HIORNS

Directeur de Recherche / CNRS-UPPA, France



THESIS

submitted in fulfillment of the requirements for the degree of

Doctor of Philosophy in Polymer Chemistry

at

University of Pau and Pays de l'Adour

Doctoral School Exact Sciences and their Applications

presented by

Giovana Miti Aibara Paschoal

Thesis title:

Modeling of Stable and Novel Organic Materials for High Efficiency OPV Cells

expected to be defended on September 9th, 2024

for the commission composed by

JURY

RAPPORTEURS

Lucimara Roman

Sergey Krasnoshchekov

Professor / Federal University of Parana, Brazil

Professor / Lomonosov Moscow State University, Russia

EXAMINATORS

Laurence Vignau

Aurélien Viterisi

Professor / Bordeaux-INP, France

Researcher associate (HDR) / University of Pau and Pays de l'Adour, France

SUPERVISORS

Didier Bégué

Roger Hiorns

Professor / University of Pau and Pays de l'Adour, France

Research director / National Centre for Scientific Research (CNRS), France

*To Paulo, my family and friends,
who believed in me and remembered me that
everything I need is already inside of me.*

*To all women and immigrants
who fight for their dreams to come true.*

Acknowledgements

I would like to express my deepest gratitude to all the people and organizations involved in developing my PhD degree.

To EDENE coordinators, Elisabeth and Gilles, for their unwavering dedication and commitment to the development of the program; to all the members from Doctor School and Welcome Desk, for making it possible to start and keep following my doctorate in UPPA.

To Didier, who stood by me throughout the entire project, introducing me to the complex world of quantum chemistry and whose guidance was crucial in shaping my decisions and improving my ideas.

To Roger, for turning great ideas into European projects and providing support during the initial stages of the work, as well as constructive feedback on my thesis.

To professors from Brazil, Deuber, Clarissa, and Neto, who foster connections and create opportunities for many to develop their research. Their dedication and collaborative spirit have been instrumental in advancing academic pursuits and enabling researchers to thrive.

To William, his patience and guidance in teaching me how to conduct calculations and code in Python for improved data analysis. I am grateful for sharing the office space and his assistance in my development as a researcher.

To Germain, for his invaluable advice on having French experiences and for sharing his scientific expertise.

To Panos, for consistently checking on the progress in his unique way and never discouraging me throughout my process.

To Christine Lartigau-Dagron, Nadia Barbero, and Robert Vianello, for their valuable insights, which immensely helped me explore alternative approaches for conducting my research.

To Patricia de Coux, whose advice was very precious to me.

To Elise, Michel, and Falk, for the beautiful and funny moments we spent together.

To my Brazilian friends, *por todo o suporte emocional que me deram desde que cheguei aqui em Pau, desde resolver problemas com a burocracia francesa até em diminuir a saudade da nossa cultura brasileira (e não falo somente das comidas, mas da alegria de viver um sonho).*

To all the friends from IPREM and other UPPA labs, for making this PhD journey more enjoyable with celebrations and adventures. I am deeply grateful for all kinds of support they have given me.

To my family, *muito obrigada por terem dado a base para me tornar quem eu sou hoje e por nunca medirem esforços para me ver feliz.*

To Paulo, *com quem sou eternamente grata por dividir todos os momentos.*

This research was developed as part of the EDENE program that has received funding from the European Union's Horizon H2020 Research and Innovation under the Marie Skłodowska-Curie Grant Agreement N° 945416.

The author acknowledges the computing facilities provided by GENCI-IDRIS (Grant 2022-102485), MCIA (Mésocentre de Calcul Intensif Aquitain) and Pyrene Cluster.

Table of Contents

General Introduction	5
References	8
Chapter 1	11
Molecular Design Parameters for OPV Materials.....	11
1.1 Energy Gap Optimization in OPV Cells	12
1.1.1 Definition of Energy Gap.....	15
1.1.2 Strategies for Tuning the Bandgap.....	21
1.2 Conjugation Length.....	22
1.2.1 Geometrical Optimization Techniques.....	22
1.2.2 Influence on Optical and Electronic Properties.....	23
1.3 Nature of Blocks in the Polymer Backbone.....	24
1.3.1 Coupling Donor, Acceptor and Other Types of Blocks in the Polymer Chain	25
1.3.2 Investigating Optical and Electronic Properties for Assessing Donor-Acceptor Interaction	26
1.4 Side Chains.....	27
1.4.1 Impact of Side Chains on Material Solubility and Morphology	28
1.4.2 Correlation between Side Chains and Electronic Properties.....	28
1.5 Intermolecular interactions.....	30
1.5.1 π -interactions in Conjugated Systems	30
1.5.2 Effect of π -interactions in Optoelectronic Properties.....	32
References	33
Chapter 2	39
Marcus Theory in Charge Transfer Dynamics for OPV Materials	39
2.1 $\Delta G_{\text{separation}}^{\ddagger}$ energy of separation $D^* + A \rightarrow D^+ + A^-$	41

2.2	$\Delta G_{\text{transfer}}^{\ddagger}$ energy of separation $D^* \leftrightarrow D^+$	49
2.3	Global process	54
2.4	Distance dependences of electron transfer rates	54
2.5	Voltage losses in Typical Photovoltaic Cells.....	62
	References	66
Chapter 3		67
Theoretical Framework for Computational Modeling		67
3.1	Principles of Density Functional Theory (DFT)	70
3.1.1	Thomas-Fermi model	71
3.1.2	Thomas-Fermi-Dirac model.....	71
3.1.3	Slater model.....	72
3.1.4	Hohenberg and Kohn theorems.....	72
	3.1.4.1 Uniqueness Theorem.....	72
	3.1.4.2 Hohenberg-Kohn Variational Principle	73
3.1.5	Kohn-Sham approach.....	73
3.1.6	Classification of exchange-correlation functionals.....	75
	3.1.6.1 Local Density Approximation (LDA).....	76
	3.1.6.2 Generalized Gradient Approximation (GGA).....	76
	3.1.6.3 Hybrid functionals.....	77
3.1.7	Dispersion correction for KS-DFT energy.....	78
3.1.8	Challenges of DFT	79
3.2	Method for calculating properties of molecules in excited state.....	79
3.3	Non-Covalent Interactions (NCI) analysis.....	80
3.3.1	Quantum Theory of Atom in Molecules (QTAIM)	81
3.3.2	Reduced density gradient (RDG)	83
3.3.3	Independent gradient model (IGM).....	84

3.4	Fukui Indices	88
3.5	Correlating Computational Predictions with Experimental Results	90
3.6	The Role of Benchmarking in Validating Models	91
3.7	Challenges in Accurate Predictions and Limitations	93
	References	94
Chapter 4	99
Methods	99
4.1	Calculation method	99
4.2	Optical and electronic properties	100
4.3	Structure parameters.....	101
4.3.1	Benchmarking	101
4.3.2	Isolated chains	102
4.3.3	Double chains (or stacked or dimer systems).....	102
4.4	Analysis of intermolecular interactions	103
4.4.1	Boltzmann distribution.....	104
4.4.2	Noncovalent interactions visualization using IGM analysis.....	104
	References	105
Chapter 5	107
Results	107
5.1	Benchmarking of OPV molecules.....	107
5.2	Optical and Electronic Properties.....	113
5.3	Effect of modifications on isolated chain structures	124
5.3.1	Conjugation length	124
5.3.2	Nature of blocks	127
5.3.3	Side chains.....	129
5.4	Analysis of intermolecular interactions	131

References	139
Conclusions and perspectives.....	141
Appendices	143
Appendix A	145
Appendix B.....	163

General Introduction

The dynamic and wide-ranging field of solar technology is at the forefront of research into sustainable energy. Materials science, electronics, physics and mechanical engineering are used to develop, optimize and implement solar energy harvesting devices in this technological field. The wide range of solar devices, such as solar thermal systems, photovoltaic cells and new technologies, all demand an exploration of the fundamentals of energy conversion and require innovative materials and system integration for high efficiency.

Even though sunlight is the most available energy source, many constraints exist on fully exploiting it. For example, countries in South America and Africa have abundant solar irradiation during most of the year. However, it is challenging to implement PV technologies due to the high manufacturing and installation costs. On the other hand, while it is affordable and even subsidized by government programmes to explore renewable energy sources in the face of increasing pollution, northern hemisphere countries encounter severe periods with low levels of light. Therefore, much can be done regarding cell efficiency optimization to ensure low-cost production that both ease installations and make the most of supportive government policies.

According to life cycle assessment (LCA) studies of photovoltaic technologies, the most significant impact derives directly from the conversion efficiency, which steadily reduces the environmental impact of cells as it increases [1]. This is not only due to the electricity produced being more per electricity used to make the device but also because of the reduced need for substrates, supports and infrastructure when using highly efficient and therefore smaller, devices.

Towards more sustainable solutions, the development of organic photovoltaic (OPV) cells plays an essential role in addressing the current limitations of solar energy deployment. These devices use semiconductor materials to generate photocurrent from incident light, offering promising advantages including flexibility, lightweight and potential for low-cost production through solution processing.

The best achievements of emerging photovoltaic devices, including OPVs, have been pointed out by Almora and collaborators [2] as a function of performance parameters and the absorber material bandgap. Regarding the power conversion efficiency of cells, their survey was

complemented by the work of the National Renewable Energy Laboratory (NREL), which has been tracking the evolution of different types of photovoltaic cells since 1976. The development of polymer and fullerene-based OPV cells started in 1992 (although shown from 2001 in that graph) with discovery done by Serdar Sariciftchi *et al.* [3], while polymer-polymer devices by Richard Friend and collaborators [4] in 1995.

Almora *et al.* report and NREL chart remain important records and, indeed, challenges to scientists to improve cell efficiencies. Long-term stability under continuous illumination and heating aligned to visible transmittance and cell flexibility are key elements of past research.

Photovoltaic devices based on crystalline and amorphous silicon in multi-layer panels are still the most commercially used technology. To be processed into panels and become an accessible technology for the economic generation of electricity, the cost of silicon solar cells had to be reduced, and the purification of silicon had to be improved. Impurities can introduce so-called deep levels, making the energy difference between the conduction and valence bands greater than the thermal energy [5].

In the category of non-silicon-based solar cells, inorganic thin-film PV technologies such as solar cells of cadmium telluride (CdTe) and copper indium gallium selenide (CIGS) combine heavy and minor metals. The producing cost of thin film solar cells (TFSCs) is two times lower than multi-crystalline silicon-based modules and they emit around five times less greenhouse gas (GHG) compared to fossil-fuel power plants [6]. The CIGS has a bandgap range of 1.02~1.68 eV, presenting a high light absorption coefficient and good anti-radiation performance [7].

As part of emerging or third-generation PV technologies, OPV cells have innovative designed applications due to their low weight and high mechanical flexibility, like in portable chargers and integrating architectural structures such as facades, windows, shades and blinds, and in building-integrated photovoltaic (BIPV) systems [8,9] where they are structurally integrated into the building. TFSCs can also be flexible devices due to the techniques to produce the layer of the photoactive material, which works well with the plastic substrate without compromising the sunlight absorption [7]; however, the metal availability is becoming lower and lower with time and the high metal emissions during module manufacturing can mean that their production is not entirely without environmental impact [6].

There is a light intensity dependence of the photocurrent generation in organic photovoltaic devices [10]. Even in non-ideal light conditions, OPVs can achieve extremely high efficiencies

(upwards of 33%) as they are composed of materials with very high photon harvesting abilities even in low illumination levels. For example, indoor OPVs achieved more than 30% of PCE under a 1000 lux light-emitting diode (LED) illumination [11] and over 20% under 125 lux LED [12], due to the extremely high photon to exciton conversion rates – often close to 100%.

Organic cells require manufacturing processes with lower energy-intensive processes than those required for silicon and, in most cases, they present less environmental impacts than first-generation cells [1,8,13]. Even though the embedded energy per square of OPV module produced in the laboratory is half of the average value for crystalline silicon technologies [14], the use of some materials, such as fullerenes and ITO electrodes, which have large embodied energy, should be evaluated carefully [1]. Concerning external parameters, if low solar irradiance levels are considered, organic devices have the lowest energy cost among the PV technologies [14].

Optimizations can be done with large-scale industrial production using techniques that cause lower material wastes and minimize the energy used in material processing [14]. However, the lack of data about process and resource consumption of raw materials [1,8] and disposal stage (recycling scenario) [9] when evaluating the LCA of third generation technologies is a significant gap that needs to be filled.

The cell efficiency of OPVs is still lower than inorganic cells, primarily due to organic materials having larger exciton binding energies, around 0.5 eV [15]. Consequently, the optical absorption in organic semiconductors results in a spatially localized electron-hole pair that must dissociate, while in inorganic ones it creates free charge carriers immediately [16]. The efficiency of OPV devices is also affected by energy losses, typically due to incomplete light absorption and recombination of charges in the material interfaces, interrupting charge collection in the electrodes.

Materials with light absorption in the range of the highest intensity solar irradiance, such as conjugated systems, are highly effective due to their aromatic rings, which create overlaps of π -orbitals, facilitating the delocalization of electrons along the polymer backbone. Tailoring the properties of conjugated polymers through molecular engineering allows the optimization of cell performance, leading to significant advances in solar energy materials.

Ab initio modeling is a powerful technique to design materials at the atomistic level and predict electronic properties, such as optical and electronic gaps, electronic affinity and ionization potential, that are strongly related to the OPV performance. The correlation between the method

and accurate estimation of these properties is well-known. Designing a novel molecule from computational investigation requires a deep understanding of the parameters of the polymer structure that can affect the optoelectronic properties.

This work aims to show how molecular structure can affect the electronic properties from a theoretical study targeting trends on such properties for a series of compounds, based on density functional theory (DFT) and time-dependent DFT (TD-DFT), then to guide researchers on designing a new material with a high light absorption appropriate for use in daylight.

References

- [1] V. Muteri, M. Cellura, D. Curto, V. Franzitta, S. Longo, M. Mistretta, M.L. Parisi, *Energies* 13 (2020) 252.
- [2] O. Almora, D. Baran, G.C. Bazan, C.I. Cabrera, S. Erten-Ela, K. Forberich, F. Guo, J. Hauch, A.W.Y. Ho-Baillie, T.J. Jacobsson, R.A.J. Janssen, T. Kirchartz, N. Kopidakis, M.A. Loi, R.R. Lunt, X. Mathew, M.D. McGehee, J. Min, D.B. Mitzi, M.K. Nazeeruddin, J. Nelson, A.F. Nogueira, U.W. Paetzold, B.P. Rand, U. Rau, H.J. Snaith, E. Unger, L. Vaillant-Roca, C. Yang, H. Yip, C.J. Brabec, *Advanced Energy Materials* 13 (2023) 2203313.
- [3] N.S. Sariciftci, L. Smilowitz, A.J. Heeger, F. Wudl, *Science* 258 (1992) 1474–1476.
- [4] J.J.M. Halls, C.A. Walsh, N.C. Greenham, E.A. Marseglia, R.H. Friend, S.C. Moratti, A.B. Holmes, *Nature* 376 (1995) 498–500.
- [5] J.S. Connolly, in: *Photochemical Conversion and Storage of Solar Energy*, Academic Press, 1981, pp. 229–242.
- [6] V. Fthenakis, *Renewable and Sustainable Energy Reviews* 13 (2009) 2746–2750.
- [7] G. Wang, in: *Technology, Manufacturing and Grid Connection of Photo-Voltaic Solar Cells*, John Wiley & Sons, Ltd, 2018, pp. 187–221.
- [8] D. Hengevoss, C. Baumgartner, G. Nisato, C. Hugi, *Solar Energy* 137 (2016) 317–327.
- [9] M.D. Chatzisideris, N. Espinosa, A. Laurent, F.C. Krebs, *Solar Energy Materials and Solar Cells* 156 (2016) 2–10.
- [10] S. Zeiske, W. Li, P. Meredith, A. Armin, O.J. Sandberg, *Cell Reports Physical Science* 3 (2022) 101096.
- [11] T.H. Kim, N.W. Park, M.A. Saeed, S.Y. Jeong, H.Y. Woo, J. Park, J.W. Shim, *Nano Energy* 112 (2023) 108429.
- [12] X. Zhou, H. Wu, U. Bothra, X. Chen, G. Lu, H. Zhao, C. Zhao, Q. Luo, G. Lu, K. Zhou, D. Kabra, Z. Ma, W. Ma, *Mater. Horiz.* 10 (2023) 566–575.
- [13] M.P. Tsang, G.W. Sonnemann, D.M. Bassani, *Solar Energy Materials and Solar Cells* 156 (2016) 37–48.

-
- [14] R. García-Valverde, J.A. Cherni, A. Urbina, *Prog. Photovolt: Res. Appl.* 18 (2010) 535–558.
- [15] B. Kippelen, J.-L. Brédas, *Energy Environ. Sci.* 2 (2009) 251.
- [16] J.-L. Brédas, J.E. Norton, J. Cornil, V. Coropceanu, *Acc. Chem. Res.* 42 (2009) 1691–1699.

Chapter 1

Molecular Design Parameters for OPV Materials

Photovoltaics is a multidisciplinary field that combines materials science, electrical engineering and physics to develop, optimise, and perform solar-to-electricity conversion systems to achieve the highest efficiency. Solar energy conversion of organic solar cells (OSCs) is being advanced via device engineering [1–3], in which the photoactive layer is composed of materials with strong near-infrared light absorption and, when required depending on design constraints, visible light transmittance, therefore it is at the forefront of renewable energy technologies. Device engineering explores concepts to guide the production of high-performance photovoltaic devices, with material selections around dopants, solvents, conjugated polymers [4], substrates [5], device architectures [1] and manufacturing procedures, all playing important roles [6].

For the OSC active layer, semiconductor materials enable improved charge transfer efficiencies and charge mobilities. Of particular interest are conjugated molecules with non-metal and metalloid atoms which exhibit strongly delocalised electronic structures. The molecular design of these compounds is a remarkable strategy to improve cell performance [7,8]. It is well discussed among the scientific community with extensive revisions for small organic molecules such as non-fullerene acceptors and molecular donors [1,9–14], analysing the influence of fused-rings core, side chains and end groups.

Beyond these parameters, the design of conjugated polymers involves other structural parameters such as conjugation length, substituents and π - π stacking between backbones, responsible for stabilising interactions to effectively delocalise of charges along the chains [15–19]. The comprehensive molecular design of conjugated polymers for application in organic photovoltaic (OPV) technologies is investigated in this work. First, explanations of the optical and electronic properties are elaborated, which are then correlated with structural parameters to emphasise the crucial role of molecular design in developing of new materials.

1.1 Energy Gap Optimization in OPV Cells

The classical scheme of the photovoltaic effect in OPV cells is represented in Figure 1.1 [11,17,20–23], in which processes are: (i) light absorption generating a bound electron-hole pair (exciton), (ii) exciton diffusion in the donor-acceptor interface, (iii) exciton dissociation into free charge carriers, (iv) charges carrying until electron and hole transport layers (ETL and HTL), and (v) charge collection at the electrodes.

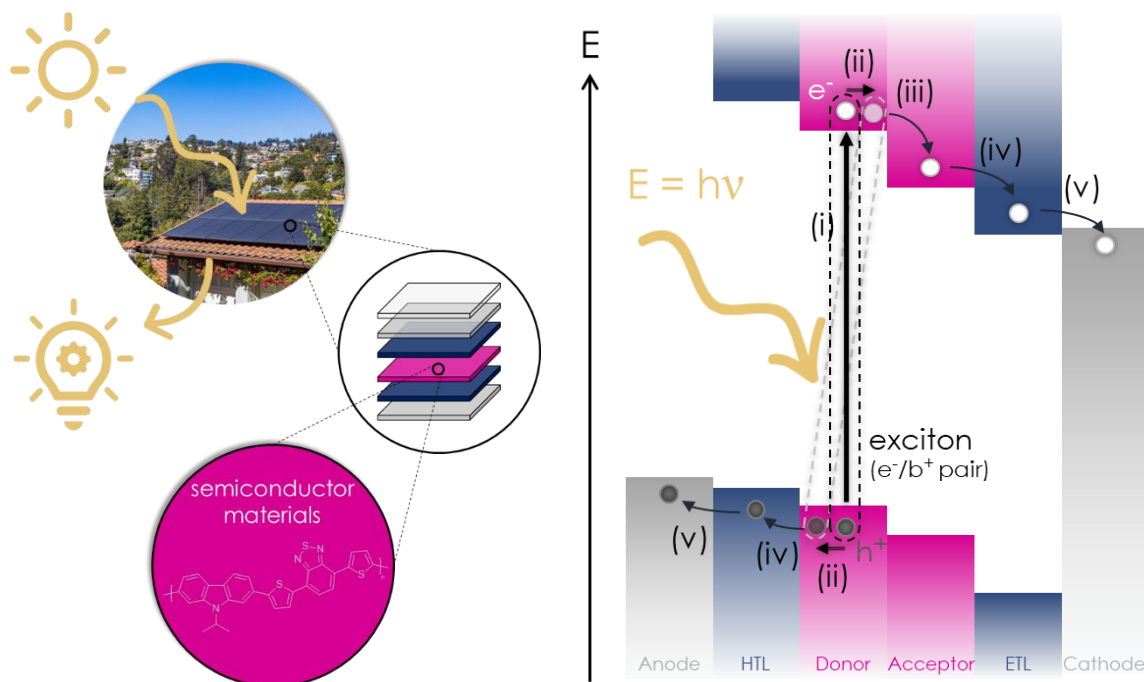


Figure 1.1 - Conventional architecture of an OPV device and mechanisms of PV effect. Electrons (light circles) and holes (dark circles).

This diagram with electronic properties of materials in their ground states is very common in the literature, even though it neglects electronic interactions such as the polarization effect and charge transfers that possibly occur between the layers [20], as well as the exciton up-conversion process from triplet to first singlet excited states via reverse intersystem crossing in a ternary cell, *i.e.*, a cell which contains an active layer composed of three materials [5].

Device engineering of OSCs combines infinite possibilities to achieve the highest power conversion as each layer has its own particularities [24], starting from the encapsulation. To protect the device against atmosphere oxidizing agents such as water vapor and oxygen gas, a substrate with an encapsulating material must ensure barrier performance to prevent mechanical

degradation [25,26], directly affecting the device's lifetime [27]. Moreover, plastic substrates such as poly(ethylene terephthalate) (PET) are used instead of rigid glass to produce flexible OSCs [28]. Nevertheless, it is essential that the barrier material presents affordable light permittivity and couples with the interfacial electrode.

Electrodes are high (low) work function metals to collect holes (electrons), assuming the role of the anode (cathode). These layers can drive charges and have low recombination losses, such as when they contain transparent conductive oxide, conductive polymer, carbon nanotubes, graphene, or nanostructured materials [29]. These charge-selective layers can comprise materials with high transparency in visible light and high conductivity, such as indium tin oxide (ITO) surfaces. More recently, dielectric/metal/dielectric multiple layers have been developed as less expensive alternatives for the replacement of indium [30–32].

For a material made part of efficient interface layers, it should promote an Ohmic contact between electrodes, have low absorption in the visible and near-infrared region (Vis-NIR) light for reducing optical losses, have energy levels appropriate to conduct charges to the electrodes, have a large bandgap to keep excitons in the active layer, have good conductivity for minimizing resistive losses and have chemical and physical stabilities for avoiding undesirable reactions with materials of the other layers [33].

Transition metal oxides are more employed than conjugated polyelectrolytes as a material for OPV-interfacial contacts due to their higher charge selectivity (efficient electron extraction and hole blocking) and maintaining a good cell performance even under low light conditions [34]. Molybdenum oxides (MoO_3) and a p-doped conducting polymer (PEDOT:PSS) are the most common materials for HTL of OPVs, while n-type metal oxides, particularly zinc oxide (ZnO), titanium dioxide (TiO_2) and tin oxide (SnO_2) are used as ETL [35]. Their properties can be tuned; for example, ZnO doped with a fullerene derivative forming a ZnO- C_{60} film showed an increase of around 1.5% in relation to only ZnO cathode, even varying the materials of the active layer [35]. Another technique to tune optical properties is the nitrogen doping of SnO_2 , which slightly increases the absorption in the visible region compared to the undoped oxide [36].

The active layer of OSC typically consists of a mix of semiconductor photoactive materials, including electron-donor and electron-acceptor materials, in which the photovoltaic mechanisms start. Absorption of photons in solar cells happens for photon energy greater than the donor bandgap energy. Electrons are excited from the valence band's top edge to the

conduction band's bottom, corresponding to a charge transfer mechanism. The unabsorbed energy causes rapid emission of phonons, and it is converted to unwanted heat that is transformed into thermal energy instead of electricity [37].

The exciton diffusion within the layers occurs along approximately 10 to 20 nm in organic semiconductor materials and its low dissociation [38,39], demanding a high density of interfaces between the materials to avoid energy losses. Therefore, it is required to apply effective techniques to the material to tailor its self-assembly and layer morphology, such as thermal annealing [40] and adding a ternary component in the bulky active layer [41] respectively.

Ternary solar cells combine three materials with complementary absorption spectra (see examples in Figure 1.2) in the active layer to create a device with a wide range of photon harvesting [41,42]. The choice of materials for the photoactive blended layer is initially investigated from the cascade energy levels, as shown in Figure 1.2. However, to verify if the cell can achieve the highest efficiency, it is necessary to probe an appropriate ratio of the blend miscibility by having a homogeneous bulky distribution during film production.

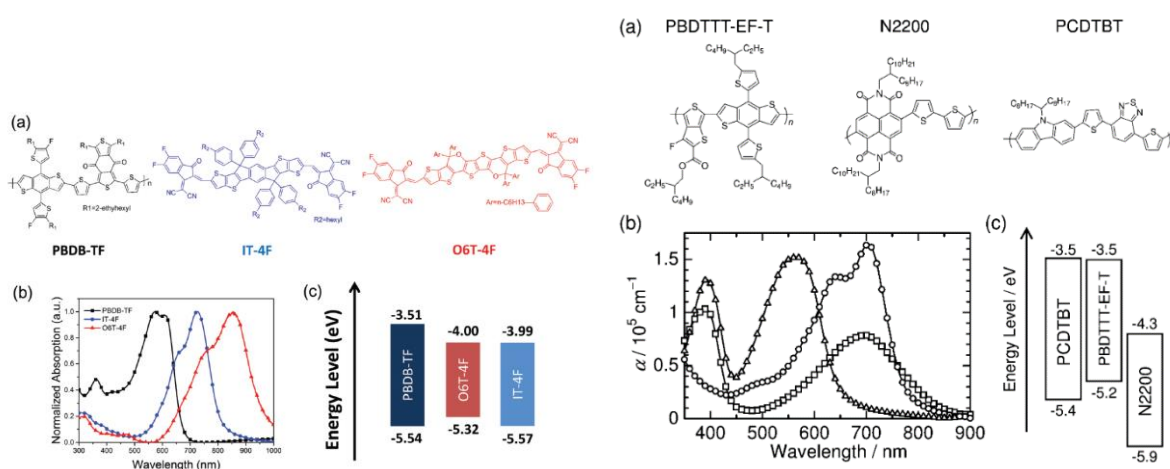


Figure 1.2 – Ternary blend of semiconductor materials, (a) their molecular structures, (b) complementary absorption spectra covering the range 400~800 nm, and (c) energy level diagrams from the works of Wang *et al.* (left) [44] and Benten *et al.* (right) [46].

The compatibility between the materials can enable a fluid charge transfer which will enhance OPV efficiency [43–46]. Care is required during this process. Should the materials be too

interspersed, they might create zones that lead to charge trapping and recombination, and excitons cannot meet interfaces between the materials to be converted to charges.

The optical and electronic properties of semiconductor materials are known to directly affect the photovoltaic properties of OPV cells, and the structural and electronic characteristics of each molecule will impact device efficiency in numerous ways [9,17]. To pursue the highest cell performances, tuning the energy of the bandgap and the energy levels of conjugated polymers are key elements and can be done by varying the structural elements of the participating molecules and macromolecules [19,47–49].

Indeed, many researchers have pointed to the critical role of the energy gap in optical absorption [23], excitons formation and dissociation [9,50], charge transport [20,51] and, consequently, performance device parameters [52]. However, there are several concepts of energy gap with specific meanings, causing much confusion to the scientific community when interpreting data and comparing results of different authors. Some of their terminologies are discussed below, mainly based on explanations of Brédas [53].

1.1.1 Definition of Energy Gap

Conjugated polymers are organic semiconductor materials constituted of a molecular structure engaged in covalent bonding interactions between atoms, such as carbon, nitrogen, oxygen, and sulphur, comprising hybrid atomic orbitals. These bonds arise from shared electrons that lead to the formation of π and π^* molecular orbitals in which the electrons and holes are energetically located, respectively. The significant overlap between them with increasing conjugation length gives rise to the valence and conductive bands, as described in Figure 1.3 [54].

Electronic transitions within conjugated polymers predominantly occur between the frontier electronic levels [56], that is, from the highest-occupied molecular orbital (HOMO) to the lowest-unoccupied molecular orbital (LUMO). This gap is simply named the electronic gap or HOMO-LUMO gap (E_g^{HL}), and it represents the energy difference between these two orbitals, as shown in Equation (1.1).

$$E_g^{\text{HL}} = E_{\text{LUMO}} - E_{\text{HOMO}} \quad (1.1)$$

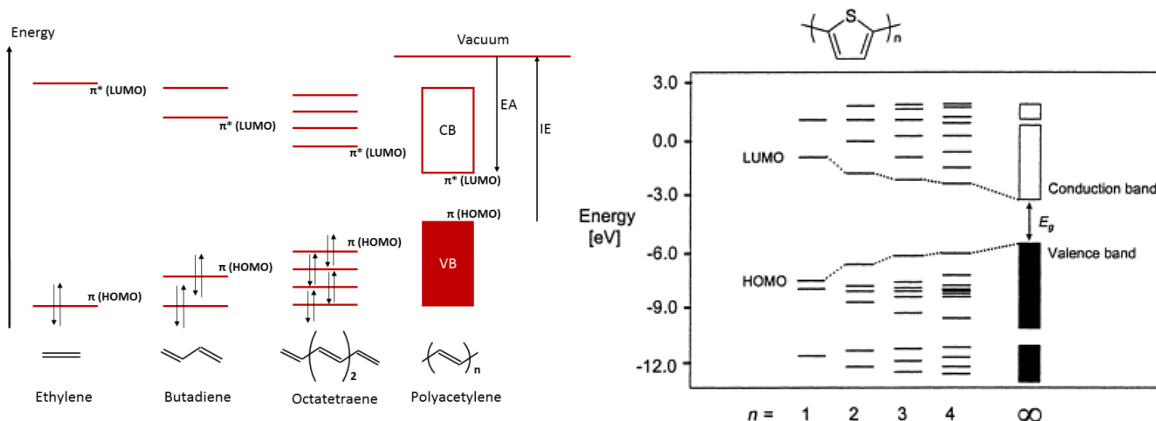


Figure 1.3 – Diagram of molecular orbitals forming bands with the coupling of conjugated systems[47], from Gueye *et al.* (left) [55] and van Mullekom *et al.* (right) [47].

It is important to clarify that molecular orbitals correspond to one-electron wave functions. Experimentally, they are accessed from a molecule in the N -electron ground state upon excitation (N -electron excited state) or ionization ($N\pm 1$ -electrons ionized states) [53]. Therefore, it is a misleading approximation to compare the difference in energies of orbitals with the differences in molecular energies.

Concerning optical properties, the optical gap is the energy of the lowest electronic transition accessible via the absorption of one photon. In both the solid state and the gas phase, it is measured from the transition energy of molecules in a ground state to the first excited state. The optical gap is the property that quantifies the energy required for a material to absorb light in a specific wavelength.

Considering principles of quantum mechanics (Planck-Einstein theory about the dual character of light), the photon energy is calculated in terms of the Dirac constant \hbar (Planck's constant divided by 2π) and the speed of light C , demonstrated in Equation (1.2).

$$E = \frac{\hbar \lambda}{C} \quad (1.2)$$

At the molecular level, materials can absorb light of corresponding photon energy when $E_{\text{gmolecule}} = E_{\text{photon}}$. Taking Planck's constant as equal to 6.6261×10^{-34} J.s and the speed of light as 2.9979×10^8 m.s⁻¹, so the optical gap is calculated as:

$$E_g^{\text{opt}} = \frac{1239.8}{\lambda}, \quad (1.3)$$

in which λ is the wavelength given in nanometres (nm).

The wavelength of the highest intensity of the spectrum of photo flux of sunlight is in the range of 400~800 nm, with a peak at around 680 nm [49] (see Figure 1.4). Taking into account Equation (1.3), materials with an optical gap of 1.6~1.9 eV (775~650 nm) are needed to obtain the highest sunlight harvesting [54]. Nevertheless, only verifying the optical gap value of the main device layer does not give the absolute absorption level of quality for an OPV cell. Until January 2023, the best performances were achieved for the highest absorber material bandgap energy from 1.35 to 1.45 eV [52].

Despite this, analysis of the optical gap is still an initial strategy to achieve the best device performance. Therefore, the active layer should cover the highest intensity of sunlight irradiance spectrum, in other words, opting for a blend of photoactive materials with complementary absorption spectra is a good strategy [57].

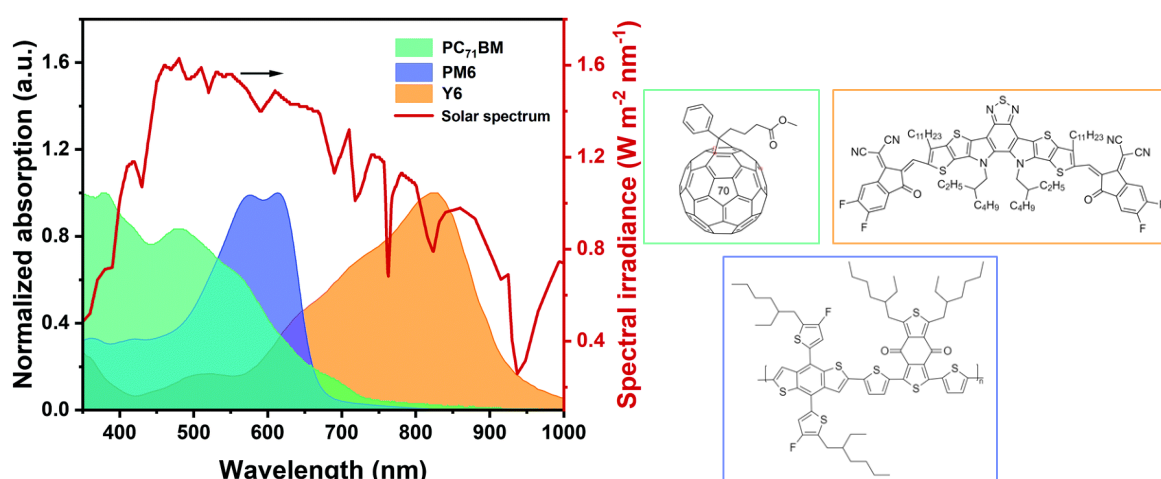


Figure 1.4 – Complementary absorption spectra of conjugated molecules [57].

The conjugated polymer regioregular poly(3-hexylthiophene) (P3HT) has a relatively large bandgap (around 1.9 eV, absorption range of 350~650 nm), very similar to gallium-indium-potassium bandgap (1.85 eV), and it was pioneer material in the development of solution-processed OPV devices [51].

Over the past few years, new conjugated polymers such as PM6 and PTB7-Th have come out with stronger electron push-pull effects and, consequently, better device performance, as chain backbones are composed of alternating donor and acceptor blocks [58,59].

According to UV-vis absorption measurements [35,43,46,59–61] and theoretical calculations with TD-DFT [59,62], the UV-vis spectrum of the polymer PTB7-Th has two main peaks: the stronger at around 700 nm and a shoulder at 640 nm, with energies that can correspond to the transitions between the ground state E_{0-0} and the first two vibronic levels of excited state E_{0-1} , respectively.

Kim and collaborators [59] observed photodegradation phenomena for the PTB7-Th polymer in solid and molecular states. The measured UV-vis absorption spectra showed a gradual reduction of the absorption peak at 640 nm during the illumination exposure. This peak is often assigned to the 0-1 transition in π -conjugated systems, then its intensity reduction indicates a decrease on the conjugation length and π - π stacking interaction.

In another work [62], only the absorption peak A_{0-0} depends on the solution concentration of PTB7-Th polymer in chlorobenzene, arising from intra and interchain disorders due to reduction of concentration. Both peaks are temperature-dependent, meaning that the copolymer chains are strongly aggregated in the room temperature solution and interchain interactions become weaker when heating the solution.

The absorption band in the range of 400~420 nm corresponds to π - π^* transitions of the aromatic ring of donor building blocks, while the peaks at 500~700 nm are related to an intramolecular charge transfer transition [63].

Photocurrent generation also depends on how the material relates to charge carriers, associating to molecules and materials to atomic properties which translate this correlation. The ionization potential (IP) corresponds to the amount of energy necessary to remove one electron of a neutral specie. A high IP means it is hard to remove electrons from the molecule, describing that the material has a strong stability concerning the oxidation. The energy of a neutral-state molecule required to receive one electron is interpreted as electronic affinity (EA); a small EA means the molecule tends to accept electrons. The energy difference between them is called the fundamental gap.

$$E_g^{\text{fund}} = IP - EA \quad (1.4)$$

Considering Koopmans' theorem [64,65], the HOMO energy can be estimated as equal to the ionization potential, as well as the LUMO energy in relation to the negative value of electronic affinity, as shown in Equation (1.5) and Equation (1.6), respectively.

$$E_{\text{HOMO}} \cong -IP \quad (1.5)$$

$$E_{\text{LUMO}} \cong -EA \quad (1.6)$$

Therefore, according to Koopmans' theorem, the HOMO-LUMO gap is approximated as the fundamental gap for infinite chain systems [50]:

$$E_{\text{g}}^{\text{HL}} \cong E_{\text{g}}^{\text{fund}} \quad (1.7)$$

We want to emphasise that this approximation ignores relaxation effects of ionized species, and for which reason it provides incorrect predictions for molecules absorbing photons. In addition, in quantum-chemistry, Koopmans' theorem is only valid for Hartree-Fock orbitals, so it could be erroneous to estimate HOMO and LUMO energies from Kohn-Sham orbitals (considering exchange energy) as it is the case for calculations performed using DFT [66].

Following on from the processes of the photovoltaic effect, to generate photocurrent it is necessary to dissociate exciton into free charges and transport them to the other layers up to the electrodes. There, another property comes out characterizing the interaction of charges into the material: the exciton binding energy E_b . In other words, it is the energy of an electron and a hole bound electrostatically.

In inorganic semiconductors, the exciton binding energy is measured from the classical Coulombic interaction, and it is strongly dependent on the material dielectric constant ϵ_r and charge distribution on the molecule; however, this correlation cannot be used for organic materials due to their high disorder degree [67].

Regarding organic semiconductors, the energy connecting the electron-hole pairs can vary significantly as a function of the conjugation length of the compound [68], as it is usually found E_b in the range of 0.1 to 0.5 eV for conjugated copolymers [22,69]. For Brédas *et al.*, the completely unbound electron-hole pair is measured from the adiabatic IP of the donor and EA of the acceptor, corresponding to the energy of the final charge-separated state [20].

For conjugated polymers in solid state, the exciton binding energy is estimated from the difference between optical and transport gaps, correlating ionized and excited states:

$$E_b = E_g^{\text{fund}} - E_g^{\text{opt}} \quad (1.8)$$

Then, considering the fundamentals of Koopmans' theorem, from Equation (1.7), the exciton binding energy can be approximated as:

$$E_b \cong E_g^{\text{HL}} - E_g^{\text{opt}} \quad (1.9)$$

As it was mentioned before, these approximations do not take into account the relaxation effect on the other orbitals, so correction factors must be added to solve this problem [70].

After an intensive review of the correlation between molecular structure and electronic properties of small organic compounds, Zhu and collaborators [67] found that E_b is inversely proportional to the conjugation length of the backbone, the dipole moment of end-groups, and properties of side chains, such as steric hindrance and dielectric constant.

According to Bhatta and Tsige [50], E_b can only be extracted directly from HOMO-LUMO and optical gaps calculated for the infinite chain molecule, as E_g^{HL} only approaches E_g^{fund} when the conjugation length is infinitely long.

To clarify all the concepts about optical and electronic properties, Figure 1.5 was produced, in which the molecule was represented as an electronic cloud.

More recent works have come up with the concept of the device bandgap, in which equation and methods to extract this property from external quantum efficiency spectrum are presented at respectively references: Almora and collaborators [52] showed the effective absorber bandgap as a function of cell-performance parameters for several photovoltaic technologies, while Saito, Ohkita and Osaka [71] related the bandgap of materials with the energy from open-circuit voltage of the OPV cell to obtain information on the photon energy loss.

Given all these arguments, it is indispensable to map the main approaches to tune optoelectronic properties, correlating them with chemical structure when designing novel molecules for the highest efficiency of OPV cells.

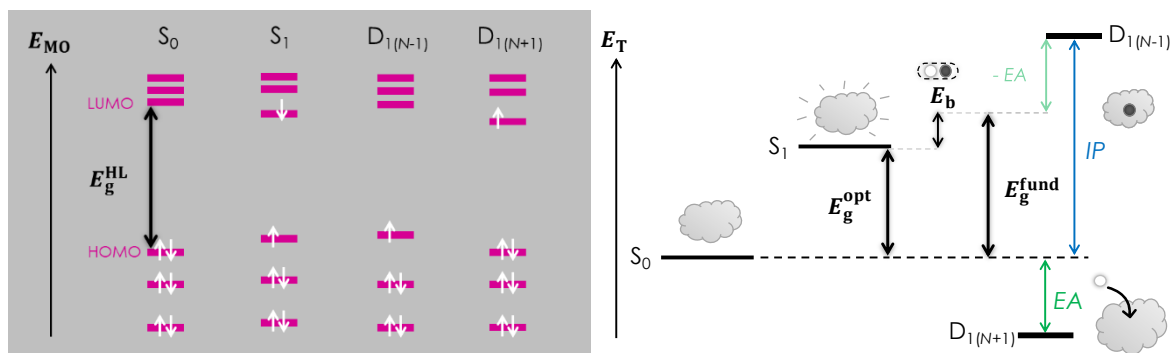


Figure 1.5 - Diagrams summing molecular orbital energies, properties from ionized states, energy gaps and correlations, and the approximation to calculate the exciton binding energy.

1.1.2 Strategies for Tuning the Bandgap

The orientation of a polymer chain in a solid state has a critical role in the photocurrent generation of OPV devices, seeing that electronic coupling for interactions in the active layer blend must be adjusted to eliminate geminate recombination [72,73]. Structure-property optimizations come out to fully correlate the polymer structure with properties at molecular level [17], in an approach also called molecular design.

Structural parameters such as replacing carbon and hydrogen atoms in the polymer backbone with heteroatoms or incorporating side chains are widely investigated for tuning the bandgap of π -conjugated systems [62,74,75].

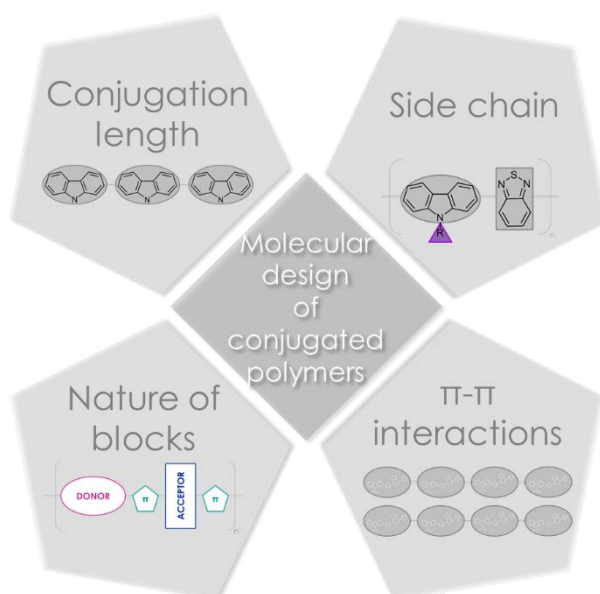


Figure 1.6 - Diagram of structural modifications in molecular design studied in this work.

For Roncali [19], modifications in the polymer backbone are verified on changes of bond length alternation and dihedral angle between blocks, directly acting in the HOMO-LUMO gap energy, as a covalent rigidification of the system interferes with the delocalization of π -electrons along the chain.

Keeping in mind the importance of intra and intermolecular interactions, the following text describes the effect of conjugation length, side chains, nature of the blocks and π - π interactions of conjugated polymers, as for us they are the most important structure parameters for tuning optoelectronic properties.

1.2 Conjugation Length

For an organic semiconductor to be an ideal material for photocurrent generation, a delocalization of π -electrons along the polymer chain is expected to happen, with as few losses of energy as possible. Even though conjugated polymers consist of an infinite chain, the optoelectronic properties converge at a certain conjugation length.

The oligomer approach is used in computational investigations of semiconductor materials for estimating polymer properties from the modeling of oligomers, that is, molecular models composed of a few repeating units of polymer. It reduces the computational cost of the analysis ensuring great predictions. It is essential to model a molecular system with a conjugation length that accurately represent the convergence of the property.

1.2.1 Geometrical Optimization Techniques

It was often noted that the backbone's high planarity enhances intramolecular charge transport and molecular packing [1]. Thus, methods to control the torsion of the chain can be applied during the molecular design only by playing with blocks with different behaviours of push and pull electrons [50].

It is also important to mention that mechanical distortions of the molecular structure may lead to modifications in the device's performance. It was found that the elongation of conjugated chain increases electronic gap energy and causes meaningful changes of the absorption spectrum, exciton binding and reorganization energies [76].

1.2.2 Influence on Optical and Electronic Properties

Since 1983, Brédas and collaborators [77] have shown the conjugation length dependence of electronic and electrochemical properties for polymeric systems. Not taking this into account, it is common to find works that compare experimental results with theoretical data calculated from only one repeating unit structure [78,79], consequently encountering huge energy differences and making incorrect assumptions on structure-property correlations.

Concerning optical properties, Demadrille and his research group [80] confirmed a bathochromic shift of the π - π^* transition with increasing conjugation length; that is, the absorption peak moved to a longer wavelength as adding more repeating units of the 2,7-bis(4-octylthien-2-yl)-fluoren-9-one.

Kim and co-authors [59] presented some good highlights concerning the proper conjugation length. Initially, a PTB7-Th model with two repeating units of acceptor-donor (AD) structures was used to calculate the UV-vis absorption spectrum with TD-DFT. As this model was unable to reproduce the experimental results (a main absorption peak was at 702 nm for the pristine PTB7-Th against the predicted 603 nm), a 4 AD-unit molecule was modelled, also replacing the alkyl side chains (2-ethylhexyl) by H atoms to reduce computational costs. From the calculation of UV-vis spectrum of this AD-AD-AD-AD model, an absorption peak was found at 707 nm, that can correspond to the ground state transition, referenced as 0-0. This result is not only in agreement with their laboratory results but also with other works [35,43,46,60–62], even under different measurement conditions.

Kim and collaborators [59] suggested that AD-AD-AD-AD (4u) structure is the minimum size model for reasonable predictions of electrical properties of PTB7-Th polymer. It is important to mention some methodological details: geometry optimizations were done at 6-31G(d) level, while TD-DFT calculations were performed at 6-31G+(d) basis set, both using B3LYP as functional. In addition, in all the calculations, chlorobenzene ($\epsilon=5.7$) was used as a solvent to introduce the solvent effect with a conductor-like polarized continuum model (C-PCM).

Regarding electronic properties, the team of McCormick [81] concluded that the suitable conjugation length are 6 and 4 repeating units for homopolymers and copolymers, respectively, as variations lower than 0.1 eV are found when adding an extra monomer. On the other hand, Turan and collaborators [82] found that the energy difference between trimers and tetramers was negligible for the HOMO energies as well as for LUMO ones. Therefore, in their study,

copolymer chains longer than four monomers were not considered to gain computational time, justifying that calculation accuracy was maintained.

Exciton dissociation into free charges is largely related to the exciton binding energy of the organic semiconductor material. This is a property strongly affected by the conjugation length. Thus, small values of exciton binding energy as longer is the molecule size [68]. It means that less energy is needed to separate the electron-hole pair of molecules with a bigger conjugation length than for small molecular systems.

Extrapolation approaches are used to estimate the energy gaps of polymers from the oligomer systems, discussing the method accuracy, saturation chain length, or effective number of repeating units [50,81,83–86], giving preference to nonlinear fitting to avoid errors in the saturation of energy gaps [87]. Fitting based on a Frenkel exciton theory and the other based on the model of independent electrons in a box with sinusoidal modulation of potential have significant outcomes for comparing among computational methods, showing the best estimation of the exciton model for the asymptotic values of the transition energies [88].

1.3 Nature of Blocks in the Polymer Backbone

Conjugated polymers, whose main chain is composed of fused aromatic rings of carbon and other non-metallic atoms, are more commonly employed as donor material in the active layer due to their photoresponse in the highest intensity solar spectra range. Even though most conjugated polymers have lower electron mobility, they also can work as an electron-withdrawing material [21].

At this point of the text, it is important to distinguish donor and acceptor materials from the chemical structures of the repeating unit of polymers, electron-rich and electron-deficient, assumed as donor and acceptor blocks, respectively; those are under investigation here.

Aromatic rings employed in these blocks are affected by the resonance energy, which quantifies how much one conformation tends to confine π -electrons. Polymers containing aromatic rings transit from quinoid structure to its aromatic form, exhibiting limited stability [19,47,49]. Incorporating certain thiophene rings in the backbone disfavours the quinoid form, thus causing benefits for electronic properties [89].

A technique used to increase solubility and facilitate the polymerization of single rings is to add carbon atoms as covalent bridges between aromatic rings and between high electronegative atoms in side chains, like in cyclopenta[*c*]dithiophene (CPT) and 3,4-ethyldioxythiophene (EDOT) [19].

Fused-ring blocks such as benzodithiophene (BDT) enhance the planarity of the conjugated structure and form stronger π - π stacking interactions than single-ring blocks, improving the hole mobility [22,49]. The high rigidity of these larger molecular blocks can mean that the polymer backbones do not lose their conjugation length and π - π stacking interactions in solution [62] but they are not enough to be electronically stable under sunlight [59].

Structures classified as electron-deficient, such as thienothiophene (TT) blocks, are added with BDT blocks to stabilize their strong quinoid character, leading to a lower energy bandgap [22,90].

Playing with the polymer backbone by connecting various blocks in the repeating unit is a strategy employed to change electronic cloud distribution and tune the optoelectronic properties.

1.3.1 Coupling Donor, Acceptor and Other Types of Blocks in the Polymer Chain

Electron-donor (D) coupled with electron-acceptor (A) blocks create D-A conjugated polymers, structures with electron push-pull effect under certain conditions. When classifying a block as donor or acceptor it is to affirm that this structure needs less energy to withdraw or receive electrons, respectively.

Even though this coupling is beneficial for electron delocalization along the chain, it induces large deviations in the planarity of the conjugated backbone, attributed to interactions between the hydrogen atoms on the donor rings and the neighbouring atoms of the electron-acceptor unit. Indeed, coupling donor and acceptor may result in a self-rigidification of the conjugated structure from the noncovalent interactions between neighbouring blocks [19]. The non-planarity of the polymer chain impacts on the π -electron delocalization and, consequently, on the intramolecular charge transfer [82].

Another approach to solve problems of interactions between acceptor and donor moieties and improve the performance of organic chromophores is to add thiophenes as π -bridges, creating Donor-Thiophene-Acceptor-Thiophene (D-T-A-T) or simply D- π -A structures.

Comparing D- π -A compounds to reciprocal D-A systems, the one thiophene ring additions in the polymer backbone cause a redshift in the absorption peaks of the steady-state spectrum and create charge-transfer states [91]. It is possible to conclude π -bridges can increase the electron delocalization [82], improving the spatial overlap of wave functions [92]. However, adding thiophene rings is limited as too long π -bridges result in nongeminate recombination, which is not beneficial for photovoltaic conversion [91].

This strategy of combining donor, acceptor and π -spacers in the polymer backbone impacts in the optical and electronic properties, summarized in Figure 1.7 and more detailed below.

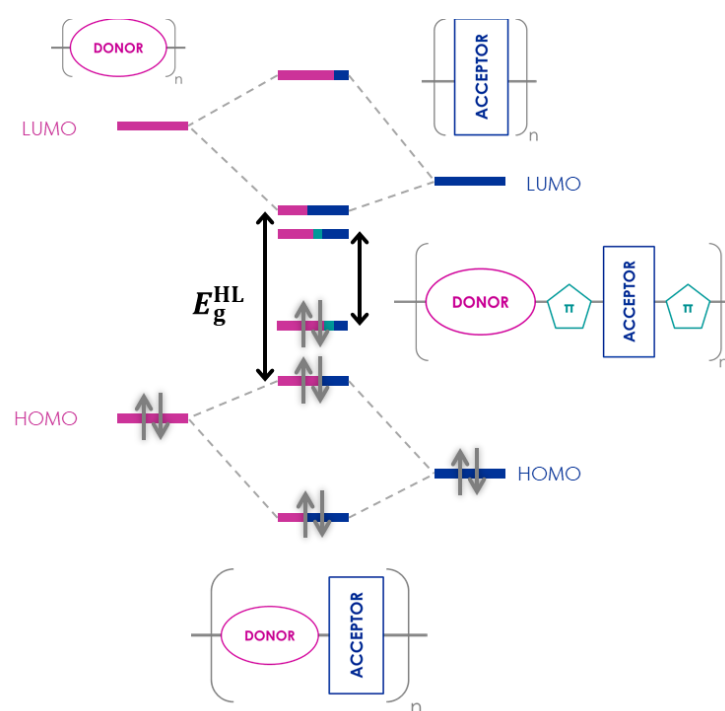


Figure 1.7 – Diagram of the effect of the nature of blocks of polymer backbone on its energy gap.

1.3.2 Investigating Optical and Electronic Properties for Assessing Donor-Acceptor Interaction

The bandgap of conjugated polymers is easily sensitised to steric hindrance between two adjacent units, so for better charge transport, it is important to choose conjugated units that cause very small steric hindrances between neighbouring groups, such as 4,9-bis-alkoxy-BDT, which has no substituent in the 1, 3, 5 and 7 positions [49].

The hybridization of orbitals as well as the coplanarity and packing degree of donor/acceptor moieties contribute to the orbital energy levels of D-A copolymers [93].

The higher the ratio of electron-donating block in the polymer backbone, the higher the HOMO energy [94]. While HOMO wavefunctions are delocalized over donor and acceptor units, LUMO wavefunctions are generally composed of the acceptor block [92].

The addition of thiophene bridges to the polymer main chain decreases the HOMO-LUMO gap [91] and optical gap as they extend the wavefunction delocalization [92].

Replacing the heteroatoms on the backbone has a bigger effect on acceptor moieties than on donors [56,82,95]. In comparison of the same donor moiety, D-A systems showed no significant effect on optical gaps for C/N substitution, as opposed to N substitution by Si due to its bigger atomic size decreasing the backbone curvature, resulting in a HOMO energy difference of 0.5 eV depending on the acceptor motif [82,92].

In the electron-withdrawing units, replacing the sulphur atom with oxygen or selenium atoms, both HOMO and LUMO energy levels slightly decrease [95,96] because of the backbone planarity loss due to their interaction with neighbouring monomers. This difference increases with S/N and C/N substitutions [82,95], an effect explained by the increased number of free-electron pairs.

Furthermore, localization or delocalization of the wavefunctions of LUMO is negligible over heteroatom substitutions in both moieties of copolymer backbones [82].

It was shown that including an acceptor block with greater delocalization of the electrons can be related to a stronger quinoidal nature of the benzothiadiazole (BTD) block in comparison to a fluorenone group [63].

1.4 Side Chains

An optimum combination amongst the type, size and position of side chains in the polymer backbone still needs to be defined in the scientific community, as these are very specific for each polymer [17].

The side chains impact upon the planarity of the conjugated backbone, for example, small molecules were found to have more planar structures with branched side groups compared to those with linear ones, and thus presented greater light absorption and a smaller bandgap [97].

However, when it comes to polymers, devices containing materials with linear alkyl side chains in the chain backbone showed better performances than those with branched 2-ethylhexyl, justified by the main variation of HOMO levels [63].

Carrying an X-ray diffraction (XRD), an out-of-plane measurement resulted in 20.5 Å of distance between polymer chains in the same plan (named in that work as interlayer), indicating that the bulky side chains promote a high degree of crystallinity in orientations perpendicular to the substrate [98].

1.4.1 Impact of Side Chains on Material Solubility and Morphology

The importance of side chains for the solubilisation of the polymer backbone is well known. Long alkyl side chains increase solubility, but also promote greater steric hindrance effects, and decrease a compound's crystallinity [40].

Side chains are also determinant in the interactions between the main polymer chains, consequently changing the material's morphology. Including linear and branched alkyl side groups increases the π - π stacking distance between aromatic rings of polymer core [99]; therefore, the morphology of the film containing the polymer is affected, reflecting in the OPV efficiency [100].

Moving forward from these effects on the material, side chains modify the polymer structure and, consequently, the delocalization of charges along the chain, confirmed when investigating their electronic properties [17].

1.4.2 Correlation between Side Chains and Electronic Properties

Molecular energy levels are tuneable by modifying the side chains, as well as the bandgap, as can be seen in poly(3-alkylthiophene) (P3AT) whose bandgap decreased from 1.85 to 1.55 eV after the 3-position substitution of alkyl groups for alkoxy ones [49].

Including the main polymer chain electron-withdrawing substituents, such as nitro, trifluoromethyl, sulfone, nitrile (cyano) and methylene malononitrile cause a reduction of the gap and the HOMO and LUMO level energies [101]. In contrast, electron-donating groups such as amines, long alkyl chains and alkoxy groups increase the energy of frontier orbitals [19] but do not affect the HOMO-LUMO gap [101].

Even though these approaches aim for better energetic performance of conjugated systems, both deal with a lower solubility of the material and difficulties in the polymerization by the lack of electrochemical stabilization, as electron-withdrawing (donating) substituents reduce (increase) the oxidation potential [19].

From UV-vis absorption measurements of polythiophene films, as increasing the size of the alkyl side chain, there was a decrease in the absorption coefficient, although the optical gap remained around 1.92 eV, showing that this property is not dependent on side chain length [102].

In simulations, it is common to replace long alkyl side chains with short chains (methyl or ethyl) or even by hydrogen atoms. Some literature results show that this replacement does not affect the structure of molecule systems from a computational point of view (calculated HOMO energies and optical gaps presenting a small difference with and without side chains), achieving accurate results and reducing calculation costs [59,81,82,94,95].

Evaluating the structure of D-A copolymers with different side chains attached to the electron-donating moiety, the angles between the donor unit and the thiophene ring linkers calculated were approximately 0° for all alkyl side chains, meaning that there was a coplanarity on this part of the 3-unit oligomers [103]. Also, it was reported that there was no dependence of the dihedral angles on the alkyl side-chain length and no relation between this and electronic properties looking just to the electron-donating unit.

On the other hand, when calculating it for oligomers in whose side-chain substitutions are on the electron-withdrawing unit, the dihedral angle between the adjacent thiophene unit and the acceptor moiety increase with a bulky side-chain (H and methyl substituents with a $\phi \approx 0^\circ$, against $\phi \approx 72.5^\circ$ of isopropyl substituent) [82]. They affirm that bulky side chains create a steric repulsion to the sulphur of the adjacent thiophene unit, resulting in structures with large deviation from coplanarity, decreasing the π -conjugation and consequently increasing the energy gap.

The parameters of polymer structure discussed previously are part of the intramolecular interactions, that is, between units or atoms of the same chain. However, polymers are not isolated systems in the material, so it is also important to investigate chain interplays driven by a special intermolecular interaction: the π - π interactions.

1.5 Intermolecular interactions

The origin of these interactions is the Van der Waals forces that explain most physical properties of materials, such as boiling point, melting point and solubility, and are briefly explained below [104,105]:

- Dipole-dipole force: it occurs between permanent dipole molecules when the partial negative-charged part of a polar molecule attracts the partial positive-charged end of another;
- Dipole-induced dipole force: known as Debye force, it can happen as a polar molecule induces an instantaneous polarization of the electron cloud of a nonpolar molecule;
- London dispersion force: it is induced dipole-induced dipole interactions that occur between nonpolar molecules; it is the weakest of all intermolecular interactions;
- Hydrogen bonding ($X-H\cdots Y$): it is a special kind of dipole-dipole interaction between a hydrogen atom bonded to an atom X with higher electronegativity, as oxygen, fluorine and nitrogen, and lone-pair electrons of another electronegative atom Y.

In conjugated polymers, the fused aromatic rings of the main chain promote electrostatic attraction and repulsion of π -orbitals between molecules, called π - π interactions.

1.5.1 π -interactions in Conjugated Systems

The π - π interactions are generally used to describe the interactions between aromatic rings. It is commonly termed π -stacking and is an interaction due to the alignment of the π -orbitals of parallel molecules, leading to attractive forces between them. However, as Martinez and Iverson [106] summarised the discussion around this topic, parallel face-to-face aromatic rings are not the most stable systems; π - π interactions also involve electrostatic forces of the quadrupole moment of each molecule.

Investigating crystal structure, electronic and optical properties of D-A polymers such as polymers of the PTB family composed by thieno[3,4b]thiophene (TT) and benzodithiophene (BDT) blocks, there was found stronger π - π interactions in the BDT-BDT stacking, that is, between the electron-rich fused aromatic rings of one chain with the same block, than the intermolecular interactions between TT units [107], due to the greater π -conjugation along the polymer backbone in BDT blocks.

Conformational studies on dimer systems (double chains) are a computational strategy to investigate intermolecular interactions in conjugated molecules, as it was done for polymers composed of benzothiadiazole (BT) with cyclopentadithiophene (CPDT) or dithieno-silole (SBT), which one only replace a silicon atom with the 5-position carbon [108]. Comparing the binding energies for three different positions, dimers of PSBTBT showed that the stacking of SBT-SBT and BT-BT was more favourable than SBT-BT stacking. Also, the DFT calculation in the software Gamess using MO5-2X level showed around 3.56 Å of the distance between parallel blocks, almost the same 3.48 Å observed in grazing incidence X-ray diffraction (GIXD) result.

Attraction and repulsion of atoms, overlapping of π -orbitals and steric hindrance of side chains to the backbone are the main actors of the intermolecular interactions between polymer chains, playing a function as a zipper illustrated in Figure 1.8.

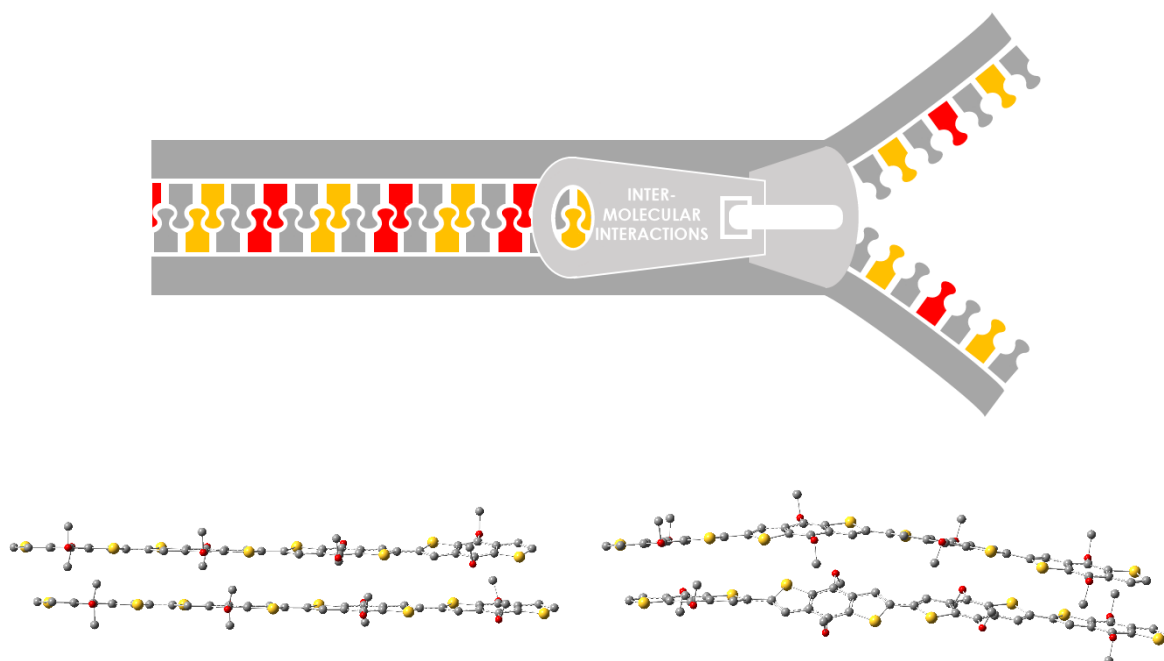


Figure 1.8 – Sketch of intermolecular interactions working as a zipper connecting chains.

Atoms of carbon, oxygen and sulphur respectively coloured in grey, red and yellow.

Structures plotted without hydrogen atoms to produce clear images.

The π - π interactions have a critical role in photovoltaic performance as they can enhance charge transport along the polymer backbone with a formation of ordered arrangements of polymer chains, as it has been seen in many cases of self-assembly studies to control the surface

roughness of films [109]. The replacing of short bulky (2-ethylhexyl) by long branched (3,7-methyloctyl) side chains resulted in a better π - π stacking as it decreased the steric effect, increasing the solubility of the material in addition and consequently improving the solar cell performance (1.0 % higher PCE) [110].

Some structural modifications can be done in the polymer chain favour π - π stacking. It was observed that the presence of long alkyl side chains (called substituents in that work) increases solubility mainly because it leads to a reduction of close π -stacking, but it negatively affects the oxidation stability of the material due to a lower packing system [19].

1.5.2 Effect of π -interactions in Optoelectronic Properties

Quantum-chemistry calculations are essential to describe the origin of HOMO and LUMO one-electron levels in isolated chains. Molecular orbitals split into valence and conduction bands as consequence of interchain interactions of polymers and oligomers [111].

Stacked dimers (see Figure 1.9) are modelled to investigate the main interactions that governed organic π -conjugated materials. However, the discussion stays in turn of the interaction energy calculation [112], the charge distribution in relation to kinds of interactions and to the intermolecular distance [113], or even using semiempirical approaches [111]. These fields go beyond the scope of this research.

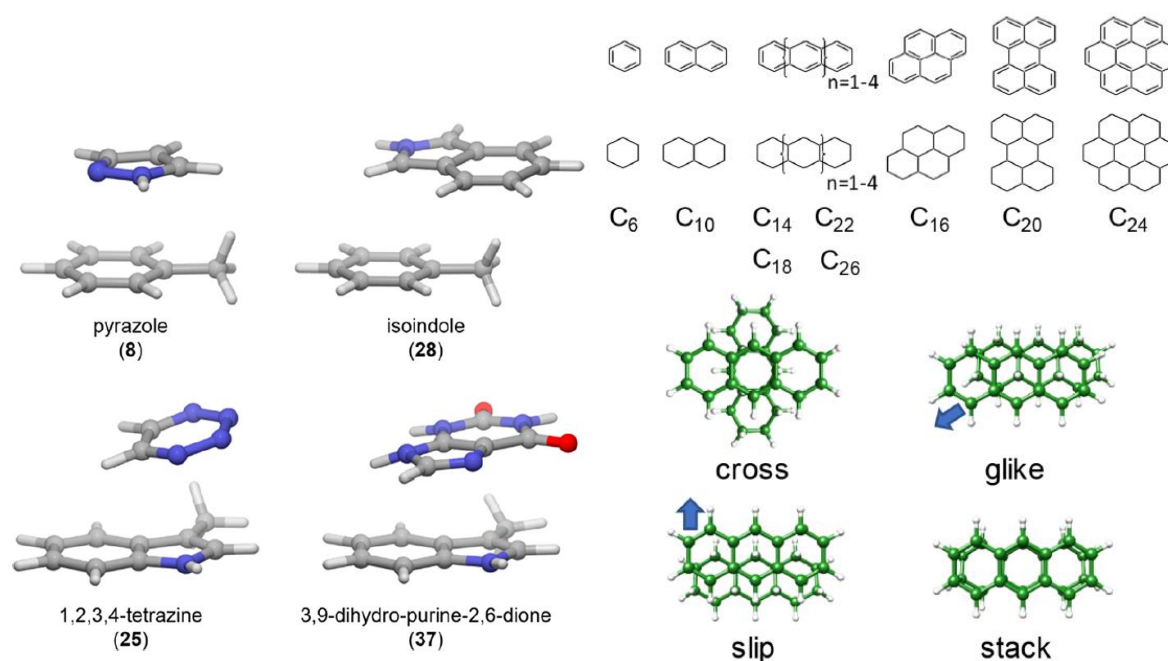


Figure 1.9 – Stacked dimers with different kinds of interactions [112,113].

The evaluation of intermolecular forces is primordial for bandgap prediction, considering interactions among polymer chains in a material [19]. However, until now, there has been no evidence of the correlation of polymer structure with optical and electronic properties. We only could find analysis such as that obtained by Benatto and collaborators [114] from calculations of two small molecules at ω B97XD/6-31G(d,p) theory level and the respective spatial distribution of the frontier orbitals. It was shown that for the most of them HOMO and LUMO are delocalized along the two molecules.

In face of all these arguments, we decide to investigate the correlation between the polymer structure and its optoelectronic properties. To this end, the main principles of computational methodology of density functional theory and tools for visualization analysis are explored in Chapter 3.

References

- [1] D. Luo, W. Jang, D.D. Babu, M.S. Kim, D.H. Wang, A.K.K. Kyaw, *J. Mater. Chem. A* 10 (2022) 3255–3295.
- [2] Q. Wang, Y. Xie, F. Soltani-Kordshuli, M. Eslamian, *Renewable and Sustainable Energy Reviews* 56 (2016) 347–361.
- [3] G. Li, R. Zhu, Y. Yang, *Nature Photon* 6 (2012) 153–161.
- [4] S.E. Yoon, J.M. Han, B.E. Seo, S.-W. Kim, O.-P. Kwon, B.-G. Kim, J.H. Kim, *Organic Electronics* 90 (2021) 106061.
- [5] H. Zhang, Y. Li, X. Zhang, Y. Zhang, H. Zhou, *Mater. Chem. Front.* 4 (2020) 2863–2880.
- [6] H. Youn, H.J. Park, L.J. Guo, *Small* 11 (2015) 2228–2246.
- [7] D. Kim, F.S. Kim, *Chem. Mater.* 33 (2021) 7572–7594.
- [8] Q. Wang, Y. Qin, M. Li, L. Ye, Y. Geng, *Adv. Energy Mater.* 10 (2020) 2002572.
- [9] B. Schweda, M. Reinfelds, P. Hofstadler, G. Trimmel, T. Rath, *ACS Appl. Energy Mater.* 4 (2021) 11899–11981.
- [10] J. Chen, Y. Chen, L.-W. Feng, C. Gu, G. Li, N. Su, G. Wang, S.M. Swick, W. Huang, X. Guo, A. Facchetti, T.J. Marks, *EnergyChem* 2 (2020) 100042.
- [11] H. Tang, C. Yan, J. Huang, Z. Kan, Z. Xiao, K. Sun, G. Li, S. Lu, *Matter* 3 (2020) 1403–1432.
- [12] Z. Rostami, L. Saedi, K.S. Beheshti, V. Vahabi, N. Ostadhosseini, *Solar Energy* 186 (2019) 72–83.

-
- [13] R. Ilmi, A. Haque, M.S. Khan, *Organic Electronics* 58 (2018) 53–62.
- [14] J. Roncali, P. Leriche, P. Blanchard, *Advanced Materials* 26 (2014) 3821–3838.
- [15] X. Guo, M. Baumgarten, K. Müllen, *Progress in Polymer Science* 38 (2013) 1832–1908.
- [16] H. Zhou, L. Yang, W. You, *Macromolecules* 45 (2012) 607–632.
- [17] R.L. Uy, S.C. Price, W. You, *Macromolecular Rapid Communications* 33 (2012) 1162–1177.
- [18] Z.-G. Zhang, J. Wang, *J. Mater. Chem.* 22 (2012) 4178–4187.
- [19] J. Roncali, *Macromolecular Rapid Communications* 28 (2007) 1761–1775.
- [20] J.-L. Brédas, J.E. Norton, J. Cornil, V. Coropceanu, *Acc. Chem. Res.* 42 (2009) 1691–1699.
- [21] A. Facchetti, *Materials Today* 16 (2013) 123–132.
- [22] L. Lu, L. Yu, *Advanced Materials* 26 (2014) 4413–4430.
- [23] F.C. Franco, A.A.B. Padama, *Polymer* 97 (2016) 55–62.
- [24] Z. Yin, J. Wei, Q. Zheng, *Advanced Science* 3 (2016) 1500362.
- [25] J. Ahmad, K. Bazaka, L.J. Anderson, R.D. White, M.V. Jacob, *Renewable and Sustainable Energy Reviews* 27 (2013) 104–117.
- [26] S. Cros, R. de Bettignies, S. Berson, S. Bailly, P. Maise, N. Lemaitre, S. Guillerez, *Solar Energy Materials and Solar Cells* 95 (2011) S65–S69.
- [27] C.H. Peters, I.T. Sachs-Quintana, J.P. Kastrop, S. Beaupré, M. Leclerc, M.D. McGehee, *Adv. Energy Mater.* 1 (2011) 491–494.
- [28] W. Cao, Z. Li, Y. Yang, Y. Zheng, W. Yu, R. Afzal, J. Xue, *Renewable Energy* 72 (2014) 134–139.
- [29] J.-J. Shen, *Synthetic Metals* 271 (2021) 116582.
- [30] R. Pandey, C.H. Wie, X. Lin, J.W. Lim, K.K. Kim, D.K. Hwang, W.K. Choi, *Solar Energy Materials and Solar Cells* 134 (2015) 5–14.
- [31] L. Cattin, J.C. Bernède, M. Morsli, *Physica Status Solidi (a)* 210 (2013) 1047–1061.
- [32] Z. Yang, T. Zhang, J. Li, W. Xue, C. Han, Y. Cheng, L. Qian, W. Cao, Y. Yang, S. Chen, *Sci Rep* 7 (2017) 9571.
- [33] H.-L. Yip, A.K.-Y. Jen, *Energy Environ. Sci.* 5 (2012) 5994.
- [34] M. Nam, S. Baek, D.-H. Ko, *Applied Surface Science* 526 (2020) 146632.
- [35] S.-H. Liao, H.-J. Jhuo, Y.-S. Cheng, S.-A. Chen, *Adv. Mater.* 25 (2013) 4766–4771.
- [36] S. Livraghi, N. Barbero, S. Agnoli, C. Barolo, G. Granozzi, F. Sauvage, E. Giamello, *Phys. Chem. Chem. Phys.* 18 (2016) 22617–22627.
- [37] J.S. Connolly, in: *Photochemical Conversion and Storage of Solar Energy*, Academic Press, 1981, pp. 229–242.
- [38] L. Zhu, M. Zhang, J. Xu, C. Li, J. Yan, G. Zhou, W. Zhong, T. Hao, J. Song, X. Xue, Z. Zhou, R. Zeng, H. Zhu, C.-C. Chen, R.C.I. MacKenzie, Y. Zou, J. Nelson, Y. Zhang, Y. Sun, F. Liu, *Nat. Mater.* 21 (2022) 656–663.
- [39] H.-C. Liao, P.-H. Chen, R. Chang, W.-F. Su, *Polymers* 6 (2014) 2784–2802.

-
- [40] O. Doat, B.H. Barboza, A. Batagin-Neto, D. Bégué, R.C. Hiorns, *Polymer International* 71 (2022) 6–25.
- [41] M. Zhang, J. Wang, X. Ma, J. Gao, C. Xu, Z. Hu, L. Niu, F. Zhang, *APL Materials* 8 (2020) 090703.
- [42] Q. An, F. Zhang, J. Zhang, W. Tang, Z. Deng, B. Hu, *Energy Environ. Sci.* 9 (2016) 281–322.
- [43] Y. Sun, C. Yang, Q. Li, K. Liu, X. Xue, Y. Zhang, M. Azam, K. Ren, Y. Chen, Z. Wang, S. Qu, Z. Wang, *Journal of Power Sources* 449 (2020) 227583.
- [44] B. Wang, Y. Fu, Q. Yang, J. Wu, H. Liu, H. Tang, Z. Xie, *J. Mater. Chem. C* 7 (2019) 10498–10506.
- [45] L. Zhong, L. Gao, H. Bin, Q. Hu, Z.-G. Zhang, F. Liu, T.P. Russell, Z. Zhang, Y. Li, *Adv. Energy Mater.* 7 (2017) 1602215.
- [46] H. Benten, T. Nishida, D. Mori, H. Xu, H. Ohkita, S. Ito, *Energy Environ. Sci.* 9 (2016) 135–140.
- [47] H.A.M. van Mullekom, J.A.J.M. Vekemans, E.E. Havinga, E.W. Meijer, *Materials Science and Engineering: R: Reports* 32 (2001) 1–40.
- [48] T. Hacıfendioğlu, E. Yildirim, *ACS Omega* 7 (2022) 38969–38978.
- [49] J. Hou, M.-H. Park, S. Zhang, Y. Yao, L.-M. Chen, J.-H. Li, Y. Yang, *Macromolecules* 41 (2008) 6012–6018.
- [50] R.S. Bhatta, M. Tsige, *Polymer* 55 (2014) 2667–2672.
- [51] G. Li, W.-H. Chang, Y. Yang, *Nat Rev Mater* 2 (2017) 17043.
- [52] O. Almora, D. Baran, G.C. Bazan, C.I. Cabrera, S. Erten-Ela, K. Forberich, F. Guo, J. Hauch, A.W.Y. Ho-Baillie, T.J. Jacobsson, R.A.J. Janssen, T. Kirchartz, N. Kopidakis, M.A. Loi, R.R. Lunt, X. Mathew, M.D. McGehee, J. Min, D.B. Mitzi, M.K. Nazeeruddin, J. Nelson, A.F. Nogueira, U.W. Paetzold, B.P. Rand, U. Rau, H.J. Snaith, E. Unger, L. Vaillant-Roca, C. Yang, H. Yip, C.J. Brabec, *Advanced Energy Materials* 13 (2023) 2203313.
- [53] J.-L. Bredas, *Mater. Horiz.* 1 (2014) 17–19.
- [54] B. Kippelen, J.-L. Brédas, *Energy Environ. Sci.* 2 (2009) 251.
- [55] M.N. Gueye, A. Carella, J. Faure-Vincent, R. Demadrille, J.-P. Simonato, *Progress in Materials Science* 108 (2020) 100616.
- [56] X. Liu, R. He, W. Shen, M. Li, *Journal of Power Sources* 245 (2014) 217–223.
- [57] J. Zhao, C. Yao, M.U. Ali, J. Miao, H. Meng, *Mater. Chem. Front.* 4 (2020) 3487–3504.
- [58] M. Zhang, X. Guo, W. Ma, H. Ade, J. Hou, *Adv. Mater.* 27 (2015) 4655–4660.
- [59] S. Kim, M.A.M. Rashid, T. Ko, K. Ahn, Y. Shin, S. Nah, M.H. Kim, B. Kim, K. Kwak, M. Cho, *J. Phys. Chem. C* 124 (2020) 2762–2770.
- [60] Y. Lin, J. Wang, Z.-G. Zhang, H. Bai, Y. Li, D. Zhu, X. Zhan, *Adv. Mater.* 27 (2015) 1170–1174.
- [61] Z. Xiao, X. Jia, D. Li, S. Wang, X. Geng, F. Liu, J. Chen, S. Yang, T.P. Russell, L. Ding, *Science Bulletin* 62 (2017) 1494–1496.
-

-
- [62] F. Bencheikh, D. Duché, C.M. Ruiz, J.-J. Simon, L. Escoubas, *J. Phys. Chem. C* 119 (2015) 24643–24648.
- [63] N. Delbosc, W.Z.N. Yahya, N. Lemaitre, S. Berson, F. Fuchs, B. Grévin, J. Faure-Vincent, J.-P. Travers, R. Demadrille, *RSC Adv.* 4 (2014) 15236–15244.
- [64] J. Luo, Z.Q. Xue, W.M. Liu, J.L. Wu, Z.Q. Yang, *J. Phys. Chem. A* 110 (2006) 12005–12009.
- [65] C.J. Cramer, *Essentials of Computational Chemistry: Theories and Models*, John Wiley & Sons, 2013.
- [66] J.-L. Brédas, *Chem. Mater.* 29 (2017) 477–478.
- [67] Y. Zhu, F. Zhao, W. Wang, Y. Li, S. Zhang, Y. Lin, *Adv Energy and Sustain Res* 3 (2022) 2100184.
- [68] M. Knupfer, *Appl. Phys. A* 77 (2003) 623–626.
- [69] Y. Li, *Acc. Chem. Res.* 45 (2012) 723–733.
- [70] L. Benatto, C.F.N. Marchiori, C.M. Araujo, M. Koehler, *J. Mater. Chem. C* 7 (2019) 12180–12193.
- [71] M. Saito, H. Ohkita, I. Osaka, *J. Mater. Chem. A* 8 (2020) 20213–20237.
- [72] H. Lee, D. Lee, D.H. Sin, S.W. Kim, M.S. Jeong, K. Cho, *NPG Asia Mater* 10 (2018) 469–481.
- [73] N.A. Ran, S. Roland, J.A. Love, V. Savikhin, C.J. Takacs, Y.-T. Fu, H. Li, V. Coropceanu, X. Liu, J.-L. Brédas, G.C. Bazan, M.F. Toney, D. Neher, T.-Q. Nguyen, *Nat Commun* 8 (2017) 79.
- [74] T.L.D. Tam, T.T. Lin, *Macromolecules* 49 (2016) 1648–1654.
- [75] M.C. Scharber, M. Koppe, J. Gao, F. Cordella, Maria.A. Loi, P. Denk, M. Morana, H. Egelhaaf, K. Forberich, G. Dennler, R. Gaudiana, D. Waller, Z. Zhu, X. Shi, C.J. Brabec, *Advanced Materials* 22 (2010) 367–370.
- [76] J.P. Cachaneski-Lopes, A. Batagin-Neto, *Polymers* 14 (2022) 1354.
- [77] J.L. Bredas, R. Silbey, D.S. Boudreaux, R.R. Chance, *J. Am. Chem. Soc.* 105 (1983) 6555–6559.
- [78] S. Beaupré, M. Belletête, G. Durocher, M. Leclerc, *Macromol. Theory Simul.* 20 (2011) 13–18.
- [79] G. Long, X. Wan, J. Zhou, Y. Liu, Z. Li, G. He, M. Zhang, Y. Hou, Y. Chen, *Macro Chemistry & Physics* 213 (2012) 1596–1603.
- [80] R. Demadrille, P. Rannou, J. Bleuse, J.-L. Oddou, A. Pron, M. Zagorska, *Macromolecules* 36 (2003) 7045–7054.
- [81] T.M. McCormick, C.R. Bridges, E.I. Carrera, P.M. DiCarmine, G.L. Gibson, J. Hollinger, L.M. Kozycz, D.S. Seferos, *Macromolecules* 46 (2013) 3879–3886.
- [82] H.T. Turan, O. Kucur, B. Kahraman, S. Salman, V. Aviyente, *Phys. Chem. Chem. Phys.* 20 (2018) 3581–3591.
- [83] S.S. Zade, N. Zamoshchik, M. Bendikov, *Acc. Chem. Res.* 44 (2011) 14–24.
- [84] B.H. Barboza, O.P. Gomes, A. Batagin-Neto, *J Mol Model* 27 (2021) 17.
-

-
- [85] J. Torras, J. Casanovas, C. Alemán, *J. Phys. Chem. A* 116 (2012) 7571–7583.
- [86] L. Zhang, M. Yu, H. Zhao, Y. Wang, J. Gao, *Chemical Physics Letters* 570 (2013) 153–158.
- [87] S.S. Zade, N. Zamoshchik, M. Bendikov, *Acc. Chem. Res.* 44 (2011) 14–24.
- [88] M. Kowalczyk, N. Chen, S.J. Jang, *ACS Omega* 4 (2019) 5758–5767.
- [89] T.L.D. Tam, C.K. Ng, S.L. Lim, E. Yildirim, J. Ko, W.L. Leong, S.-W. Yang, J. Xu, *Chem. Mater.* 31 (2019) 8543–8550.
- [90] C. An, Z. Zheng, J. Hou, *Chem. Commun.* 56 (2020) 4750–4760.
- [91] Z. Jiao, T. Jiang, Z. Zhou, C. Qin, J. Long, Y. Liu, Y. Jiang, *Nanoscale Res Lett* 16 (2021) 51.
- [92] L. Pandey, C. Risko, J.E. Norton, J.-L. Brédas, *Macromolecules* 45 (2012) 6405–6414.
- [93] Y. Li, B. Xu, H. Li, W. Cheng, L. Xue, F. Chen, H. Lu, W. Tian, *J. Phys. Chem. C* 115 (2011) 2386–2397.
- [94] X.-F. Zhang, J.-Z. Cheng, H. Liu, Q. Shan, G.-X. Jia, H.-R. Wen, S.-Y. Liu, *Dyes and Pigments* 172 (2020) 107819.
- [95] N. Blouin, A. Michaud, D. Gendron, S. Wakim, E. Blair, R. Neagu-Plesu, M. Belletête, G. Durocher, Y. Tao, M. Leclerc, *J. Am. Chem. Soc.* 130 (2008) 732–742.
- [96] X. Liu, R. He, W. Shen, M. Li, *J Mol Model* 19 (2013) 4283–4291.
- [97] Y.J. Kim, K.H. Park, J. Ha, D.S. Chung, Y.-H. Kim, C.E. Park, *Phys. Chem. Chem. Phys.* 16 (2014) 19874–19883.
- [98] E. Zhou, J. Cong, K. Hashimoto, K. Tajima, *Macromolecules* 46 (2013) 763–768.
- [99] T. Marszalek, M. Li, W. Pisula, *Chem. Commun.* 52 (2016) 10938–10947.
- [100] J.M. Szarko, J. Guo, Y. Liang, B. Lee, B.S. Rolczynski, J. Strzalka, T. Xu, S. Loser, T.J. Marks, L. Yu, L.X. Chen, *Advanced Materials* 22 (2010) 5468–5472.
- [101] N. Meftahi, M. Klymenko, A.J. Christofferson, U. Bach, D.A. Winkler, S.P. Russo, *Npj Comput Mater* 6 (2020) 1–8.
- [102] M. Al-Ibrahim, H.-K. Roth, M. Schroedner, A. Konkin, U. Zhokhavets, G. Gobsch, P. Scharff, S. Sensfuss, *Organic Electronics* 6 (2005) 65–77.
- [103] F. Franco Jr., *Molecular Simulation* 43 (2017) 222–227.
- [104] P.Y. Bruice, *Organic Chemistry*, 4th ed, Pearson/Prentice Hall, Upper Saddle River, NJ, 2004.
- [105] J.C. Kotz, P. Treichel, J.R. Townsend, D.A. Treichel, *Chemistry & Chemical Reactivity*, 10th edition / John C. Kotz, State University of New York, College at Oneonta, Paul M. Treichel, University of Wisconsin-Madison, John R. Townsend, West Chester University of Pennsylvania, David A. Treichel, Nebraska Wesleyan University, Cengage Learning, Australia, 2019.
- [106] C.R. Martinez, B.L. Iverson, *Chem. Sci.* 3 (2012) 2191.
- [107] L.-H. Li, O.Y. Kontsevoi, A.J. Freeman, *Phys. Rev. B* 90 (2014) 195203.
- [108] H.-Y. Chen, J. Hou, A.E. Hayden, H. Yang, K.N. Houk, Y. Yang, *Advanced Materials* 22 (2010) 371–375.
-

-
- [109] T. Ghosh, J. Panicker, V. Nair, *Polymers* 9 (2017) 112.
- [110] M. Chen, J. Hou, Z. Hong, G. Yang, S. Sista, L. Chen, Y. Yang, *Advanced Materials* 21 (2009) 4238–4242.
- [111] J. Cornil, D. Beljonne, J.-P. Calbert, J.-L. Brédas, *Advanced Materials* 13 (2001) 1053–1067.
- [112] A.N. Bootsma, A.C. Doney, S.E. Wheeler, *J. Am. Chem. Soc.* 141 (2019) 11027–11035.
- [113] E.M. Cabaleiro-Lago, J. Rodríguez-Otero, *ACS Omega* 3 (2018) 9348–9359.
- [114] L. Benatto, K.R. de A. Sousa, M. Koehler, *J. Phys. Chem. C* 124 (2020) 13580–13591.

Chapter 2

Marcus Theory in Charge Transfer Dynamics for OPV Materials

The exciton binding energy E_b is not the only parameter limiting the conversion of sunlight into electricity using organic materials. Energy loss is another parameter that limits the power conversion efficiency of organic solar cells (OSCs). Generally, the energy loss in the OSCs mainly arises from two aspects: the driving force for exciton dissociation and non-radiative recombination.

Accordingly, many strategies have been proposed to reduce the energy losses, either by reducing the exciton binding energy by regulating molecular packing, which will minimize the driving force required for exciton dissociation, or by suppressing the non-radiative recombination during the photoelectric conversion processes, such as exciton decay, charge-transfer (CT) state decay and nongeminate (bimolecular) recombination.

These non-radiative recombinations are all associated with the electron-vibration coupling (namely reorganization energy λ , which describes the deformations of the molecular geometries during the electron-transfer process and reflects the interactions between electrons and intramolecular vibrations).

In 1956, R. A. Marcus [1] proposed a theory to describe electron transfer kinetics based on a semi-classical model. This theory is an important step in understanding many processes in chemistry (redox systems) and biology (information transfer). The approach uses an Eyring (or Arrhenius) type description to define kinetics. The thermodynamic quantities defining the activation free enthalpy ΔG^\ddagger (or activation energy E_a) are derived from a quantum description. This speculation was later confirmed (1984) by various experiments.

The initial kinetic studies that led R. A. Marcus to propose his theory focused on self-exchange redox reactions in solution involving a radioisotope. Such reactions are particularly valuable from a fundamental study perspective since the chemical nature of the reactants and products

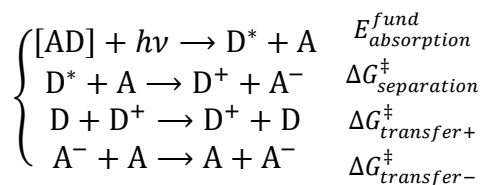
remains unchanged, and no chemical bond is truly affected. It is worth noting that the coordination spheres of both isotopes are altered as their oxidation states evolve, but no change is observed thermodynamically. Hence, the kinetics of such reactions are likely to be high.

From an experimental standpoint, data acquisition saw significant advancement during the same period with the advent of stop-flow techniques. The rapidity of electron transfer reactions prohibits the use of standard techniques. The entire realm of electrochemistry, both experimental and theoretical, experienced a paradigm shift in the understanding of electron transfer phenomena. Let us revisit the transfer reactions triggered a wide range of discussions within the physicochemical community in the early 1950s:

- Exchange reactions are relatively slower involving small cations (*e.g.*, Fe^{2+} , Fe^{3+}) than those involving larger ions (*e.g.*, $\text{Fe}(\text{CN})_6^{3-}$, $\text{Fe}(\text{CN})_6^{4-}$). An initial rationalization based on the Franck-Condon principle (*i.e.*, vertical transition) was proposed by W. F. Libby [2,3];
- The significant difference from a chemical reaction lies in the absence of formation or destruction of chemical bonds during an electron transfer process. The concept of a trajectory defined by reaction coordinates, leading from the reactants' valley to that of the products, disappears;
- The solvent then becomes also crucial in the search for a scenario. Indeed, immediately after electron transfer, solvent molecules have not had time to spatially reorganize around the newly formed species.

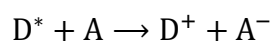
All these findings led R. A. Marcus to propose a theory that aligns with them. The fluctuations of the various nuclear coordinates play a determining role, allowing reactants and products as well as the different solvent molecules to satisfy energy conservation and vertical transition. Starting from the curves, the potential energy of reactants R and products P are described as a function of nuclear coordinates (see Figure 2.1).

In our demonstration, we will place ourselves within the framework of the displaced harmonic oscillator (DHO) formalism. The Energy Gap Hamiltonian has been used extensively in describing charge transport reactions, such as electron and proton transfer (step 2). The case of the charge transfers (steps 3 and 4) will be addressed just after. These mechanisms occur when solar energy is absorbed by the material (step 1).



2.1 $\Delta G_{\text{separation}}^{\ddagger}$ energy of separation $\text{D}^* + \text{A} \rightarrow \text{D}^+ + \text{A}^-$

Here, we describe the electron transfer rates between weakly coupled donor and acceptor states when the potential energy depends on a nuclear coordinate, *i.e.*, nonadiabatic electron transfer. These results come across with the findings of Marcus' theory of electron transfer.



For simplification, we will limit ourselves in this subchapter to electron transfer exchanges without the influence of the solution/solvent. The influence of collective solvent rearrangements or intramolecular vibrations is then neglected. Within the scope of this assumption, electron transfer rates are correlated with the free energy along the electron transfer coordinate q . Visual representations like those above (see Figure 2.1), depicting system states with electrons localized on either the donor or acceptor, with electrons hopping between them, are conceptually depicted through diabatic energy surfaces.

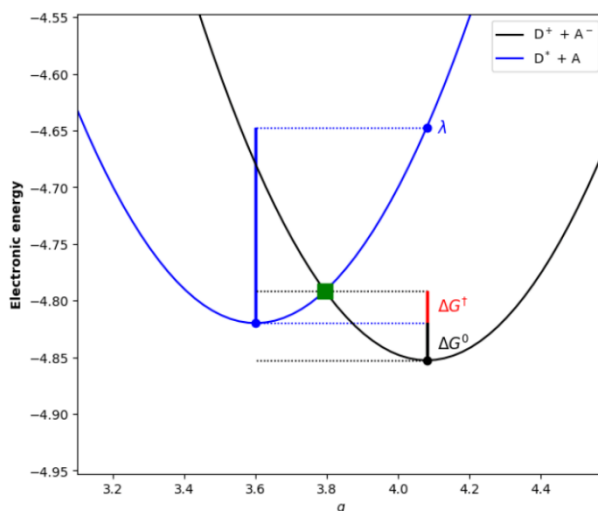


Figure 2.1 – Potential energy curves of the reactants and the products. Electron transfer occurs at the intersection of the curves. ΔG^0 conditions the thermodynamics of equilibrium between reactants and products, while λ represents the reorganization energy.

Arising from the transfer process, the electronic coupling J blends these diabatic states within the crossing region. The rate of transfer for the forward reaction, originating from this adiabatic surface, is correlated with the flux across the barrier. Employing classical transition state theory, we can correlate the rate with the free energy barrier:

$$k = A \times \exp \left\{ \left(\frac{-\Delta G^\ddagger}{k_B T} \right) \right\}$$

If the coupling is weak, we can describe the transfer rates between donor and acceptor on the diabatic basis with perturbation theory. This accounts for nonadiabatic effects and tunnelling through the barrier.

To begin, we consider that the description of the potential energy curves hypothesis in our demonstration is considered according to the following assumptions:

- We will denote ‘ q ’ as the reaction coordinate;
- The transfer occurs for a given position of the atoms, thus respecting the Franck-Condon principle (Vertical transition - with fixed nuclear positions), while $G_R(q_C) = G_P(q_C)$ (R for reactant, P for product and q_C the q value at this intersection) at the intersection ensuring energy conservation. Let us assume for simplicity that the harmonic approximation remains valid but that the curvatures of these surfaces are not necessarily equal (which would be too restrictive);
- The potential energy of the overall system, G_P , comprising products and solvent (or G_R , comprising reactants and solvent), is a function of numerous parameters, particularly the positions and orientations of surrounding solvent molecules and the vibrations of the coordination spheres of solvated ions. It is important to note that in our demonstration, we are neglecting the solvent effect;
- After the electron transfer, the system’s potential energy becomes G_P , and these two curves intersect, initially neglecting the electronic coupling ($J \rightarrow 0$).

Let’s assume that:

$$G_P(q) = \frac{1}{2}(m\omega_0)^2(q - q_P)^2 + \Delta G_P^0$$

$$G_R(q) = \frac{1}{2}(m\omega'_0)^2(q - q_R)^2 + \Delta G_R^0$$

1) In addition, assuming that we can decompose the problem as:

$$G_{D^+}(q) = \frac{1}{2}\sigma_1(q - t_1)^2 - d_1$$

$$G_{A^-}(q) = \frac{1}{2}\sigma_2(q - t_2)^2 - d_2$$

$$G_D(q) = \frac{1}{2}\sigma_3(q - t_3)^2 - d_3$$

$$G_A(q) = \frac{1}{2}\sigma_4(q - t_4)^2 - d_4$$

So,

$$G_P(q) = \frac{1}{2}\sigma_1(q - t_1)^2 - d_1 + \frac{1}{2}\sigma_2(q - t_2)^2 - d_2 \cong \frac{1}{2}(m\omega_0)^2(q - q_P)^2 + \Delta G_P^0$$

$$G_P(q) = \frac{1}{2}(\sigma_1 + \sigma_2) \times q^2 - (\sigma_1 t_1 + \sigma_2 t_2)q + \frac{1}{2}(\sigma_1 t_1^2 + \sigma_2 t_2^2) - (d_1 + d_2)$$

$$G'_P(q) = (\sigma_1 + \sigma_2) \times q - (\sigma_1 t_1 + \sigma_2 t_2) \rightarrow$$

$$\left\{ \begin{array}{l} q_P^{\min} = \frac{(\sigma_1 t_1 + \sigma_2 t_2)}{(\sigma_1 + \sigma_2)} \\ G_P(q_P^{\min}) = \frac{1}{2}(\sigma_1 + \sigma_2) \times (q_P^{\min})^2 - (\sigma_1 t_1 + \sigma_2 t_2) \times (q_P^{\min}) \\ \quad + \frac{1}{2}(\sigma_1 t_1^2 + \sigma_2 t_2^2) - (d_1 + d_2) \end{array} \right.$$

Identification of q_P and ΔG_P^0 :

$$G_P(q) = \frac{1}{2}(m\omega_0)^2(q - q_P)^2 + \Delta G_P^0 \rightarrow$$

$$G_P(q) = \frac{1}{2}(m\omega_0)^2 q^2 - (m\omega_0)^2 q_P \times q + \frac{1}{2}(m\omega_0)(q_P)^2 + \Delta G_P^0$$

$$\left\{ \begin{array}{l} (m\omega_0)^2 \cong (\sigma_1 + \sigma_2) \\ (m\omega_0)^2 q_P \cong (\sigma_1 t_1 + \sigma_2 t_2) \rightarrow q_P = \frac{(\sigma_1 t_1 + \sigma_2 t_2)}{(\sigma_1 + \sigma_2)} \\ \frac{1}{2}(m\omega_0)(q_P)^2 + \Delta G_P^0 \cong \frac{1}{2}(\sigma_1 t_1^2 + \sigma_2 t_2^2) - (d_1 + d_2) \rightarrow \end{array} \right.$$

$$\Delta G_P^0 = \frac{1}{2}(\sigma_1 t_{1_1}^2 + \sigma_2 t_2^2) - (d_1 + d_2) - \frac{1}{2}(m\omega_0)(q_P)^2 \rightarrow$$

$$\Delta G_P^0 = \frac{1}{2}(\sigma_1 t_{1_1}^2 + \sigma_2 t_2^2) - (d_1 + d_2) - \frac{1}{2} \frac{(\sigma_1 t_1 + \sigma_2 t_2)^2}{(\sigma_1 + \sigma_2)} \rightarrow$$

$$\Delta G_P^0 = \frac{1}{2}(\sigma_1 t_{1_1}^2 + \sigma_2 t_2^2) - (d_1 + d_2) - \frac{1}{2} q_P \times (\sigma_1 t_1 + \sigma_2 t_2)$$

Similarly, we have:

Identification of q_R and ΔG_R^0 :

$$G_R(q) = \frac{1}{2}(m\omega'_0)^2(q - q_R)^2 + \Delta G_R^0 \rightarrow$$

$$G_R(q) = \frac{1}{2}(m\omega'_0)^2 q^2 - (m\omega'_0)^2 q \times q_R + \frac{1}{2}(m\omega'_0)q_R^2 + \Delta G_R^0$$

$$\left\{ \begin{array}{l} (m\omega'_0)^2 \cong (\sigma_3 + \sigma_4) \\ q_R = \frac{(\sigma_3 t_3 + \sigma_4 t_4)}{(\sigma_3 + \sigma_4)} \\ \Delta G_R^0 = \frac{1}{2}(\sigma_3 t_3^2 + \sigma_4 t_4^2) - (d_3 + d_4) - \frac{1}{2} q_R \times (\sigma_3 t_3 + \sigma_4 t_4) \end{array} \right.$$

and:

$$\left\{ \begin{array}{l} q_R^{\min} = \frac{(\sigma_3 t_3 + \sigma_4 t_4)}{(\sigma_3 + \sigma_4)} \\ G_R(q_R^{\min}) = \frac{1}{2}(\sigma_3 + \sigma_4) \times (q_R^{\min})^2 - (\sigma_3 t_3 + \sigma_4 t_4) \times (q_R^{\min}) \\ \quad + \frac{1}{2}(\sigma_3 t_3^2 + \sigma_4 t_4^2) - (d_3 + d_4) \end{array} \right.$$

2) To find the barrier height ΔG^\ddagger , as reported in the previous assumptions, we first find the crossing point q_C , in which: $G_R(q_C) = G_P(q_C)$

$$\frac{1}{2}(\sigma_3 + \sigma_4)(q_C - q_R)^2 + \Delta G_R^0 = \frac{1}{2}(\sigma_1 + \sigma_2)(q_C - q_P)^2 + \Delta G_P^0$$

$$\frac{1}{2}(\sigma_3 + \sigma_4)(q_C^2 + q_R^2 - 2q_C q_R) = \frac{1}{2}(\sigma_1 + \sigma_2)(q_C^2 + q_P^2 - 2q_C q_P) + \Delta G^0$$

$$\text{with } \Delta G^0 = \Delta G_P^0 - \Delta G_R^0$$

$$\frac{1}{2}[(\sigma_3 + \sigma_4) - (\sigma_1 + \sigma_2)] \times q_C^2 - [(\sigma_3 + \sigma_4)q_R - (\sigma_1 + \sigma_2)q_P] \times q_C$$

$$+ \frac{1}{2}[(\sigma_3 + \sigma_4)q_R^2 - (\sigma_1 + \sigma_2)q_P^2] - \Delta G^0 = 0$$

Solving the second-order equation:

$$U \times q_C^2 - V \times q_C + W = 0$$

It leads to the following results:

$$q_C(\#_{1,2}) = \frac{-V \pm \sqrt{\Delta}}{2U} \text{ with } \Delta = V^2 - 4UW$$

3)

a. As $\lambda_P = G_P(q_R) - G_P(q_P)$,

$$G_P(q) = \frac{1}{2}(\sigma_1 + \sigma_2)(q - q_P)^2 + \Delta G_P^0 \rightarrow$$

$$\lambda_P = \left[\frac{1}{2}(\sigma_1 + \sigma_2)(q_R - q_P)^2 + \Delta G_P^0 \right] - [\Delta G_P^0] \rightarrow (\sigma_1 + \sigma_2) = \frac{2\lambda_P}{(q_R - q_P)^2}$$

b. As $\lambda_R = G_R(q_P) - G_R(q_R)$,

$$G_R(q) = \frac{1}{2}(\sigma_3 + \sigma_4)(q - q_R)^2 + \Delta G_R^0 \rightarrow$$

$$\lambda_R = \left[\frac{1}{2}(\sigma_3 + \sigma_4)(q_P - q_R)^2 + \Delta G_R^0 \right] - [\Delta G_R^0] \rightarrow (\sigma_3 + \sigma_4) = \frac{2\lambda_R}{(q_P - q_R)^2}$$

4)

a. As $\Delta G^\ddagger(R \rightarrow P) = G_R(q_C) - G_R(q_R) \rightarrow$

$$\Delta G^\ddagger(R \rightarrow P) = \left[\frac{1}{2}(\sigma_3 + \sigma_4)(q_C - q_R)^2 + \Delta G_R^0 \right] - (0 + \Delta G_R^0)$$

b. As $\Delta G^\ddagger(P \rightarrow R) = G_P(q_C) - G_P(q_P) \rightarrow$

$$\Delta G^\ddagger(P \rightarrow R) = \left[\frac{1}{2}(\sigma_1 + \sigma_2)(q_C - q_P)^2 + \Delta G_P^0 \right] - (0 + \Delta G_P^0)$$

5) Classical demonstration: $(m\omega'_0) = (m\omega_0) \rightarrow (\sigma_1 + \sigma_2) = (\sigma_3 + \sigma_4)$

$$\frac{1}{2}(\sigma_1 + \sigma_2)(q_C - q_R)^2 + \Delta G_R^0 = \frac{1}{2}(\sigma_1 + \sigma_2)(q_C - q_P)^2 + \Delta G_P^0$$

$$\frac{1}{2}(\sigma_1 + \sigma_2)(q_C^2 + q_R^2 - 2q_C q_R) = \frac{1}{2}(\sigma_1 + \sigma_2)(q_C^2 + q_P^2 - 2q_C q_P) + \Delta G^0$$

with $\Delta G^0 = \Delta G_P^0 - \Delta G_R^0$

$$(\sigma_1 + \sigma_2)(q_P - q_R) \times q_C = \frac{1}{2}(\sigma_1 + \sigma_2)(q_P^2 - q_R^2) + \Delta G^0$$

$$q_C = \frac{(q_P^2 - q_R^2)}{2(q_P - q_R)} + \frac{\Delta G^0}{(\sigma_1 + \sigma_2)} \times \frac{1}{(q_P - q_R)}$$

$$q_C = \frac{(q_P + q_R)}{2} + \frac{\Delta G^0}{(\sigma_1 + \sigma_2)} \times \frac{1}{(q_P - q_R)} \text{ with } (q_P^2 - q_R^2) = (q_P + q_R)(q_P - q_R)$$

As in this hypothesis:

$$(\sigma_3 + \sigma_4) = \frac{2\lambda_R}{(q_P - q_R)^2} \rightarrow (\sigma_1 + \sigma_2) = \frac{2\lambda}{(q_P - q_R)^2}$$

$$(\sigma_1 + \sigma_2) = \frac{2\lambda_P}{(q_R - q_P)^2} \rightarrow (\sigma_1 + \sigma_2) = \frac{2\lambda}{(q_R - q_P)^2}$$

then:

$$q_C = \frac{(q_P + q_R)}{2} + \frac{\Delta G^0}{\frac{2\lambda}{(q_R - q_P)^2}} \times \frac{1}{(q_P - q_R)}$$

$$q_C = \frac{(q_P + q_R)}{2} + \frac{\Delta G^0}{2\lambda} \times (q_P - q_R)$$

Expression of $(q_C - q_R)$ in terms of λ :

$$(q_C - q_R) = \frac{(q_P + q_R)}{2} + \frac{\Delta G^0}{2\lambda}(q_P - q_R) - \frac{2q_R}{2} = \frac{(q_P - q_R)}{2} + \frac{\Delta G^0}{2\lambda}(q_P - q_R) \rightarrow$$

$$(q_C - q_R) = \frac{(q_P - q_R)}{2} \left[1 + \frac{\Delta G^0}{2\lambda} \right] = \frac{(q_P - q_R)}{2\lambda} [\lambda + \Delta G^0]$$

As $(\sigma_1 + \sigma_2) = \frac{2\lambda}{(q_R - q_P)^2} \rightarrow (q_C - q_R) = \pm \sqrt{\frac{2\lambda}{(\sigma_1 + \sigma_2)}}$, so:

$$(q_C - q_R) = \frac{(q_P - q_R)}{2\lambda} [\lambda + \Delta G^0] = \frac{\pm \sqrt{\frac{2\lambda}{(\sigma_1 + \sigma_2)}}}{2\lambda} [\lambda + \Delta G^0]$$

$$= \frac{\pm 1}{\sqrt{2\lambda(\sigma_1 + \sigma_2)}} [\lambda + \Delta G^0]$$

As $\Delta G^\ddagger(P \rightarrow R) = \frac{1}{2}(\sigma_1 + \sigma_2)(q_C - q_P)^2$ [see 4)a4)b]:

$$\Delta G^\ddagger = \frac{1}{2}(\sigma_1 + \sigma_2) \times \left(\frac{\pm 1}{\sqrt{2\lambda(\sigma_1 + \sigma_2)}} [\lambda + \Delta G^0] \right)^2 = \frac{1}{4\lambda} [\lambda + \Delta G^0]^2$$

6) So, the Arrhenius rate constant is for electron transfer via activated barrier crossing is:

$$k = A \times \exp \left\{ \left(\frac{-\Delta G^\ddagger}{k_B T} \right) \right\} = A \times \exp \left\{ \left(\frac{-[\lambda + \Delta G^0]^2}{4\lambda k_B T} \right) \right\}$$

7)

a. Example₁ – classical demonstration

$$(m\omega'_0) = (m\omega_0) \rightarrow (\sigma_1 + \sigma_2) = (\sigma_3 + \sigma_4) = 0.6 + 0.9 = 1.5$$

$$\sigma_1 = 0.6, \sigma_2 = 0.9, \sigma_3 = 0.6, \sigma_4 = 0.9$$

$$t_1 = 1.2, t_2 = 6.0, t_3 = 3.0, t_4 = 4.0$$

$$d_1 = 1.0, d_2 = 8.0, d_3 = 1.5, d_4 = 3.5$$

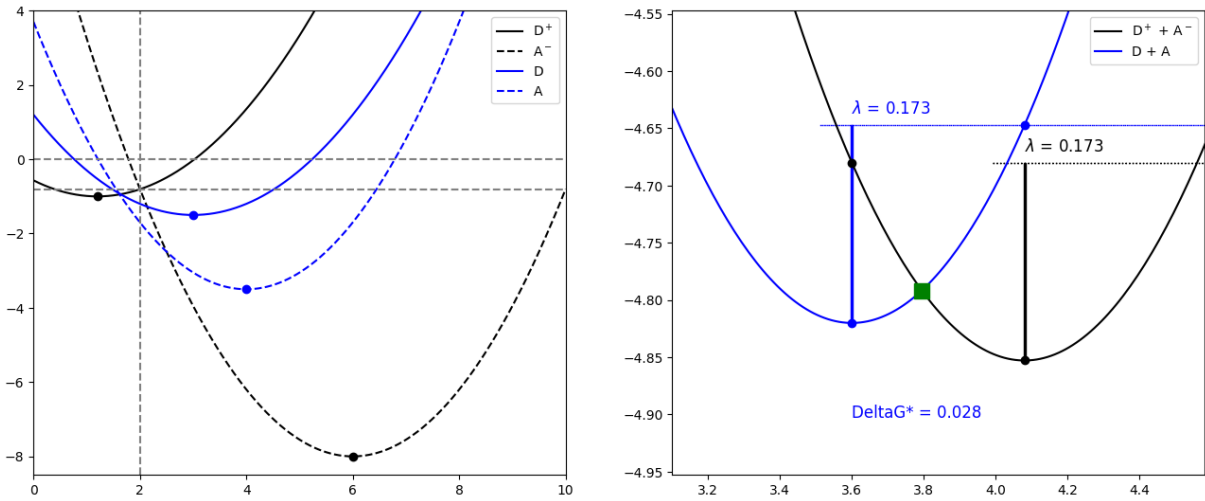


Figure 2.2 – Example₁ $G_{D^+}(q)$, $G_{A^-}(q)$, $G_D(q)$ and $G_A(q)$ (left), $G_R(q)$ ($R = D^+ + A^-$) and $G_P(q)$ ($P = D + A$) (right) curves.

b. Example₂ – unclassical demonstration

$$(m\omega'_0) \neq (m\omega_0) \rightarrow (\sigma_1 + \sigma_2) \neq (\sigma_3 + \sigma_4) \rightarrow 0.6 + 0.9 \neq 1.2 + 0.6$$

$$\sigma_1 = 0.6, \sigma_2 = 0.9, \sigma_3 = 1.2, \sigma_4 = 0.9$$

$$t_1 = 1.2, t_2 = 6.0, t_3 = 3.0, t_4 = 4.0$$

$$d_1 = 1.0, d_2 = 8.0, d_3 = 1.5, d_4 = 3.5$$

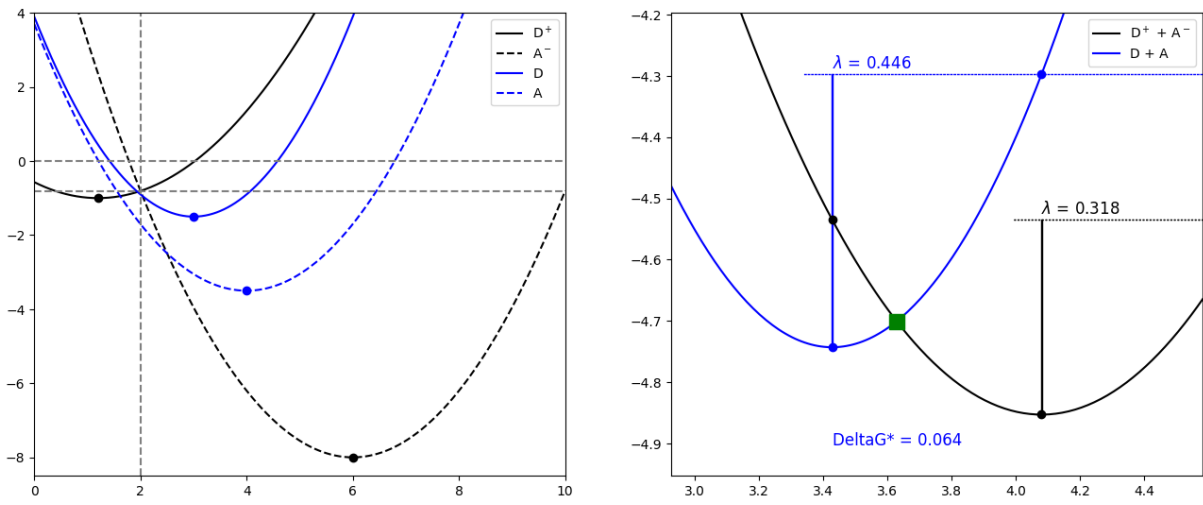


Figure 2.3 – Example₂ $G_{D^+}(q)$, $G_{A^-}(q)$, $G_D(q)$ and $G_A(q)$ (left), $G_R(q)(R = D^+ + A)$ and $G_P(q)(P = D^+ + A^-)$ (right) curves.

c. Example₃ – inverse unclassical demonstration

$$(m\omega'_0) \neq (m\omega_0) \rightarrow (\sigma_1 + \sigma_2) \neq (\sigma_3 + \sigma_4) \rightarrow 0.6 + 0.9 \neq 1.2 + 0.6$$

$$\sigma_1 = 0.6, \sigma_2 = 0.9, \sigma_3 = 0.6, \sigma_4 = 0.9$$

$$t_1 = 1.2, t_2 = 6.0, t_3 = 3.0, t_4 = 4.0$$

$$d_1 = 1.0, d_2 = 8.0, d_3 = 3.5, d_4 = 2.5$$

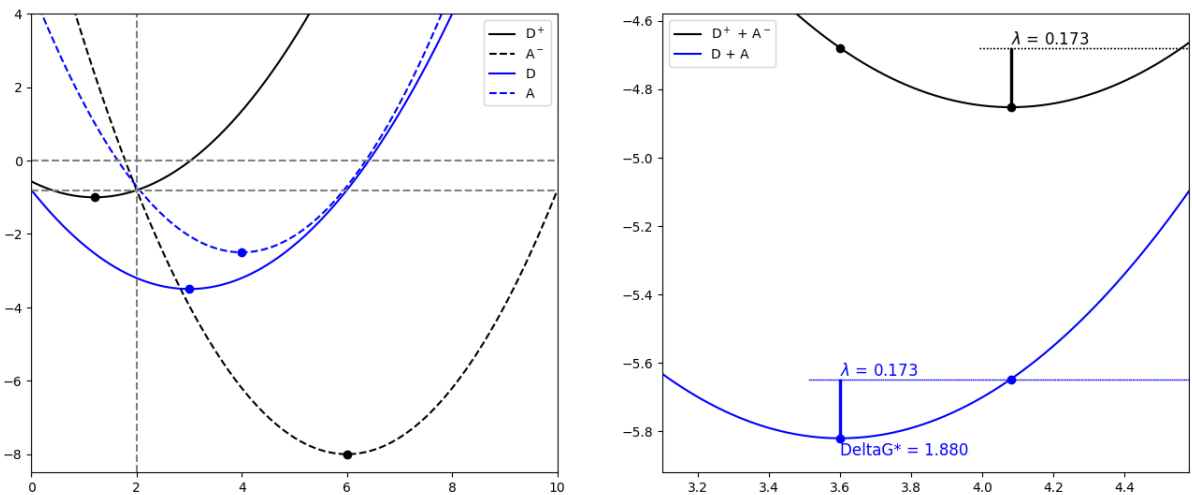


Figure 2.4 – Example₃ $G_{D^+}(q)$, $G_{A^-}(q)$, $G_D(q)$ and $G_A(q)$ (left), $G_R(q)(R = D^+ + A)$ and $G_P(q)(P = D^+ + A^-)$ (right) curves.

As reported in this demonstration, we can conclude that in this classical description, the kinetics are, therefore then, essentially controlled by the two quantities ΔG^0 and λ .

- $\Delta G^0 \gg -\lambda$ (example₃): the kinetics follow the variations of ΔG^0 . This is referred to as the normal region. Thus, a decrease in ΔG^0 leads to an acceleration of the electron transfer.
- $\Delta G^0 \ll -\lambda$ (example₁ and example₂): a decrease in ΔG^0 results in a slowing down of the transfer kinetics. This is referred to as the inverted region.

2.2 $\Delta G^{\ddagger}_{\text{transfer}}$ energy of separation $\mathbf{D}^* \leftrightarrow \mathbf{D}^+$

1) Assuming that we can decompose the problem as:

$$G_{D^*}(q) = \frac{1}{2}(m_{D^*}\omega_0)^2(q - q_{D^*})^2 + \Delta G_{D^*}^0 = \frac{1}{2}\sigma_{D^*}(q - q_{D^*})^2 + \Delta G_{D^*}^0$$

$$G_{D^+}(q) = \frac{1}{2}(m_{D^+}\omega_0)^2(q - q_{D^+})^2 + \Delta G_{D^+}^0 = \frac{1}{2}\sigma_{D^+}(q - q_{D^+})^2 + \Delta G_{D^+}^0$$

So,

$$G_{D^*}(q) = \frac{1}{2}\sigma_{D^*} \times q^2 - \sigma_{D^*}q_{D^*} \times q + \frac{1}{2}\sigma_{D^*}q_{D^*}^2 + \Delta G_{D^*}^0$$

$$G_{D^*}(q) = \sigma_{D^*} \times q - \sigma_{D^*}q_{D^*} \rightarrow$$

$$\left\{ \begin{array}{l} q_{D^*}^{\min} = q_{D^*} \\ G_{D^*}(q_{D^*}^{\min}) = \frac{1}{2}\sigma_{D^*}(q_{D^*} - q_{D^*})^2 + \Delta G_{D^*}^0 = \Delta G_{D^*}^0 \end{array} \right.$$

Similarly, we have:

$$G_{D^+}(q) = \frac{1}{2}\sigma_{D^+} \times q^2 - \sigma_{D^+}q_{D^+} \times q + \frac{1}{2}\sigma_{D^+}q_{D^+}^2 + \Delta G_{D^+}^0$$

$$G_{D^+}(q) = \sigma_{D^+} \times q - \sigma_{D^+}q_{D^+} \rightarrow$$

$$\left\{ \begin{array}{l} q_{D^+}^{\min} = q_{D^+} \\ G_{D^+}(q_{D^+}^{\min}) = \frac{1}{2}\sigma_{D^+}(q_{D^+} - q_{D^+})^2 + \Delta G_{D^+}^0 = \Delta G_{D^+}^0 \end{array} \right.$$

- 2) To find the barrier height ΔG^\ddagger , as reported in the previous assumptions, we first find the crossing point q_C , in which: $G_{D^+}(q_C) = G_{D^*}(q_C)$

$$\frac{1}{2}\sigma_{D^*}(q_C - q_{D^*})^2 + \Delta G_{D^*}^0 = \frac{1}{2}\sigma_{D^+}(q_C - q_{D^+})^2 + \Delta G_{D^+}^0$$

$$\frac{1}{2}\sigma_{D^*}(q_C^2 + q_{D^*}^2 - 2q_C q_{D^*}) = \frac{1}{2}\sigma_{D^+}(q_C^2 + q_{D^+}^2 - 2q_C q_{D^+}) + \Delta G_0$$

$$\text{With } \Delta G_0 = \Delta G_{D^+}^0 - \Delta G_{D^*}^0$$

$$\frac{1}{2}[\sigma_{D^*} - \sigma_{D^+}] \times q_C^2 - [\sigma_{D^*} q_{D^*} - \sigma_{D^+} q_{D^+}] \times q_C + \frac{1}{2}[\sigma_{D^*} q_{D^*}^2 - \sigma_{D^+} q_{D^+}^2] - \Delta G_0 = 0$$

Solving the second-order equation:

$$U' \times q_C^2 - V' \times q_C + W' = 0$$

Leading to the following results:

$$q_C(\#_{1,2}) = \frac{-V' \pm \sqrt{\Delta'}}{2U'} \text{ with } \Delta' = (V')^2 - 4U'W'$$

3)

- a. As $\lambda_{D^+} = G_{D^+}(q_{D^*}) - G_{D^+}(q_{D^+})$:

$$G_{D^+}(q) = \frac{1}{2}\sigma_{D^+}(q - q_{D^+})^2 + \Delta G_{D^+}^0 \rightarrow$$

$$\lambda_{D^+} = \left[\frac{1}{2}\sigma_{D^+}(q_{D^*} - q_{D^+})^2 + \Delta G_{D^+}^0 \right] - [\Delta G_{D^+}^0] \rightarrow \sigma_{D^+} = \frac{2\lambda_{D^+}}{(q_{D^*} - q_{D^+})^2}$$

- b. As $\lambda_{D^*} = G_{D^*}(q_{D^+}) - G_{D^*}(q_{D^*})$:

$$G_{D^*}(q) = \frac{1}{2}\sigma_{D^*}(q - q_{D^*})^2 + \Delta G_{D^*}^0 \rightarrow$$

$$\lambda_{D^*} = \left[\frac{1}{2}\sigma_{D^*}(q_{D^+} - q_{D^*})^2 + \Delta G_{D^*}^0 \right] - [\Delta G_{D^*}^0] \rightarrow \sigma_{D^*} = \frac{2\lambda_{D^*}}{(q_{D^+} - q_{D^*})^2}$$

4)

- a. As $\Delta G^\ddagger(D^* \rightarrow D^+) = G_{D^*}(q_C) - G_{D^*}(q_{D^*})$:

$$\rightarrow \Delta G^\ddagger(D^* \rightarrow D^+) = \left[\frac{1}{2}\sigma_{D^*}(q_C - q_{D^*})^2 + \Delta G_{D^*}^0 \right] - (0 + \Delta G_{D^*}^0)$$

- b. As $\Delta G^\ddagger(D^+ \rightarrow D^*) = G_{D^+}(q_C) - G_{D^+}(q_{D^+})$:

$$\rightarrow \Delta G^\ddagger(D^+ \rightarrow D^*) = \left[\frac{1}{2}\sigma_{D^+}(q_C - q_{D^+})^2 + \Delta G_{D^+}^0 \right] - (0 + \Delta G_{D^+}^0)$$

5) Classical demonstration: $(m_{D^*}\omega_0)^2 = (m_{D^+}\omega_0)^2 \rightarrow \sigma_{D^*} = \sigma_{D^+}$

$$\frac{1}{2}\sigma_{D^*}(q_C - q_{D^*})^2 + \Delta G_{D^*}^0 = \frac{1}{2}\sigma_{D^*}(q_C - q_{D^+})^2 + \Delta G_{D^+}^0$$

$$\frac{1}{2}\sigma_{D^*}(q_C^2 + q_{D^*}^2 - 2q_C q_{D^*}) = \frac{1}{2}\sigma_{D^*}(q_C^2 + q_{D^+}^2 - 2q_C q_{D^+}) + \Delta G_0$$

$$\text{with } \Delta G_0 = \Delta G_{D^+}^0 - \Delta G_{D^*}^0$$

$$\sigma_{D^*}(q_{D^+} - q_{D^*}) \times q_C = \frac{1}{2}\sigma_{D^*}(q_{D^+}^2 - q_{D^*}^2) + \Delta G^0$$

$$q_C = \frac{(q_{D^+}^2 - q_{D^*}^2)}{2(q_{D^+} - q_{D^*})} + \frac{\Delta G^0}{\sigma_{D^*}} \times \frac{1}{(q_{D^+} - q_{D^*})}$$

$$q_C = \frac{(q_{D^+} + q_{D^*})}{2} + \frac{\Delta G^0}{\sigma_{D^*}} \times \frac{1}{(q_{D^+} - q_{D^*})} \text{ with } (q_{D^+}^2 - q_{D^*}^2) = (q_{D^+} + q_{D^*})(q_{D^+} - q_{D^*})$$

As in this hypothesis:

$$\sigma_{D^*} = \frac{2\lambda_{D^*}}{(q_{D^+} - q_{D^*})^2} \rightarrow \sigma_{D^*} = \frac{2\lambda}{(q_{D^+} - q_{D^*})^2}$$

$$\sigma_{D^+} = \frac{2\lambda_{D^+}}{(q_{D^*} - q_{D^+})^2} \rightarrow \sigma_{D^+} = \frac{2\lambda}{(q_{D^*} - q_{D^+})^2}$$

then:

$$q_C = \frac{(q_{D^+} + q_{D^*})}{2} + \frac{\Delta G^0}{\frac{2\lambda}{(q_{D^+} - q_{D^*})^2}} \times \frac{1}{(q_{D^+} - q_{D^*})}$$

$$q_C = \frac{(q_{D^+} + q_{D^*})}{2} + \frac{\Delta G^0}{2\lambda} \times (q_{D^+} - q_{D^*})$$

Expression of $(q_C - q_{D^*})$ in terms of λ :

$$q_C - q_{D^*} = \frac{(q_{D^+} + q_{D^*})}{2} + \frac{\Delta G^0}{2\lambda} \times (q_{D^+} - q_{D^*}) - \frac{2q_{D^*}}{2}$$

$$q_C - q_{D^*} = \frac{(q_{D^+} - q_{D^*})}{2} + \frac{\Delta G^0}{2\lambda} \times (q_{D^+} - q_{D^*})$$

$$\rightarrow (q_C - q_{D^*}) = \frac{(q_{D^+} - q_{D^*})}{2} \left[1 + \frac{\Delta G^0}{\lambda} \right] = \frac{(q_{D^+} - q_{D^*})}{2\lambda} [\lambda + \Delta G^0]$$

$$\text{As } \sigma_{D^+} = \frac{2\lambda}{(q_{D^*} - q_{D^+})^2} \rightarrow (q_{D^*} - q_{D^+}) = \pm \sqrt{\frac{2\lambda}{\sigma_{D^+}}}, \text{ so:}$$

$$(q_C - q_{D^*}) = \frac{(q_{D^+} - q_{D^*})}{2\lambda} [\lambda + \Delta G^0] = \frac{\pm \sqrt{\frac{2\lambda}{\sigma_{D^+}}}}{2\lambda} [\lambda + \Delta G^0] = \pm \frac{1}{\sqrt{2\lambda\sigma_{D^+}}} [1 + \Delta G^0]$$

As $\Delta G^\ddagger(D^+ \rightarrow D^*) = \frac{1}{2}\sigma_{D^+}(q_c - q_{D^+})^2$ (see 4b):

$$\Delta G^\ddagger(D^+ \rightarrow D^*) = \frac{1}{2}\sigma_{D^+} \left(\pm \frac{1}{\sqrt{2\lambda\sigma_{D^+}}} [1 + \Delta G^0] \right)^2 = \frac{1}{4\lambda} [\lambda + \Delta G^0]^2$$

6) So, the Arrhenius rate constant for electron transfer via activated barrier crossing is:

$$k = A \times \exp \left\{ \left(\frac{-\Delta G^\ddagger}{k_B T} \right) \right\} = A \times \exp \left\{ \left(\frac{-[\lambda + \Delta G^0]^2}{4\lambda k_B T} \right) \right\}$$

7)

a. Example₁ – classical demonstration

$$\sigma_{D^+} = \sigma_{D^*}$$

$$\sigma_{D^+} = 0.6, \sigma_{D^*} = 0.6$$

$$t_1 = 1.2, t_2 = 6.0$$

$$d_1 = 1.0, d_2 = 8.0$$

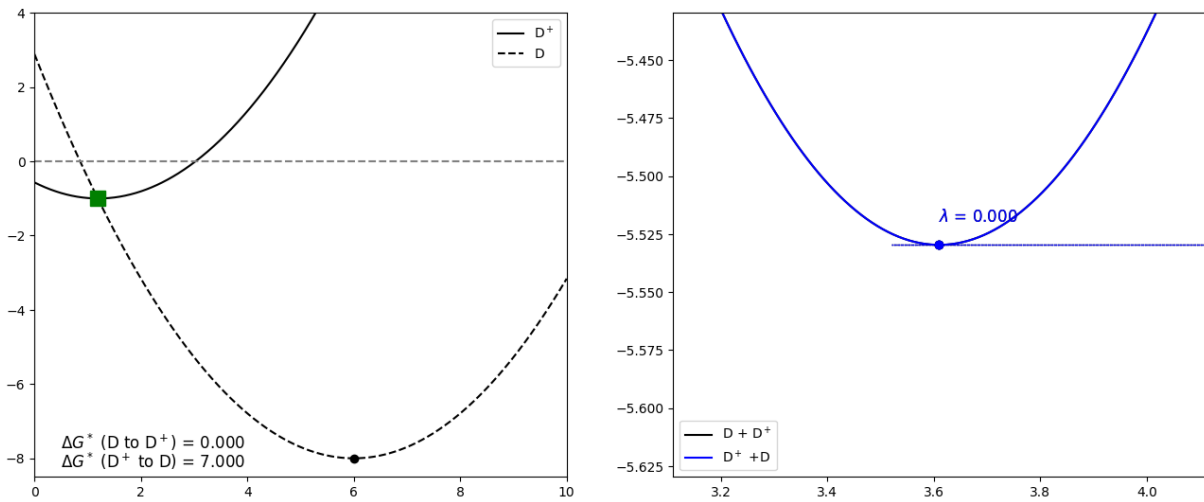


Figure 2.5 – Example₁ $G_{D^*}(q)$ and $G_{D^+}(q)$ (left), and $G_{D^* \leftrightarrow D^+}(q)$ (right) curves.

b. Example₂ – unclassical demonstration

$$\sigma_{D^+} \neq \sigma_{D^*}$$

$$\sigma_{D^+} = 0.6, \sigma_{D^*} = 0.9$$

$$t_1 = 1.2, t_2 = 6.0$$

$$d_1 = 1.0, d_2 = 8.0$$

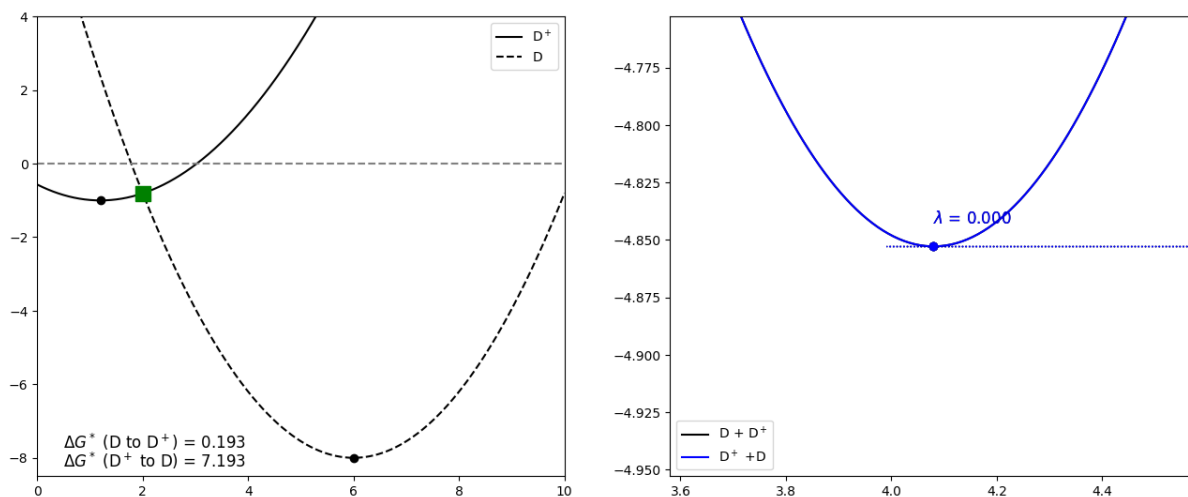


Figure 2.6 – Example₂ $G_{D^*}(q)$ and $G_{D^+}(q)$ (left), and $G_{D^* \leftrightarrow D^+}(q)$ (right) curves.

c. Example₃ – inverse unclassical demonstration

$$\sigma_{D^+} \neq \sigma_{D^*}$$

$$\sigma_{D^+} = 3.2, \sigma_{D^*} = 0.6$$

$$t_1 = 1.2, t_2 = 6.0$$

$$d_1 = 3.0, d_2 = 2.0$$

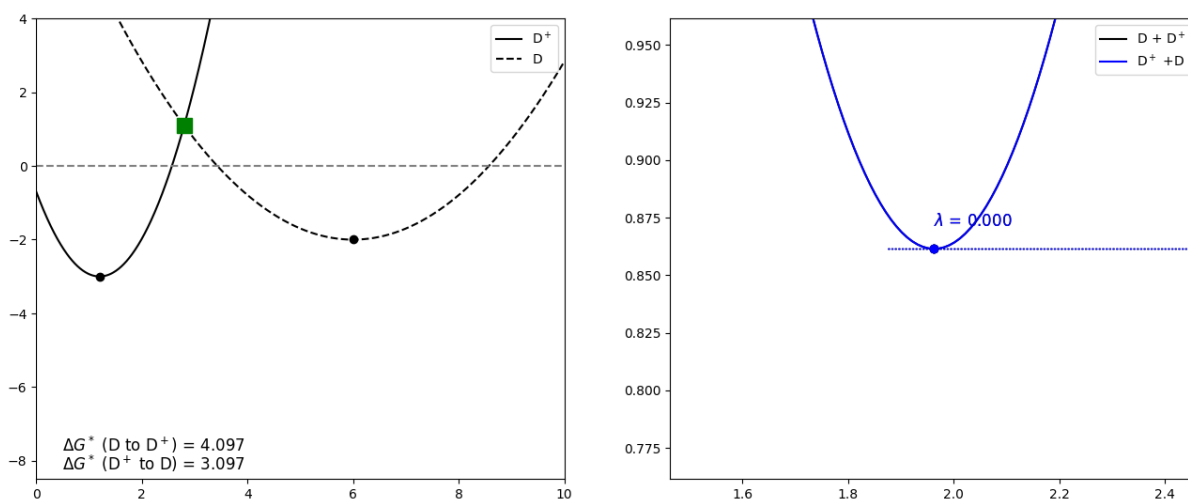
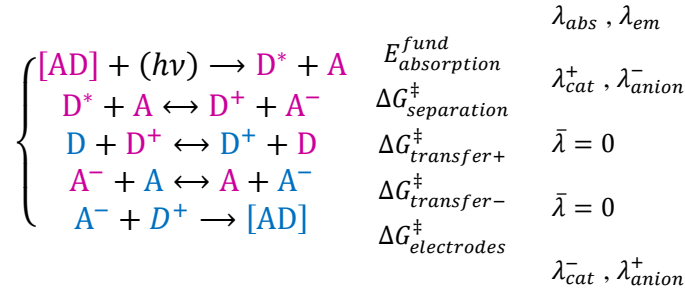


Figure 2.7 – Example₃ $G_{D^*}(q)$ and $G_{D^+}(q)$ (left), and $G_{D^* \leftrightarrow D^+}(q)$ (right) curves.

Due to the reversibility of the process $D^*(or D) \leftrightarrow D^+$, the global reorganization energy is null ($\bar{\lambda} = 0$). The same is applied to the process $A \leftrightarrow A^-$.

2.3 Global process



Since exciton binding energy E_b depends on both E_g^{fund} and E_g^{opt} (see Chapter 1), it also depends on the combination of all the associated reorganization energies of each elementary (and reversible) process outlined just above (see refs. [4] and [5] where all the terms in relation with the reorganization were introduced). However, it is important to note here that still need to include in our demonstration aspects related to the presence of solvent (see refs. [6] and [7] to read a comprehensive study on the subject of the solvent's contribution).

Note, however, there exists a simple way to reintroduce *a posteriori* the repolarization of the solvent molecules into the initial model. Marcus first introduced this correction and it will be the subject of a part of the following paragraph.

$$E_b^v = E_g^{\text{fund},v} - E_g^{\text{opt}} = [IP^v - EA^v] - [E_{S_1} - E_{S_0}]$$

$$E_b^v = f(\lambda_{\text{abs}}, \lambda_{\text{em}}, \lambda_{\text{cat}}^+, \lambda_{\text{anion}}^-, \lambda_{\text{cat}}^-, \lambda_{\text{anion}}^+)$$

2.4 Distance dependences of electron transfer rates

Due to their low mass, electrons can tunnel over long distances (equal to or over 15 Å). An exponential decrease of electron transfer rates (k) with increasing donor-acceptor distance is usually observed for tunnelling, governed by the intervening medium and the nature of the donor and the acceptor.

According to the previous demonstrations (semi-classical theory), electron transfer rates depend on the reaction free energy, the reorganization energy associated with electron transfer (λ), and the electronic coupling (H_{DA}) between the donor and the acceptor:

$$k = A \times \exp\left\{\left(\frac{-\Delta G^{\ddagger}}{k_B T}\right)\right\} \propto (H_{DA})^2 \times \exp\left\{\left(\frac{-[\lambda + \Delta G^0]^2}{4\lambda k_B T}\right)\right\}$$

The exponential term in the formula reported just above is often referred to as the nuclear factor because it captures the effect of nuclear motions occurring during electron transfer.

The nuclear factor is responsible for the well-known Gaussian free energy dependence of k . In the normal regime of the plot in Figure 2.8, k increases with increasing the driving force, due to a decreasing activation barrier between the reactant $G_R(q)$ and product potential energy wells $G_P(q)$. k reaches a maximum when $\Delta G^0 = \Delta G_P^0 - \Delta G_R^0$ is equal to λ , at which point the reaction proceeds activationless (Figure 2.8, middle).

A further increase in driving-force entails the re-appearance of an activation barrier, leading to a decrease of k . This so-called inverted driving-force effect was predicted by theory, and, after some initial struggle, unambiguous experimental evidence for this phenomenon could be found. Nowadays, this effect is well documented and understood.

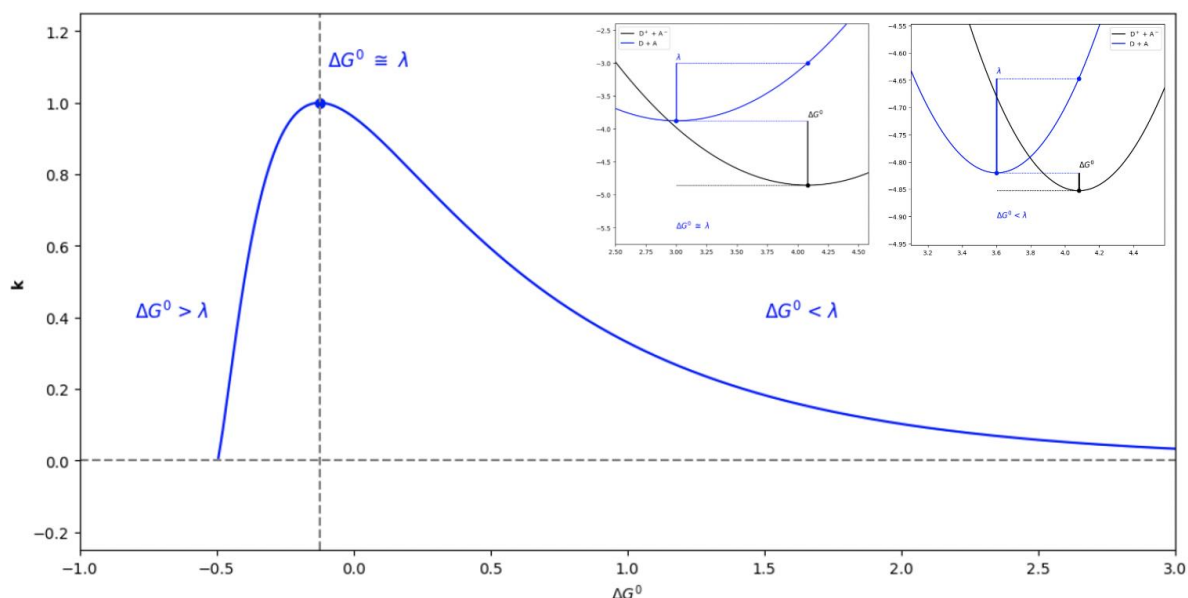


Figure 2.8 – Lower part: dependence of electron transfer rates k on ΔG^0 . Upper part: Reaction and product potential energy wells ($G_R(q)$, $G_P(q)$) in the activationless (middle) and the inverted regimes (right). The inverted driving-force effect is well explored and understood.

Thanks to modeling, it is also possible to understand and postulate the evolution of other system parameters λ and ΔG^\ddagger as a function of ΔG^0 (see Figure 2.9). It is possible to determine the values of λ and ΔG^\ddagger when ΔG^0 equals λ (at which point the reaction proceeds activationless). These quantities are marked on the figure by coloured points.

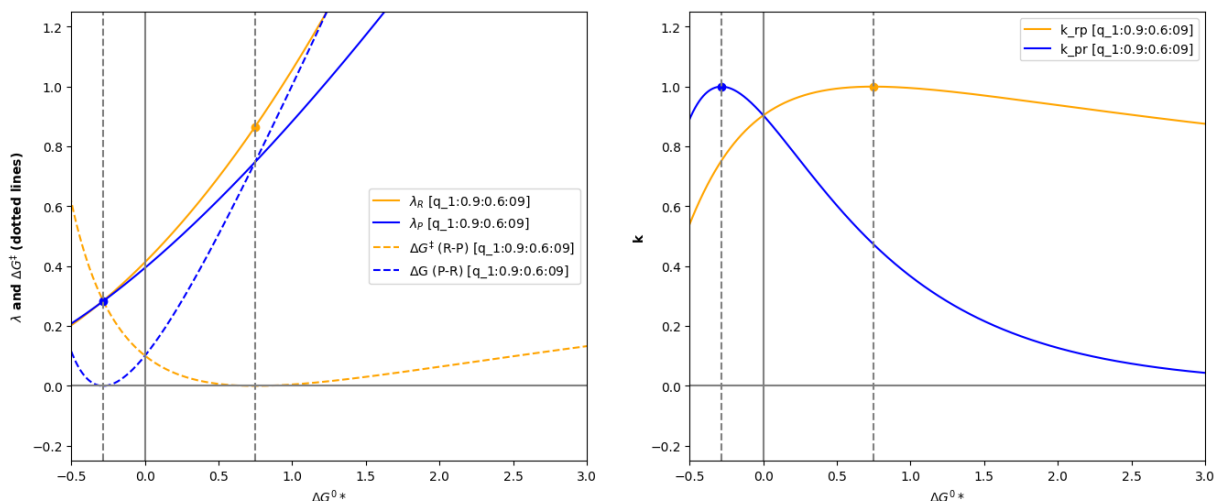


Figure 2.9 – Dependence λ and ΔG^\ddagger as a function of ΔG^0 .

Moreover, the reorganization energy¹ will remain very low as long as ΔG^0 is positive (orange curve - representing the phenomenon of charge transfer from reactants to products), which will not significantly affect the rate constant k ; this is no longer accurate for the phenomenon of inverse transfer (blue curves - representing the phenomenon of charge transfer from products to reactants).

However, our modeling has not yet introduced what will greatly affect the value of k .

$$k = A \times \exp\left\{\left(\frac{-\Delta G^\ddagger}{k_B T}\right)\right\} = \sqrt{\frac{\pi}{\hbar \lambda k_B T}} \times (H_{DA})^2 \exp\left\{\left(\frac{-[\lambda + \Delta G^0]^2}{4 \lambda k_B T}\right)\right\}$$

According to super-exchange theory [8], the electronic coupling term H_{DA} can be non-zero even when the donor and acceptor are far apart ($r_{DA} \geq 15 \text{ \AA}$) because the intervening medium (*e.g.*, covalent bridges or solvent molecules) can mediate long-range electronic coupling. H_{DA} unusually decreases exponentially with increasing distance r_{DA} , as shown in Figure 2.10.

The steepness of this decrease is captured by the distance decay parameter β_{el} :

$$H_{DA}(r_{DA}) = H_{DA}^0 \times \exp\{(-\beta_{el} \times (r_{DA} - r_{DA}^0))\}$$

¹as a reminder, these examples are fictitious and are intended solely to illustrate the behaviour of physical quantities related to each other.

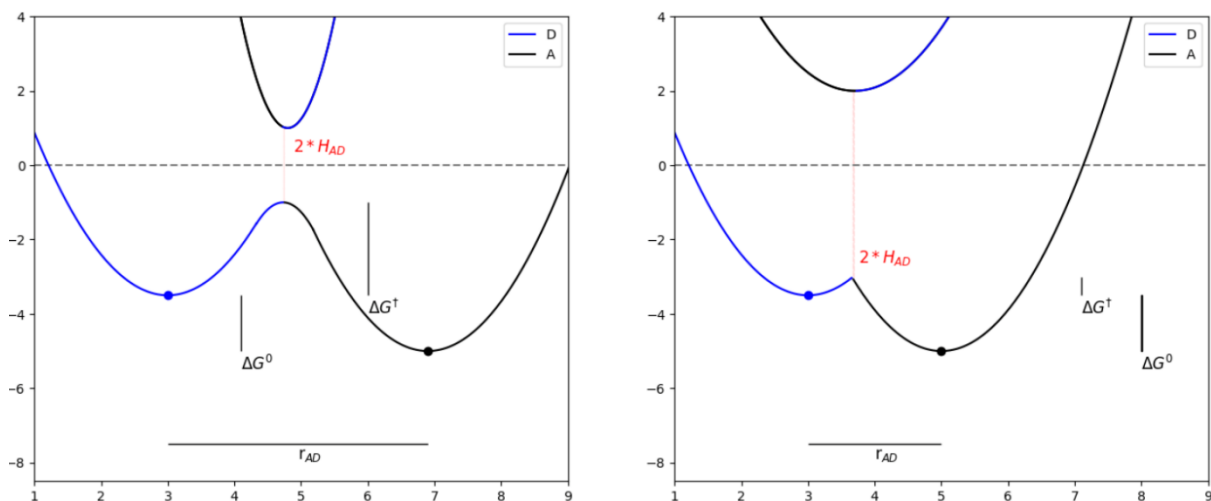


Figure 2.10 – Evolution of H_{DA} (and ΔG^\ddagger) for two fictives r_{DA} selected values (r_{DA} (left) $>$ r_{DA} (right)). The same $G_D(q)$ and $G_A(q)$ are used for the two simulations. Only the distance between A and D changes.

In which H_{DA}^0 is the electronic coupling between reactants at van-der-Waals contact distance r_{DA}^0 and β_{el} , a parameter governed by the combination of donor, acceptor and intervening medium. More precisely, quantum effects must be considered during the electronic transfer step. They are characterized by H_{DA}^0 essentially a transfer integral $\langle \Psi_R | H | \Psi_P \rangle$ where $\Psi_{R,P}$ signalling the wave functions of the reactants and products.

In a first approximation, this integral can be approximated by considering a purely mono-electronic process involving two orbitals Ψ_D and Ψ_A localized on a site, then we will call the donor and on a designated acceptor site:

$$H_{DA} \propto \langle \Psi_R | H | \Psi_P \rangle \rightarrow \langle \Psi_D | H | \Psi_A \rangle$$

In Figure 2.10, we also illustrate the dependency of ΔG^\ddagger on the value of H_{DA} . The left part of this figure corresponds to the adiabatic electron transfer case. Nuclear motion is coupled to electron motion, the system remains on one surface, and H_{DA} (electronic coupling) is large. The larger H_{DA} is, the larger k is. The transfer of charge is facilitated.

Conversely, the right of Figure 2.10 corresponds to the non-adiabatic electron transfer; *nuclei* do not move during electron transfer, a jump between states is required, and H_{DA} (electronic coupling) is small. The lower H_{DA} is, the lower k is. The transfer of charge is inhibited.

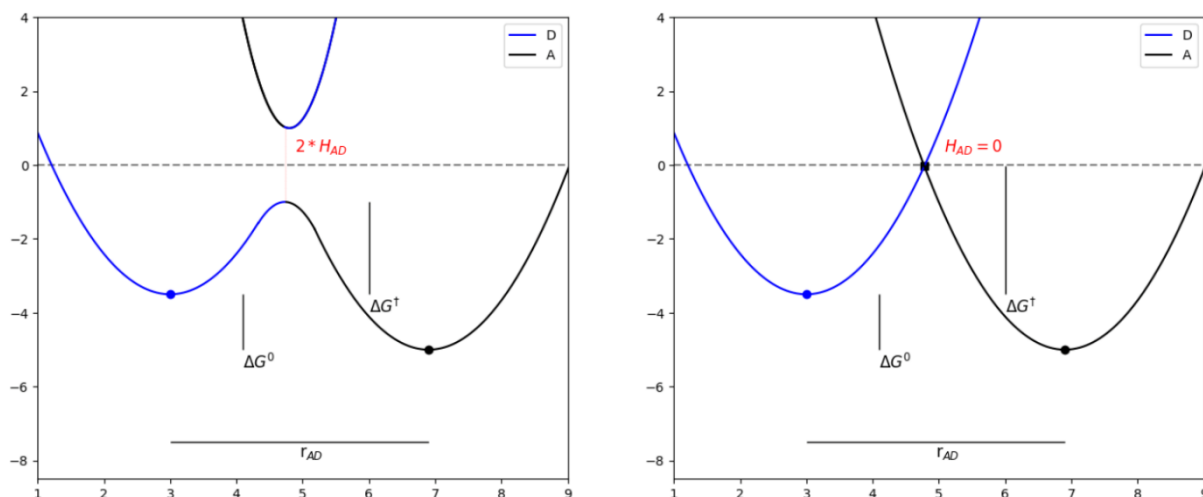


Figure 2.11 – Adiabaticity: smoothing out the Potential Energy Surface. The simulations were conducted using the following parameters: $G_D(q)$ ($\sigma_D = 2.19$, $t_D = 3.0$, and $d_D = 3.5$); $G_A(q)$ ($\sigma_A = 2.21$, $t_A = 6.9$ and $d_A = 5.0$). $r_{DA} = t_A - t_D$ is constant in the two cases.

H_{DA} is thus a distance-dependent parameter that separates the donor from the acceptor (Figure 2.11), similar to the parameters ΔG^0 and λ (Figure 2.10), but it is important to note also that the reorganization energy dependency on the position of the different partners can be substantial and not totally complete in Figure 2.10.

The overall reorganization energy is a sum of inner (λ_i) and outer (λ_o) contributions reflecting the energy required for nuclear reorganization on the donor and the acceptor in the course of electron transfer, as well as reorganization of their chemical environment (solvent, counterions...) [9]:

$$\lambda = \lambda_i + \lambda_o$$

As show in the previous paragraphs, λ_i is commonly treated as a distance-independent parameter. Contrary, λ_o strongly depends on r_{DA} and on solvent polarity. λ_o implies, in one hand, the repolarization of the solvent molecule's electronic cloud (known as the “optical” effect), and in the other hand, the orientation of dipole moments linked to nuclear displacements. Marcus theory derived an expression for λ_o within the framework of an electrostatic model:

$$\lambda_o = \frac{(\Delta e)^2}{4\pi\epsilon_0} \times \left[\frac{1}{2a_1} + \frac{1}{2a_2} - \frac{1}{r_{DA}} \right] \times \left[\frac{1}{n^2} - \frac{1}{\epsilon_s} \right]$$

in which Δe is the quantity of charge transferred, a_1 , a_2 , and r_{DA} are the radii of the donor, acceptor, and the distance between the two species during the transfer. n is the refractive index (optical dielectric constant $D_{op} = n^2$), and ϵ_s is the dielectric constant of the solvent. Obviously, the solvent plays a crucial role when the species are charged, attenuating electrostatic repulsions especially. However, by enhancing the activation energy, it slows down the electron transfer compared to the gas phase when neutral species are involved.

More sophisticated model treats the reactants as ellipsoids and permit more precise predictions. Nevertheless, the key point is that λ_0 increases with increasing r_{DA} and thus opposes the distance dependence of H_{DA} .

In order to estimate the numerical weight of these corrections, we have chosen to add to our previous model the two corrections on λ (and all the properties on which λ depends) and on k , and to present them using an example taken by Kuss-Petermann and Wenger [10] to conduct their demonstrations, *i.e.*, for spherical donors and acceptors with radii (a_1 , a_2) of 4 Å in CH₃CN ($n = 1.3341$, $\epsilon_s = 35.7$) at 298 K we assumed $H_{DA}^0 = 200 \text{ cm}^{-1}$ and $\beta_{el} = 0.8 \text{ Å}^{-1}$.

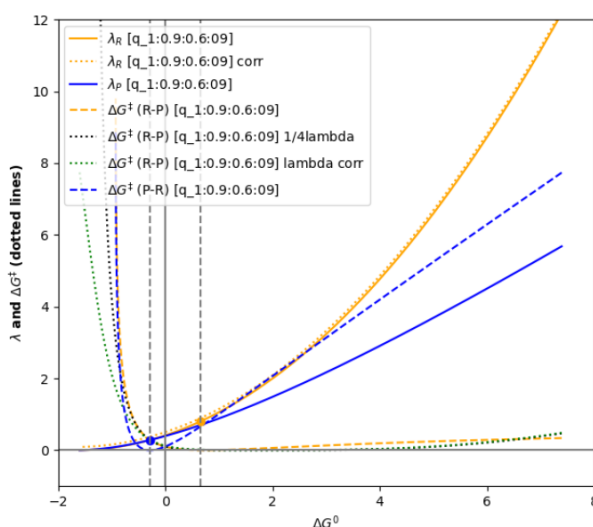


Figure 2.12 – Dependence of both λ and ΔG^\ddagger corrected as a function of ΔG^0 .

As shown in Figure 2.13, the corrections made to λ appear to have little numerical weight (mainly close to the $\Delta G^0 = \lambda$ situation). However, a more detailed analysis conducted on k (right in Figure 2.13) reveals that this effect could be finally significant for the reaction rate.

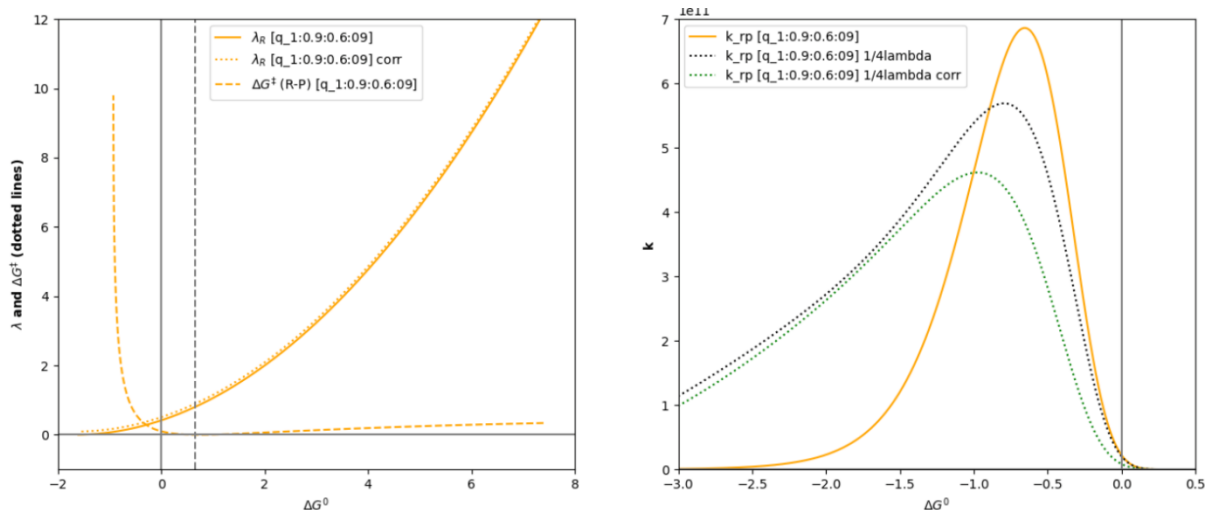


Figure 2.13 – Dependence of both λ and ΔG^\ddagger corrected as a function of ΔG^0 (left).

Dependence of rate constant k as a function of ΔG^0 (right).

The Influence of Donor-Acceptor Distance on Electron Transfer Rates could also be easily explained [11] as illustrated in Figure 2.14. In this context, three well-defined zones can be distinguished. For a small r_{DA} , it is into an inverted region and $\Delta G_{D \rightarrow A}^\ddagger$ is smaller than λ (left part of Figure 2.14). For an intermediate r_{DA} , a barrierless reaction is observed with $\lambda \cong \Delta G^0$ (middle part of Figure 2.14). For a large r_{DA} , it is considered in a normal region, and $\Delta G_{D \rightarrow A}^\ddagger$ is greater than λ (right part of Figure 2.14).

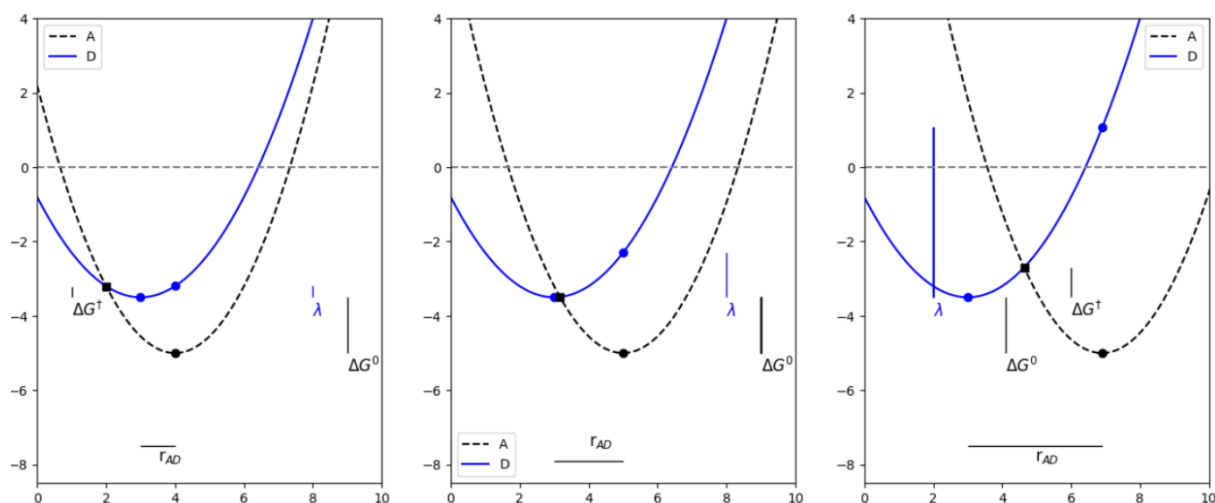


Figure 2.14 – The Influence of Donor-Acceptor Distance on Electron Transfer Rates.

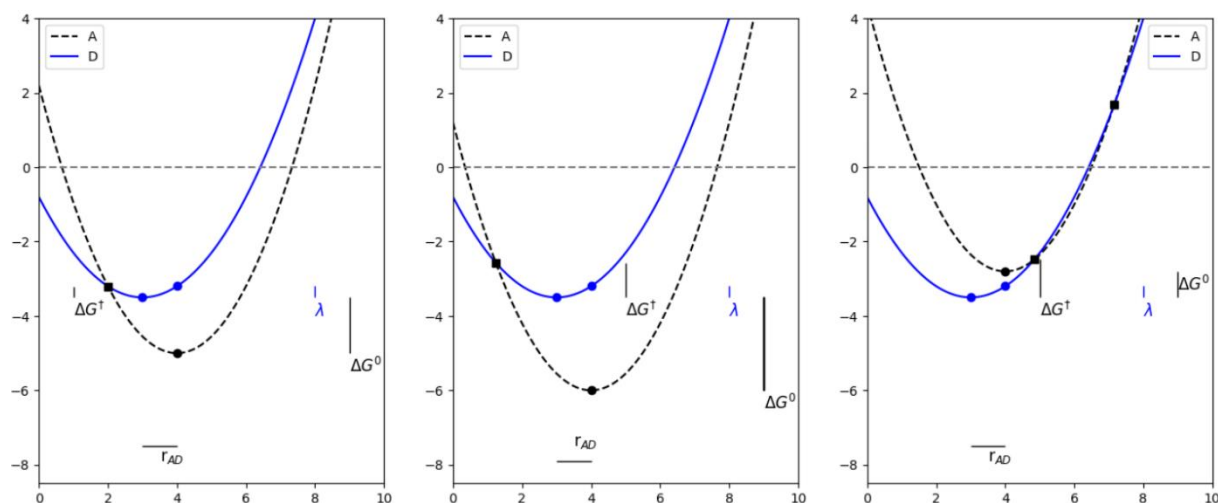


Figure 2.15 – The Effect of Thermodynamics on the Kinetic Barrier.

The Effect of Thermodynamics on the Kinetic Barrier could also be anticipated. As reported in Figure 2.15 (r_{DA} constant), we can see that:

- more exothermic reactions tend to be faster;
- more endothermic reactions tend to be slower;
- exothermic reactions tend to have early TS;
- endothermic reactions tend to have late TS (the Hammond postulate).

The Marcus parabola [12] obtained for four fictive $r_{DA}^0 < r_{DA}^1 < r_{DA}^2 < r_{DA}^3$ causes a downward shift of the k values, while the increase of λ displaces the parabola to the right (identifiable by the position of the maximum where the activationless point is reached, *i.e.*, $\Delta G^0 = \lambda$ shifting towards the right).

The two vertical lines in Figure 2.16 illustrate that at constant driving-force different distance dependences for k can result, depending on the exact driving-force. At $\Delta G^0 = -0.794$ eV, k decreases with increasing r_{AD} , whereas at $\Delta G^0 = -2.5$ eV, there is a decrease of k between r_{AD}^0 and r_{AD}^1 (green and black squares) and an increase of k between r_{AD}^2 and r_{AD}^3 Å (brown and magenta squares).

In other words, there are regimes in which one expects electron transfer rate maxima at large donor–acceptor distances. The black star on the graph marks the position of the maximum of k when λ_0 is neglect and when the electronic coupling term H_{DA} is not taken into account for r_{AD}^0 .

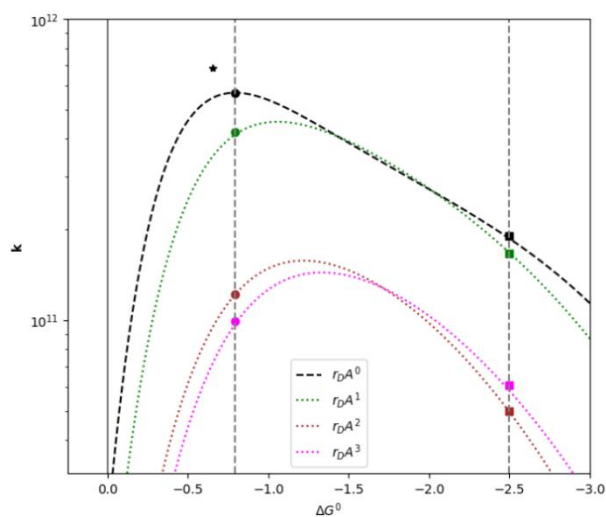


Figure 2.16 – Driving-force dependences of k for four different donor-acceptor distances (r_{DA}). The calculations were performed using λ and H_{DA} corrections and the following set of input parameters: spherical donors and acceptors with radii (a_1, a_2) of 4°\AA in CH_3CN ($n = 1.3341$, $\epsilon_s = 35.7$) at 298 K, we assumed $H_{DA}^0 = 200 \text{ cm}^{-1}$ and $\beta_{el} = 0.8 \text{ \AA}^{-1}$.

2.5 Voltage losses in Typical Photovoltaic Cells

In the context of organic electronic devices, charge mobility is crucial for their efficient operation. Reorganization energy λ is linked to the material's ability to redistribute charges and electron orbitals during charge transport.

A low reorganization energy implies more efficient charge redistribution during transport, promoting high electron mobility. Consequently, this can improve organic electronic devices' performances as charges can move more easily through the material.

On the other hand, exciton binding energy E_b is related to the interaction between electrons and atoms in the material, and electrostatic interactions at interfaces. A low binding energy can facilitate charge transport by reducing energy losses during electron movement through the material.

Direct equations linking reorganization energy to exciton binding energy exist. These two concepts are intimately linked by their influence on charge mobility and, therefore, on the performance of organic electronic devices. Manipulating reorganization energy is crucial to optimize charge mobility and enhance the overall performance of these devices.

We then introduce a last concept related to voltage losses V_{loss} in relation to both band gap E_g^{opt} , driving force and non-radiative recombination.

Voltage losses, also known as voltage drops, are a crucial aspect to consider in photovoltaic cells. These losses occur at various stages of the light conversion into electricity and can stem from several sources. Here are some of the main causes of voltage losses in photovoltaic cells:

- Ohmic voltage loss: these losses arise from the internal resistance of the photovoltaic cell and components throughout the entire system, including metal contacts, conducting wires, and junctions between materials;
- Recombination voltage loss: charge carriers generated within the photovoltaic cell may recombine before being collected by electrical contacts. This recombination results in a voltage loss as it reduces the available potential difference for current generation;
- Diffusion voltage loss: as charge carriers move through the photovoltaic cell, they may encounter obstacles leading to energy loss in the form of heat. This reduces the cell's output voltage;
- Thermal voltage loss: PV cells can also experience voltage losses due to thermal effects, such as cell overheating from exposure to sunlight or heat build-up within the system.

Reducing voltage losses is an important goal in developing more efficient photovoltaic cells. Research is underway to design materials and cell architectures that minimize these losses and maximize the overall conversion efficiency of light into electricity. Modeling and simulation are valuable tools in this process as they enable the prediction and optimization of photovoltaic cell performance, considering the various sources of voltage losses.

Voltage loss is generally defined as:

$$V_{loss} = \frac{E_g^{opt}}{q} - V_{oc} = \frac{E_{S_1} + \lambda_{abs} - E_{S_0} + \lambda_{em}}{q} - V_{oc}$$

in which E_g^{opt} is the bandgap, V_{oc} is the open-circuit voltage, and q is the elementary charge.

The voltage loss of photovoltaic cells can be divided into three parts [13,14]:

$$V_{loss} = \left(\frac{E_g^{opt}}{q} - V_{oc}^{SQ} \right) + (V_{oc}^{SQ} - V_{oc}^{rad}) + (V_{oc}^{rad} - V_{oc}) = \Delta E_1 + \Delta E_2 + \Delta E_3$$

in which V_{oc}^{SQ} is the maximum voltage according to the Shockley–Queisser limit, V_{oc}^{rad} is the voltage attainable when there is only radiative recombination, $\Delta E_2 = (V_{oc}^{SQ} - V_{oc}^{rad})$ is the voltage loss from additional radiative recombination at absorption below E_g^{opt} , and $\Delta E_3 = (V_{oc}^{rad} - V_{oc})$ is the non-radiative voltage loss.

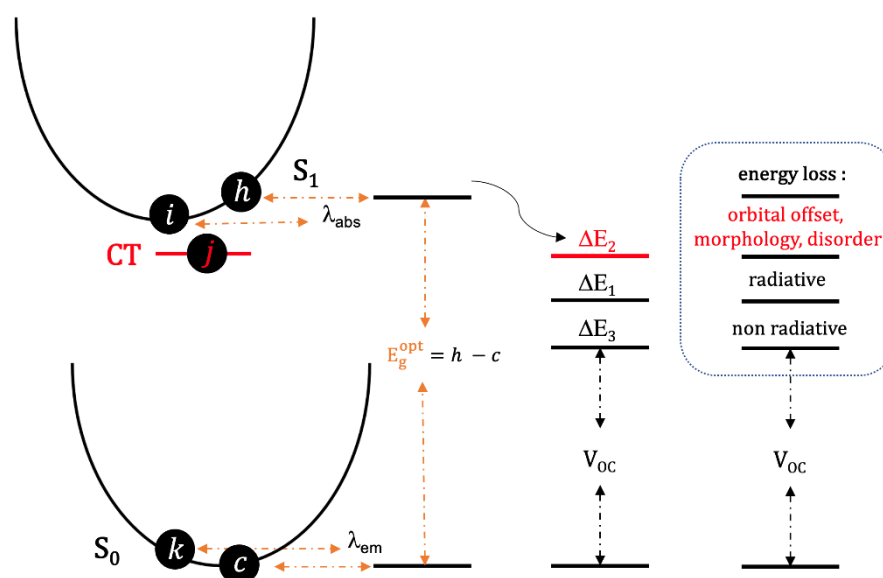


Figure 2.17 – Diagram of the energy of the ground state, the lowest excited state and charge transfer state as a function of a generalized coordinate (left). Diagram of energy losses in OPV cells (middle). A voltage loss diagram determined by the charge transfer state (right).

ΔE_1 is inevitable for any photovoltaic cell and only depends on E_g^{opt} in conditions where irradiation and temperature are stable.

ΔE_2 is the main distinction between OPVs and other photovoltaic technologies. For perovskite photovoltaic cells, this term is almost equal to zero; for OPVs, in particular fullerene-based OPVs, the existence of a charge transfer (CT)² state results in the additional absorption in low

² In OPV cells, CT states play a crucial role in the energy recombination process and are the active centres of charge separation (during charge migration, recombination may occur; this leads to the formation of CT excitons, with either singlet (SCT) or triplet (TCT) - see [15]). These states form when electrons are transferred from a donor polymer to an electron acceptor, creating an excited state where the electron is localized on the acceptor and the hole is localized on the donor.

Energy recombination occurs when these CT states decay, releasing energy in the form of photons. This energy is often lost as heat, thus reducing the quantum yield of the solar cell. The nature and kinetics of energy recombination from CT states are critical for OPV performance. Competitive recombination processes, such as geminate recombination (where the electron and hole recombine without emitting a photon) or non-radiative recombination (where energy is dissipated as heat without light emission), can diminish the cell's overall efficiency.

energy regions and reduces the maximum voltage attainable. In some OPVs based on non-fullerene acceptors, this term decreases from approximately 0.7 eV to 0.1 eV, because of the negligible energy offset between the CT and singlet states.

Assuming the photo charge loss is taken into account, one may calculate the maximal open-circuit voltage by subtracting the donor's HOMO from the acceptor's LUMO [16,17]. The V_{oc} was found to have a low dependence on the electrodes' work functions. Therefore, the open-circuit voltage of the bulk-heterojunction solar cell is often calculated using the following equation, in which e is the elementary charge:

$$V_{oc} = \frac{1}{e} (|\varepsilon_{HOMO}^D| - |\varepsilon_{LUMO}^A|) - 0.3$$

Considering the frequent inaccuracies and misinterpretations of eigenvalues ε from DFT calculations highlighted in Chapter 1, and the empirical nature of the term 0.3, it is important to emphasize to the reader that these factors raise two significant concerns when employing these approximations.

Therefore, reduction of voltage losses in OPVs is an urgent requirement. Moreover, as mentioned by Shi and collaborators [18], the understanding of the relationship between reorganization energy and energy losses has rarely been studied and constitute a new challenge. Indeed, it is evident that with each new aspect integrated into the understanding or research of the ideal process, a new challenge arises. Modeling can aid in predicting these challenges with varying degrees of precision.

The ideal device would be the one that possesses both a low bandgap, low bending energy, and minimal reorganization energy while allowing control over charge losses during the electron diffusion process towards the electrodes. Only when all these conditions are met can we obtain efficient compounds.

Therefore, understanding and controlling charge transfer states and their associated energy recombination mechanisms are essential for designing efficient organic solar cell materials and architectures. Advanced experimental techniques, such as time-resolved spectroscopy, and computational simulations, are used to study and optimize these processes in OPV development.

References

- [1] R.A. Marcus, *The Journal of Chemical Physics* 24 (1956) 966–978.
- [2] W.F. Libby, *J. Phys. Chem.* 56 (1952) 863–868.
- [3] W.F. Libby, *The Journal of Chemical Physics* 38 (1963) 420–425.
- [4] G.R. Hutchison, M.A. Ratner, T.J. Marks, *Journal of the American Chemical Society* 127 (2005) 2339–2350.
- [5] G.B. Alves, E.F. Oliveira, A. Batagin-Neto, F.C. Lavarda, *Computational Materials Science* 152 (2018) 12–19.
- [6] M.D. Driver, M.J. Williamson, J.L. Cook, C.A. Hunter, *Chem. Sci.* 11 (2020) 4456–4466.
- [7] S.M. Ryno, Y.-T. Fu, C. Risko, J.-L. Brédas, *ACS Applied Materials & Interfaces* 8 (2016) 15524–15534.
- [8] H. Weihe, H.U. Güdel, *Inorg. Chem.* 36 (1997) 3632–3639.
- [9] J.-L. Brédas, D. Beljonne, V. Coropceanu, J. Cornil, *Chem. Rev.* 104 (2004) 4971–5004.
- [10] M. Kuss-Petermann, O.S. Wenger, *Phys. Chem. Chem. Phys.* 18 (2016) 18657–18664.
- [11] M. Kuss-Petermann, O.S. Wenger, *Journal of the American Chemical Society* 138 (2016) 1349–1358.
- [12] J.R. Miller, L.T. Calcaterra, G.L. Closs, *Journal of the American Chemical Society* 106 (1984) 3047–3049.
- [13] J. Liu, S. Chen, D. Qian, B. Gautam, G. Yang, J. Zhao, J. Bergqvist, F. Zhang, W. Ma, H. Ade, O. Inganäs, K. Gundogdu, F. Gao, H. Yan, *Nat Energy* 1 (2016) 16089.
- [14] M. Zhang, J. Wang, X. Ma, J. Gao, C. Xu, Z. Hu, L. Niu, F. Zhang, *APL Materials* 8 (2020) 090703.
- [15] G. Han, T. Hu, Y. Yi, *Advanced Materials* 32 (2020) 2000975.
- [16] T. Ameri, P. Khoram, J. Min, C.J. Brabec, *Advanced Materials* 25 (2013) 4245–4266.
- [17] M.C. Scharber, D. Mühlbacher, M. Koppe, P. Denk, C. Waldauf, A.J. Heeger, C.J. Brabec, *Adv. Mater.* 18 (2006) 789–794.
- [18] Y. Shi, Y. Chang, K. Lu, *Nat. Commun* 13 (2022) 3256.

Chapter 3

Theoretical Framework for Computational Modeling

This chapter gives the concise context of the computational modeling performed in this work and emphasises its role in predicting electronic structures and properties of materials. First, an overview of quantum chemistry approaches is provided, including approximations, main ideas for developing the Hartree-Fock method, DFT principles from models and theorems, and interactions to be considered in the calculations. After that, it is presented other methods based on electron density for investigating properties, such as noncovalent interaction isosurfaces and Fukui indexes. Finally, the correlation between theoretical and experimental methods, the importance of model validation from benchmarking and the challenges still found to predict molecular properties are discussed.

To describe a molecular system and its properties, quantum chemical approaches come out with the molecular wavefunction from a solution of the time-independent Schrödinger equation:

$$\hat{H}\Psi = E\Psi, \quad (3.1)$$

where \hat{H} is the Hamiltonian operator that describes the molecular system, Ψ is the real wavefunction in terms of the electronic and nuclear coordinates, and E is the system's total energy.

Generally, a partition of the Hamiltonian is used to preserve the two contributions of it: the kinetic \hat{T} and the potential \hat{V} energies. Therefore, \hat{H} operator for a molecule with N electrons and M nuclei is defined as shown in Equation (1.3, in which \hbar is the Dirac constant (Planck constant divided by 2π), m is the mass, ∇^2 is the Laplace operator (three-dimensional derivative, $\nabla_i^2 = \frac{\partial^2}{\partial x_i^2} + \frac{\partial^2}{\partial y_i^2} + \frac{\partial^2}{\partial z_i^2}$), Z is the atomic number, e is the charge of one electron, ϵ_0 is the vacuum permittivity and r is the relative distance between species ($r_{iA} = |\vec{r}_i - \vec{r}_A|$).

Kinetic energy operator \hat{T}

Potential energy operator \hat{V}

$$\hat{H} = - \sum_{i=1}^N \frac{\hbar^2 \nabla_i^2}{2m_i} - \sum_{A=1}^M \frac{\hbar^2 \nabla_A^2}{2m_A} \quad (3.2)$$

$$- \sum_{i=1}^N \sum_{A=1}^M \frac{Z_A e^2}{4\pi\epsilon_0 r_{iA}} + \sum_{A=1}^M \sum_{B>A}^M \frac{Z_A Z_B e^2}{4\pi\epsilon_0 r_{AB}} + \sum_{i=1}^N \sum_{j>i}^N \frac{e^2}{4\pi\epsilon_0 r_{ij}},$$

electron-nucleus
nucleus-nucleus
electron-electron
attraction
repulsion
repulsion

An exact solution is hard to find as molecules are composed of many atoms. Many approaches are proposed to simplify the resolution of the Schrödinger equation.

Considering the Bohr-Oppenheimer approximation, as the mass of the nucleus is significantly large compared to the mass of electrons, it is assumed there is no movement of nuclei. It is also relevant to clarify that, unlike in liquids and plasmas, the nuclei in solids remain almost immobile, forming a molecular structure, an amorphous conformation, or an ordered crystalline lattice [1]. Therefore, the kinetic energy of nuclei is negligible.

Assuming the nuclear coordinates \vec{r}_A as external parameters and the system wavefunction as a function of the electron coordinates $\Psi = \Psi(\vec{r}_1, \dots, \vec{r}_N)$ [1], the Coulombic potential of the nuclei is constant (Bohr Oppenheimer approximation), defined as:

$$V_n(\vec{r}) = - \sum_A \frac{Z_A}{r_A} = cte \quad (3.3)$$

From here, it will be separated the nucleic and electronic contributions.

The Equation (1.3 can be written in terms of the coordinates of electrons as:

$$\hat{H}_{el}\Psi = E\Psi \quad (3.4)$$

$$\hat{H}_{el} = - \sum_i \frac{\nabla_i^2}{2} + \sum_i V_n(\vec{r}_i) + \frac{1}{2} \sum_{i \neq j} \frac{1}{r_{ij}} \quad (3.5)$$

This is the fundamental equation of electronic structure theory.

In a first approximation, it is possible to deduce that the solution of the wavefunction of the whole system is the product of wavefunctions of electrons [1]:

$$\Psi(\vec{r}_1, \vec{r}_2, \dots, \vec{r}_N) = \phi_1(\vec{r}_1) \cdots \phi_N(\vec{r}_N) \quad (3.6)$$

Then, the wavefunctions are solutions of N single-electron Schrödinger equations:

$$\hat{h}_i(\vec{r}_i)\phi_i(\vec{r}_i) = E_i\phi_i(\vec{r}_i) \quad (3.7)$$

The trial solution becomes:

$$\left[\sum_i \hat{h}_i(\vec{r}_i) \right] \phi_1(\vec{r}_1) \cdots \phi_N(\vec{r}_N) = E \phi_1(\vec{r}_1) \cdots \phi_N(\vec{r}_N) \quad (3.8)$$

As the single-electron Hamiltonian of electron 1 only acts on its function, and so on, it is rewritten as:

$$\begin{aligned} & [\hat{h}_1(\vec{r}_1)\phi_1(\vec{r}_1)]\phi_2(\vec{r}_2) \cdots \phi_N(\vec{r}_N) + \phi_1(\vec{r}_1)[\hat{h}_2(\vec{r}_2)\phi_2(\vec{r}_2)] \cdots \phi_N(\vec{r}_N) + \cdots \\ & = [E_1]\phi_1(\vec{r}_1) \cdots \phi_N(\vec{r}_N) + [E_2]\phi_1(\vec{r}_1) \cdots \phi_N(\vec{r}_N) + \cdots \end{aligned} \quad (3.9)$$

Finally, the energy of the system in fact can be described as the sum of each electronic energy:

$$E = \sum_i^N E_i \quad (3.10)$$

The Hartree-Fock (HF) approximation turns the many-body Schrödinger equation into many coupled single-particle equations regarding wavefunctions. HF method was proposed by Fock in 1930, applying the Slater determinant (that describes the antisymmetric wavefunctions) to the Hartree method [2]. The one-electron equation is:

$$\hat{F}\phi_i = \varepsilon_i\phi_i, \quad (3.11)$$

in which the Fock matrix, in terms of the Coulomb operator \hat{J} and exchange operator \hat{K} , is defined as:

$$\hat{F} = \hat{h} + \sum_j^N (2\hat{J}_j - \hat{K}_j) \quad (3.12)$$

So, the orbital energy ε_i and the total electron energy E_{HF} are represented as:

$$\varepsilon_i = h_i + \sum_{j=1}^{N/2} (2J_{ij} - K_{ij}) \quad (3.13)$$

$$E^{\text{HF}} = 2 \sum_{i=1}^{N/2} \varepsilon_i - \sum_{i \neq j}^{N/2} (2J_{ij} - K_{ij}) \Rightarrow E = \sum_{i=1}^{N/2} (\varepsilon_i + h_i) \quad (3.14)$$

It is important here to make a remark: many times, the electronic energy of molecules in various states is estimated from the energy levels of the highest-occupied molecular orbital (HOMO) and the lowest-unoccupied molecular orbital (LUMO), which are one-electron wave functions. It is a very crude approximation in HF approach.

The total energy of the system is sum of the total electron energy and the nucleus-nucleus repulsion energy:

$$E_{\text{T}} = E^{\text{HF}} + V_{\text{nucleus-nucleus}} \quad (3.15)$$

Despite the huge advance with the HF method in quantum chemistry, this method presented some errors in chemical calculations. It became necessary to incorporate at least the electronic correlation to calculate the exact energy of molecules as accurately as possible, but it depended on a much higher computational time. Density functional theory (DFT) was developed to sustain this problem.

3.1 Principles of Density Functional Theory (DFT)

Unlike HF and *a fortiori* post-HF methods (more details at ref. [3]) describe the electronic system from wavefunction $\Psi_{(\vec{r})}$, DFT includes electron correlations and exchange to describe it from the electronic density $\rho_{(\vec{r})}$, which correlation with wavefunction $\Psi_{(\vec{r})}$ according the electronic coordinate \vec{r} is given below:

$$\rho_{(\vec{r})} = \Psi_{(\vec{r})}^* \Psi_{(\vec{r})} \quad (3.16)$$

$$\rho_{(\vec{r})} = |\Psi_{(\vec{r})}|^2 \quad (3.17)$$

Semiempirical theories come up to describe correctly the ground state energy of molecules from their electron density.

3.1.1 Thomas-Fermi model

Thomas-Fermi (TF) theory was the first DFT fundament, relying only on the electronic density [4]. The electronic structure was described in an inhomogeneous situation, such as in an atom, molecule, or solid, correlating the electron density and the maximum or Fermi momentum p_f [5]:

$$\rho(\vec{r}) = \left(\frac{1}{3}\pi^2\right) \hbar^3 p_f^3(\vec{r}) \quad (3.18)$$

In 1927, they expressed the kinetic energy term as a function of electronic density [3]:

$$\hat{T}^{\text{TF}}[\rho] = \frac{3}{10} (3\pi)^{2/3} \int \rho^{5/3}(\vec{r}) \cdot d\vec{r} \quad (3.19)$$

While the approximation of kinetic energy considered a uniform electron gas, the interactions between electrons were based on the classical electrostatic Coulomb repulsion [4], so the energy of the system is expressed as [5]:

$$E^{\text{TF}} = (\hbar^2/2m)(3\pi)^{2/3} \rho^{2/3}(\vec{r}) + V_{ee}(\vec{r}) + V_{ne}(\vec{r}) \quad (3.20)$$

Since this expression is classical, it can only be used in regions that satisfy $E - V > 0$, though the kinetic energy density must be positive, meaning that where $\rho(\vec{r}) = 0$ are forbidden regions [5].

3.1.2 Thomas-Fermi-Dirac model

Thomas-Fermi method represented the Hamiltonian operator as functional only of the electron density, but it still encountered many failures in calculating electronic states [2]. To solve this problem due to a lack of exchange energy, in 1930, Dirac proposed a model including the exchange term E_x from the exchange energy per electron $\epsilon_x[\rho]$ [3], known as the first local density approximation (LDA) [2], expressed as:

$$K[\rho] = E_x[\rho] = \int \rho \epsilon_x[\rho] \cdot d\vec{r} \quad (3.21)$$

$$E_x^{\text{LDA}}[\rho] = -\frac{3}{4} \left(\frac{3}{\pi}\right)^{1/3} \int \rho^{4/3}(\vec{r}) \cdot d\vec{r} \quad (3.22)$$

The exchange term of this model is combined with $\hat{T}^{\text{TF}}[\rho]$ (Equation (3.19)) and $V_{\text{ne}}[\rho]$, not considering the electronic correlation.

3.1.3 Slater model

In 1951, Slater approximated the interactions in a ground-state system by improving the HF method with the Pauli exclusion principle [4]. The exchange term from the HF formalism is expressed including the parameter α (after empirical analysis based on different types of chemical systems, $\alpha = 3/4$) [3]:

$$E_{\text{x}}[\rho] = -\frac{9\alpha}{8} \left(\frac{3}{\pi}\right)^{1/3} \int \rho_{(\vec{r})}^{4/3} \cdot d\vec{r} \quad (3.23)$$

Another important contribution of Slater was the importance given to holes for explaining interactions between electrons very close to each other [4].

3.1.4 Hohenberg and Kohn theorems

The previous models gave some fundamentals on which DFT was developed, showing the importance of electron density in estimating the total energy of a molecular system. It was in 1964 [6] when Walter Kohn and Pierre Hohenberg proved the existence of a universal functional of density, independent of an external potential, that exactly predicts the ground-state energy. The two main achievements of their theorems are highlighted below.

3.1.4.1 Uniqueness Theorem

The system's total energy in a ground state can be calculated from a universal functional F_{HK} of a unique or nearly constant electronic density [3], only if there is an external potential v_{ext} [5]:

$$E^{\text{HK}}[\rho] = T_{\text{e}}[\rho] + V_{\text{ee}}[\rho] + \int \rho_{(\vec{r})} v_{\text{ext}} \cdot d\vec{r} \quad (3.24)$$

in which:

$$T_e[\rho] + V_{ee}[\rho] = F^{\text{HK}}[\rho] \quad (3.25)$$

$$v_{\text{ext}} = V_{\text{ne}}[\rho] \quad (3.26)$$

Note that the universal functional is not linked to the external potential. As there is no need for approximations, this solution is said to be exact.

3.1.4.2 Hohenberg-Kohn Variational Principle

This second theorem implies that each electronic density ρ determines a system's unique potential energy and wavefunction, so determining its electronic density in the fundamental state ρ_0 [3]:

$$E[\rho] \geq E[\rho_0] \quad (3.27)$$

Therefore, the minimum energy of the system is determined according to the following relation:

$$E[\rho_0] = \min_{\rho} \left(\min_{\Psi \rightarrow \rho} \left(F[\rho] + \int \rho_{\vec{r}} v_{\vec{r}} \cdot d\vec{r} \right) \right) \quad (3.28)$$

Even though it was described how to calculate the energy of ground-state system, to use DFT it is necessary to approximate the universal functional [4].

3.1.5 Kohn-Sham approach

In 1965, this time with Lu Sham [7], W. Kohn described the reference Hamiltonian in terms of n particles without interactions but in the same density of a real system, so the same as for HF equations, the resolution of the system problem becomes mono-electronic equations [3], expressed as:

$$\hat{H}^{\text{KS}} = -\frac{1}{2}\nabla^2 + v_{\text{H}}[\rho] + v_{\text{xc}}[\rho] + v_{\text{ext}}[\rho], \quad (3.29)$$

in which:

$$v_{\text{H}}[\rho] = \int \frac{\rho(\vec{r}) - \rho(\vec{r}')}{|\vec{r} - \vec{r}'|} \cdot d\vec{r} \quad (3.30)$$

$$v_{xc}[\rho] = \frac{\partial E_{xc}[\rho(\vec{r})]}{\partial \rho(\vec{r})} \quad (3.31)$$

where $v_H[\rho]$ and $v_{xc}[\rho]$ are respectively the Hartree potential and the exchange-correlation potential, and $E_{xc}[\rho(\vec{r})]$ is the exchange-correlation energy.

The KS orbitals ψ_i are introduced at this moment as:

$$\hat{H}^{KS}\psi_i(\vec{r}) = \epsilon_i\psi_i(\vec{r}) \quad (3.32)$$

As in the case of the HF method, the expression of system energy is minimized in a few terms, but now, according to KS orbitals equations, as Slater's theory predicted the solution is exact if the exact functional is known [4]. Therefore, in KS theory [3,8], the energy of a system in a ground state is expressed as:

$$E^{KS} = T_s[\rho] + J[\rho] + V_{ne}[\rho] + E_{xc}[\rho] , \quad (3.33)$$

in which:

ρ : is the electron density of the KS reference system

$$\rho(\vec{r}) = \sum_i |\psi_i(\vec{r})|^2 \quad (3.34)$$

$T_s[\rho]$: is the kinetic energy for the KS noninteracting electrons

$$T_s[\rho] = \sum_i \left\langle \psi_i \left| -\frac{1}{2} \nabla^2 \right| \psi_i \right\rangle \quad (3.35)$$

$J[\rho]$: is the classical electron-electron repulsion energy

$$J[\rho] = \frac{1}{2} \int \int \frac{\rho(\vec{r})\rho(\vec{r}')}{|\vec{r} - \vec{r}'|} d\vec{r} d\vec{r}' \quad (3.36)$$

$V_{ne}[\rho]$: is the interaction energy with the external potential due to the nuclei

$$V_{ne}[\rho] = \int V_{ext}(\vec{r})\rho(\vec{r}) \cdot d\vec{r} \quad (3.37)$$

The total energy of the real system E^{HK} according to Hohenberg and Kohn theory must be equal to the energy of the system described by KS orbitals E^{KS} , so the exchange-correlation functional can be formulated as:

correction of the kinetic energy due to electronic interactions

$$E_{\text{xc}}[\rho] = T[\rho] - T_{\text{s}}[\rho] + V_{\text{ee}}[\rho] - J[\rho] \quad (3.38)$$

non-classic correction of electron-electron repulsions

DFT is based on the Kohn-Sham theory. It has been the most popular computational method to estimate electronic properties of molecular and periodic structures, with relatively low computational cost compared to other high-level methods including electron correlation [9].

3.1.6 Classification of exchange-correlation functionals

As previously detailed, DFT is an exact method if the universal functional $F_{\text{HK}}[\rho]$ or its exchange-correlation functional $F_{\text{xc}}[\rho]$ is known. However, for calculating the exchange-correlation energy, approximations are still needed. Though, it can be extracted from its functional:

$$E_{\text{xc}}[\rho] = \int F_{\text{xc}}[\rho(\vec{r})] \cdot d\vec{r} \quad (3.39)$$

There are many approximations for calculating the exchange-correlation functional, classified according to their general characteristics [2]:

- Local density approximation (LDA): functionals in function of electron density ρ
- Generalized gradient approximation (GGA): functionals correcting LDA ones with the density gradient $\nabla\rho$
- Hybrid: functionals mixing LDA and GGA ones with a fixed ratio of the HF exchange
- Meta-GGA: functionals correcting GGA ones with the kinetic energy density τ
- Semiempirical: functionals that accurately reproduce properties with semiempirical parameters (for example, B97 and M06 functionals)
- Progressive: functionals transforming in accordance with combined functionals.

Below, some of them are better detailed to contextualize the hybrid functional B3LYP used in this work.

3.1.6.1 Local Density Approximation (LDA)

In LDA, the exchange-correlation function is described from the energy of exchange and correlation of one electron immersed in a uniform gas of electrons with electron density [3,10]. The energy for LDA is written as:

$$E_{xc}^{LDA}[\rho(\vec{r})] = \int \epsilon_{xc}^{\text{unif}}[\rho(\vec{r})] \cdot d\vec{r} \quad (3.40)$$

The first LDA was the kinetic energy of the electron density. It was based on the Thomas model of electrons being distributed uniformly in solid crystals, assuming that the nucleus-electron interaction potential without an electromagnetic field depends only on the nuclear distances [2]. Dirac, in 1930, proposed the first exchange functional [8], as it is expressed by Equation (3.22). Another example is the SVWN functional, which describes exchange term using Slater functional (from an LDA) and correlation term using Vosko-Wilk-Nusair functional.

3.1.6.2 Generalized Gradient Approximation (GGA)

Unlike LDA, GGA consider the inhomogeneity of the electron density [3] that “the exchange hole is ‘off centre’ concerning the electron it surrounds” [11]. The electronic exchange energy described in GGA depends on the reduced gradient of density s , formulated as:

$$E_x^{\text{GGA}}[\rho(\vec{r})] = A_x \int \rho^{4/3} F[s] \cdot d\vec{r} \quad (3.41)$$

in which $A_x = -\frac{3}{4} \left(\frac{3}{\pi}\right)^{1/3}$ and:

$$F[s] = (1 + 1.296s^2 + 14s^4 + 0.2s^6)^{1/15} \quad (3.42)$$

$$s = \frac{|\nabla\rho(\vec{r})|}{2k_F\rho(\vec{r})} \quad (3.43)$$

$$k_F = (3\pi^2\rho(\vec{r}))^{1/3} \quad (3.44)$$

Then s becomes:

$$s = \frac{1}{2(3\pi^2)^{1/3}} \frac{|\nabla\rho(\vec{r})|}{\rho^{4/3}(\vec{r})} \quad (3.45)$$

Note that s is defined not only in terms of the electron density but also the gradient norm $|\nabla\rho(\vec{r})|$ [12], representing its magnitude, given by:

$$|\nabla\rho(\vec{r})| = \sqrt{\left(\frac{\partial\rho(\vec{r})}{\partial x}\right)^2 + \left(\frac{\partial\rho(\vec{r})}{\partial y}\right)^2 + \left(\frac{\partial\rho(\vec{r})}{\partial z}\right)^2} \quad (3.46)$$

One example of GGA functional is the Perdew-Burke-Ernzerhof (PBE).

Until here, it was discussed about conventional functionals, that were very important in the development of exchange-correlation corrections, but they were not sufficient to describe some interactions.

Some limitations are found in calculations with LDA and GGA due to the delocalization error, that is, the self-interaction of charges is not taken into account [13]. This provides fundamental gaps as small as KS gap (that is the difference between KS HOMO and LUMO energy eigenvalues) [10] and an overestimation of binding energies [2]. Hybrid functionals were developed to solve this self-interaction error of the standard functionals by including HF exchange integral.

3.1.6.3 Hybrid functionals

The first and widely used hybrid functional is the B3LYP functional, that includes a 20% contribution of HF functional to the exchange term in the GGA BLYP functional, which is a combination of Becke-88 (B88) functional for the exchange gradient correction and Lee-Yang-Park (LYP) functional for the correlation term. The B3LYP approximation terms are detailed below [2]:

$$E_{xc}^{B3LYP} = E_{xc}^{LDA} + a_0(E_x^{HF} - E_x^{LDA}) + a_x\Delta E_x^{B88} + a_c(E_c^{LYP} + E_c^{VWN-LDA}) \quad (3.47)$$

with the optimized semiempirical parameters a_0 , a_x and a_c equal to 0.20, 0.72 and 0.81, respectively, according to Becke [14].

Another very popular hybrid functional is the PBE0, a mix of the standard GGA PBE functional with 25% of HF exchange.

Many other hybrid functionals were developed and compared in many works [9,15–17]. Moreover, the HOMO and LUMO eigenvalues calculated using functionals from different categories of DFT methods were already discussed among the theoretical researchers [18–20], showing that the smaller percentage of HF exchange (as in the B3LYP functional) resulted in lower errors as calculating the HOMO-LUMO gap for the studied molecules.

In our work, we decided to use one functional for calculating all the systems, then we could investigate the deep dependence of molecular structure for estimating optoelectronic properties.

3.1.7 Dispersion correction for KS-DFT energy

A lack of accuracy in the description of the interactions in the system is found in KS calculations using LDA and GGA correlation functionals, as the long-range attraction of van der Waals (vdW) interactions is neglected [2]. Therefore, it led to adding a dispersion correction into KS-DFT energy for capturing London classical forces, an approximation known as DFT-D.

That is a functional in terms of nuclear geometry (not density-dependent) involving empirically parameterized coefficients C_n^{AB} , high-order behaviour of correction $1/R^n$ (with $n = 6, 8, 10 \dots$) and an appropriate damping functional f^{damp} [8], which dissipate fast enough in the presence of perturbation caused by weak interaction in small distances between atoms A and B R_{AB} [21]. The dispersion energy is generally described as:

$$E_{\text{disp}} = - \sum_{A>B} \frac{C_6^{AB}}{R_{AB}^6} f_{\text{damp}}(R_{AB}) \quad (3.48)$$

Approximations were done along the years to find even more accurate dispersion energy, with D2 model [22] and functionals that already include this empirical atom-atom dispersion correction, such as ω B97X-D [21]. In 2011, Grimme, Ehrlich and Goerigk [23] elaborated a D3 version of the Becke-Johnson damping:

$$E_{\text{disp}}^{\text{GD3BJ}} = - \frac{1}{2} \sum_{A \neq B} s_6 \frac{C_6^{AB}}{R_{AB}^6 + [f(R_{AB}^0)]^6} + s_8 \frac{C_8^{AB}}{R_{AB}^8 + [f(R_{AB}^0)]^8} \quad (3.49)$$

in terms of the n-th order global scaling factor (functional dependent) s_n and in which:

$$f(R_{AB}^0) = a_1 R_{AB}^0 + a_2 \quad (3.50)$$

$$R_{AB}^0 = \sqrt{\frac{C_8^{AB}}{C_6^{AB}}} \quad (3.51)$$

The optimized parameters s_i and a_i are tabulated for each density functional.

Other empirical dispersion models as APF-D [24] and an extension of the D3 model, the D4 [25], were developed, including more approximations to provide an efficient computation of molecular dipole-dipole dispersion.

3.1.8 Challenges of DFT

As was already mentioned here, there are still many limitations of DFT in describing efficiently all the covalent bonding energy, van der Waals interactions and transition states.

The scientific community is facing many challenges, such as decreasing the complexity of functionals, that is, as methods try to englobe the entire energy of the system, remaining more computationally consumed, it is necessary to simplify them, but not until turn it into an empirical method [8].

Standard DFTs also lack accuracy due to delocalization error, that is, the self-interaction of electron density, which occurs for any interatomic distance [13]. It causes, for example, overestimation of the bandgap on calculations, where hybrid functionals come to solve it [26].

DFT is a method for accurately computing the total energy of the molecular system and estimating other important electronic components, such as orbitals and eigenvalues, as exactly as possible [8]. It means that DFT is appropriate for calculating ground-state properties. When the molecules are under electronic excitations, other approaches should be considered.

3.2 Method for calculating properties of molecules in excited state

In analogy to the exchange-correlation energy in DFT, the exchange-correlation potential in time-dependent DFT (TD-DFT) varies in terms of electron density $\rho(\vec{r},t)$, which is now spatially and time dependent. It is a linear-response method in which the self-consistent perturbation in an adiabatic limit (low frequency) can compute the dynamic polarizability of the system [27,28].

TD-DFT is an exact theory because the Coulomb and exchange-correlation interactions between occupied and unoccupied KS-orbitals are considered in the estimation of the transition energy of the molecule [28].

Some works report that linear-response TD-DFT gives a satisfactory approximation of the optical gap [28], while others say that the HOMO-LUMO energy gap is best predicted by the first excitation energy calculated from TD-DFT [29].

Using B3LYP functional, the $S_0 \rightarrow S_1$ transition corresponds to the electron-hole pairs to be delocalized along the polymer chain [13]. Therefore, the excitation energies calculated from TD-DFT can be well-approximated with this hybrid functional [27,29].

Aligned to quantum chemical calculations of optoelectronic properties, conformational approaches with dimer systems are performed to get insights about intermolecular interactions, which means double n-mers chains modelled in distinguished conformations to analyse as many possibilities as possible of interactions. This strategy is specially used for finding explanations of π - π stacking of conjugated molecules [30,31].

3.3 Non-Covalent Interactions (NCI) analysis

The visual analysis method has been widely employed as a practical tool in weak interaction studies, not only providing substantial three-dimensional surfaces of the main overlap of electron densities but also making it possible to identify their nature. In the NCI method, weak interaction regions are revealed from isosurfaces of the reduced gradient density (RGD) function [32], which only requires geometry as input for quantum chemical calculations with a low computational cost.

From the many applications of NCI analysis, there is the identification of the nature and strength of interactions between π and σ electrons-cloud aromatic and saturated hydrocarbon dimers [33], the explanation for a more repulsive vdW interactions among a series of tetracyanoethylene and benzene derivatives [34] and the comparison between *cyclo*-pentazole metal hydrates, with all kinds of interactions in different intensities showed by RDG isosurface and scatter graphs [35].

An NCI-derivative approach has emerged to enhance the visual analysis of interactions, named independent gradient model (IGM). It is commonly used to justify interactions between compounds in biological fields. For example, it was possible to compare the π - π interactions between the side chains of the tyrosine residues in the dimers of the halogenated and dehalogenated polypeptides [36] or to verify that H-bonds were broken and replaced by vdW interactions between solvents and monoethanolamine-based absorbents after CO₂ absorption [37].

In the same context, density-based bonding descriptors were developed to assist the visualization of interactions between molecules, like density overlap region indicator (DORI) showing a dense electronic packing in the molecular crystal of quaterthiophene dimers [38] and interaction region indicator (IRI) proving why electron-withdrawing substituents in benzene create stronger π -stacking interaction with gold cluster [39].

The aim of using NCI analysis in this work is to investigate molecular preferential conformation in the same spirit as the findings of Guevara Level *et al.* (2017) [40]. However, this time, using other molecules and the IGM analysis, which could bring more meaningful insights of novel compound design.

All these techniques differ from the quantum theory of atom-in-molecules, which theory is discussed below, as well as more details about the RDG parameter and NCI method, and the IGM approach.

3.3.1 Quantum Theory of Atom in Molecules (QTAIM)

Briefly explaining, in QTAIM, the molecular or crystal space is divided into non-overlapping atomic basins (real space functions), making it possible to characterize topological properties (critical points, bond paths, and others) [36] represented in a molecular graph, *i.e.*, a network of bond paths linking all system nuclei [41].

The electron density distribution in space presents special points of extremum called critical points (CP) [42]. They are easily identified because the first derivative of $\rho(\vec{r}_{CP})$ is equal to zero (Equation (3.52)) and the second derivative defines the sign of the CP. Nine values for the second derivative are possible, forming a Hessian matrix (Equation (3.53)). The magnitude of the second derivative, the Laplacian, is given from the diagonalization of its principal axes, that is, the sum of the eigenvalues λ_1 , λ_2 and λ_3 (Equation (3.54)).

$$\nabla\rho(\vec{r}_{CP}) = \frac{\partial\rho(\vec{r}_{CP})}{\partial x} + \frac{\partial\rho(\vec{r}_{CP})}{\partial y} + \frac{\partial\rho(\vec{r}_{CP})}{\partial z} = 0 \quad (3.52)$$

$$\nabla\nabla^T\rho(\vec{r}) = \begin{bmatrix} \frac{\partial^2\rho(\vec{r})}{\partial x^2} & \frac{\partial^2\rho(\vec{r})}{\partial x\partial y} & \frac{\partial^2\rho(\vec{r})}{\partial x\partial z} \\ \frac{\partial^2\rho(\vec{r})}{\partial y\partial x} & \frac{\partial^2\rho(\vec{r})}{\partial y^2} & \frac{\partial^2\rho(\vec{r})}{\partial y\partial z} \\ \frac{\partial^2\rho(\vec{r})}{\partial z\partial x} & \frac{\partial^2\rho(\vec{r})}{\partial z\partial y} & \frac{\partial^2\rho(\vec{r})}{\partial z^2} \end{bmatrix} \quad (3.53)$$

$$\nabla^2\rho(\vec{r}) = \frac{\partial^2\rho(\vec{r})}{\partial x^2} + \frac{\partial^2\rho(\vec{r})}{\partial y^2} + \frac{\partial^2\rho(\vec{r})}{\partial z^2} = \lambda_1 + \lambda_2 + \lambda_3 \quad (3.54)$$

Each CP is defined by a pair of (ω, σ) , in which ω is the rank (the number of non-zero eigenvalues) and σ is the signature (the algebraic sum of the signs of eigenvalues). The most important CP are: (3,-1) corresponding to the bond CP (BCP); (3,+1) being the ring CP, that bonds a ring surface; and (3,+3) appearing as a cage CP, the main point of the connection of ring surfaces.

The BCP is associated with the bond path, an atomic interaction line between two atoms, which are bonded if they are in a stable state of electrostatic equilibrium [41].

Chemical bonds and weak interactions can be characterized from density and Laplacian of BCP [42]. Although, if the topological properties of the systems in analysis are too complicated as for different substituents in molecular complexes, the variation of BCP values is required to explain electron density changes due to interactions [39].

The mathematical description of QTAIM can be checked by Bader and Nguyen-Dang [43], more details of bond path indicator is given by Bader [41], and many examples of QTAIM analysis are described by Kumar and collaborators [42].

Contrary to AIM theory, density-based local approaches express regions in space where the total electron density results from the overlap of atomic or molecular electron clouds [36].

3.3.2 Reduced density gradient (RDG)

Methods for visualisation of covalent bonds and electrostatic interactions of conjugated molecules and polymers are well established, such as AIM theory and molecular electrostatic potential (MEP) maps [39,44], respectively. The application of QTAIM provided several contributions for characterizing noncovalent interactions [42], but the BCPs cannot reveal regions where π - π stacking occurs [32].

In 2010, Yang and collaborators [45] developed an electron density-based approach to detect the nonbonded interactions in real space. NCI approach provides a three-dimensional representation of interactions in the molecular systems, which are taken from isosurfaces of a local descriptor - in the case of NCI method is s or RDG.

RDG is defined in the Equation (3.45), and ignoring the constant coefficient it becomes:

$$s = \frac{|\nabla\rho(\vec{r})|}{\rho(\vec{r})^{4/3}} \quad (3.55)$$

The electron density profile in covalent bonds has a saddle sign, in which $s=0$. From the NCI method, the parameter of the Laplacian of the electron density, the sign of the second Hessian eigenvalue $sign(\lambda_2)\rho$, is used to distinguish bonded ($\lambda_2 < 0$) from nonbonded ($\lambda_2 > 0$) interactions.

The main feature of the NCI method is that, at low-density areas, the reduced gradient is large for monomers, while it tends to zero for dimer conformations [45]. Therefore, the reduced gradient is efficient for mapping regions of weak interactions and specifying if it is a hydrogen bond, vdW interaction, or steric crowding. In Figure 3.2, it is given an example of RDG plot of benzothiophene dimer calculated at ω B97X-D/6-311++G(d,p) level of theory, highlighting intra-ring nuclear repulsion (red colour) and noncovalent interactions between the two structures (green colour).

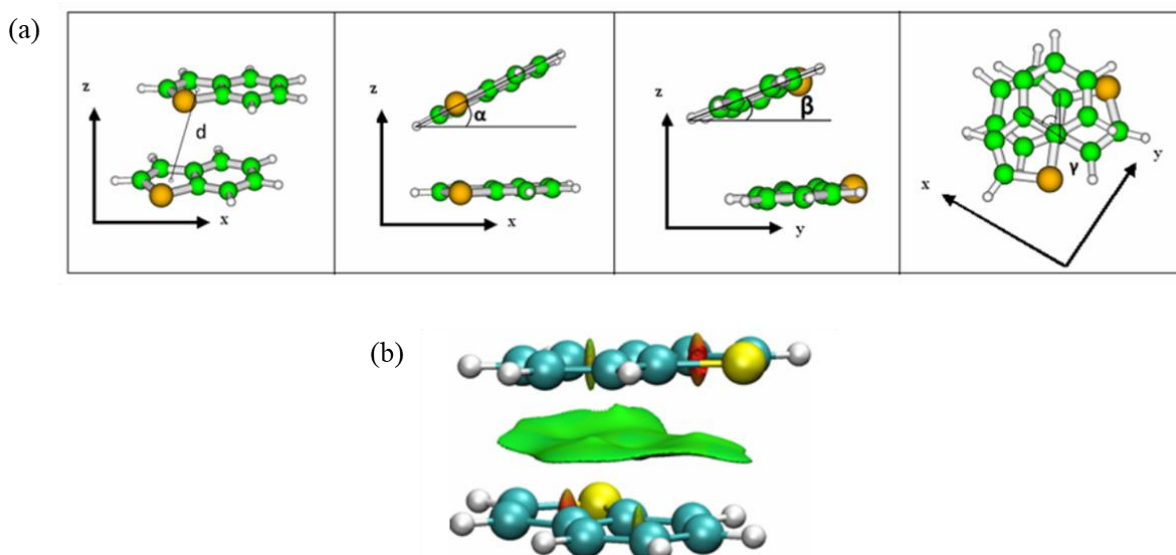


Figure 3.1 – RDG application in benzothiophene dimer for the conformation with (a) structural parameters $d=4.49 \text{ \AA}$, $\alpha=2.23^\circ$, $\beta=5.07^\circ$ and $\gamma=68.92^\circ$, and (b) interactions color mapping of RDG surfaces. Adapted from Guevara-Level *et al.* [40].

New NCI methods and software were developed to characterize the interactions among molecules even better.

3.3.3 Independent gradient model (IGM)

As the RDG method, IGM is based on electron density from promolecular approximations or quantum mechanics calculations, meanwhile with an innovative feature of analysing separately covalent and noncovalent patterns, treated as intra and inter interactions between selected fragments [46]. In IGM analysis, the isosurfaces are created from a local descriptor, the δg index, described below.

The aim is to reveal and quantify the interactions of a molecular system separated in two fragments, A and B. The total electron density is determined from a sum of M^3 neutral atomic densities $\rho(\vec{r}) = \sum_{i=1}^M \rho_i(\vec{r}_i)$. In the IGM method, absolute values are used to avoid contra gradient due to regions of atomic orbitals overlapping (atoms sharing electrons). The absolute

³ letter M was used instead of N because N was used as number of electrons in this thesis manuscript

electron density gradient $\nabla\rho$ of a real system of two fragments, A and B, and its upper limit $\nabla\rho^{\text{IGM}}$ describes the local descriptor δg , respectively expressed in Equations (3.56) to (3.58).

$$\nabla\rho = \sum_{i=1}^{M_A} \nabla\rho_i + \sum_{i=1}^{M_B} \nabla\rho_i \quad (3.56)$$

$$\nabla\rho^{\text{IGM}} = \sum_{i=1}^{M_A} |\nabla\rho_i| + \sum_{i=1}^{M_B} |\nabla\rho_i| \quad (3.57)$$

$$\delta g = |\nabla\rho^{\text{IGM}}| - |\nabla\rho| \quad (3.58)$$

The greatest feature of IGM among NCI approach is to produce the isosurfaces of intra and inter interactions between the two fragments with the descriptors δg^{inter} (Equation (3.59)) and δg^{intra} (Equation (3.60)), representing the noncovalent and covalent interactions of the molecular system respectively. These descriptors are dependent to the norm of $\nabla\rho^{\text{IGM,inter}}$ (Equation (3.61)), that is a partitioning procedure which

$$\delta g^{\text{inter}} = |\nabla\rho^{\text{IGM,inter}}| - |\nabla\rho| \quad (3.59)$$

$$\delta g^{\text{intra}} = |\nabla\rho^{\text{IGM}}| - |\nabla\rho^{\text{IGM,inter}}| \quad (3.60)$$

$$\nabla\rho^{\text{IGM,inter}} = \left| \sum_{i=1}^{M_A} \nabla\rho_i \right| + \left| \sum_{i=1}^{M_B} \nabla\rho_i \right| \quad (3.61)$$

The visualization of surfaces makes it possible to distinguish the nature of interactions which are associated with a colour code available in Figure 3.2 with an example of δg^{inter} isosurfaces used for visualizing the intermolecular interactions between benzene molecules in relation to their distance. It is very important to understand that the IGM visualization map of intermolecular interactions is dependent on the isosurface value, so in this case, if $\delta g^{\text{inter}} < 0.01$ a.u. can make appear the interactions between fragments.

A new variant of IGM based on the Hirshfeld partition of molecular density was proposed, named IGM based on Hirshfeld partition of molecular density (IGMH) [47,48]. It provided a more rigorous physical basis than the previous version by replacing the atomic densities in the

free state (already included in the IGM method) with the wavefunction information derived from the Hirshfeld partition of the actual molecular electron density.

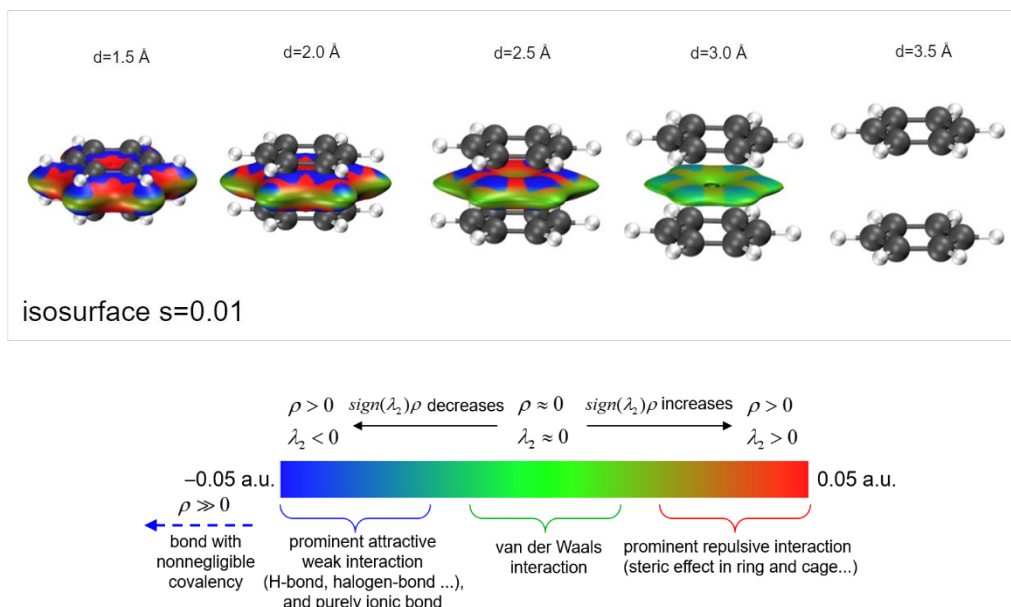


Figure 3.2 – Visualization map of noncovalent interactions in function of the distance d between benzene molecules, produced from IGM analysis done in MultiWFN software [12].

Apply the IGMH approach instead of IGM (based on gradient-based partition) is generally recommended in cases that are necessary to include electron density relaxation and describe covalent situations [49], but it also can be a good method to distinguish weak repulsive interactions such as noncovalent interactions between pollutants and microplastics [50].

Descriptors based on IGM were also introduced, such as the intrinsic bond strength index (IBSI) [51] and the atomic degree of interaction (DoI) [52], in a way to characterize atomic interactions.

In the same context, the local descriptor $\delta g^{\text{inter}/\text{At}}$ (Equation (3.65)) can be used to qualify an atom At with its contribution to the interaction between fragments A and B [53], and it can be integrated over IGM surface to find the associated relative atomic contribution $\Delta g^{\text{inter}/\text{At}} = \int \delta g^{\text{inter}/\text{At}} dV$.

$$\delta g^{\text{inter}/\text{At}} = |\nabla \rho_{\text{At}(1)}| - |\nabla \rho_{\text{At}(2)}| \geq 0 \quad (3.62)$$

in which:

$$\nabla\rho_{At(1)} = |\nabla\rho_{At}| + \left| \sum_{i=1}^{M_B} \nabla\rho_i \right| + \left| \sum_{i \neq At}^{M_A-1} \nabla\rho_i \right| \quad (3.63)$$

$$\nabla\rho_{At(2)} = \left| \nabla\rho_{At} + \sum_{i=1}^{M_B} \nabla\rho_i \right| + \left| \sum_{i \neq At}^{M_A-1} \nabla\rho_i \right| \quad (3.64)$$

Figure 3.3 illustrates an example of isosurface δg^{inter} and relative atomic contribution $\Delta g^{\text{inter}/\text{At}}$. A fullerene C_{60} was incorporated in the cavity of a macrocyclic oligothiophene, a ring of eight thiophenes linked by seven acetylenes and one ethylene (system called Saturn-like complex **III**) [53]. From the IGM analysis, it was possible to map van der Waals interactions between the fullerene and the host sulphur atoms, apart from 3.07 to 3.9 Å, with a special emphasis on the sulphur closely to the ethylene.

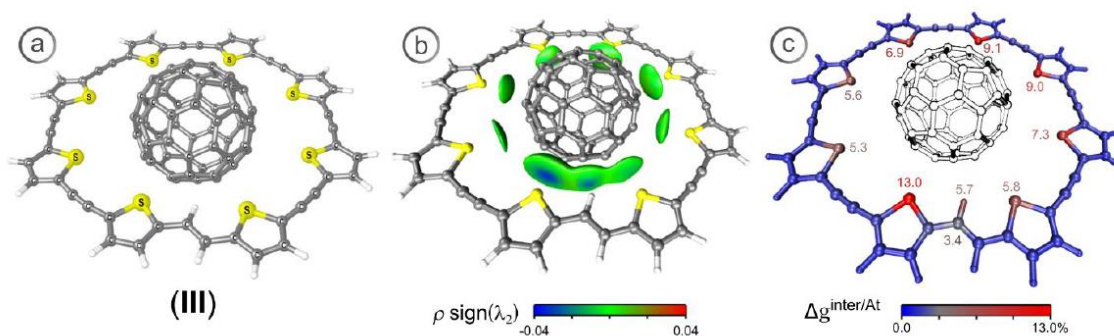


Figure 3.3 – Application of IGM approach in a buckycatcher: δg^{inter} 0.01 a.u. isosurface identifying and qualifying the intermolecular interactions and atoms coloured according to their contribution on δg^{inter} [53].

In order to have complementary insights about charge-transfer processes, other methods based on electron density can be used, like Fukui functions, which evidence favourable spots of reactivity in the molecular structures, predicting electron-donating and electron-accepting parts.

3.4 Fukui Indices

The Fukui function or frontier function reveals qualitatively chemical-reactive sites in a molecule when varying the N number of electrons [54], as shown in Equation (3.65).

$$f(\vec{r}) = \left[\frac{\partial \rho(\vec{r})}{\partial N} \right]_v \quad (3.65)$$

From this, it is possible to calculate the Fukui functions $f^-(\vec{r})$, $f^+(\vec{r})$ and $f^0(\vec{r})$ that represent regions of the molecule with bigger probability to:

- Donate electrons, interacting with electrophilic radical (the acceptor unit of another molecule), and approximate the contribution of the HOMO:

$$f^-(\vec{r}) = \left[\frac{\partial \rho(\vec{r})}{\partial N} \right]_v^- \approx \rho_{(\vec{r})}^{\text{HOMO}} \quad (3.66)$$

- Receive electrons, interacting with nucleophilic radical (the donor unit of another molecule), and approximate the contribution of the LUMO:

$$f^+(\vec{r}) = \left[\frac{\partial \rho(\vec{r})}{\partial N} \right]_v^+ \approx \rho_{(\vec{r})}^{\text{LUMO}} \quad (3.67)$$

- Do not share electrons, interacting with free radicals, and approximate the contribution of the HOMO and LUMO:

$$f^0(\vec{r}) = \left[\frac{\partial \rho(\vec{r})}{\partial N} \right]_v^0 \approx \frac{1}{2} [\rho_{(\vec{r})}^{\text{HOMO}} + \rho_{(\vec{r})}^{\text{LUMO}}] \quad (3.68)$$

Analogously, as applying a linear approximation on these Fukui functions for $N=1$, atomic components called Condensed-in-Atoms Fukui Indexes (or simply as Fukui indices) are estimated for a k -th atom, according to its partial charge for the same molecule in the neutral, cationic and anionic states, with N , $N - 1$ and $N + 1$ electrons, respectively [55,56], without modifications in its geometry [57].

$$f_k^- = q_k(N) - q_k(N - 1) \quad (3.69)$$

$$f_k^+ = q_k(N + 1) - q_k(N) \quad (3.70)$$

$$f_k^0 = \frac{1}{2} [q_k(N + 1) - q_k(N - 1)] \quad (3.71)$$

It is essential to use the Hirshfeld charge partition approach to estimate the electronic populations to avoid negative values for Fukui indices [55,58].

In the literature, these functions and indices have a widely range of applications. They are used to identify important polymerization centres in melanin compounds [55], to pinpoint regions where charge-transfer processes occurs in cyanopyridone molecules [56], to highlight strong electrophilicity spots and different nucleophilic areas of several in potential spiro derivatives of heterocyclic units [57], and to identify areas of possible interactions with singlet oxygen (electrophilic attack) in the structure of the OPV polymer PTB7-Th during the photodegradation process [59]. Each of these examples is illustrated in Figure 3.4.

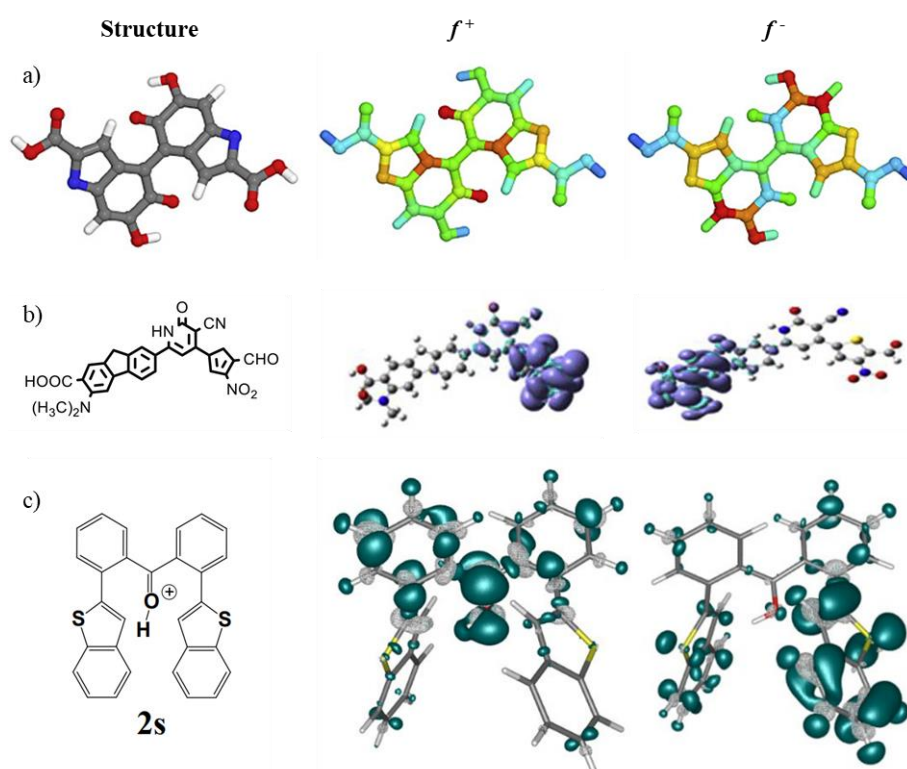


Figure 3.4 – Electrophilic (f^+) and nucleophilic (f^-) Fukui functions plots from the literature, with the reciprocal molecular structure: (a) dimer QIQI in 5–5' connection [55]; (b) cyanopyridone derivative CP2 [56]; (c) cation of 2s, with a cut-off value of 25%, which white hollow surfaces (negative Fukui functions) are due to the orbital relaxation [57].

In a recent publication to which we contributed, Fukui indices were used to describe the reactivity properties of molecules for organic solar cells (OSCs), employing the building block strategy. An available version can be found in the Appendices session of this thesis.

3.5 Correlating Computational Predictions with Experimental Results

Quantum-chemical codes, particularly the ones based on DFT, are used to calculate computational molecular properties and compare them with experimental data. The model size and computational method mainly dictate the limits of the calculation, as they consider specific interactions and parameters directly related to the cost of simulation in optimizing the molecular structure and calculating such properties.

Many studies about computational chemistry methodology are carried out, discussing, for example, which function of density functional, basis set and percentage of HF exchange term are the “best” parameters to predict accurately bandgap and orbital level values [9].

Experimentally, occupied and unoccupied electronic states of organic semiconductor materials are measured using ultraviolet photoelectron spectroscopy (UPS) and inverse photoelectron spectroscopy (IPES), respectively [60]. These surface-sensitive techniques measure the hole and electron energies from the material’s relaxed positive and negative polarons, respectively, which approximation is done by neglecting lattice relaxation contributions [61].

In computational methods based on TD-DFT, the optical gap is generally calculated as the vertical energy transition from the ground state to the first excited state [62]. However, using experimental techniques, it is indirectly measured from the edge (also mentioned as onset) of a low-lying electronic absorption band of UV-vis spectra [60,63,64] and sometimes from the absorption maximum.

Another difficulty in comparing optical properties is their dependence on the ambient conditions for the polymer, either in solution (wide set of solvents and temperature) or thin films (varying in thickness, processing procedure and post-treatment) [65–72].

Cyclic voltammetry is a technique to measure the oxidation and reduction potentials in solution, used to approximate the *IP* and *EA* of a solid-state compound [60]. In general, they are underestimated, and electrochemical techniques involve an assortment of solvents and electrodes, which creates a variable property for the same material [68]. Also, the onset of redox potentials is used to indirectly measure the HOMO and LUMO energies [69,73,74], an inappropriate correlation according to Brédas [75].

Machine learning (ML) models can predict the power conversion efficiencies (PCEs) from large molecular property datasets of donor and acceptor materials to identify patterns and correlations that can guide the modeling strategies for highly efficient organic solar cells. Some works discuss the accuracy of ML models [76,77]. Others highlight the most relevant structural descriptors for modulating the HOMO, LUMO, HOMO-LUMO gap, PCE, and other cell performance properties [78].

Comparing UPS/IPES and CV measurements, it was found that both techniques have not revealed effects of the molecular packing and π - π stacking in HOMO and LUMO energies, while UV-vis spectroscopy is able described such interactions [79].

So far, computational investigation of potential molecules is very important to validate a model starting from benchmarking.

3.6 The Role of Benchmarking in Validating Models

Slight differences in optoelectronic properties as small as 0.1 eV are found in methods of evaluating them, being crucial to the performance of OPV cells [80–84] as it can mainly affect the absorption of light and the recombination of excitons.

Very contrasted data are found when comparing computationally calculated and experimentally measured results of properties of conjugated polymers such as the one whose structure is presented in Figure 3.5. This comparison among different kinds of calculations (based on density functional theory DFT and time-dependent DFT, TD-DFT) and measurements (cyclic voltammetry CV and UV-vis spectroscopy, UV-vis) is available in Figure 3.6. More detailed information of each work is showed in Table 3.1.

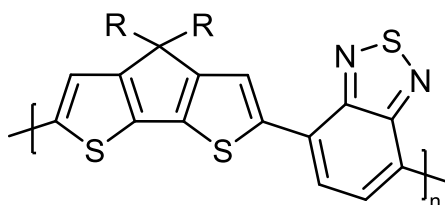


Figure 3.5 – Structure of conjugated polymer used as semiconductor material in OPV cells.

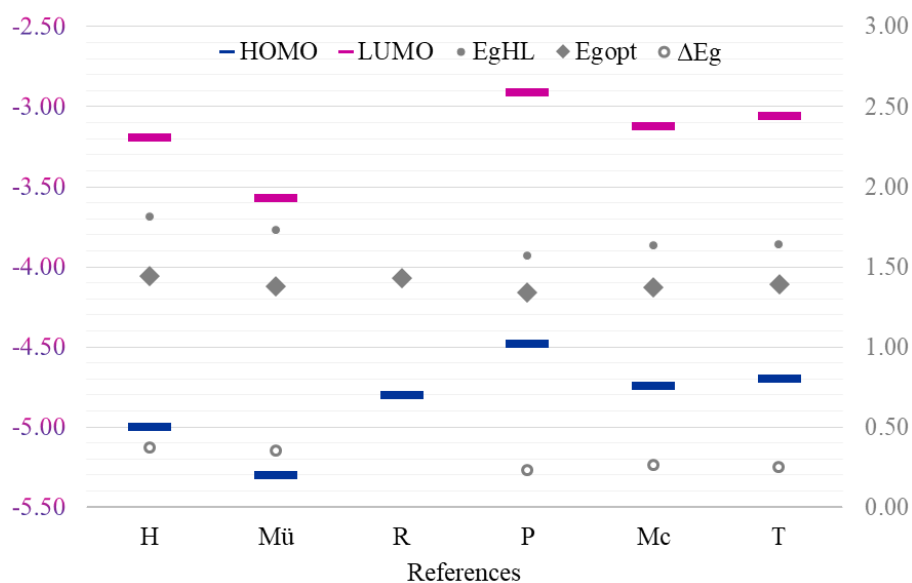


Figure 3.6 – Comparison of experimental and theoretical results from literature for the molecule in the Figure 3.5. Property values in eV. References: H [69], Mü [85], R [86], P [68], Mc [29] and T [87].

There are many limitations in correlating results, as the conditions and parameters in each calculation and measurement differ a lot. The comparison between approximations for oligomer systems in the gas phase and for polymers in dissolved states should include the solvation effect [88].

Despite this, many researchers discuss the validation of quantum-mechanical methods for estimating the electronic and optical properties of oligomers and polymers accurately [9,15–17,89], checking the compatibility of each material at the molecular level with the other layers or finding the best candidate for the photoactive materials blend [64,84,90,91].

Benchmarking is a strategy to investigate the influence of some parameter in the properties of a material that has already been analysed in other studies [9,29,87], which provides the first insights into a huge campaign of calculations.

Here, the aim is to find tendencies in molecular properties with the variation of polymer structure, a study of molecular design of conjugated polymers freezing the quantum-mechanical method for all the models.

Table 3.1 – Details of experimental and theoretical data from literature for analysis of the molecule in the Figure 3.5, classified according its molecule’s name in the referenced work.

Compound			S_0			E_g^{opt}	ΔE_g	Methods		Ref
Name	R	n	H	L	E_g^{HL}			H	L	
PCPDTBT	C6C2	∞	-5.00	-3.19	1.81	1.44	0.37	CV	UV-vis	[69]
PCPDTBT	C6C2	∞	-5.30	-3.57	1.73	1.38	0.35	CV	UV-vis	[85]
PCPDTBT	C6C2	∞	-4.80			1.43		CV	UV-vis	[86]
C/CPDT-BT	C1	4	-4.48	-2.91	1.57	1.34	0.23	DFT B3LYP 6-31G(d,p)	TD-DFT B3LYP 6-31G(d,p)	[68]
17	C1	4	-4.74	-3.12	1.63	1.37	0.26	DFT B3LYP 6-311G(d)	TD-DFT B3LYP 6-311G(d)	[29]
CPT-BT	H	4	-4.70	-3.06	1.64	1.39	0.25	DFT B3LYP 6-311G(d)	TD-DFT B3LYP 6-311G(d)	[87]

Abbreviations: Ref, work reference; R, side chain (C6C2 is 2-ethylhexyl and C1 is methyl); n, number of repeating units (∞ refers to infinite chain); H, HOMO energy in eV; L, LUMO energy in eV; E_g^{HL} , energy gap between HOMO and LUMO, in eV; E_g^{opt} , optical gap* in eV; ΔE_g , calculated difference of energy gaps** in eV.

* In computational calculation, the optical gap was considered as the transition energy of the molecule in the neutral ground state to the first excited state ($S_0 \rightarrow S_1$)

$$** \Delta E_g = E_g^{HL} - E_g^{opt}$$

3.7 Challenges in Accurate Predictions and Limitations

The major difficulty in comparing laboratory-measured and computationally predicted properties is the variability and lack of repeatability of experimental conditions [77]. Different laboratories may have different environmental factors, such as humidity and temperature, which can affect OPV cell performance and lead to inconsistent results. Furthermore, even within the same laboratory, there may be variations in critical operating details in polymer materials, such as differences in molecular weight and distribution, material purity, and others.

The accuracy of predicting molecular properties for organic compounds also depends on the methodology chosen, as deeply discussed by Niskanen and Hukka [15], Ari and Büyükmumcu [9], Kowalczyk, Chen and Jang [17] and more recently by Nakata and Maeda [92]. In this work,

one computational method is settled for all compounds in the study to provide a consistent comparison among them, only concerning the molecular structure in all selected parameters.

Against the background of this theoretical overview, the following chapters present the details of the modelling of molecular systems and the outcomes of the extensive calculation campaign to investigate the optoelectronic properties of conjugated polymers for photovoltaic solar cells.

References

- [1] F. Giustino, *Materials Modelling Using Density Functional Theory: Properties and Predictions*, Oxford University Press, 2014.
- [2] T. Tsuneda, *Density Functional Theory in Quantum Chemistry*, Springer Japan, Tokyo, 2014.
- [3] M.A.D. Arnaud, *Modélisation multi-échelle de polymères conjugués pour le photovoltaïque organique : confrontation expérience / théorie*, Doctoral thesis, Université de Pau et des Pays de l'Adour, 2013.
- [4] A. Pribram-Jones, D.A. Gross, K. Burke, *Annual Review of Physical Chemistry* 66 (2015) 283–304.
- [5] J. Callaway, N.H. March, in: H. Ehrenreich, D. Turnbull, F. Seitz (Eds.), *Solid State Physics*, Academic Press, 1984, pp. 135–221.
- [6] P. Hohenberg, W. Kohn, *Phys. Rev.* 136 (1964) B864–B871.
- [7] W. Kohn, L.J. Sham, *Phys. Rev.* 140 (1965) A1133–A1138.
- [8] A.J. Cohen, P. Mori-Sánchez, W. Yang, *Chem. Rev.* 112 (2012) 289–320.
- [9] H. Ari, Z. Büyükmumcu, *Computational Materials Science* 138 (2017) 70–76.
- [10] K. Burke, L.O. Wagner, *International Journal of Quantum Chemistry* 113 (2013) 96–101.
- [11] J.P. Perdew, Y. Wang, *Phys. Rev. B* 33 (1986) 8800–8802.
- [12] T. Lu, F. Chen, *Journal of Computational Chemistry* 33 (2012) 580–592.
- [13] T. Körzdörfer, J.-L. Brédas, *Acc. Chem. Res.* 47 (2014) 3284–3291.
- [14] A.D. Becke, *The Journal of Chemical Physics* 98 (1993) 5648–5652.
- [15] M. Niskanen, T.I. Hukka, *Phys. Chem. Chem. Phys.* 16 (2014) 13294–13305.
- [16] R.S. Bhatta, G. Pellicane, M. Tsige, *Computational and Theoretical Chemistry* 1070 (2015) 14–20.
- [17] M. Kowalczyk, N. Chen, S.J. Jang, *ACS Omega* 4 (2019) 5758–5767.
- [18] G. Zhang, C.B. Musgrave, *J. Phys. Chem. A* 111 (2007) 1554–1561.
- [19] Z. Rostami, A. Hosseinian, A. Monfared, *Journal of Molecular Graphics and Modelling* 81 (2018) 60–67.
- [20] J.P. Cachaneski-Lopes, A. Batagin-Neto, *J Nanostruct Chem* 12 (2022) 141–157.

-
- [21] J.-D. Chai, M. Head-Gordon, *Physical Chemistry Chemical Physics* 10 (2008) 6615–6620.
- [22] S. Grimme, *Journal of Computational Chemistry* 27 (2006) 1787–1799.
- [23] S. Grimme, S. Ehrlich, L. Goerigk, *Journal of Computational Chemistry* 32 (2011) 1456–1465.
- [24] A. Austin, G.A. Petersson, M.J. Frisch, F.J. Dobek, G. Scalmani, K. Throssell, *J. Chem. Theory Comput.* 8 (2012) 4989–5007.
- [25] E. Caldeweyher, S. Ehlert, A. Hansen, H. Neugebauer, S. Spicher, C. Bannwarth, S. Grimme, *The Journal of Chemical Physics* 150 (2019) 154122.
- [26] A. Stoliaroff-Pépin, *Modélisation ab initio des défauts ponctuels chargés et de leur impact sur les propriétés opto-électroniques de matériaux semiconducteurs cristallins*, Doctoral thesis, Université de Nantes, 2020.
- [27] R. Bauernschmitt, R. Ahlrichs, *Chemical Physics Letters* 256 (1996) 454–464.
- [28] L. Kronik, T. Stein, S. Refaely-Abramson, R. Baer, *J. Chem. Theory Comput.* 8 (2012) 1515–1531.
- [29] T.M. McCormick, C.R. Bridges, E.I. Carrera, P.M. DiCarmine, G.L. Gibson, J. Hollinger, L.M. Kozycz, D.S. Seferos, *Macromolecules* 46 (2013) 3879–3886.
- [30] H.-Y. Chen, J. Hou, A.E. Hayden, H. Yang, K.N. Houk, Y. Yang, *Advanced Materials* 22 (2010) 371–375.
- [31] E.M. Cabaleiro-Lago, J. Rodríguez-Otero, *ACS Omega* 3 (2018) 9348–9359.
- [32] T. Lu, Q. Chen, in: *Reference Module in Chemistry, Molecular Sciences and Chemical Engineering*, Elsevier, 2023, p. B9780128219782000763.
- [33] M. Alonso, T. Woller, F.J. Martín-Martínez, J. Contreras-García, P. Geerlings, F. De Proft, *Chemistry – A European Journal* 20 (2014) 4931–4941.
- [34] L.R. Domingo, M. Ríos-Gutiérrez, *Org. Biomol. Chem.* 17 (2019) 6478–6488.
- [35] X. Li, Y. Long, C. Zhang, C. Sun, B. Hu, P. Lu, J. Chen, *ACS Omega* 7 (2022) 6627–6639.
- [36] E.K. Wieduwilt, J.-C. Boisson, G. Terraneo, E. Hénon, A. Genoni, *J. Chem. Inf. Model.* 61 (2021) 795–809.
- [37] Q. Luo, Y. Ouyang, S. Hong, N. Wang, Y. Li, H. Gao, G.S. Hwang, B. Yoon, T. Sema, P. Tontiwachwuthikul, P. Luo, C. Saiwan, Z. Liang, *Separation and Purification Technology* 308 (2023) 122856.
- [38] P. De Silva, C. Corminboeuf, *J. Chem. Theory Comput.* 10 (2014) 3745–3756.
- [39] Q. Zhao, *J Mol Model* 27 (2021) 328.
- [40] P. Guevara Level, H. Santos Silva, F. Spillebout, K.H. Michaelian, J.M. Shaw, I. Baraille, D. Bégué, *J. Phys. Chem. A* 121 (2017) 7205–7218.
- [41] R.F.W. Bader, *J. Phys. Chem. A* 102 (1998) 7314–7323.
- [42] P.S.V. Kumar, V. Raghavendra, V. Subramanian, *J Chem Sci* 128 (2016) 1527–1536.
- [43] R.F.W. Bader, T.T. Nguyen-Dang, in: P.-O. Löwdin (Ed.), *Advances in Quantum Chemistry*, Academic Press, 1981, pp. 63–124.
-

-
- [44] G.G.B. Alves, A. Batagin-Neto, *J. Phys. Chem. C* 127 (2023) 3819–3829.
- [45] E.R. Johnson, S. Keinan, P. Mori-Sánchez, J. Contreras-García, A.J. Cohen, W. Yang, *J. Am. Chem. Soc.* 132 (2010) 6498–6506.
- [46] C. Lefebvre, G. Rubez, H. Khartabil, J.-C. Boisson, J. Contreras-García, E. Hénon, *Phys. Chem. Chem. Phys.* 19 (2017) 17928–17936.
- [47] T. Lu, Q. Chen, *Journal of Computational Chemistry* 43 (2022) 539–555.
- [48] T. Lu, Q. Chen, Erratum to “Independent Gradient Model Based on Hirshfeld Partition: A New Method for Visual Study of Interactions in Chemical Systems,” *Chemistry*, 2022.
- [49] C. Lefebvre, J. Klein, H. Khartabil, J.-C. Boisson, E. Hénon, *Journal of Computational Chemistry* 44 (2023) 1750–1766.
- [50] A. Pulitika, P. Karamanis, M. Kovačić, A.L. Božić, H. Kušić, *ChemPhysChem* 25 (2024) e202300854.
- [51] J. Klein, H. Khartabil, J.-C. Boisson, J. Contreras-García, J.-P. Piquemal, E. Hénon, *J. Phys. Chem. A* 124 (2020) 1850–1860.
- [52] C. Lefebvre, H. Khartabil, E. Hénon, *Phys. Chem. Chem. Phys.* 25 (2023) 11398–11409.
- [53] M. Ponce-Vargas, C. Lefebvre, J.-C. Boisson, E. Hénon, *J. Chem. Inf. Model.* 60 (2020) 268–278.
- [54] R.G. Parr, W. Yang, ACS Publications (2002).
- [55] G.G.B. Alves, F.C. Lavarda, C.F.O. Graeff, A. Batagin-Neto, *Journal of Molecular Graphics and Modelling* 98 (2020) 107609.
- [56] A.S. Khazaal, M. Springborg, C. Fan, K. Huwig, *Journal of Molecular Graphics and Modelling* 100 (2020) 107654.
- [57] C. Dalinot, V. Jeux, L. Sanguinet, T. Cauchy, M. Allain, Y. Morille, V. Bonnin, P. Leriche, *ACS Omega* 4 (2019) 4571–4583.
- [58] R.K. Roy, S. Pal, K. Hirao, *The Journal of Chemical Physics* 110 (1999) 8236–8245.
- [59] S. Kim, M.A.M. Rashid, T. Ko, K. Ahn, Y. Shin, S. Nah, M.H. Kim, B. Kim, K. Kwak, M. Cho, *J. Phys. Chem. C* 124 (2020) 2762–2770.
- [60] J. Sworakowski, *Synthetic Metals* 235 (2018) 125–130.
- [61] I.G. Hill, A. Kahn, Z.G. Soos, R.A. Pascal, (2000).
- [62] R.S. Bhatta, M. Tsige, *Polymer* 55 (2014) 2667–2672.
- [63] E. Zhou, J. Cong, K. Hashimoto, K. Tajima, *Macromolecules* 46 (2013) 763–768.
- [64] J.-H. Kim, C.E. Song, N. Shin, H. Kang, S. Wood, I.-N. Kang, B.J. Kim, B. Kim, J.-S. Kim, W.S. Shin, D.-H. Hwang, *ACS Appl. Mater. Interfaces* 5 (2013) 12820–12831.
- [65] E. Wang, L. Wang, L. Lan, C. Luo, W. Zhuang, J. Peng, Y. Cao, *Applied Physics Letters* 92 (2008) 033307.
- [66] S.C. Price, A.C. Stuart, L. Yang, H. Zhou, W. You, *J. Am. Chem. Soc.* 133 (2011) 4625–4631.
- [67] D. Qian, L. Ye, M. Zhang, Y. Liang, L. Li, Y. Huang, X. Guo, S. Zhang, Z. Tan, J. Hou, *Macromolecules* 45 (2012) 9611–9617.
- [68] L. Pandey, C. Risko, J.E. Norton, J.-L. Brédas, *Macromolecules* 45 (2012) 6405–6414.
-

-
- [69] M. Horie, J. Kettle, C.-Y. Yu, L.A. Majewski, S.-W. Chang, J. Kirkpatrick, S.M. Tuladhar, J. Nelson, B.R. Saunders, M.L. Turner, *J. Mater. Chem.* 22 (2012) 381–389.
- [70] M. Zhang, X. Guo, W. Ma, H. Ade, J. Hou, *Adv. Mater.* 27 (2015) 4655–4660.
- [71] F. Bencheikh, D. Duché, C.M. Ruiz, J.-J. Simon, L. Escoubas, *J. Phys. Chem. C* 119 (2015) 24643–24648.
- [72] Z. Zheng, H. Yao, L. Ye, Y. Xu, S. Zhang, J. Hou, *Materials Today* 35 (2020) 115–130.
- [73] C.M. Cardona, W. Li, A.E. Kaifer, D. Stockdale, G.C. Bazan, *Adv. Mater.* 23 (2011) 2367–2371.
- [74] R.M.G. Rajapakse, D.L. Watkins, T.A. Ranathunge, A.U. Malikaramage, H.M.N.P. Gunarathna, L. Sandakelum, S. Wylie, P.G.P.R. Abewardana, M.G.S.A.M.E.W.D.D.K. Egodawele, W.H.M.R.N.K. Herath, S.V. Bandara, D.R. Strongin, N.H. Attanayake, D. Velauthapillai, B.R. Horrocks, *RSC Adv.* 12 (2022) 12089–12115.
- [75] J.-L. Bredas, *Mater. Horiz.* 1 (2014) 17–19.
- [76] H. Wang, J. Feng, Z. Dong, L. Jin, M. Li, J. Yuan, Y. Li, *Npj Comput Mater* 9 (2023) 1–11.
- [77] Y. Wu, J. Guo, R. Sun, J. Min, *Npj Comput Mater* 6 (2020) 1–8.
- [78] N. Meftahi, M. Klymenko, A.J. Christofferson, U. Bach, D.A. Winkler, S.P. Russo, *Npj Comput Mater* 6 (2020) 1–8.
- [79] C. Arantes, M. Scholz, R. Schmidt, V. Dehm, M.L.M. Rocco, A. Schöll, F. Reinert, F. Würthner, *Appl. Phys. A* 108 (2012) 629–637.
- [80] Y. Liang, L. Yu, *Acc. Chem. Res.* 43 (2010) 1227–1236.
- [81] G. Li, W.-H. Chang, Y. Yang, *Nat Rev Mater* 2 (2017) 17043.
- [82] K. Ramki, N. Venkatesh, G. Sathiyam, R. Thangamuthu, P. Sakthivel, *Organic Electronics* 73 (2019) 182–204.
- [83] O. Almora, D. Baran, G.C. Bazan, C.I. Cabrera, S. Erten-Ela, K. Forberich, F. Guo, J. Hauch, A.W.Y. Ho-Baillie, T.J. Jacobsson, R.A.J. Janssen, T. Kirchartz, N. Kopidakis, M.A. Loi, R.R. Lunt, X. Mathew, M.D. McGehee, J. Min, D.B. Mitzi, M.K. Nazeeruddin, J. Nelson, A.F. Nogueira, U.W. Paetzold, B.P. Rand, U. Rau, H.J. Snaith, E. Unger, L. Vaillant-Roca, C. Yang, H. Yip, C.J. Brabec, *Advanced Energy Materials* 13 (2023) 2203313.
- [84] M. Zhang, J. Wang, X. Ma, J. Gao, C. Xu, Z. Hu, L. Niu, F. Zhang, *APL Materials* 8 (2020) 090703.
- [85] D. Mühlbacher, M. Scharber, M. Morana, Z. Zhu, D. Waller, R. Gaudiana, C. Brabec, *Advanced Materials* 18 (2006) 2884–2889.
- [86] V.J. Rodrigues de Oliveira, E. Assunção da Silva, M.L. Braunger, H. Awada, H. de Santana, R.C. Hiorns, C. Lartigau-Dagron, C. de Almeida Olivati, *Journal of Molecular Liquids* 268 (2018) 114–121.
- [87] H.T. Turan, O. Kucur, B. Kahraman, S. Salman, V. Aviyente, *Phys. Chem. Chem. Phys.* 20 (2018) 3581–3591.
- [88] R. Holze, *Organometallics* 33 (2014) 5033–5042.

-
- [89] S. Fauvel, A.J. Riquelme, J.-M.A. Castán, V.M. Mwalukuku, Y. Kervella, V.K. Challuri, F. Sauvage, S. Narbey, P. Maldivi, C. Aumaître, R. Demadrille, *Chem. Sci.* 14 (2023) 8497–8506.
- [90] N. Kleinhenz, L. Yang, H. Zhou, S.C. Price, W. You, *Macromolecules* 44 (2011) 872–877.
- [91] R. Demadrille, N. Delbosc, Y. Kervella, M. Firon, R. De Bettignies, M. Billon, P. Rannou, A. Pron, *J. Mater. Chem.* 17 (2007) 4661.
- [92] M. Nakata, T. Maeda, *J. Chem. Inf. Model.* 63 (2023) 5734–5754.

Chapter 4

Methods

This chapter describes the steps for molecular design of a new conjugated polymer in details. We started setting up the method of calculations; then, we could run the calculations to discuss the parameters of polymer structures and their influence on optical and electronic properties.

4.1 Calculation method

Recent literature on conjugated polymers has revealed that density functional theory (DFT) is the most popular computational method to predict oligomers' electronic and periodic geometry [1–5]. So, first of all, polymer structures were modelled at GaussView 5.1 and 6.1 [6], and then geometry optimization for molecular singlet ground state (S_0) was carried out using the Gaussian 16 package, versions B.01 and C.01 [7].

About functional, the hybrid functional that incorporates Becke's three-parameter gradient-corrected exchange potential and the Lee–Yang–Parr gradient-corrected correlation potential, named as B3LYP, is often employed in calculations of donor-acceptor (D-A) copolymers to reduce computational cost [1,2,4]. Counting with 20% Hartree-Fock (HF) exchange ratio, B3LYP is a reasonable quota despite a long-range correction lack, once high exact HF exchange ratio used in the calculations results in high bandgaps [8]. Therefore, using B3LYP in geometry optimizations and property calculation is appropriate, since the interest is to describe trends among molecular systems.

The polarized split-valence basis set 6-31G(d) (or 6-31G*) is normally chosen in huge quantum-computational campaigns for conjugated polymers [4,9,10], bringing suitable results, as the goal is to compare structural modifications.

As we were modeling molecules with conjugated structures involving the long-range attraction of van der Waals interactions, it was necessary to include the dispersion energy in the calculations, especially following the equations and parameters from Grimme, Ehrlich and Goerigk [11].

To save computational cost and focus on the structure-property analysis, we configured as default 6-31G(d) basis set and D3(BJ) long-range correction in all the calculations to predict optical and electronic properties of the conjugated polymers, providing good correlations with low computational cost.

To avoid any incompatibility of methods, all the DFT and TD-DFT calculations of this study were performed at the same level of theory, B3LYP-D3(BJ)/6-31G(d).

4.2 Optical and electronic properties

Geometry of each molecular system in the ground state S_0 were optimized until a local minimum. Calculations were executed in a vacuum not to consider other effects. Even knowing that orbital energies cannot be approximated Kohn-Sham orbitals, energies of the highest-occupied molecular orbital (HOMO) and the lowest-unoccupied molecular orbital (LUMO) were estimated from the last occupied and first virtual Alpha eigenvalues, respectively.

Taking the fully-optimized molecules in S_0 , we carried out DFT calculations for compounds at the oxidized $D_1(N + 1)$ and the reduced $D_1(N - 1)$ doublet states, with $N + 1$ electron and $N - 1$ electron, respectively, extracting total energy from the S_0 geometry and the fully-optimized molecule in each of these states; then calculating the *EA* and *IP* energies, respectively, for each system. Finally, their sum gives the value of the vertical and the adiabatic fundamental gaps.

Besides that, TD-DFT calculations were also performed from S_0 optimized molecules, resulting in absorption wavelength and corresponding energy of vertical transitions to excited states (until the 10th excited state or third one to minimize the computation cost) and the composition of molecular orbital contributions. The optical gap E_g^{opt} was considered equal to the vertical transition from the ground state to the first excited state ($S_0 \rightarrow S_1$).

A sketch in Figure 4.1 illustrated all these details.

As method parameters were settled, we could move on to study of polymer structure and its correlation with the optical and electronic properties.

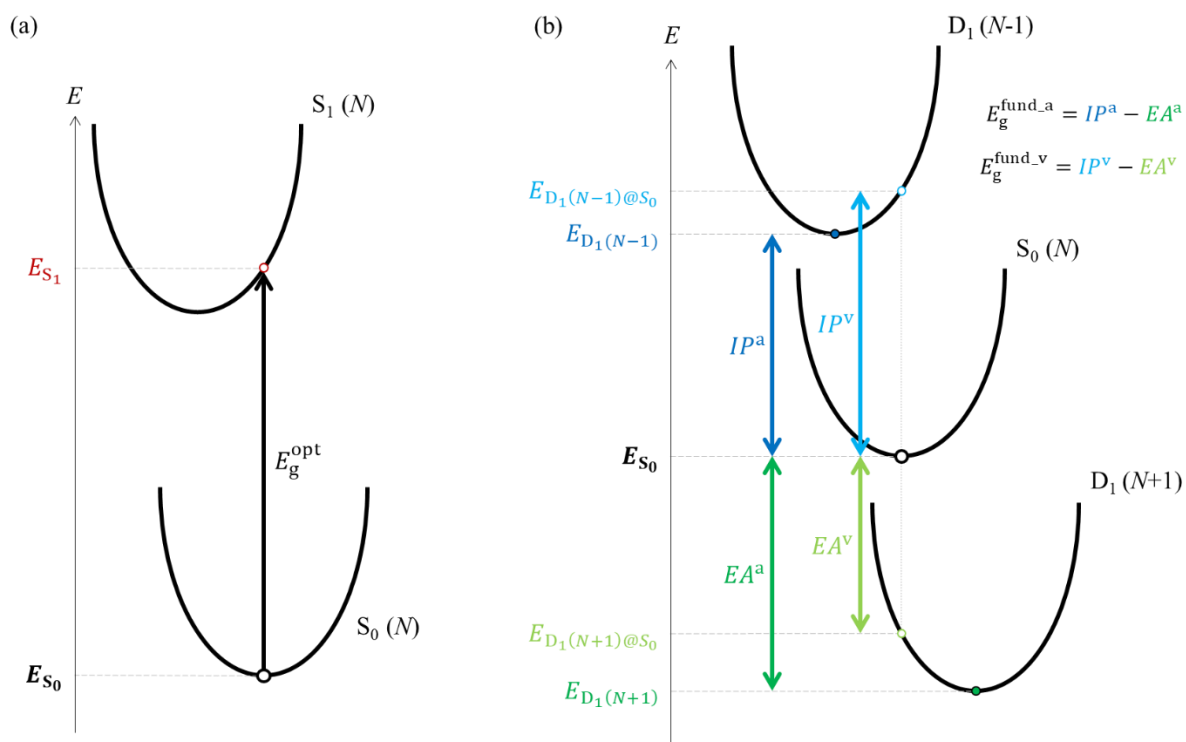


Figure 4.1 – Sketch of molecular states about their energy and correlated properties

4.3 Structure parameters

The molecular design of conjugated polymers is based on the analysis of energetic effects at the molecular scale due to modifications in the polymer structure, with the purpose of creating a new semiconductor material able to satisfy the demands of high power of solar-to-electricity conversion.

For consistent parameter setting in material evaluation, it is crucial to elaborate a preliminary study of the main breakthroughs of other research groups about the components of polymer structure and their impact on molecular system energies. Considering this, a benchmark is a good starting point for model novel active materials for OPV cells.

4.3.1 Benchmarking

We started investigating the seven polymers used in Turan and collaborators' benchmarking [2] but considering other parameters. While they calculated energies and properties using three different functionals with 6-311G(d) basis set for models composed of 1, 2, 3 and 4 repeating units, we ran calculations using B3LYP functional with 6-31G(d) basis set and for molecules

with 1, 2, 4 and 8 units. As frontier orbitals of tetramers had reached the saturation energy, they neglected longer conjugated length than it. The molecular systems were modelled, replacing side chains by hydrogen atoms as they did.

Besides the calculations, we collected data from the literature about the same compounds for experimentally measured and theoretically calculated optical and electronic properties.

From the conclusions of this benchmark and review of scientific works in turn of molecular design, we saw that optoelectronic properties are not only dependent on the conjugation length of the molecular system. Many times, it was reported about the influence of the subsystem character that composes each repeating unit and the negligence on quantum-chemical calculations of the effect of the long alkyl side chain. Therefore, we decided to carry on the structure-property investigation on conjugated polymers by selecting eight structures with various natures of blocks and adding three types of side chains.

4.3.2 Isolated chains

The effect of conjugation length and nature of blocks were evaluated by modelling three homopolymers, three D-A and two D- π -A polymers with 1, 2, 4 and 8 repeating units. Also, 16-unit systems were modelled for the homopolymers.

Meanwhile, the impact of side chains on optoelectronic properties was studied by attaching methyl, butyl and 2-ethylhexyl groups to the molecular backbone in one or more blocks of each repeating unit.

As done in the benchmark, data about these selected compounds from scientifically published works were stored in tables to get a global vision of what has been found and guide our analysis.

4.3.3 Double chains (or stacked or dimer systems)

Considering the effects of molecular symmetry, four (eight) conformations were created for double chains with 1 (2 and 4) repeating unit(s), fixing one chain and rotating the other 180° in turn of axis x, y and z (see Figure 4.2). For 2 and 4-unit chains, we could also rotate the neighbouring unit in 180°. Stacked systems of 4-unit chains were done only for homopolymers, as 2-unit double chains of some copolymers were composed of more than 400 atoms, presenting high computational cost.

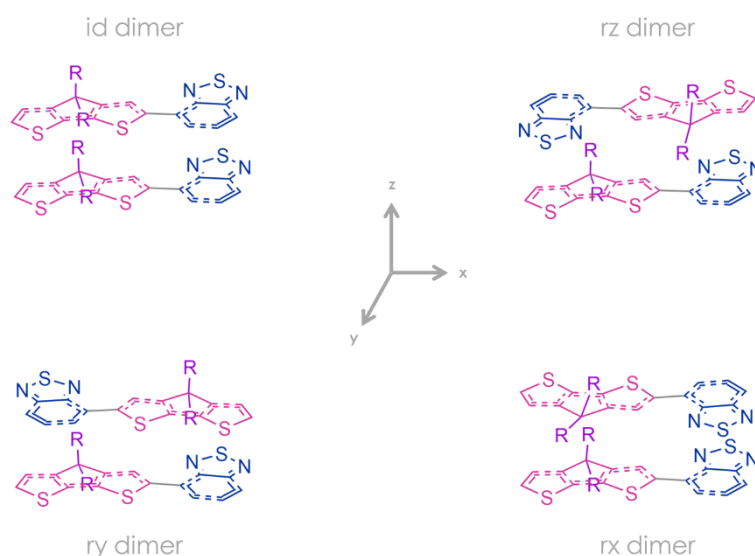


Figure 4.2 – Initial geometry of dimer structures of the 1-unit chain of a compound composed of a donor (pink) and an acceptor (blue) blocks with side chains R (purple)

The dimer systems were prepared with an initial distance of around 4.0 Å between polymeric chains, as it has been found in the literature a π - π stacking distance from 3.48 to 4.28 Å for various conjugated systems in different material and molecular states [12–16].

As done for isolated chains, methyl, butyl and 2-ethylhexyl groups were include in the molecular structure as side chains.

The stacked molecules were evaluated in energetic and electronic terms at the molecular level, followed by statistical and visual analysis methods, measuring the probability of having certain conformations in an environmental condition and identifying the main interactions that govern polymeric dimer systems, respectively.

4.4 Analysis of intermolecular interactions

From the fully optimized dimer structures in the ground state, we extracted the total energy of the systems to compare the stability of interactions and the HOMO and LUMO energies and special distribution to get the effect of interactions between chains on the energetic and electronic properties.

To compare conformations only due to interchain interactions, statistics were applied for compounds with the same conjugation length and side chain.

4.4.1 Boltzmann distribution

With application in statistical thermodynamics, Boltzmann distribution is used to explain the population dependence on the temperature T [17,18]. Our study determined the probability of having each conformation, estimating the population in the i -th state P_i , as

$$P_i = \frac{e^{-\beta E_i}}{Q}, \quad (4.1)$$

in which Q is the Canonical partition function and k_B is the Boltzmann constant.

$$Q = \sum_j e^{-\beta E_j} \quad (4.2)$$

$$\beta = \frac{1}{k_B T} \quad (4.3)$$

We represented P_i in percentage to simplify the identification of more stable conformations.

The origin of the interplaying between polymer chains still needed to be clarified. It was necessary to use an approach based on electron density descriptors to provide more information about atoms responsible for the main interactions among the molecular systems.

4.4.2 Noncovalent interactions visualization using IGM analysis

The independent gradient model (IGM) is a powerful approach for identifying and quantifying interactions among molecular systems [19–21]. To compute the local descriptors and distinguish molecular interactions between double chains of this study, we performed IGM analysis using Multiwfn 3.8 [22] and IGMPlot 3.08 [23]. The software Visual Molecular Dynamics (VMD) 1.9.3 [24] was used for plotting graphical representations of noncovalent interactions.

References

- [1] T.M. McCormick, C.R. Bridges, E.I. Carrera, P.M. DiCarmine, G.L. Gibson, J. Hollinger, L.M. Kozycz, D.S. Seferos, *Macromolecules* 46 (2013) 3879–3886.
- [2] H.T. Turan, O. Kucur, B. Kahraman, S. Salman, V. Aviyente, *Phys. Chem. Chem. Phys.* 20 (2018) 3581–3591.
- [3] F.C. Franco, A.A.B. Padama, *Polymer* 97 (2016) 55–62.
- [4] F. Franco Jr., *Molecular Simulation* 43 (2017) 222–227.
- [5] A. Guillén-López, C. Delesma, C. Amador-Bedolla, M. Robles, J. Muñiz, *Theor Chem Acc* 137 (2018) 85.
- [6] R. Dennington, T.A. Keith, J.M. Millam, (2016).
- [7] M.J. Frisch, G.W. Trucks, H.B. Schlegel, G.E. Scuseria, M.A. Robb, J.R. Cheeseman, G. Scalmani, V. Barone, G.A. Petersson, H. Nakatsuji, H. Li, M. Caricato, A.V. Marenich, J. Bloino, B.G. Janesko, R. Gomperts, B. Mennucci, H.P. Hratchian, J.V. Ortiz, A.F. Izmaylov, J.L. Sonnenberg, D. Williams-Young, F. Ding, F. Lipparini, F. Egidi, J. Goings, B. Peng, A. Petrone, T. Henderson, D. Ranasinghe, V.G. Zakrzewski, J. Gao, N. Rega, G. Zheng, W. Liang, M. Hada, M. Ehara, K. Toyota, R. Fukuda, J. Hasegawa, M. Ishida, T. Nakajima, Y. Honda, O. Kitao, H. Nakai, T. Vreven, K. Throssell, J.A. Montgomery Jr., J.E. Peralta, F. Ogliaro, M.J. Bearpark, J.J. Heyd, E.N. Brothers, K.N. Kudin, V.N. Staroverov, T.A. Keith, R. Kobayashi, J. Normand, K. Raghavachari, A.P. Rendell, J.C. Burant, S.S. Iyengar, J. Tomasi, M. Cossi, J.M. Millam, M. Klene, C. Adamo, R. Cammi, J.W. Ochterski, R.L. Martin, K. Morokuma, O. Farkas, J.B. Foresman, D.J. Fox, (2016).
- [8] M. Niskanen, T.I. Hukka, *Phys. Chem. Chem. Phys.* 16 (2014) 13294–13305.
- [9] L. Zhang, M. Yu, H. Zhao, Y. Wang, J. Gao, *Chemical Physics Letters* 570 (2013) 153–158.
- [10] L. Ling, J.B. Lagowski, *Journal of Molecular Structure: THEOCHEM* 944 (2010) 146–155.
- [11] S. Grimme, S. Ehrlich, L. Goerigk, *Journal of Computational Chemistry* 32 (2011) 1456–1465.
- [12] X. Liu, R. He, W. Shen, M. Li, *Journal of Power Sources* 245 (2014) 217–223.
- [13] E. Zhou, J. Cong, K. Hashimoto, K. Tajima, *Macromolecules* 46 (2013) 763–768.
- [14] M.-C. Yuan, Y.-J. Chou, C.-M. Chen, C.-L. Hsu, K.-H. Wei, *Polymer* 52 (2011) 2792–2798.
- [15] H.-Y. Chen, J. Hou, A.E. Hayden, H. Yang, K.N. Houk, Y. Yang, *Advanced Materials* 22 (2010) 371–375.
- [16] A. Dkhissi, J.M. Ducéré, R. Blossey, C. Pouchan, *Journal of Computational Chemistry* 30 (2009) 1179–1184.
- [17] C. Angeli, R. Cimiraglia, F. Dallo, R. Guareschi, L. Tenti, *J. Chem. Educ.* 90 (2013) 1639–1644.
- [18] I.N. Levine, *Physical Chemistry*, 6th ed, McGraw-Hill, Boston, 2009.
- [19] C. Lefebvre, G. Rubez, H. Khartabil, J.-C. Boisson, J. Contreras-García, E. Hénon, *Phys. Chem. Chem. Phys.* 19 (2017) 17928–17936.

-
- [20] C. Lefebvre, H. Khartabil, J.-C. Boisson, J. Contreras-García, J.-P. Piquemal, E. Hénon, *ChemPhysChem* 19 (2018) 724–735.
- [21] T. Lu, Q. Chen, in: *Reference Module in Chemistry, Molecular Sciences and Chemical Engineering*, Elsevier, 2023, p. B9780128219782000763.
- [22] T. Lu, F. Chen, *Journal of Computational Chemistry* 33 (2012) 580–592.
- [23] C. Lefebvre, J. Klein, H. Khartabil, J.-C. Boisson, E. Hénon, *Journal of Computational Chemistry* 44 (2023) 1750–1766.
- [24] W. Humphrey, A. Dalke, K. Schulten, *J Mol Graph* 14 (1996) 33–38, 27–28.

Chapter 5

Results

This section presents a comprehensive analysis of our findings, starting with a benchmark of existing molecules to guide the study of conjugated polymers. It is followed by the exploitation of energy gaps and correlated properties, including exciton binding energy, providing insights into the electronic behaviour of the studied compounds. The main highlights of structural parameters are discussed, showcasing significant trends and deviations in molecular design. Lastly, we dig deeper into intermolecular interactions, examining how interactions between polymer chains influence the overall stability and performance of the materials.

For all the molecules studied here, it was used the colour coding of Figure 5.1 to represent atoms in ball-and-stick models.

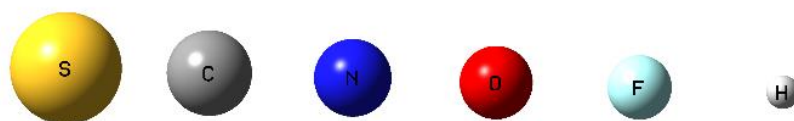


Figure 5.1 - colour coding of atoms

5.1 Benchmarking of OPV molecules

In molecular design, it is necessary to deeply review the main properties of the existing molecules, emphasising the key parameters for a desired-function material, then being able to come up with correlations that have not been done before. It can start with a comparison among the outcomes from the scientific community, including the parameters to be evaluated, a strategy commonly called benchmarking.

As the conjugation length is very important in conjugated polymers, the first parameter analysed was the number of repeating units (called n). We selected the same seven molecules used in the benchmarking from the work of Turan and collaborators [1], as they are a representative group

of different donor-acceptor (D-A) and donor-thiophene-acceptor-thiophene (D-T-A-T)⁴ copolymers. Their structures are presented in Figure 5.2.

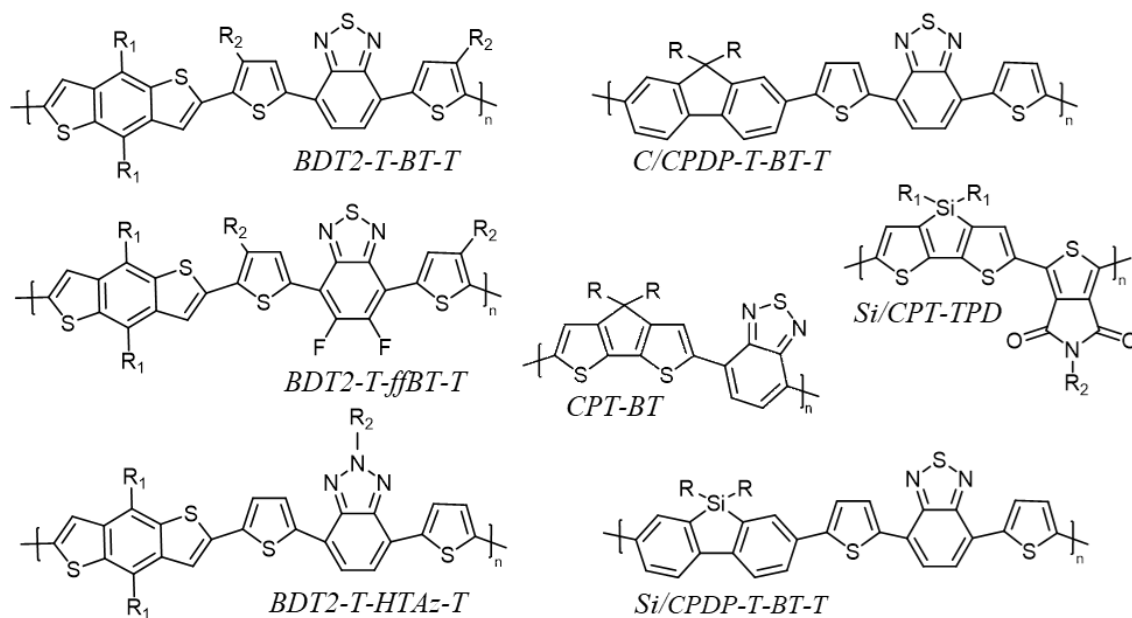


Figure 5.2 - Structure of polymers that have been used in the benchmarking calculations

We collected a set of experimental and theoretical data reported by other authors on these same systems, as represented in Figure 5.2. To compare numerically these data, we generated the property \times work graphs, available in Figure 5.3, with more details in the Appendices session. Not only details of measured and calculated data from reference works but also the calculated ΔE_g and arithmetic average values from the literature for each molecule were added.

From these comparisons, it became clear that the best agreement among all the referenced works was found for the optical gap E_g^{opt} , showing for each compound only small-amount differences even if varying techniques and other structural parameters such as side chain type and number of repeating units. Meanwhile, more distinguished outcomes were observed by comparing the approximated energies of LUMO, HOMO, E_g^{HL} and ΔE_g .

⁴ In Chapter 1, we reported this kind of copolymer as D- π -A- π , naming the general case of π -spacers between the blocks, while here, all the π -spacers are thiophene rings

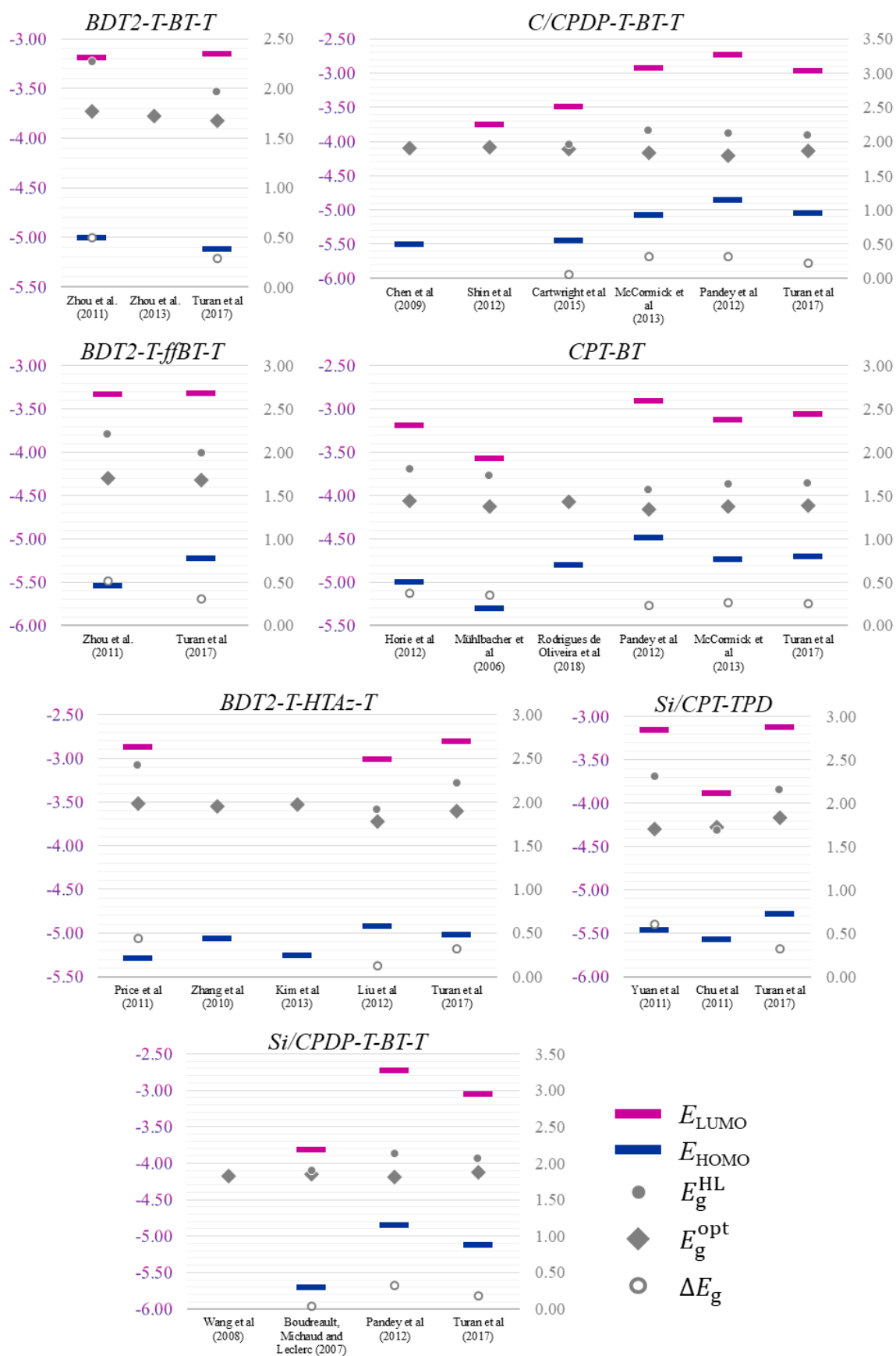


Figure 5.3 - Comparison of experimental and theoretical data (all in eV) according to each referenced work for the molecules in Figure 5.2

It is relevant to observe that the calculated ΔE_g varies from 0.1 to 0.5 eV like as it is mentioned in Chapter 1 for the energy of electron-hole interaction of organic semiconductors, with a few exceptions: 0.04 eV of Boudreault, Michaud and Leclerc [2], 0.06 eV of Cartwright [3], 0.61 eV of Yuan *et al.* [4] and -0.04 eV of Chu *et al.* [5]. These can be attributed to misconceptions of HOMO and LUMO energies provided from CV measurements, as the optical gaps agree with the values calculated and measured by the other authors.

Based on this review and previous research about molecular design of conjugated polymers, we decided to investigate the correlation between electronic properties and polymer structure. Therefore, we started by analysing the conjugation length influence, modeling these seven compounds with chains composed of 1, 2, 4 and 8 repeating units (n) and carrying out a bench of calculations for each molecular system in various states.

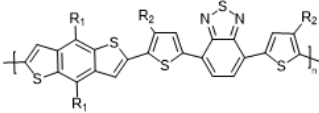
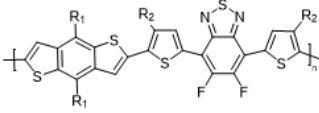
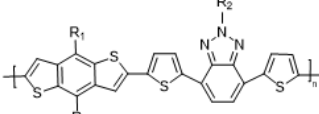
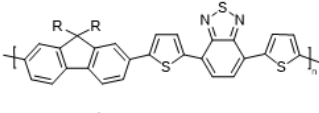
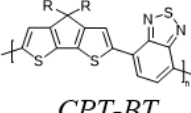
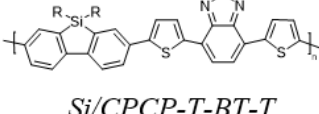
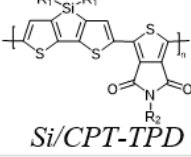
The optoelectronic properties of this benchmarking are presented in Table 5.1, with the average, maximum and minimum values of E_b , considering calculated results for each system. Besides the calculation of E_g^{HL} and E_g^{opt} , we calculated the vertical $E_g^{fund,v}$ and adiabatic $E_g^{fund,a}$, in which ionization potential IP and electronic affinity EA were calculated without and with geometry optimization, respectively. For all the systems, we replaced the sides chains $R=R_1=R_2=H$ (as done by Turan and collaborators [1]), focusing on discovering property-dependence of conjugation length during modelling each compound.

The first outcome is that $E_g^{fund,v} > E_g^{fund,a} > E_g^{HL} > E_g^{opt}$ for all the molecular systems. It can be interpreted as, for all these conjugated compounds, the difference between the estimated energy of frontier molecular orbitals is higher than the energy needed to excite the whole molecule in a ground state to the first excited state. However, it is lower than the sum of the energies required to remove and to add one electron to the molecule.

No correlation was found between average E_g^{HL} value from the literature and both vertical and adiabatic E_g^{fund} . It is a proof that estimating energy gaps from one-electron wavefunctions calculations of HOMO and LUMO approached in Koopman's theory is a crude approximation of the energy difference of molecular states with $N \pm 1$ electron, treated in IP and EA .

Moreover, it is interesting that ΔE_g results were between 0.21 and 0.33 eV regardless of chain size, with an average of 0.29 eV. This agrees with the interaction energy of an electron-hole pair of organic materials, as it has been reported in the literature [6,7]. Only CPT-BT and Si/CPT-TPD calculations encountered average values from the literature.

Table 5.1 – Benchmarking calculation of optoelectronic properties (in eV) of each compound for n repeating units with $R=R_1=R_2=H$, calculated at the B3LYP-D3(BJ)/6-31G(d) level in gas-phase

Compound	n units	Adiabatic $E_g^{\text{fund}_a}$	Vertical $E_g^{\text{fund}_v}$	S_0 E_g^{HL}	$S_0 \rightarrow S_1$ E_g^{opt}	$E_g^{\text{HL}} - E_g^{\text{opt}}$ ΔE_g
 <i>BDT2-T-BT-T</i>	1	4.49	4.70	2.37	2.08	0.29
	2	3.47	3.60	2.06	1.77	0.29
	4	2.85	2.91	1.92	1.62	0.30
	8	2.45	2.48	1.78	1.57	0.21
 <i>BDT2-T-ffBT-T</i>	1	4.49	4.72	2.36	2.06	0.30
	2	3.48	3.61	2.06	1.77	0.29
	4	2.86	2.92	1.93	1.62	0.30
	8	2.46	2.49	1.88	1.57	0.31
 <i>BDT2-T-HTAz-T</i>	1	4.78	5.00	2.74	2.53	0.22
	2	3.74	3.87	2.34	2.06	0.28
	4	3.11	3.18	2.18	1.86	0.32
	8	2.70	2.73	2.13	1.80	0.33
 <i>C/CPDP-T-BT-T</i>	1	4.62	4.88	2.46	2.14	0.33
	2	3.65	3.80	2.23	1.92	0.31
	4	3.05	3.12	2.12	1.81	0.32
	8	2.66	2.70	2.09	1.77	0.32
 <i>CPT-BT</i>	1	5.30	5.54	2.63	2.32	0.31
	2	3.73	3.91	1.94	1.72	0.22
	4	2.75	2.88	1.57	1.34	0.23
	8	2.20	2.26	1.42	1.15	0.27
 <i>Si/CPCP-T-BT-T</i>	1	4.62	4.88	2.49	2.16	0.33
	2	3.66	3.81	2.26	1.94	0.32
	4	3.06	3.14	2.15	1.83	0.32
	8	2.68	2.72	2.12	1.79	0.32
 <i>Si/CPT-TPD</i>	1	5.52	5.87	3.11	2.89	0.22
	2	4.10	4.37	2.38	2.14	0.25
	4	3.26	3.42	2.05	1.76	0.29
	8	2.75	2.82	1.93	1.62	0.31
Average						0.29
Maximum						0.33
Minimum						0.21

Comparing the results of E_g^{HL} , the systems of 2 or 4 repeating units average E_g^{HL} of published works for most of the compounds (only one exception C/CPDP-T-BT-T), while for all the compounds, the E_g^{opt} of 2 or 4-unit models were well estimated.

From this benchmarking, we concluded that it is essential to investigate carefully the correlation between conjugation length of the molecular model and the evolution of properties, setting the number of repeating units for homopolymers and copolymers.

We also observed that electronic properties can depend on the molecular structure, specifically the type of blocks in the polymer backbone. We selected eight widely studied new compounds, whose structures are shown in Figure 5.4. These compounds were classified as Core 1, Core 2, and Core 3, based on the repeating unit consisting of one, two and more than two types of blocks, respectively.

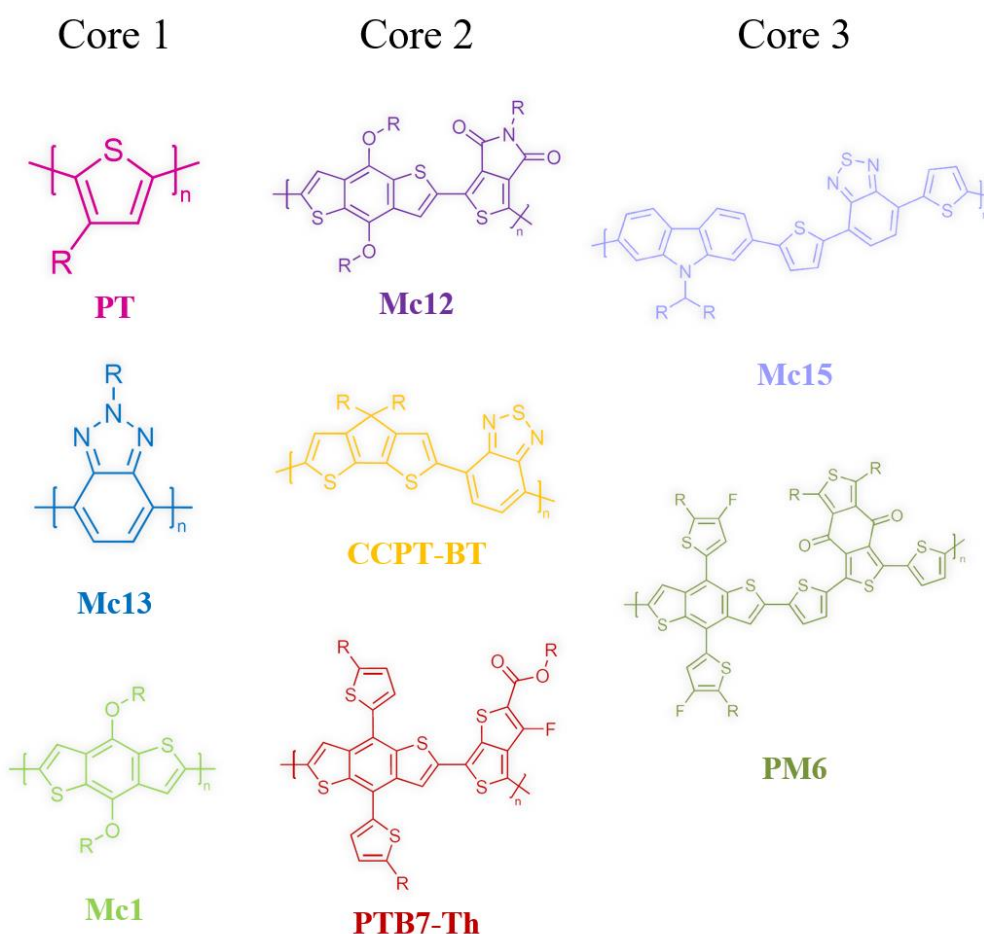


Figure 5.4 – Compounds selected for the molecular design study

Moreover, while reviewing literature, we noticed that some variation in the electronic properties can be found as modifying the side chain type. Because of this, we decided to study molecular models with three distinct alkyl side chains: methyl, butyl and 2-ethylhexyl (named in this work as C1, C4 and C6C2, respectively).

As it was done in the benchmarking, we collected the data from the literature for these eight compounds, with detailed polymer structural parameters and methodology of calculation and measurements, all available in the Appendices session, as well as the calculated average values of electronic properties of data from the literature.

5.2 Optical and Electronic Properties

Searching for trends on property-structure correlation, adiabatic fundamental gap E_g^{fund} , HOMO-LUMO gap E_g^{HL} and optical gap E_g^{opt} were evaluated for each conjugated polymer. The results are shown in Figure 5.5, Figure 5.6 and Figure 5.7 for molecules of Core 1, Core 2 and Core 3, respectively.

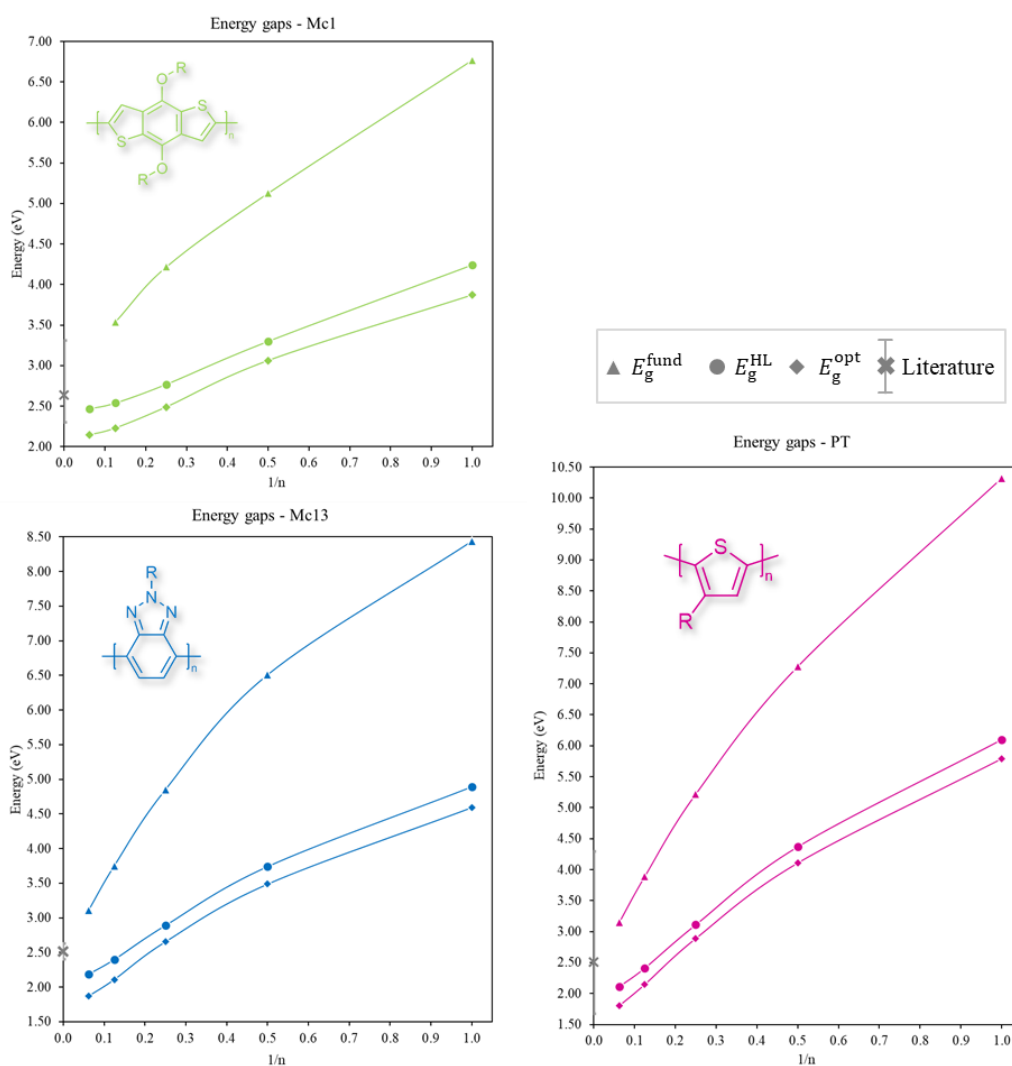


Figure 5.5 – Energy gaps (in eV) of Core-1 compounds with $R=CH_3$ plotted for the inverse of n repeating units, with the average value of HOMO-LUMO gap from the literature data.

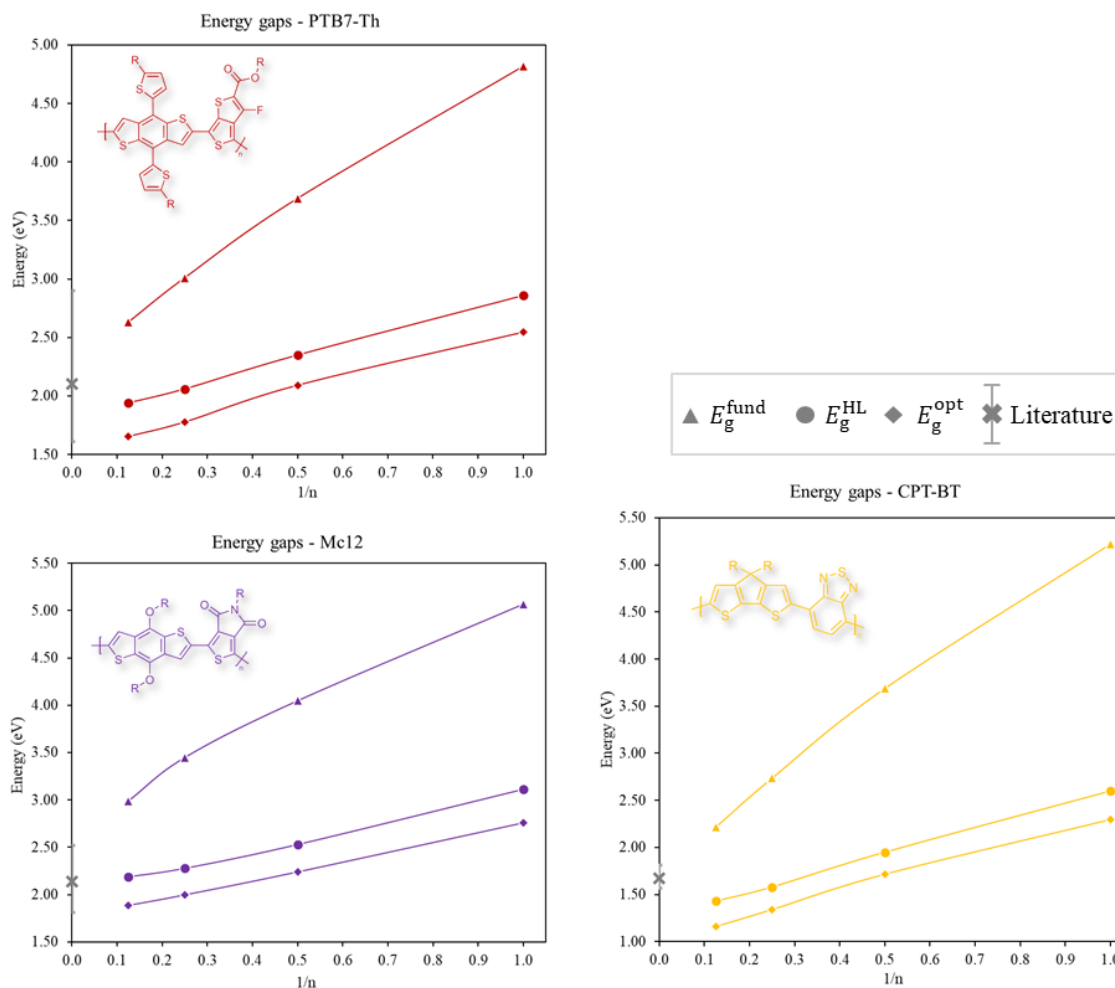


Figure 5.6 – Energy gaps (in eV) of Core-2 compounds with R=CH₃ plotted for the inverse of n repeating units, with the average value of HOMO-LUMO gap from the literature data.

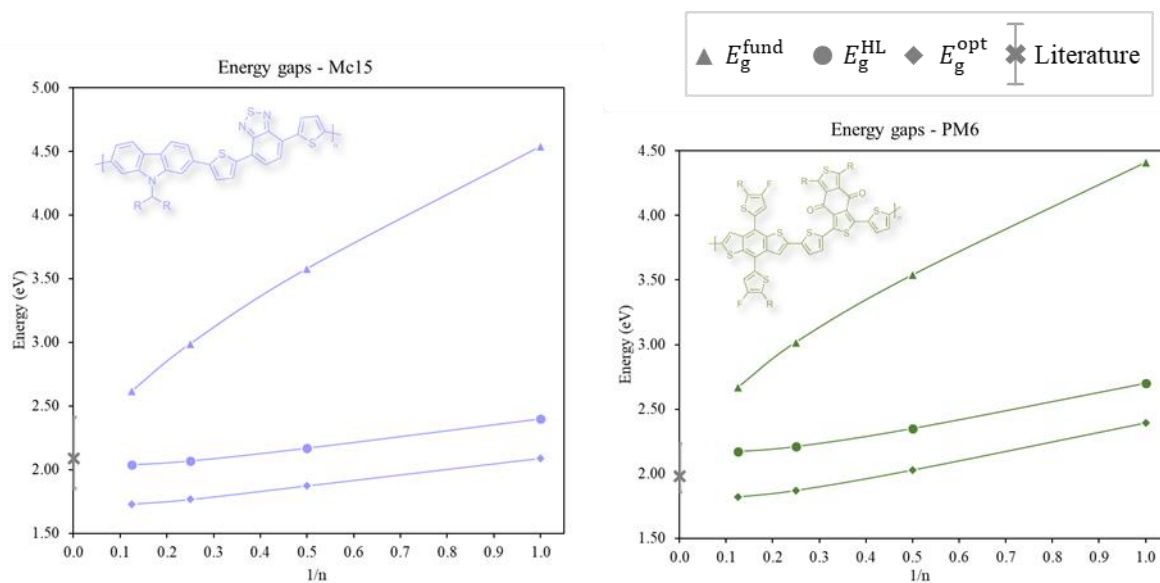


Figure 5.7 – Energy gaps (in eV) of Core-3 compounds with R=CH₃ plotted for the inverse of n repeating units, with the average value of HOMO-LUMO gap from the literature data.

In a general view, the evolution of energy gaps followed the same tendency as for other conjugated polymers of the benchmark, in which $E_g^{\text{fund}} > E_g^{\text{HL}} > E_g^{\text{opt}}$. The average E_g^{HL} from the literature for each compound was added in these graphics to guide (not compare) the analysis.

First of all, it is possible to see that 1-unit molecular models cannot predict energy gaps enough to compare with polymeric systems reported by the scientific community, especially the compounds of Core 1.

The results of E_g^{opt} showed a similar trend as E_g^{HL} values. It can be explained as the one-electron excitation from HOMO to LUMO is the biggest contribution in the molecular transition from neutral ground state (S_0) to first excited state (S_1), even if the conjugation length varies as shown in Figure 5.8, with other optical parameters summarized in Table 5.2.

Table 5.2 - MO composition of main transition contribution of optical absorption ($S_0 \rightarrow S_1$) for Mc12 systems with R=butyl, with respective vertical transition energy (E), absorption wavelength (λ) and the oscillator strength (f)

n units	Composition	E (eV)	λ (nm)	f
1	H - 1 \rightarrow L (1.58 %)	2.71	456.70	0.2271
	H \rightarrow L (47.91%)			
2	H \rightarrow L (49.33%)	2.28	544.89	1.0627
4	H - 1 \rightarrow L (2.61 %)	2.01	615.88	2.7294
	H - 1 \rightarrow L + 1 (1.52 %)			
	H \rightarrow L (43.00%)			
	H \rightarrow L + 1 (1.58 %)			

This outcome is likewise observable in the first vertical excitation results for other compounds, as delineated in Table 5.3. Note that for all molecular systems, the absorption wavelength is between 400 and 800 nm, which is the same wavelength range of the maximum intensity observed in the spectrum of solar photon flux, as mentioned in Chapter 1 of this thesis.

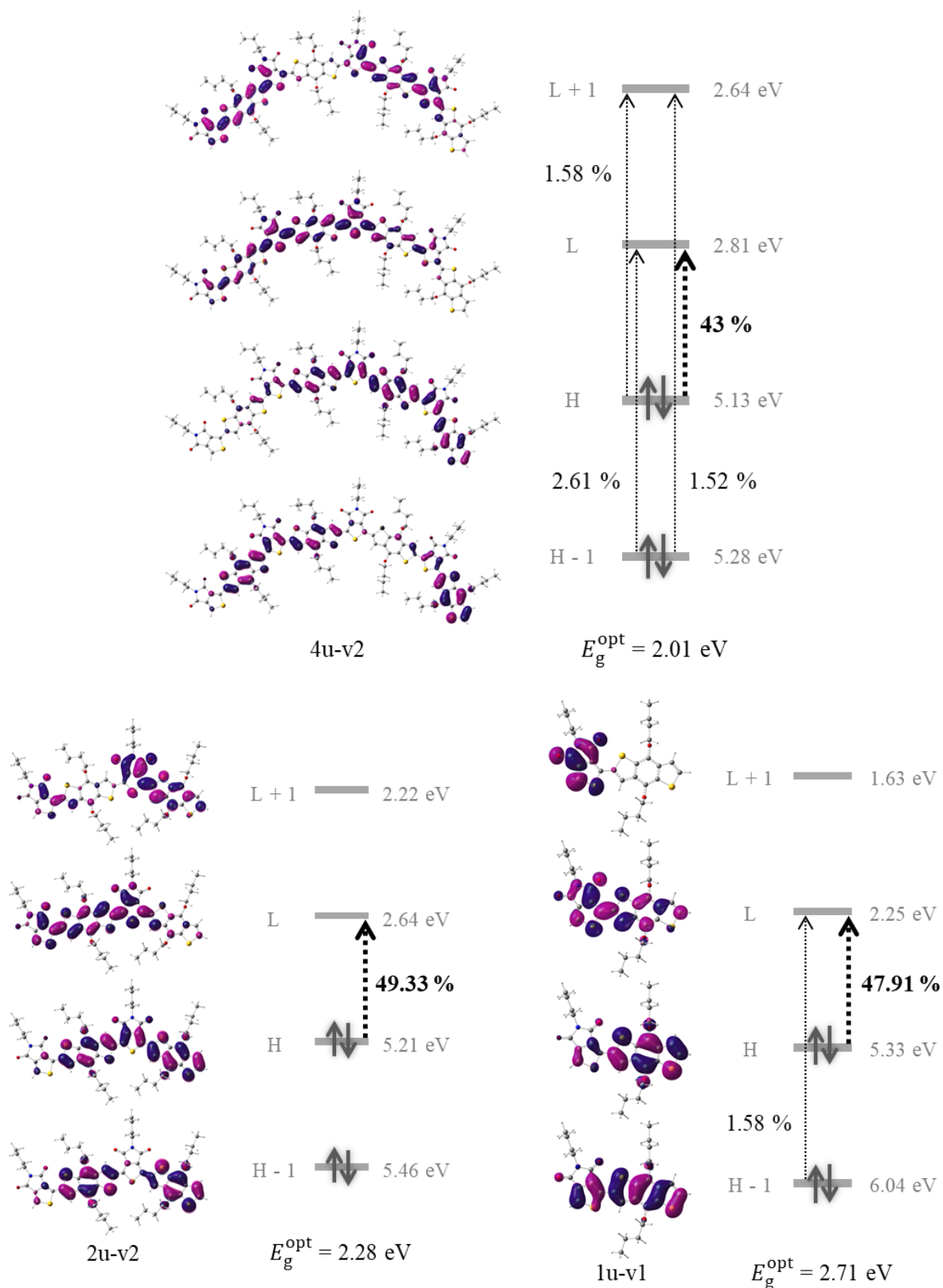


Figure 5.8 – Energy of optical absorption ($S_0 \rightarrow S_1$) and main vertical transitions (dotted arrows), in percentage, for Mc12 system with R=butyl for 1, 2 and 4 repeating units. HOMO and LUMO levels positioned out of scale and named here as H and L, respectively

Table 5.3 - MO composition of main transition contribution of optical absorption ($S_0 \rightarrow S_1$) for 4-unit systems with $R=CH_3$, with respective vertical transition energy (E), absorption wavelength (λ) and the oscillator strength (f)

Compound	Composition	E (eV)	λ (nm)	f
Mc12	H - 1 \rightarrow L (3.21 %)	2.00	621.31	2.1991
	H \rightarrow L (41.68%)			
	H \rightarrow L + 1 (3.30 %)			
PTB7-Th	H - 1 \rightarrow L + 1 (1.78 %)	1.78	697.68	3.4977
	H \rightarrow L (46.99%)			
Mc15	H - 2 \rightarrow L + 1 (1.12 %)	1.77	701.51	3.1127
	H - 2 \rightarrow L + 3 (1.23 %)			
	H - 1 \rightarrow L (2.87 %)			
	H - 1 \rightarrow L + 1 (3.01 %)			
	H - 1 \rightarrow L + 2 (2.21 %)			
	H \rightarrow L (31.88%)			
H \rightarrow L + 1 (5.96 %)				

The main difference among the compounds is noticed in curve behaviour: a steep slope for the E_g^{fund} curve, while E_g^{HL} and E_g^{opt} results smoothly approach the convergence. This is expected once E_g^{fund} is calculated from the total energy of a molecule with $N \pm 1$ electrons, whereas E_g^{HL} is estimated from one-electron wavefunctions and E_g^{opt} is the energy resulting from 1-electron excitation. Therefore, increasing the conjugation length affects the intrinsic quantum-chemistry characteristics.

Comparing the other energy gaps, E_g^{fund} variation is bigger than E_g^{opt} one due to IP (EA) values vary more than E_{HOMO} (E_{LUMO}), as it can be seen for two compounds in Figure 5.9 and Figure 5.10. It became evident that IP^a (EA^a) has a higher rate of convergence than E_{HOMO} (E_{LUMO}) as larger is the absolute value of the a coefficient from the logarithmic trend line equations ($y = a \ln x + b$).

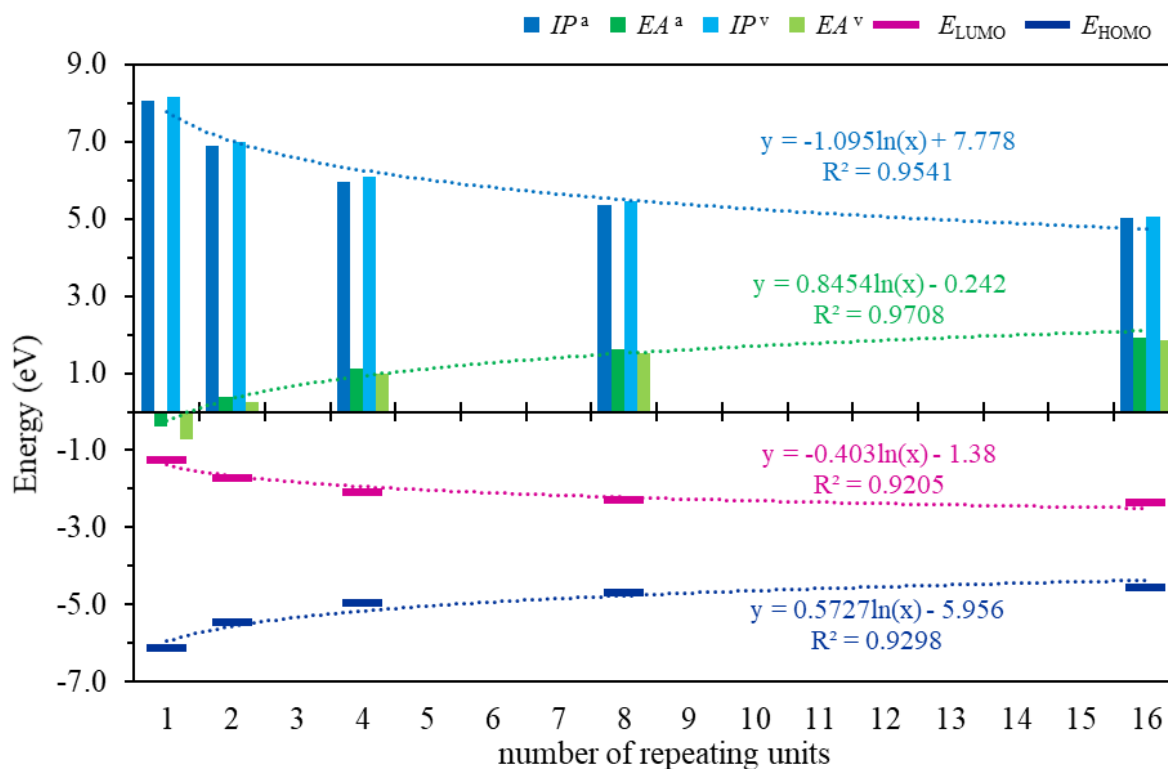


Figure 5.9 – Electronic properties for compound Mc13 with methyl side chain in different conjugation length.

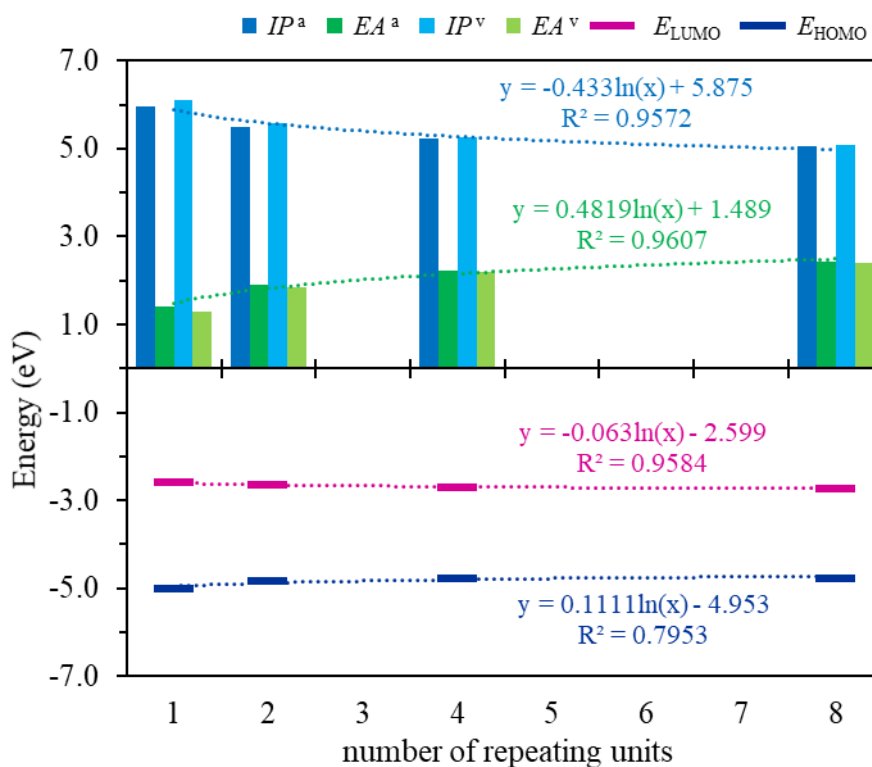


Figure 5.10 – Electronic properties for compound Mc15 with methyl side chain in different conjugation length.

The negative adiabatic and vertical EA for 1-unit Mc13 was also observed for the other molecules of Core 1. It means that the molecule at its cationic state (a molecule with $N+1$ electron) is more stable than at its ground state. So, in a vacuum, these molecules tend to link with anionic species.

Indeed, E_{HOMO} and E_{LUMO} calculated from Alpha orbitals eigenvalues and converted in electron-Volts try to translate how difficult it is to localize these molecular orbitals in a vacuum. Their values are used to correlate the pathway of electrons as being excited from one level to another, as it is the lowest difference between occupied and unoccupied orbitals.

On the other hand, IP and EA are properties that interpret the energy necessary for removing and adding one electron into molecules, respectively. As longer is a polymer chain, remove one electron to the molecular system causes less perturbation, while it becomes more difficult to include one electron.

IP and EA variation ratios are used to affirm that some polymers are more tendentious to donate or accept electrons than others. Nevertheless, it also depends on many other quantum-chemistry processes, such as photon absorption and charge transfer. Therefore, classifying the polymers as donors or acceptors only considering these variations or a property value itself can carry plenty of misleading.

Moving through energy-gap-correlated properties, we explored the exciton binding energy E_b predicted from the difference between E_g^{opt} with E_g^{fund} (see Chapter 1 for definitions). Three approaches were used to estimate this last property: vertical fundamental gap $E_g^{\text{fund}_v}$, adiabatic fundamental gap $E_g^{\text{fund}_a}$ (including relaxation of structure) and HOMO-LUMO gap E_g^{HL} , respectively shown in Table 5.4, Table 5.5 and Table 5.6.

As we mentioned in Chapter 3 of this thesis, doing $E_g^{\text{HL}} \cong E_g^{\text{fund}}$ when following Koopman's theorem is incorrect for DFT calculations; that is why we called the difference between E_g^{HL} and E_g^{opt} as ΔE_g .

From both Table 5.4 and Table 5.5, it is possible to identify that molecular system leads to smaller E_b as larger the molecule is, by increasing the conjugation length or the size of alkyl side chains, results consistent with the literature [8].

For the same molecule, it is found to have smaller exciton binding energy when calculated from the adiabatic fundamental gap (Table 5.4) than from the vertical one (Table 5.5) due to the inclusion of relaxation of structures in charged states.

Table 5.4 – Exciton binding energy, in eV, calculated from $E_b = E_g^{\text{fund.v}} - E_g^{\text{opt}}$ for all the compounds in various conjugation length and side chain. Table cells were coloured according to the colour code in the bottom

Compound	side chain	number of repeating units					
		1	2	4	8	16	
PT		C1	4.73	3.67	2.71	2.01	1.49
		C4	4.50	3.54	2.69	2.04	1.52
		C6C2	4.29	3.39	2.56	1.96	1.46
Mc13		C1	4.27	3.27	2.45	1.84	1.35
		C4	4.14	3.18	2.37	1.79	1.32
		C6C2	4.06	3.11	2.33	1.77	1.31
Mc1		C1	3.58	2.59	1.92	1.41	
		C4	3.47	2.50	1.87	1.38	
		C6C2	3.37	2.44	1.82	1.35	
Mc12		C1	3.07	2.20	1.62	1.19	
		C4	2.98	2.12	1.56		
		C6C2	2.91	2.07	1.54		
CPT-BT		C1	3.16	2.16	1.53	1.12	
		C4	3.10	2.11	1.50	1.10	
		C6C2	3.04	2.08	1.49		
PTB7-Th		C1	2.63	1.91	1.43	1.05	
		C4	2.58	1.88	1.44		
		C6C2	2.56	1.84	1.41		
Mc15		C1	2.72	1.87	1.30	0.93	
		C4	2.70	1.85	1.30		
		C6C2	2.66	1.86	1.29		
PM6		C1	2.28	1.69	1.24	0.90	
		C4	2.25	1.68	1.23		
		C6C2	2.21	1.65	1.22		



The huge variation of calculated E_b (sometimes more than 4 eV to less than 1 eV) shows how stronger excitons are bound in small molecules, while they can be easier dissociated in

polymeric systems of organic semiconductors. It does not mean that the small molecules are not good to be used in electronic devices; they just require more energy to separate electron-hole pairs.

Table 5.5 - Exciton binding energy, in eV, calculated from $E_b = E_g^{\text{fund,a}} - E_g^{\text{opt}}$ for all the compounds in various conjugation length and side chains. Table cells were coloured according to the colour code in the bottom.

Compound	side chain	number of repeating units					
		1	2	4	8	16	
PT		C1	4.53	3.18	2.33	1.75	1.35
		C4	3.94	2.95	2.12	1.55	1.19
		C6C2	3.78	2.83	1.32	1.51	1.08
Mc13		C1	3.85	3.02	2.19	1.64	1.24
		C4	3.71	2.92	2.13	1.60	1.20
		C6C2	3.65	2.82	2.06	1.53	1.17
Mc1		C1	2.90	2.07	1.73	1.31	
		C4	2.76	2.07	1.67	1.26	
		C6C2	2.70	1.81	1.58	1.25	
Mc12		C1	2.31	1.81	1.45	1.10	
		C4	2.38	1.75	1.42		
		C6C2	2.39	1.70	1.26		
CPT-BT		C1	2.92	1.97	1.40	1.06	
		C4	2.85	1.92	1.37	1.04	
		C6C2	2.79	1.88	1.34		
PTB7-Th		C1	2.28	1.60	1.24	0.97	
		C4	2.28	1.67	1.30		
		C6C2	2.24	1.63	1.27		
Mc15		C1	2.45	1.71	1.23	0.89	
		C4	2.43	1.70	1.22		
		C6C2	2.39	1.68	1.20		
PM6		C1	2.02	1.51	1.14	0.85	
		C4	1.92	1.51	1.15		
		C6C2	1.93	1.49	1.12		



To comprehend the influence of molecular structure on the relative property, we plotted the exciton binding energy against the reciprocal number of electrons in Figure 5.11. This approach allowed us to compare the relative properties of three compounds, despite the fact that the repeating units are made up of different arrangements of σ and π bonds.

For the three compounds, the difference between $E_g^{\text{fund}_a}$ and E_g^{opt} decreases as the conjugation length of the molecular model increases. Regarding to the side chains, there is no evidence of their correlation with the relative property.

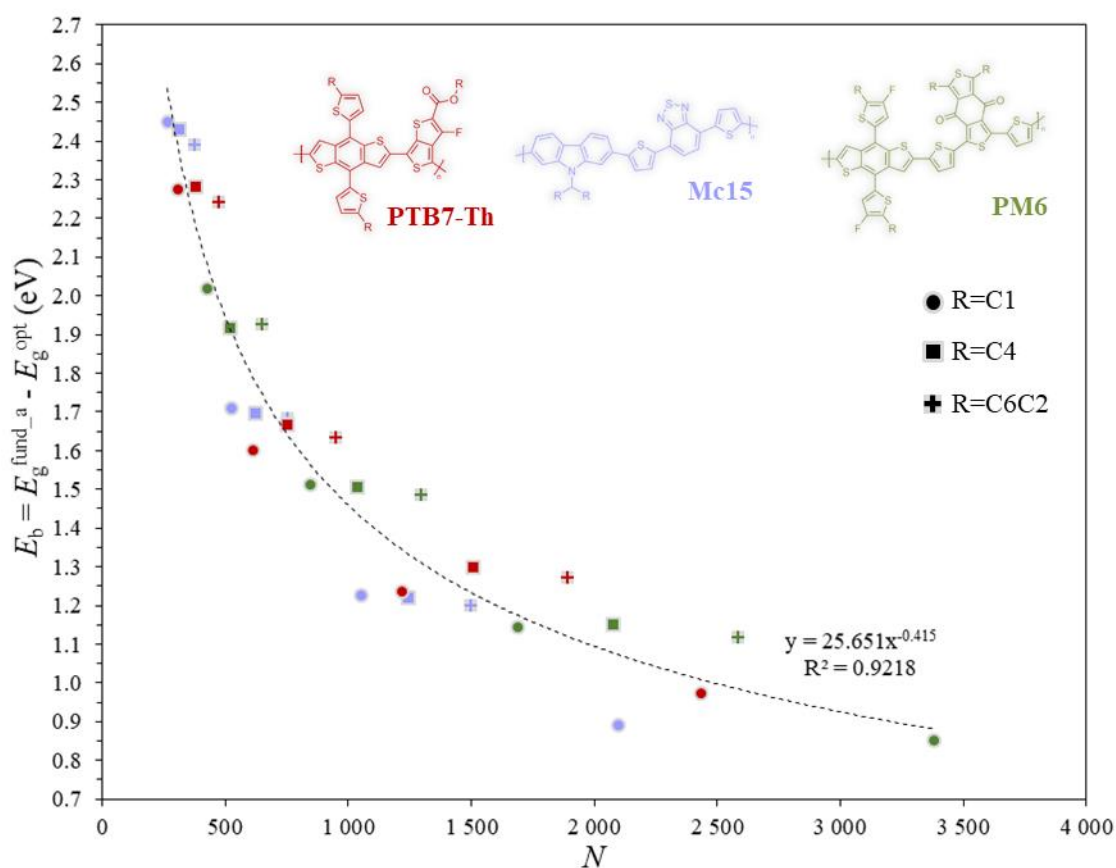
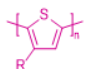
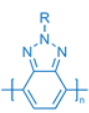
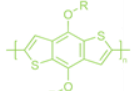
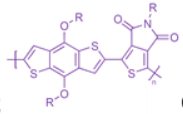
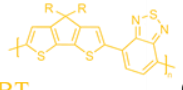
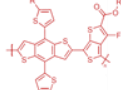
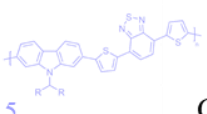
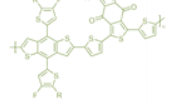


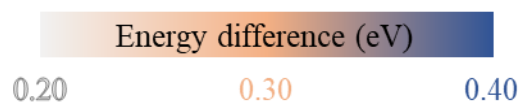
Figure 5.11 - Exciton binding energy calculated from relaxed structures in charged states and the vertical transition to the first excited state.

It is relevant to mention that some molecular systems of our study have more than 3000 electrons. Computing electronic properties in such huge models is only possible using DFT. Even though *Ab initio* methods provide more accurate results, they are limited to molecules with tenths of electrons.

Using Koopman's theorem to estimate IP and EA as equal to E_{HOMO} and E_{LUMO} is widely used with organic compounds. However, calculating molecular levels using DFT (including exchange-correlation to describe Kohn-Sham orbitals) leads to erroneous conclusions.

Table 5.6 – Difference of energy gaps, in eV, calculated from $\Delta E_g = E_g^{\text{HL}} - E_g^{\text{opt}}$ for all the compounds in various conjugation length and side chains. Table cells were coloured according to the colour code in the bottom

Compound	side chain	number of repeating units				
		1	2	4	8	16
PT	 C1	0.31	0.27	0.22	0.27	0.31
	C4	0.30	0.32	0.32	0.35	0.38
	C6C2	0.28	0.31	0.32	0.37	0.39
Mc13	 C1	0.30	0.25	0.24	0.29	0.32
	C4	0.30	0.26	0.25	0.29	0.32
	C6C2	0.31	0.28	0.26	0.31	0.33
Mc1	 C1	0.37	0.24	0.28	0.32	0.32
	C4	0.38	0.25	0.29	0.32	0.32
	C6C2	0.38	0.26	0.29	0.32	
Mc12	 C1	0.35	0.29	0.29	0.30	
	C4	0.36	0.29	0.31		
	C6C2	0.38	0.32	0.32		
CPT-BT	 C1	0.31	0.23	0.24	0.27	
	C4	0.31	0.24	0.25	0.27	
	C6C2	0.32	0.25	0.26		
PTB7-Th	 C1	0.32	0.26	0.28	0.28	
	C4	0.33	0.27	0.28		
	C6C2	0.34	0.26	0.28		
Mc15	 C1	0.31	0.30	0.31	0.31	
	C4	0.31	0.30	0.31		
	C6C2	0.32	0.30	0.31		
PM6	 C1	0.31	0.32	0.34	0.35	
	C4	0.31	0.33	0.34		
	C6C2	0.31	0.33	0.35		



Despite this, we calculated ΔE_g from the energy of π and π^* molecular orbitals, presenting the obtained results in Table 5.6. Curiously, it was found ΔE_g around 0.30 eV (arithmetic mean)

for all the molecular systems, which are results very similar to the benchmarking calculations in Table 5.1 and the calculated ΔE_g from literature data. It means that there is a correlation of 0.30 eV between E_g^{HL} and E_g^{opt} no matter how electrons are arranged in the molecule.

In conclusion to these analyses, it became clear that E_g^{fund} is largely affected by the size of the conjugation length, while E_g^{HL} and E_g^{opt} are less affected by it. This happens because:

- E_g^{fund} is a correlation of total energy of molecular systems involved in receiving and donating one electron;
- E_g^{HL} approximates the energy of π and π^* molecular orbitals so it depends in how the electrons distributed;
- E_g^{opt} is a combination of one-electron transitions from one molecular orbital to another.

It is important to keep in mind that these are conclusions made under gas-phase conditions. According to the environment in which the polymer will be expose (solvents, dopants and others), a new analysis should be done to understand the electronic characteristics of the molecule in this situation.

After discussing the electronic properties of conjugated polymers, the following text comes out to guide researchers in designing a new material for high-efficiency solar cells.

5.3 Effect of modifications on isolated chain structures

5.3.1 Conjugation length

From previous results and in agreement with the literature, electronic properties of conjugated polymers, such as energy gaps, are dependent on the conjugation length, that is, the size of the chain backbone in which σ and π bonds are arranged. Indeed, electronic properties achieve a convergence when finding a saturation length as being polymeric systems. However, their correlation with the polymer core characteristics is still not established for the scientific community.

Since the analysis of the electronic properties in Figure 5.9 and Figure 5.10, it started to be observed that molecular systems with few blocks per repeating unit suffer bigger variations of IP , EA , E_{HOMO} and E_{LUMO} , as comparing Mc13 (1 block per n) with Mc15 (4 blocks per n). To

remind, we named here a block an aromatic ring or a few fused-aromatic rings connected to another by a σ bond.

Figure 5.12 shows the results of E_g^{fund} for all the compounds of this calculation campaign. The 1-unit systems of Core-1 (PT, Mc13 and Mc1) with any type of the side chains showed high E_g^{fund} , because they presented negative EA and very high values of IP . As Mc1 has more σ and π bonds arranged along the chain and is composed of two side chains, models with few repeating units of this compound presented lower differences between the energy to remove one electron and to add one electron than PT and Mc13.

It was also interesting to note that EA and IP of Core-1 compounds converged to the same values, even when the side chains were changed. However, it is necessary to do calculations for models with more repeating units to achieve the saturation of these properties and then have a consistent conclusion.

Concerning Core-2 compounds (with two blocks per n), PTB7-Th and Mc12 showed similar ratio of E_g^{fund} variation, with around 0.35 eV of difference. In another hand, E_g^{fund} variation of CPT-BT mostly agreed with Mc1 results, with a deviation of approximately 1.45 eV for molecular systems composed with the same number of repeating units.

Finally, Core-3 compounds showed not only quite the same behaviour but also next to zero eV of difference. It might be due to the similar arrangement of σ and π bonds along the chain backbone.

As we mentioned before, increasing the conjugation length of the polymer backbone has a lower impact in the E_g^{opt} than in the E_g^{fund} , as it can be confirmed with a smaller slope of E_g^{opt} curves in Figure 5.13.

Electronic properties depend not only on the conjugation length but also on intrachain interactions between the blocks.

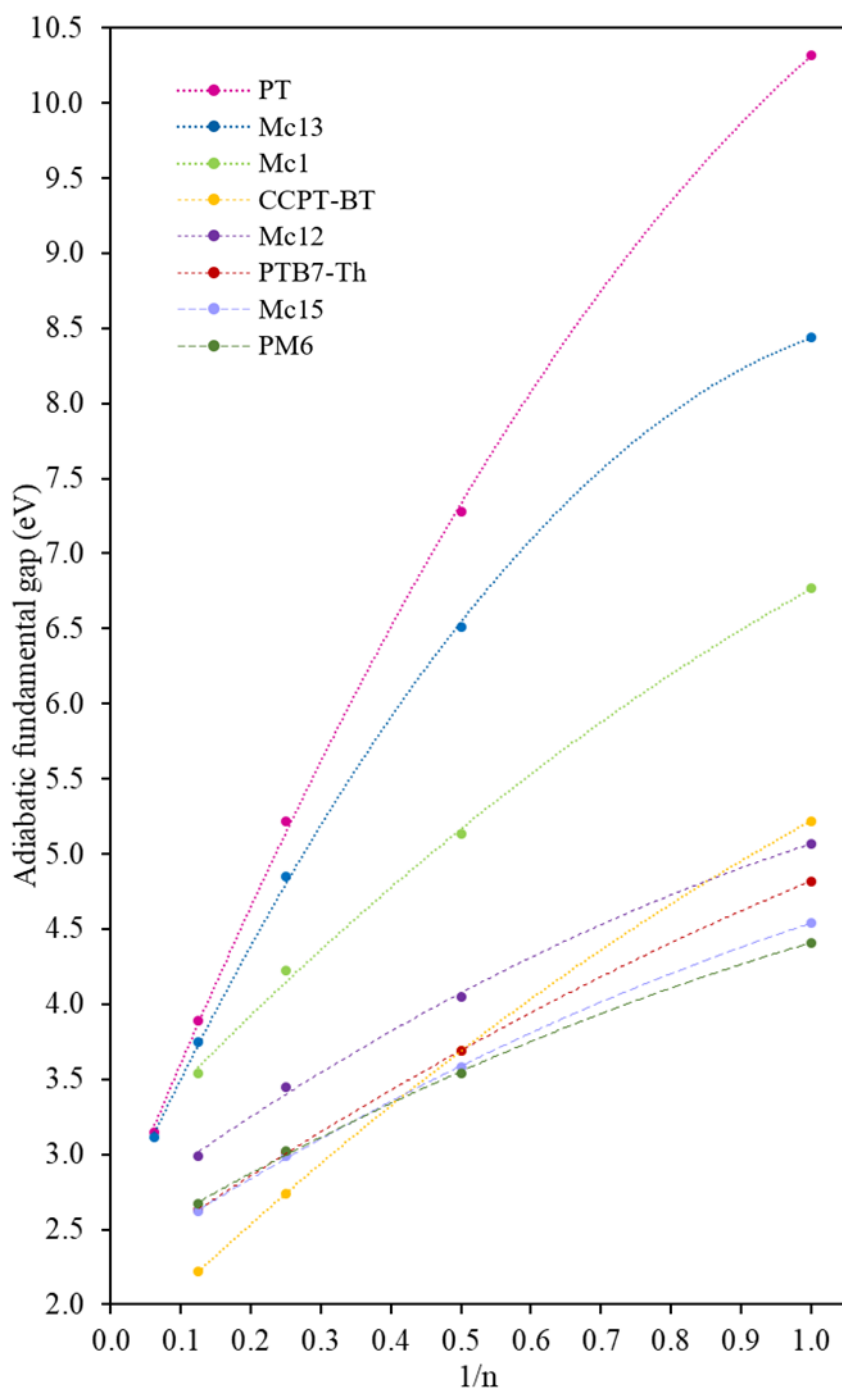


Figure 5.12 - E_g^{fund} of methyl-side-chain molecular models in relation to their reciprocal number of repeating units. Molecules correlated by Core-1 (dotted lines), Core-2 (dashed lines) and Core-3 (longer dashed lines).

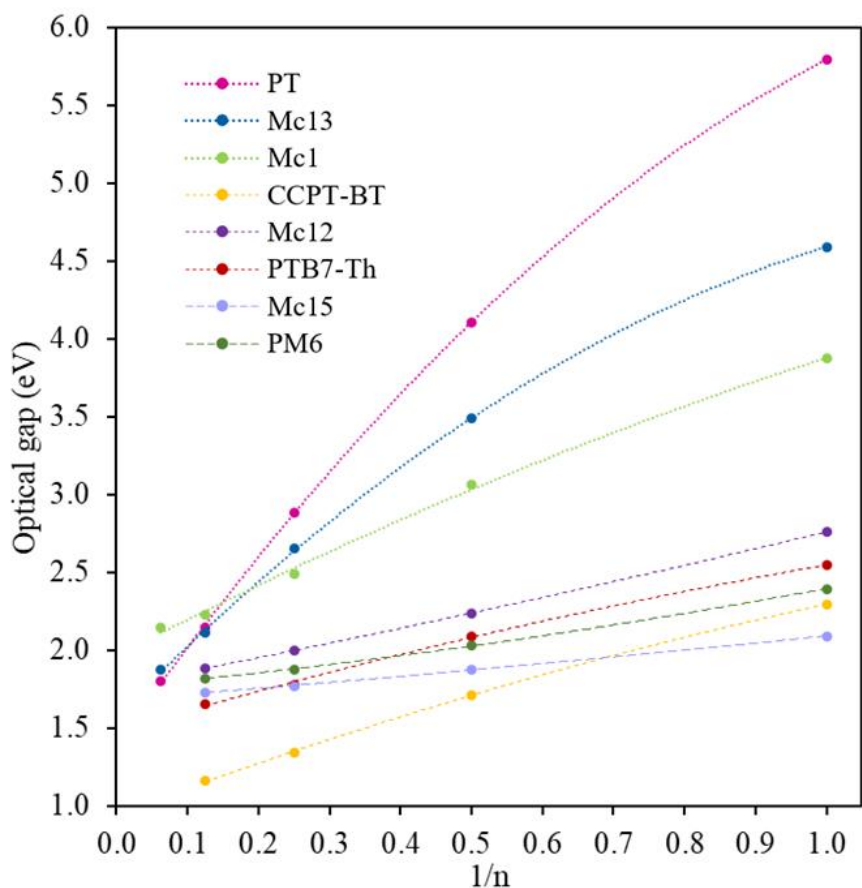


Figure 5.13 – E_g^{opt} of methyl-side-chain molecular models in relation to their reciprocal number of repeating units. Molecules correlated by Core-1 (dotted lines), Core-2 (dashed lines) and Core-3 (longer dashed lines).

5.3.2 Nature of blocks

The nature of blocks is, in fact, the distribution of σ and π orbitals. To comprehend the correlation between electronic properties and the nature of blocks, the E_g^{HL} for all the compounds about its conjugation length is shown in Figure 5.14.

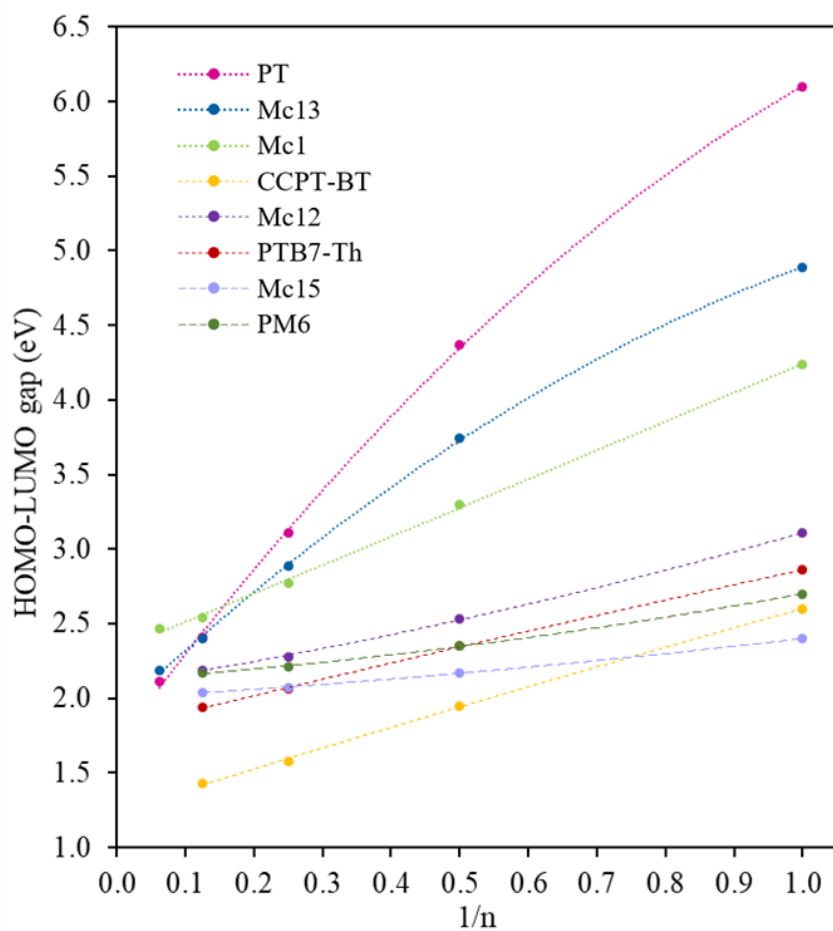


Figure 5.14 – E_g^{HL} of methyl-side-chain molecular models in relation to their reciprocal number of repeating units. Molecules correlated by Core-1 (dotted lines), Core-2 (dashed lines) and Core-3 (longer dashed lines)

Only with these eight compounds, there was no evidence that blocks having chemical functions as electron-donor, electron-acceptor and π -spacer have a direct impact on energy gaps, neither in the convergence ratio of properties.

Moreover, from calculated E_{HOMO} , E_{LUMO} and E_g^{HL} of 8-unit models in Figure 5.15, we could confirm that including thiophene rings between donor and acceptor blocks is not determinant to obtain the lowest energy gap, and the energy difference of frontier molecular levels is higher for homopolymers than for D-A copolymers.

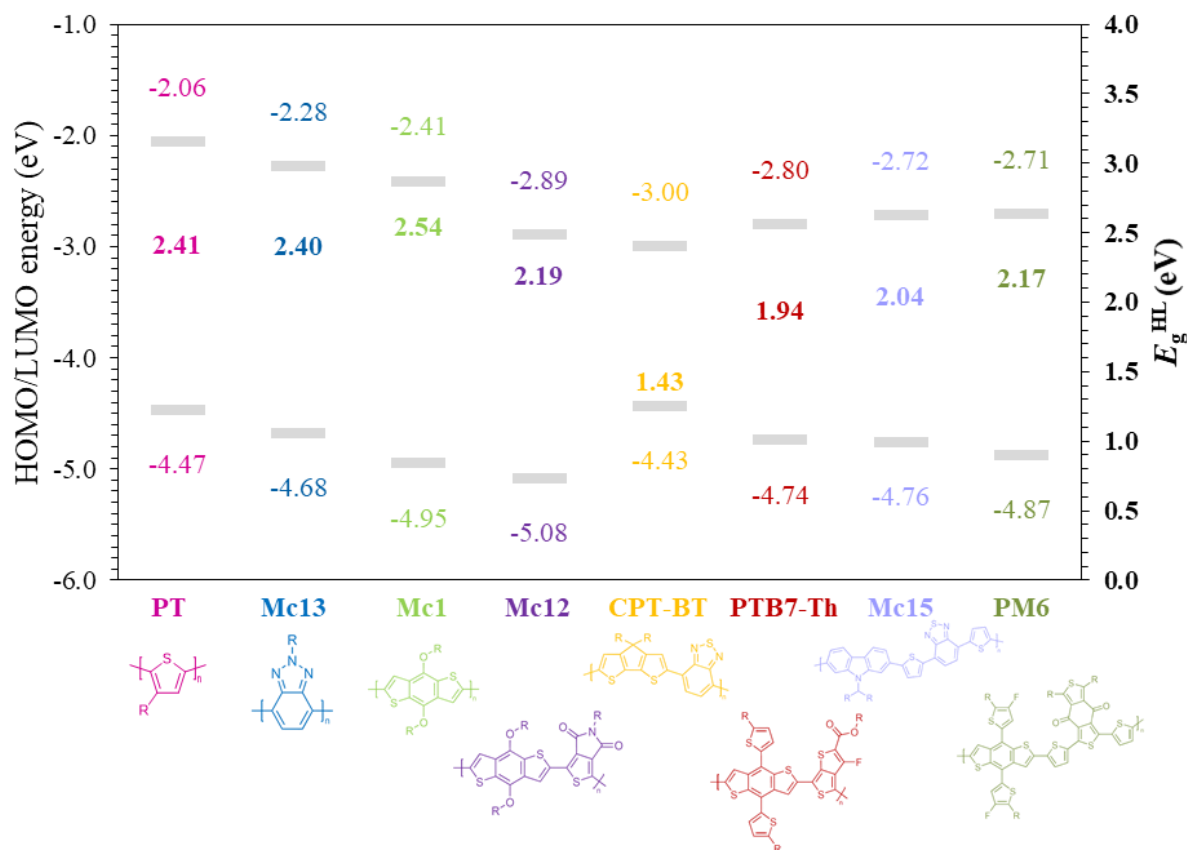


Figure 5.15 - E_{HOMO} , E_{LUMO} and E_{g}^{HL} of methyl-side-chain molecular models composed of eight repeating units

It is very common in the literature to find reports of comparison of semiconductor compounds taking isolated values of electronic properties such as E_{HOMO} , E_{LUMO} and E_{g}^{HL} , that is, computed results of a molecular model using certain methods. Our analysis made clear that this practice causes strong misleading, which might be crucial in molecular design.

With these results, it is evident that using models with a settled number of repeating units to describe the whole system as done in many works can carry huge misconceptions. Electronic properties should encounter a standard as working with conjugated polymers, that is, infinite chain of monomeric units.

5.3.3 Side chains

Alkyl side chains comprise of single-bond carbons and hydrogens, forming chains of sigma bonds attached to a σ - π conjugated backbone. Long side chains are incorporated into the main

chain of a polymeric semiconductor to increase its solubility. Small differences in optoelectronic properties are observed on modeling, even varying side chains, [9,10], but it is not valid for all the conjugated molecules [11].

Previously, in Table 5.4, Table 5.5 and Table 5.6, we have already shown slight variations as replacing methyl side chains for butyl and 2-ethylhexyl ones. Complementary to it, small differences (less than 0.1 eV) in E_{HOMO} and E_{LUMO} can be seen in Figure 5.16.

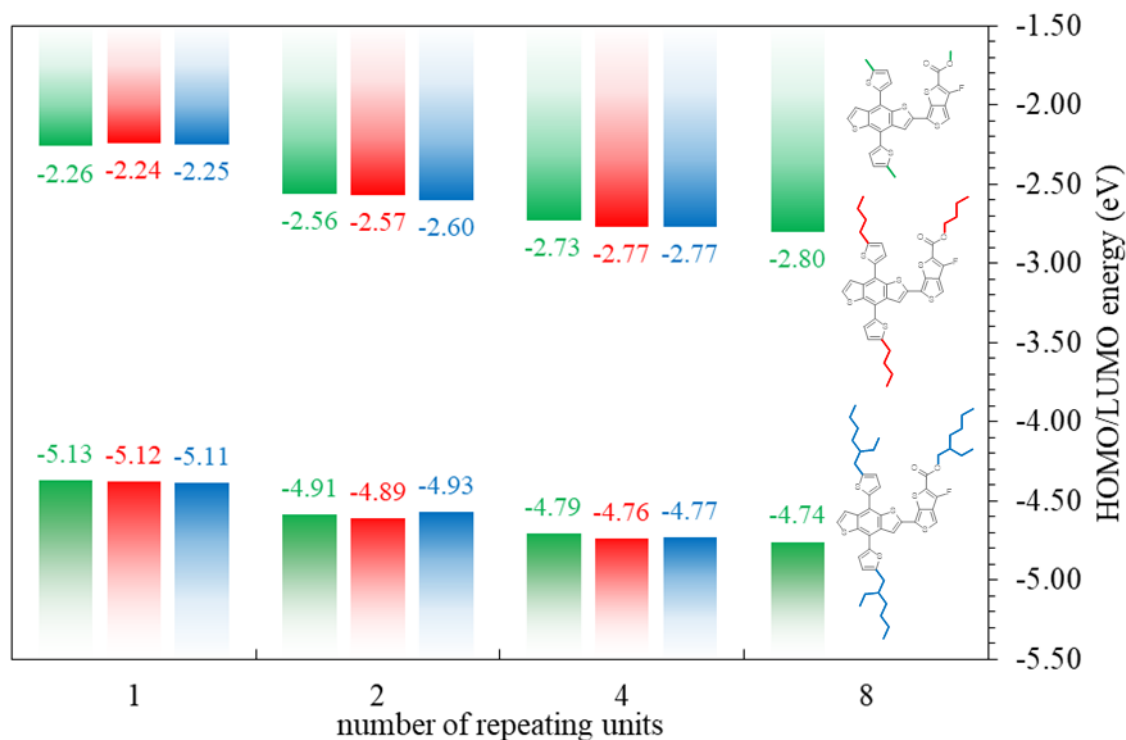


Figure 5.16 – Electronic properties of PTB7-Th in relation to its conjugation length (number of repeating units per chain) and side chain, as represented for the 1-unit model: methyl (green), butyl (red) and 2-ethylhexyl (blue).

This suggest that optical and electronic properties result from interactions in the backbone rather than the effect due to side chains. Nonetheless, all the conclusions until here were based on models of isolated chains. Conjugated polymers are connected to each other by weak forces called van der Waals interactions and structural modifications play an important role in the interactions between chains. Therefore, we carried out the study of intermolecular interactions with double-chain models.

5.4 Analysis of intermolecular interactions

Initially, the doubled-chain structures were modelled with a distance of around 4 Å. After optimization, in most of the conformations, chains maintained this distance, which could be identified as the average distance of stable overlapping of π -orbitals.

The stability of each molecular system, that is, molecules from one compound with the same conjugation length and same side chains, was investigated from a comparison among conformations. They were modelled to create as many types of interactions as possible between one chain and another, aiming to discover which exchanges of energy drive the most favourable molecular systems.

For the starting point, it was chosen a face-to-face arrangement of π -stacking of backbones, in which one chain was parallel positioned to another. After optimization of geometry, the final position of main chains and side chains took place in the lowest energetic interactions, in which blocks displaced parallelly or maintained stacked but varying the dihedral angles.

For most of the molecular systems for all the compounds, the most stable dimers were found for those chains slipped along the backbone axis due to the steric effect of side chains and repulsion of atoms (opening it) with overlapping of π -orbitals and attraction of atoms (closing it), a dimer orientation like zippers, as explained in Chapter 3. These mostly found orientations are shown in Figure 5.17.

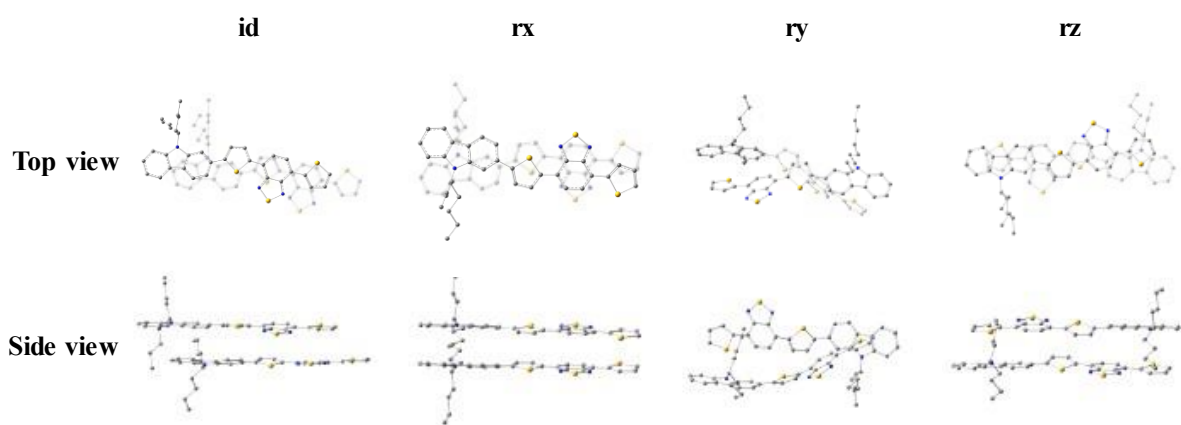


Figure 5.17 – Dimers of 1-unit Mc15 with butyl side chain, in which **id**, **rx** and **rz** presented a zipper orientation, while **ry** resulted in a not-stacked conformation.

The conformations represent states of the same molecular systems, with different interactions due to changes in their orientation. In addition, considering the molecules in a material to be processed and applied in OPV cells, all these situations coexist. Thus, the electronic properties of each conformation should be included in the final character. Even though it is relevant to supplement the molecular behaviour concerning reactivity and transition states, these subjects will not be discussed in this present study as the compounds are stable in room temperature.

Boltzmann distribution was done as a complementary analysis using Python libraries to collect the data from output files, calculate the population of each conformation for the same molecular system and colour the table cells according to a colour code to facilitate the identification of the most stable species. Considering $k_b = 8.314462618 \frac{\text{J}}{\text{K}} \cdot \text{mol}$, $T_{\text{amb}} = 298.15 \text{ K}$ (25°C), $1 \text{ Hartree} = 27.21138505 \text{ eV}$ and $1 \text{ eV} = 96.4853 \text{ kJ/mol}$, the populations of each conformation for all the compounds were calculated, and they were available in Figure 5.18.

Giving focus to the black-filled cells representing the highest populations, the distribution of species became concentrated in one conformation as bigger was the molecular system (longer side chain and conjugation length of the main chains). Another point observed is that there was no standard of pattern and rotation that could characterize the most stable molecule among the compounds.

Considering this, it was necessary to develop other kinds of evaluations to interpret the origin of what drives the energy stability of the conjugated polymers and find a correlation with the electronic properties.

The HOMO and LUMO energies of each conformation were calculated to provide the HOMO-LUMO gap (from here, it will be named E_g). A weighted average calculation of dimer E_g was done by applying the population estimated from the Boltzmann distribution. We compared these data with the difference in total energy of each conformation compared to the lowest energy one, as shown for compound Mc15 in Figure 5.19.

The average value of the HOMO-LUMO gap results from the literature for the same compound (for more details, see the Appendices session) was also added to each graphic in a way that gives some context for the calculated properties. As we mentioned many times in this work, literature data for the same compound vary a lot depending on the measurement method, ambient conditions and other factors. Therefore, comparing calculated results with them could provide incorrect conclusions.



Figure 5.18 – Population in percentage of each molecular system for compounds (a) PT, (b) Mc1, (c) Mc13, (d) Mc12, (e) CPT-BT, (f) PTB7-Th, (g) Mc15, and (h) PM6.

In the first analysis, the E_g for each molecular system varied from 0.2 to 0.3 eV, except for 1-unit butyl side chain, which variation achieved almost 0.5 eV due to the loss of backbone stacking, as can be verified in Figure 5.17. Moreover, smaller systems such as 1 and 2 units with methyl groups presented lower differences of molecular total energy compared to the 2-unit conformations with a divergence of more than 17 kcal/mol.

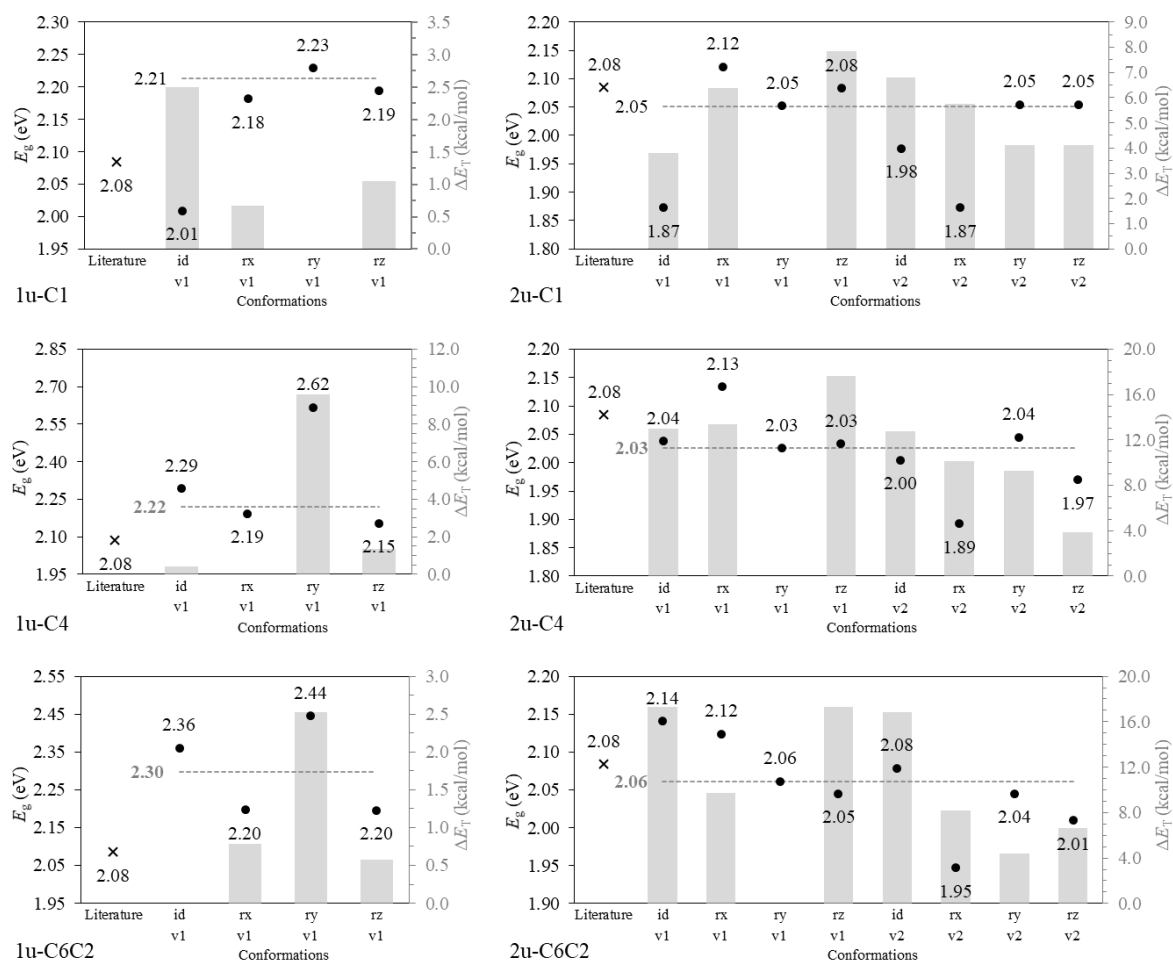


Figure 5.19 – Comparison among Mc15 dimers of total energy differences between each conformation and the most stable one (grey columns) and reciprocal E_g (black dots), with extra details of the average value from the literature (symbol \times) and the mean value of E_g of each molecular system (dashed line).

Among all the compounds, Mc15 2-unit was the only molecular system in which conformations ry-v1 were the most stable even if varying the side chains (check it in Figure 5.18). Even with the twisting of the polymer chain, the backbones maintained their stacked shape. These can be

seen in Figure 5.20, in which hydrogens were hidden from the structures only to make the visualization more understandable.

From this evaluation, it became clear that the conformation with the lowest energy (most stable) does not have the lowest energy gap, meaning that there is no direct correlation between energy stability and electronic properties. However, as it represents the major population among other species, it might dictate the electronic property of the material.

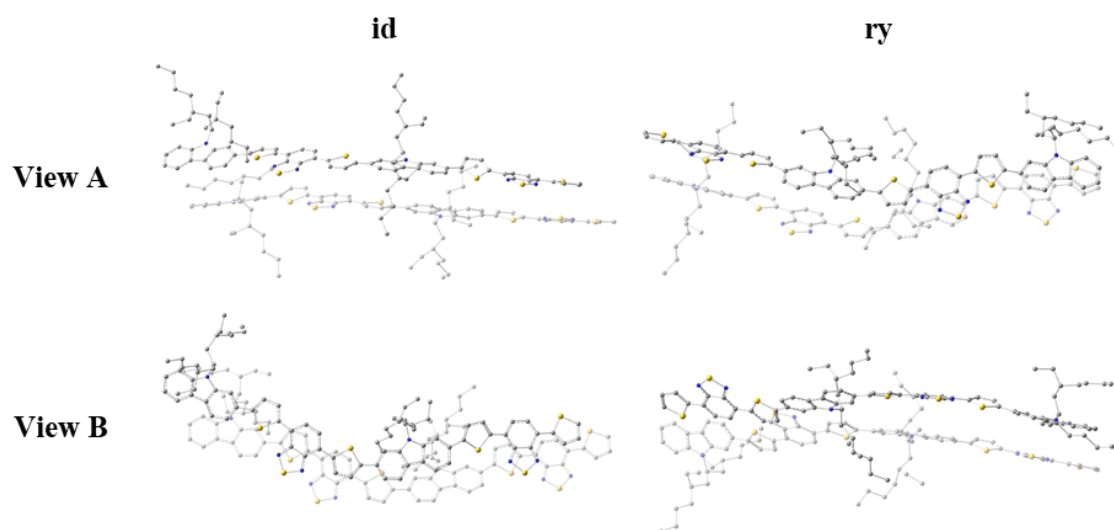


Figure 5.20 – Dimers of Mc15 composed of 2 repeating units with 2-ethylhexyl side chains
($E_T^{\text{id}} > E_T^{\text{ry}}$).

Therefore, it is indispensable to look at the forces that rule polymer chain interactions.

Using an independent gradient model (IGM) for visual analysis of molecular interactions, each atom is coloured following the colour scale in Figure 5.21 correlated to its $\Delta g^{\text{inter}/\text{At}}$ signature (details in Chapter 3), an associated local descriptor to describe the atomic contribution to the noncovalent interactions between fragments of a molecule.

It is important to remember that IGM is a tool used as a visualization map of noncovalent interactions based on electron density gradient methods, but these results have no direct correlation with electronic energy. In other words, it is impossible to affirm that one conformation is more stable than another based on the number of bigger-contribution spots. Meanwhile, with IGM, it became easier to identify the main atoms from one fragment responsible for interacting with another.



Figure 5.21 – Colour scale for $\Delta g^{\text{inter/At}}$

According to IGM analysis, the biggest contributions to the interchain interactions are indicated by red atoms. They are mainly located on the backbone for all the conformations in Figure 5.23, and the atoms of medium contribution (greyish atoms). It is possible to identify the great influence of interactions such as $\text{S}\cdots\pi$ and $\text{C}\cdots\pi$, in which carbon and sulphur atoms of one chain might interact with the fused-aromatic rings of the other chain.

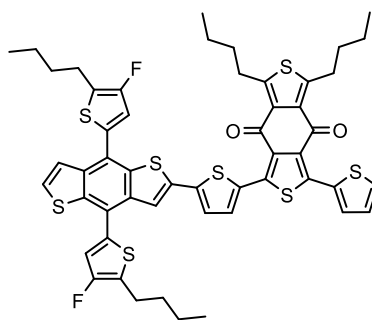


Figure 5.22 - Structure of 1-unit of PM6 with butyl side chain

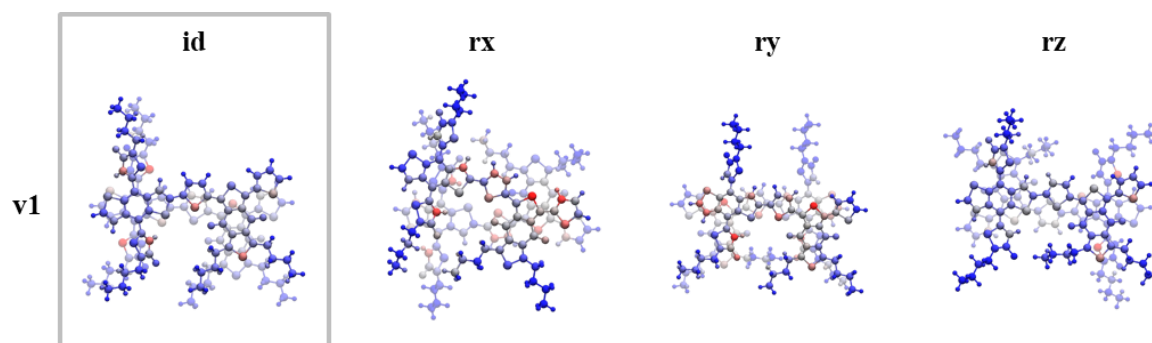


Figure 5.23 – Dimers of the molecular system of Figure 5.22 in various conformations, highlighting the most stable one. Atoms were coloured according to its $\Delta g^{\text{inter/At}}$

On the other hand, the smallest to zero contribution (blue atoms) on interactions between chains is placed on side chains and end groups of each monomer. This can explain why replacing long

alkyl side chains (with 8 to 12 carbon atoms) with methyl groups slightly affects electronic properties such as the HOMO-LUMO gap.

The same behaviour can be seen in analysing 2-unit conformations of compound Mc1 in Figure 5.25 (structures of patterns v1 and v2 are shown in Figure 5.24). Even if changing side chains, in most of conformations, the atoms that contribute most to the interactions between chains are localised in the backbones, while the lowest contributions still appear out of the polymer core.

In noncovalent interactions of Mc1 dimers, it is interesting to notice the participation of oxygen atoms, which connect benzodithiophene blocks to alkyl side chains. Despite a few cases, they presented low atomic contributions to the interplay of backbones. These alkoxy side chains seem to mainly cause steric hindrance, playing a relevant role in zipper mode in these dimers.

Finally, longer and branched side chains cause severe disturbances in backbone stacking, which may indicate less efficient packing of polymer chains. Therefore, they promote higher solubility in conjugated materials.

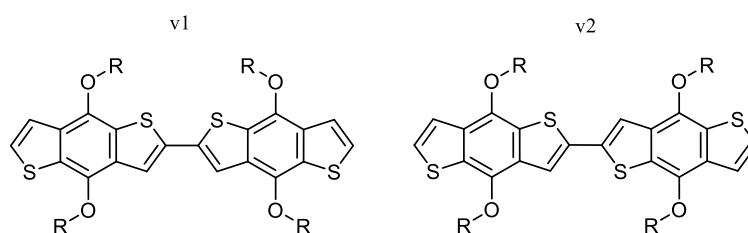


Figure 5.24 – Structure of Mc1 chains with 2 units, in which patterns v1 and v2 were modelled with sulphur atoms of adjacent unit aligned and in opposite side, respectively

To conclude this analysis about intermolecular interactions between conjugated polymers, attraction between heteroatoms and fused-aromatic rings and repulsion between side chains were what prevailed for energetic stability among these compounds, contrary to what is commonly reported by the scientific community that is the π - π stacking.

Even with this intense campaign of calculations, the potential for further research remains vast. Exploring models varying conjugation length, nature of blocks and types of side chains could yield even more definitive conclusions about the influence of σ and π bonds arrangement and intermolecular interactions between polymer chains on electronic properties. This exploration is crucial for the design of new molecules for high-efficiency electronic devices, such as solar cells, and should be a focus of future investigation in our field.

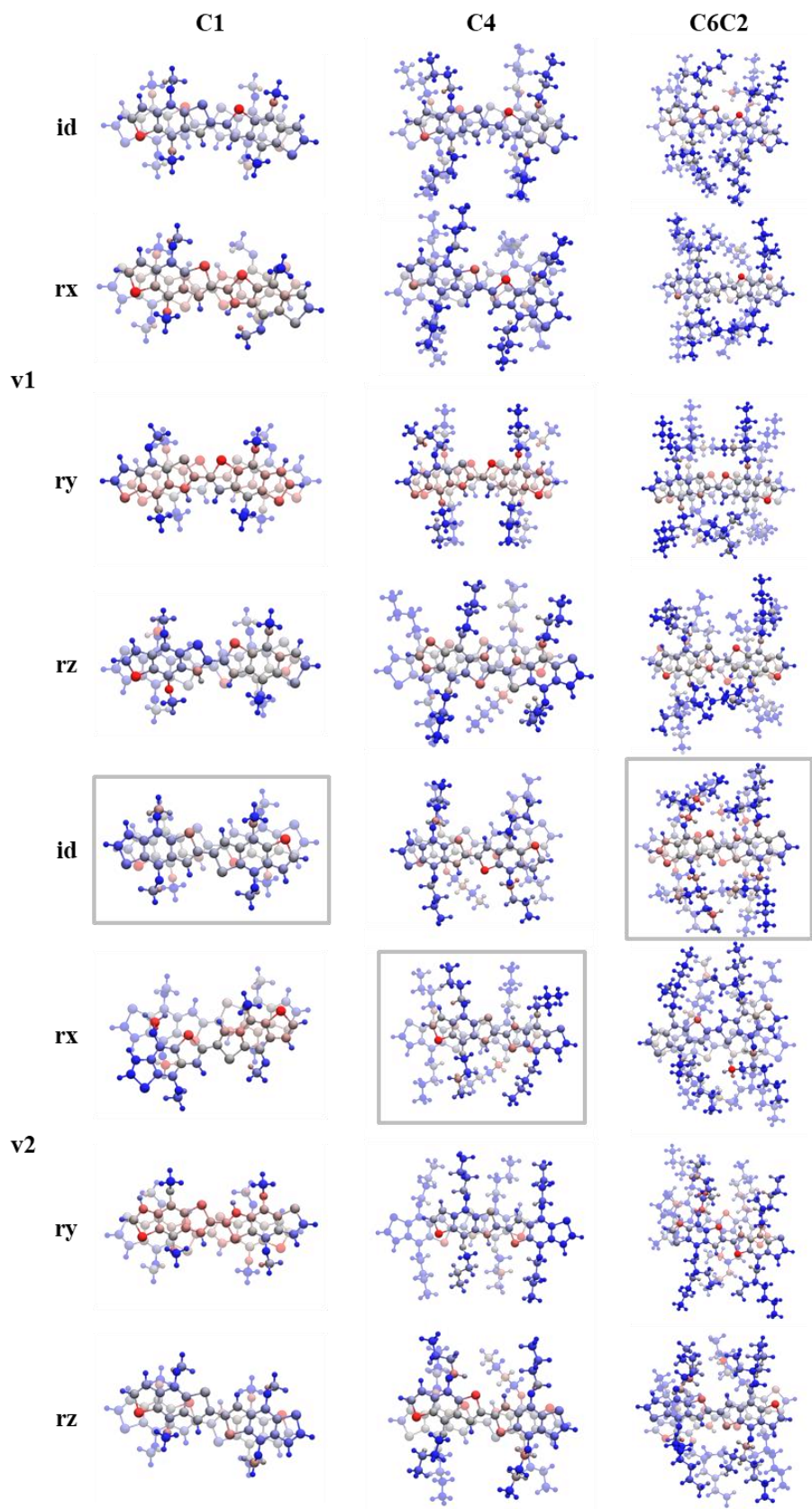


Figure 5.25 – Atomic contribution in the noncovalent interactions between Mc1 2-unit dimers varying side chains, highlighting the most stable one for each molecular system

References

- [1] H.T. Turan, O. Kucur, B. Kahraman, S. Salman, V. Aviyente, *Phys. Chem. Chem. Phys.* 20 (2018) 3581–3591.
- [2] P.-L.T. Boudreault, A. Michaud, M. Leclerc, *Macromolecular Rapid Communications* 28 (2007) 2176–2179.
- [3] L. Cartwright, A. Iraqi, Y. Zhang, T. Wang, D. G. Lidzey, *RSC Advances* 5 (2015) 46386–46394.
- [4] M.-C. Yuan, Y.-J. Chou, C.-M. Chen, C.-L. Hsu, K.-H. Wei, *Polymer* 52 (2011) 2792–2798.
- [5] T.-Y. Chu, J. Lu, S. Beaupré, Y. Zhang, J.-R. Pouliot, S. Wakim, J. Zhou, M. Leclerc, Z. Li, J. Ding, Y. Tao, *J. Am. Chem. Soc.* 133 (2011) 4250–4253.
- [6] L. Lu, L. Yu, *Advanced Materials* 26 (2014) 4413–4430.
- [7] Y. Li, *Acc. Chem. Res.* 45 (2012) 723–733.
- [8] L. Zhu, Y. Yi, Z. Wei, *J. Phys. Chem. C* 122 (2018) 22309–22316.
- [9] F. Franco Jr., *Molecular Simulation* 43 (2017) 222–227.
- [10] W. Liu, Q. Liu, C. Xiang, H. Zhou, L. Jiang, Y. Zou, *Surfaces and Interfaces* 26 (2021) 101385.
- [11] F.C. Franco, A.A.B. Padama, *Polymer* 97 (2016) 55–62.

Conclusions and perspectives

To improve photocurrent generation in organic photovoltaic cells, tuning optoelectronic properties of semiconductor materials, such as conjugated polymers, is essential. Investigating structural parameters is the key to understanding what drives intra and intermolecular interactions with respect to energetic stability.

Using DFT and TD-DFT to compute optoelectronic properties, it is possible to carry out a huge campaign of calculations for a such variety of molecular systems of this work (some with more than 3000 electrons). Even though *Ab initio* methods provide accurate results, they are limited to molecules with tens of electrons. Therefore, when the goal is to find tendencies of structure-property correlation, electron density-based methods provide substantial data for discussion.

In this work, we defined energy gaps and demonstrated their correlation with the polymer structure. Estimate the fundamental gap from the HOMO-LUMO gap is an incorrect approximation in DFT, which includes exchange-correlation to describe Kohn-Sham orbitals; therefore, diversified and overestimated exciton binding energy is found using this approach as it excludes the polymer structure relaxation as adding or removing an electron. However, we found a difference of around 0.30 eV between the energy of π and π^* molecular orbitals and the optical absorption independently of the molecular system (compound, conjugation length and side chain).

We could confirm that electronic properties of many conjugated compounds are impacted by optimizations done in the polymer backbone rather than on its alkyl side chains, showing the importance of π -bonds arrangement. Finding slight differences in optoelectronic properties as by replacing the methyl side chains with longer and branched ones, we proved that modelling molecular systems without long side chains reduces computational cost while preserving the accuracy of the electronic properties.

Indeed, conjugated molecules are not isolated in the material; it is necessary to include π - π interactions linking polymer chains and connect structural modifications with the electronic properties of these compounds. According to IGM analysis, we found that conjugated polymer structure is mainly stabilized due to the attraction between heteroatoms of one chain and fused-aromatic rings of the other and the repulsion of side chains, also called the steric effect.

To predict results as approximately as possible to experimental data, it would be necessary to calculate the optoelectronic properties using a robust basis set and/or considering the period boundary conditions (PBC) method, being aware of the limitations of using these strategies.

Furthermore, gaining insights into the electronic behaviour of the processed material by carrying out calculations for molecules in other conditions, such as organic solvents, could pave the way for their application in eco-friendly devices, inspiring hope for a more sustainable future.

Concerning molecular design, it is possible to apply modelling in steps, as done by Batagin and his team, by calculating the properties by adding each block instead of a repeating unit to have more detailed information on conjugation length evolution and its constraints. Replacing tail/head hydrogen atoms with a thiophene or benzene can also be done to avoid the board effect in visualization analysis.

The next approach to be applied in this research is to calculate the reorganization energy of the compounds, following Marcus' theory, to comprehend charge-transfer and energy loss processes in conjugated polymers, and finally, to have a more precise conclusion of semiconductor materials for high-efficiency solar cells.

Appendices

Appendix A

J Mater Sci (2024) 59:10888–10903

Computation & theory



A DFT bottom-up approach on non-fullerene acceptors: what makes highly efficient acceptors

Arthur V. Freitas¹, Gabriel G. B. Alves^{2,3,*}, Giovana M. A. Paschoal³, William Lafargue-dit-Hauret³, Roger C. Hiorns³, Didier Bégue³, and Augusto Batagin-Neto^{1,2}

¹ Institute of Sciences and Engineering, São Paulo State University (UNESP), Itapeva, SP 18409-010, Brazil

² School of Sciences, POSMAT, São Paulo State University (UNESP), Bauru, SP 17033-360, Brazil

³ Institut des Science Analytiques et Physico-Chimie pour l'Environnement et les Matériaux, CNRS Univ Pau and Pays Adour, 64000 Pau, France

Received: 13 December 2023

Accepted: 19 May 2024

Published online: 6 June 2024

© The Author(s), under exclusive licence to Springer Science+Business Media, LLC, part of Springer Nature, 2024

ABSTRACT

Over the last two decades, the demand for efficient and sustainable ways of producing electricity increased, motivating the development of high-efficient photovoltaic devices. In this context, bulk heterojunction organic solar cells based on non-fullerene acceptor (NFA) molecules have shown promising performances due to their versatility of synthesis, processing advantages, good stability to sunlight exposition, and high efficiencies (up to 18%). In particular, the high chemical versatility of these materials allows the synthesis of a number of distinct NFAs with varied performances, so that theoretical studies are essential to guide the prospection of new optimized compounds. In the present study, density functional theory-based (DFT) calculations were conducted to investigate the electronic structure of well-known building blocks of NFA, to assess how the fusion of these units influences the optoelectronic properties of the NFAs cores. The results allow us to identify relevant patterns for the design of optimized systems and define dominant sites for charge transfer processes, offering novel insights into the interpretation of operational mechanisms.

Introduction

Over the last decades it has been noticed a continuous endeavor to the development of efficient, clean and sustainable alternatives for the production of electricity. In this context, the use of solar cells has achieved great prominence, especially those based on organic materials [1, 2]. The first organic solar cells (OSCs)

were simplistic and presented very low power conversion efficiencies (PCE) [3–6]. Since then, various strategies have been employed to enhance the device's performance. One of the most notable approaches involves introducing a combination of different donor (D) and acceptor (A) materials into the active layer, resulting in the so-called bulk heterojunction solar cells (BHJSC) [7].

Handling Editor: Scott Beckman.

Address correspondence to E-mail: gabriel.gb.alves@unesp.br

Springer

<https://doi.org/10.1007/s10853-024-09811-1>

Content courtesy of Springer Nature, terms of use apply. Rights reserved.

Nowadays, the paradigm for A materials are the non-fullerene acceptors (NFAs). These small molecules are commonly based on block structures, presenting a strong optical absorption in the visible and near infrared (NIR) range [8–13]. NFAs pairs with specific D polymers such as poly[[4,8-bis[5-(2-ethylhexyl)-2-thienyl]benzo[1,2-b:4,5-b']dithiophene-2,6-diyl]-2,5-thiophenediyl][5,7-bis(2-ethylhexyl)-4,8-dioxo-4H,8H-benzo[1,2-c:4,5-c']dithiophene-1,3-diyl]] (PBDB-T) and its derivatives to build high PCE BHJSC [1, 14–18].

The first NFAs featured A-D-A block structures (acceptor–donor–acceptor structures based on specific fused/linked rings), in this context ITIC was one of the pioneering compounds, being successfully employed in BHJSCs [13]. These compounds have paved the way for new engineered materials, leading to the most recent A-DA'D-A based NFAs [18, 19]. The first member of this category of compounds was BZIC [20], and while it did not achieve an exceptional PCE (~ 6.3%), it marked a significant step in the right direction for the development of improved NFAs.

Starting from BZIC, three main aspects have been adjusted to produce new and improved NFAs: (1) changes on the DA'D core, (2) incorporation of side chains to the central cores and (3) insertion of accepting end-group (EG) on terminal sites [19, 21]. Some of these modifications lead to the widely used Y6 and its derivatives [19, 21]. In general, the attachment of appropriate side chains on the NFA cores can improve its solubility, leading to systems with enhanced fill factors (high molecular packing and more effective D–A interaction) [18, 19, 21–23]. The EG engineering can also play a relevant role on the π – π packing, improving the intermolecular interactions and charge transport processes [19]. In particular, this kind of chemical modification is associated with ITIC success and has been recently used for the search for high carrier mobility compounds [19, 24–27]. Finally, the core engineering (addition/modification of fused rings, mainly at A') has a historical relevance for the proposition of new efficient NFAs, being still a widely employed strategy for the design of new derivatives [19, 21, 22, 28–30].

However, despite the promising results associated with NFA-based BHJSC, there is still a relative scarcity of optimized donor–acceptor systems for application in devices, which defines an active research area. Most of the synthesis and engineering studies of new NFAs is still carried out by trial and error,

limiting the number of systems to be investigated. In addition, the performances of these materials are commonly estimated from devices' PCEs, hindering the investigation of intrinsic molecular features of the constituents.

In this context, here we report a series of density functional theory-based (DFT) calculations on structural, electronic and charge transfer properties of typical NFA building blocks. Fused rings and reduced cores of typical NFAs (ITIC, BZIC and Y6) were evaluated to investigate their influence on the electronic structure of these systems. Local reactivity analyses and donor–acceptor maps were also investigated to identify relevant sites/blocks for charge transfer processes. The results enable us to rationalize the contribution of building blocks to the formation of NFA frontier molecular orbitals (FMO) and their role in charge transport, providing new insights for interpreting the relevant mechanisms of operation.

Materials and methods

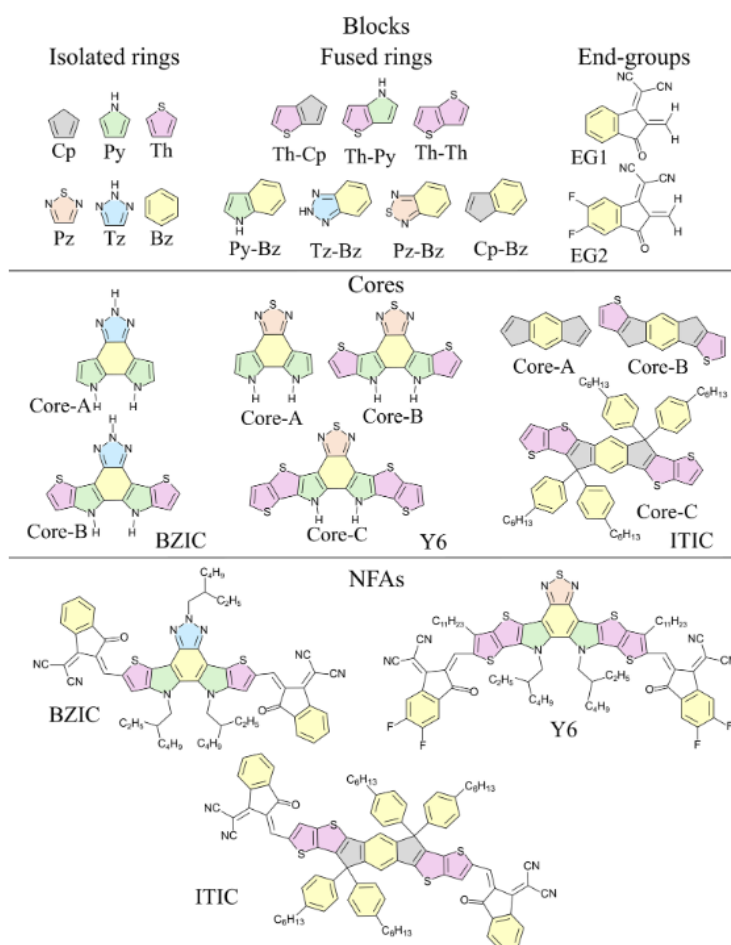
Materials

Figure 1 shows the structure of the NFAs evaluated in this report: Y6, BZIC and ITIC, as well as their basic building blocks (isolated and fused rings), reduced cores (symmetrical fused rings) and end-groups (EG1 (3-oxo-2,3-dihydro-1H-inden-1-ylidene malononitrile) and EG2 (5,6-difluoro-3-oxo-2,3-dihydro-1H-inden-1-ylidene)). The compounds have been selected based on a series of experimental results that evidence the relevance of such structures in high performance NFAs [6, 10–12].

Methodology

Two main aspects regarding NFAs electronic structure were evaluated: (1) the influence of different heterocyclic rings (thiophenes, pyrroles, furans, benzene, etc.) on the electronic structure of the central cores and (2) the effect of EG insertion on the electronic structure of NFA cores (EG1 and EG2). For this purpose, comparative studies were initially conducted considering different combinations of fused rings (see Fig. 1). Due to the hypothesis (1) the alkyl side chains become secondary in this study, as they are not part of the heterocyclic rings. Moreover, they were utterly disregarded as they have no influence on the FMO, CAFI nor MEP

Figure 1 Basic building blocks of NFAs: isolated/fused rings, end-groups (top), reduced cores (middle) and NFAs (bottom). Color was added for helping to distinguish the nature of each building ring.



(see the SI for details), and it is a common practice in the study of ramified organic compounds [31–33].

All the structures were designed with the aid of Molden 5.0 [34] and Avogadro [35] packages, being pre-optimized in a Hartree–Fock approach with the PM6 semi-empirical Hamiltonian (HF/PM6) [36]. The molecules were then fully optimized in the framework of the density functional theory (DFT), using B3LYP [37–40] hybrid exchange/correlation functional, and 6-31G(d) basis set on all the atoms. Although there are several newer and more robust

approaches for the hybrid exchange/correlation (XC) functionals (e.g., ω -B97x and derivatives) [41], being used for Y6 theoretical studies [24, 42–44], B3LYP is still used for NFA studies and has been successfully employed to evaluate several organic materials [24, 45–48]. Preliminary calculations conducted for the Y6 model with a distinct basis set and XC functional indicate the plausibility of our DFT/B3LYP/6-31G(d) approach for the evaluation of chemical reactivities (see the SI for details). Both, semi-empirical and DFT calculations, were conducted with the aid of the Gaussian 16 computational package [49].

Reactivity studies were conducted via condensed-to-atoms Fukui indexes (CAFI) [50]. These descriptors indicate how the local molecular electronic density changes when electrons are added or removed in/from the systems, enabling us to identify molecular sites that are likely to accept or donate electrons (i.e., outline electron donor and acceptor regions). Generally, three distinct CAFI can be defined: f^+ , f^- and f^0 , which describe the local reactivity of the molecule in relation to nucleophiles, electrophiles or free radicals, respectively. These indexes are calculated via finite differences of atoms' electronic populations, as described elsewhere [51] and have been successfully employed to investigate polymers and small molecules [48, 52–56].

The electronic population employed on the CAFI analysis were estimated via a DFT/B3LYP/6-31G(d) approach. Hirshfeld population analysis [57] was employed to avoid negative indexes [58, 59]. The color maps derived from these calculations were made with the aid of Jmol computational package [60] combined with a homemade Fortran 90 routine.

Additional analyses involving the energetic and spatial distribution of the frontier molecular orbitals (FMO) as well as molecular electrostatic potential map (MEP) were also conducted to interpret the influence of the distinct building blocks on the electronic structure of NFAs. The MEP calculations were conducted in the same framework as CAFI, however, considering CHelp charge partitioning scheme [61].

Donor–acceptor maps (DAM) were also employed to classify the electron donating (R_d) and electron accepting (R_a) ability of the blocks, as described elsewhere [62]. In general, low R_d values and high R_a values define compounds with high electron-acceptor and high electron-donor capacities, respectively.

Results and discussion

Frontier energy levels: the influence of rings fusion

Figures 2, 3 illustrate the comparative analysis between the FMO energy levels of NFA building blocks and the total density of states (DOS) of selected structures, respectively.

A naive comparison of the frontier energy levels of isolated and fused rings enables us to identify relevant patterns concerning the gap engineering

of NFAs. In general, the FMO levels of fused rings can be interpreted as a superposition of the building units, especially for Py–Bz (HOMO: Py and LUMO: Bz), Th–Py (HOMO: Py and LUMO: Th), Pz–Bz (HOMO: Bz and LUMO: Pz). The fusion of rings with similar FMO energies shifts the resulting electronic levels (downwards: HOMO / upwards: LUMO), reducing the band gap (oligomerization effect) as noticed in Th–Th, Pz–Bz, Bz–Cp, Tz–Bz and Th–Cp. An anomalous effect is noticed after the incorporation of the terminal end groups (EG n).

The most recent and widely used NFAs present A–DA'D–A block structure [16], as Y6. It is interesting to note that the results presented in Figs. 2, 3 are aligned with it. Note that Pz–Bz and Th–Py define A (low HOMO) and D (high LUMO) blocks, respectively, while EG1 and EG2 are strong acceptor units contributing to NFAs' LUMO. From Fig. 3, it is possible to identify the contribution of the different units to build the electronic structure of the core (A, B and C).

It is worth noting that the NFA energy gap is strongly affected by EG n species, with a significant shift of the resulting FMO levels to lower energies (stabilization of the whole system). These effects are apparently connected to the fact that the lowest energy occupied levels of the EGs are located in forbidden energy bands of the core rings, therefore defining a lower LUMO level. In a similar fashion, the final HOMO should follow the opposite path: core's rings build a HOMO that sits at EG's forbidden energy bands. However it is not exactly what happens, EG's energy gap added to the Core-C seems to be giving the core's HOMO some space to spread and relax, resulting in a final energy lower than what was expected.

Aiming to identify the dominance pattern of the building blocks in the frontier orbitals, it was sought to evaluate the spatial distribution of HOMO and LUMO from the NFAs. From the previous analysis, it is expected to see a HOMO that spreads over the core while LUMO concentrates more on the EGs. Figure 4 shows a representation of FMOs for the studied NFAs, Y6, ITIC and BZIC.

As previously discussed, the HOMO is mainly concentrated on the core, however a slight distribution is present on the EG region, which may be linked to the anomalous behavior of the NFA FMO formation after EG insertion. It is also important to

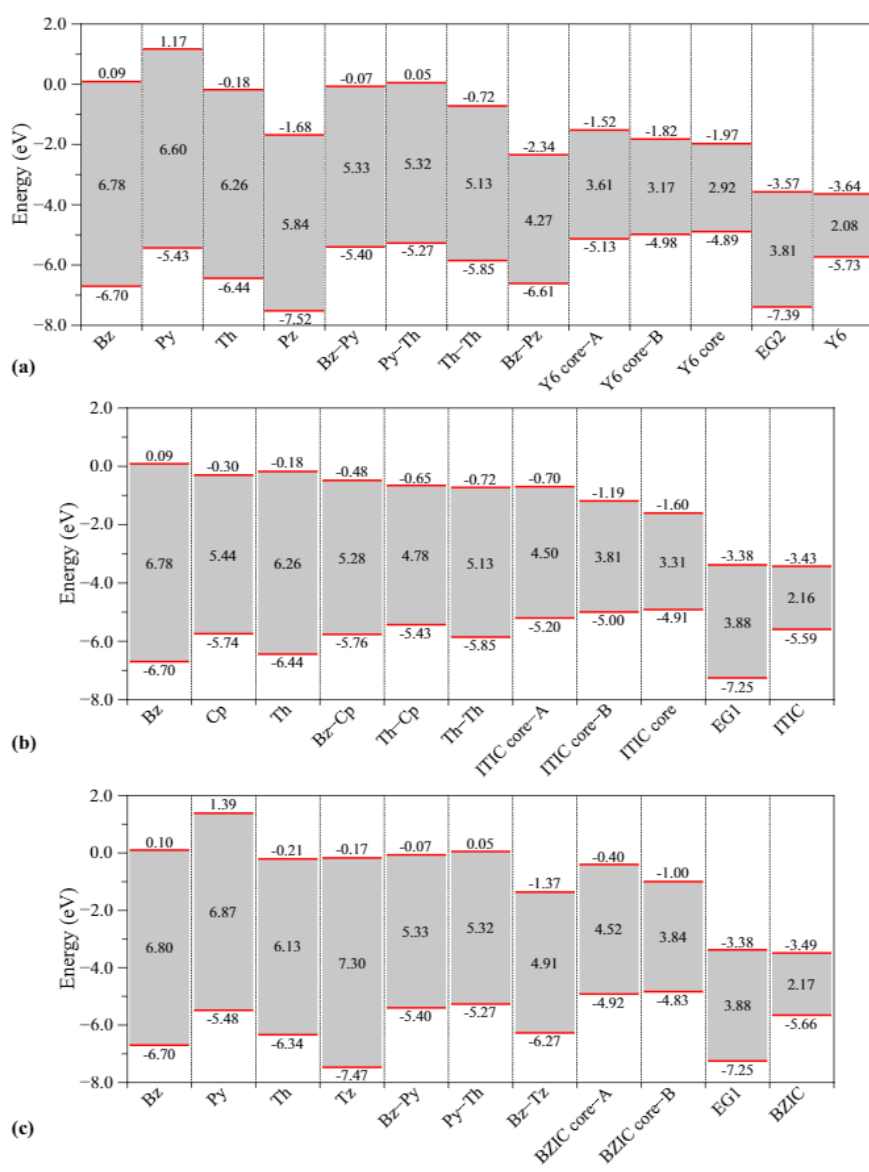


Figure 2 Frontier energy levels of **a** Y6, **b** ITIC and **c** BZIC building blocks.

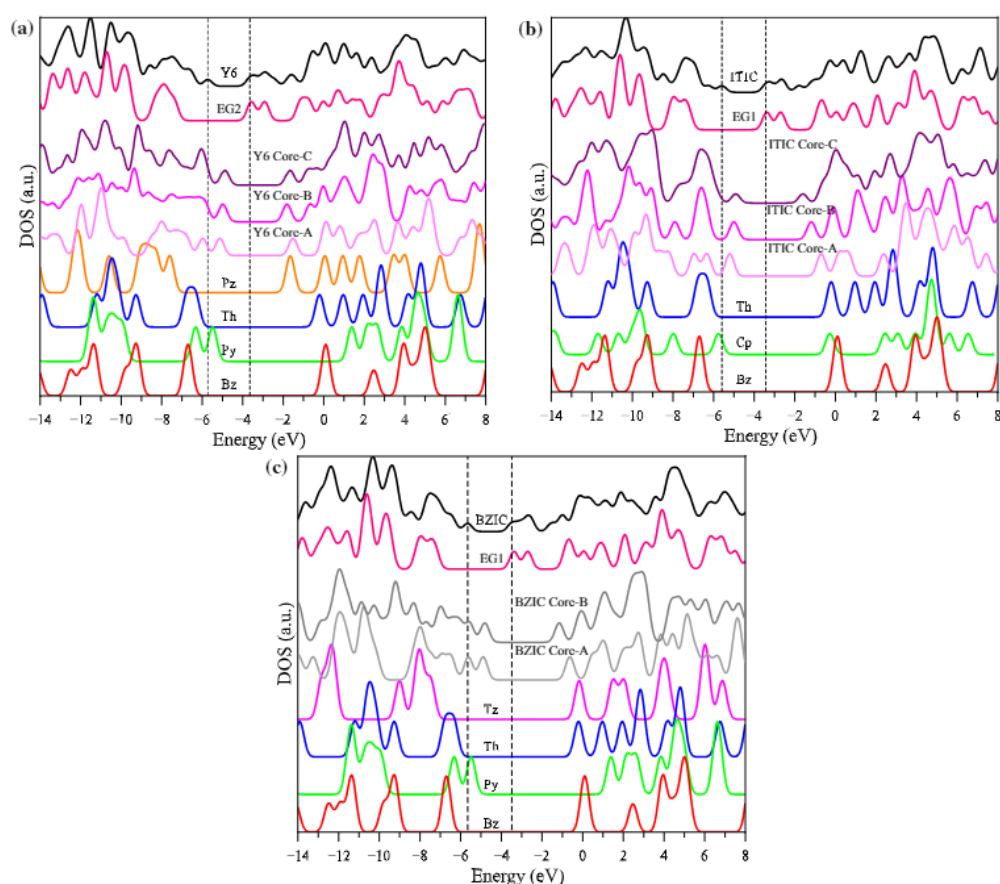


Figure 3 DOS of the NFAs building blocks. Dashed lines represent the position of HOMO and LUMO levels of the NFAs.

highlight that the LUMOs are much more concentrated over the core’s edges and EG.

It is interesting to note that the presence of EG dislocates HOMO. Such displacement is apparently linked to an inductive effect of the acceptor groups that promotes a greater delocalization of the electronic levels on the main structure, involving, especially the most external units close to the terminals (generally Th, Th–Th and Py–Th groups). This effect increases the contribution of the terminal groups to the HOMO: i.e., the HOMO of the NFA is dominated by the terminal blocks of the cores: $E_{\text{HOMO}}(\text{Th–Th}) = -5.854 \text{ eV}$,

$E_{\text{HOMO}}(\text{Py–Th}) = -5.267 \text{ eV}$, $E_{\text{HOMO}}(\text{Y6}) = -5.725 \text{ eV}$, $E_{\text{HOMO}}(\text{ITIC}) = -5.588 \text{ eV}$, $E_{\text{HOMO}}(\text{BZIC}) = -5.656 \text{ eV}$.

To get a deeper insight into the influence of isolated rings on the electronic properties of NFAs, we followed the evolution of FMO along our bottom-up approach, aiming to predict essential features of FMO based on the building blocks. The spatial distribution of FMOs of isolated and fused rings are shown in Fig. 5. The result of our analysis is depicted in Fig. 6 for Y6, similar analyses for BZIC and ITIC are reported in the Supporting Information.

Regarding the Y6 molecule, the fused Py and Th units have relevant contributions to the HOMO (see

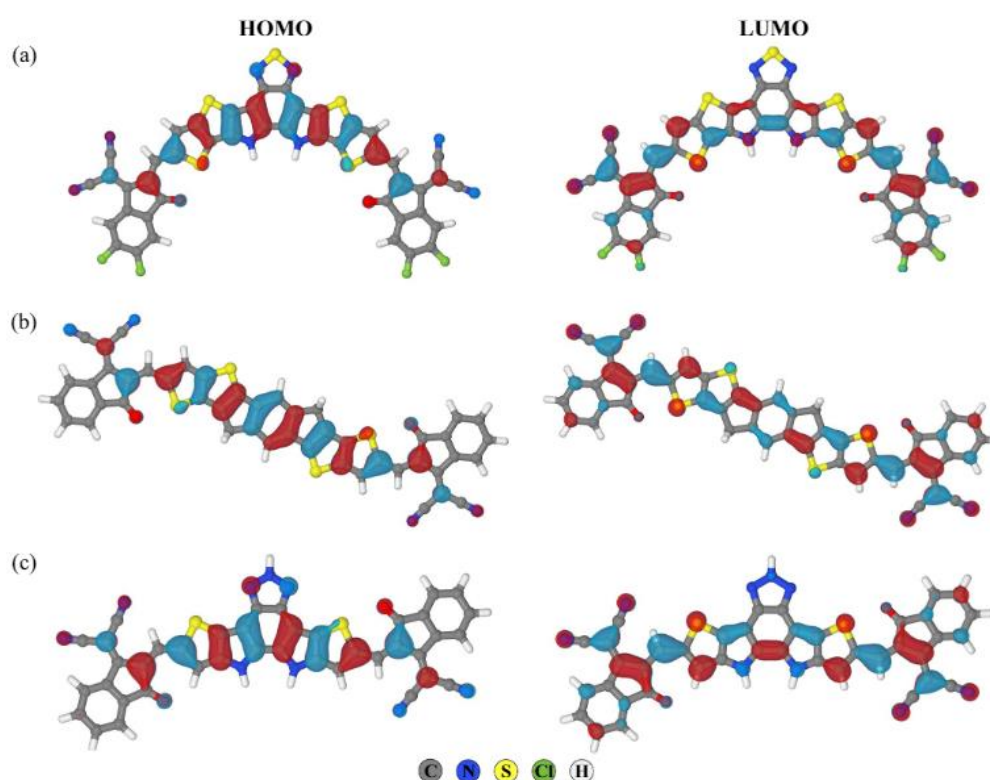


Figure 4 Frontier molecular orbitals of **a** Y6, **b** ITIC, **c** BZIC.

Fig. 6a). Unsurprisingly, one may see that the EGs units mainly contribute to the LUMO with a non-negligible participation of the Th unit. These conclusions are echoed in the analysis of the energy levels (see Fig. 6b) and further reinforce the idea that the participation of fused-ring units alone would be sufficient to predict the spatial distributions of the NFAs' FMOs. Similar analyses and conclusions can be made for the ITIC and BZIC (see Supporting Information).

Local reactivity indexes and electrostatic potential map

Figures 7, 8, 9, 10, 11 and 12 present colored maps of the local chemical reactivities (CAFI and MEP) of NFAs' building blocks. Red and blue regions define, respectively, reactive and non-reactive sites identified

by CAFIs, and negative and positive potentials for MEPs. The CAFIs' color scales are normalized for each molecule, while a same scale was employed for MEP in all the systems (it is presented in Fig. 7 and omitted for the others Figs for simplicity).

About the isolated rings, one may notice a high similarity between f^+ and f^- indexes, except for Tz which shows complementary spatial responses. In detail, Py and Cp are very similar, presenting high reactivity on the neighboring of the heteroatoms (or CH₂ for Cp). Pz and Th also show similar results, with a highly reactive sulfur. The MEPs evidence positive potentials on H atoms, especially noticeable for N–H bonds, and negative potential on N atoms (without H). Negative potentials are also noticed on the double bonds.

 Springer

Content courtesy of Springer Nature, terms of use apply. Rights reserved.

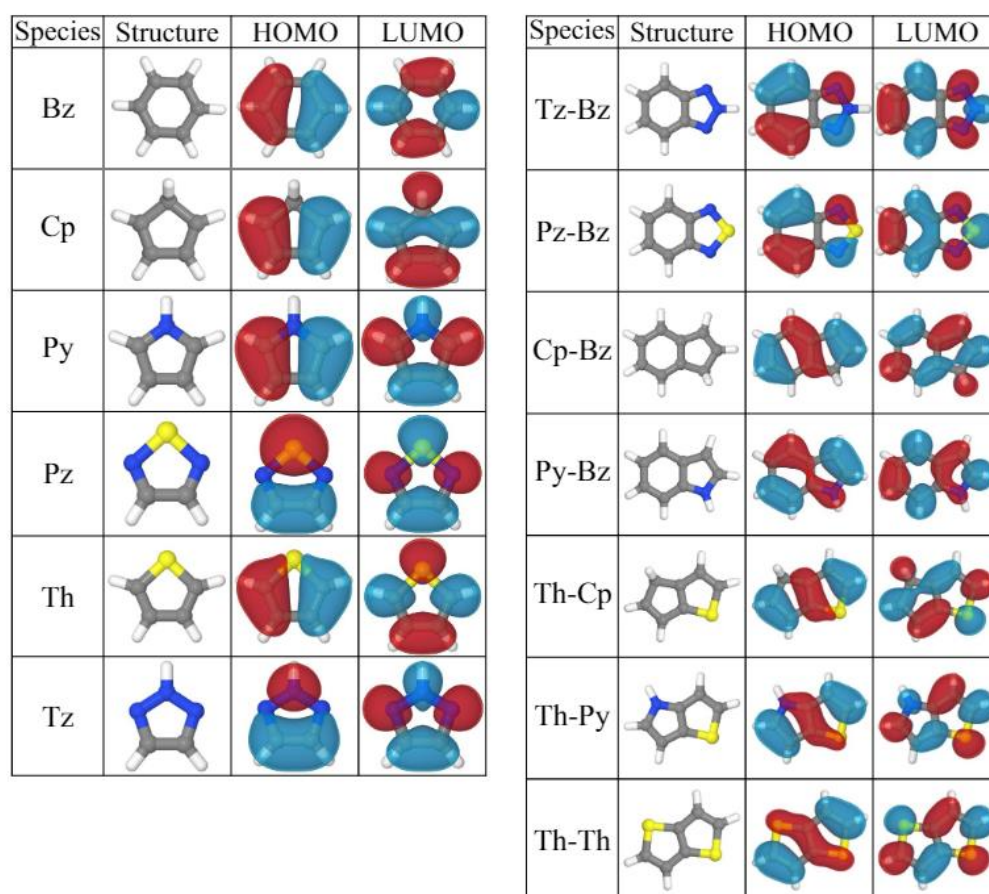


Figure 5 FMO of isolated and fused rings.

Within the fused rings it can be noticed the following reactivity dominance order in the structures: $\text{Th} > \text{Cp} > \text{Bz} \sim \text{Tz} \sim \text{Py}$, which is better evidenced by the f^{β} indexes. Again it is observed an intense negative electrostatic potential over the N (without H), S and double bonds, while positive potentials are centered on H atoms (especially for those participating of N–H bonds).

Beyond the aforementioned dominance effect noticed in fused rings, Fig. 9 illustrates the role of the core's symmetry on the reactivity of the NFAs, which has a great impact on the local reactivity. For BZIC

core A, we observe high reactivity over Tz units in relation to nucleophiles, while Py dominates the reactivity for electrophilic species. The insertion of Th units, however, drives the local reactivity (f^{α} and f^{β}) of the system to the terminal groups (over Th), with some participation of Tz in f^{α} . Concerning ITIC, both intermediate cores (core A and B) present chemical reactivities at the termination units (for f^{α} and f^{β}), which are spread out between adjacent Th units in ITIC core C. Finally, for Y6 core A, it is noticed high reactivity over Pz and Py units in relation to

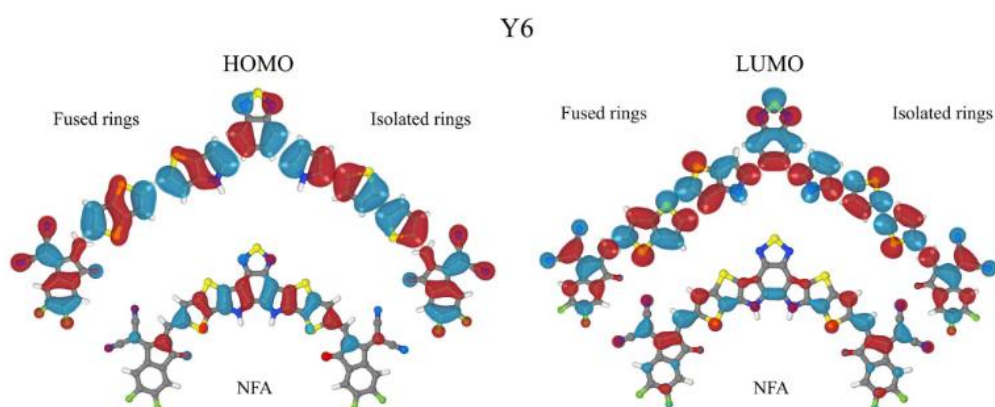


Figure 6 FMO spatial distribution of Y6 and from Y6's building blocks as fused and isolated rings, evidentiating their individual contributions.

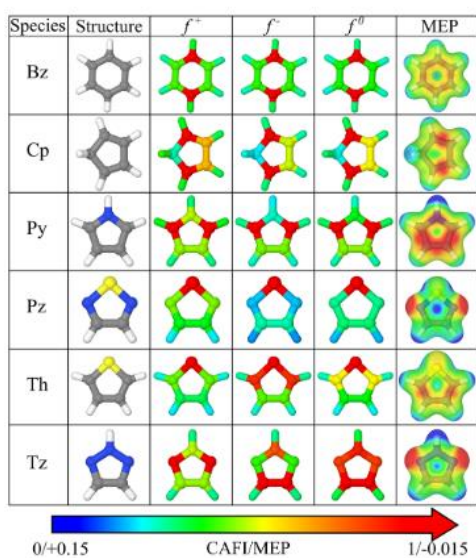


Figure 7 CAFE and MEP results of the isolated rings.

nucleophiles and electrophiles, respectively. A dominance of Pz is noticed in more extended cores, which is dissonant with the previously observed dominance

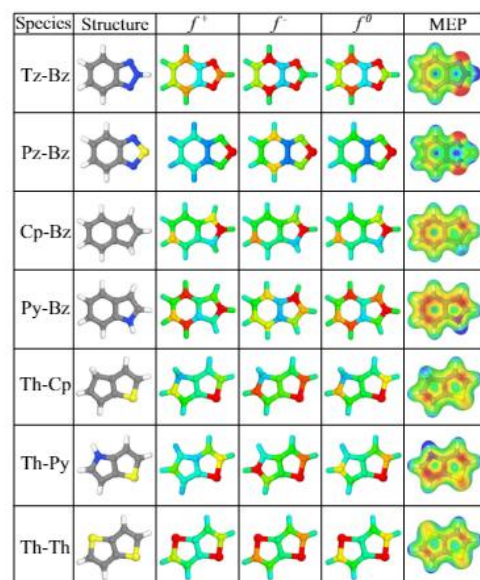


Figure 8 CAFE and MEP results of the fused rings.

order. All of the cores show the same MEP pattern obtained for the fused rings.

Figure 10 illustrates the local reactivity of isolated acceptor groups EG1 and EG2 (passivated with H atoms).

Species	Structure	f^+	f^-	f^0	MEP
BZIC Core-A					
BZIC Core-B					
ITIC Core-A					
ITIC Core-B					
ITIC Core-C					
Y6 Core-A					
Y6 Core-B					
Y6 Core-C					

Figure 9 CAFI and MEP results of the in construction NFA (cores).

Species	Structure	f^+	f^-	f^0	MEP
EG1					
EG2					

Figure 10 CAFI and MEP results of the completed acceptors used.

EG1 and EG2 present similar MEPs and CAFIs, presenting similar roles when added to NFAs' cores (as indeed noticed for the FMO levels and spatial distributions). In general, a high reactivity is observed over these the N atoms of C=N side branches. These sites also present high electron density (negative potential), over the O atoms (and fluorine to a lesser extent in EG2). Another important aspect is the similarity between f^+ and f^- , with high reactivity on N

	BZIC	ITIC	Y6
Structure			
f^+			
f^-			
f^0			
MEP			

Figure 11 CAFI and MEP results of the NFA molecules.

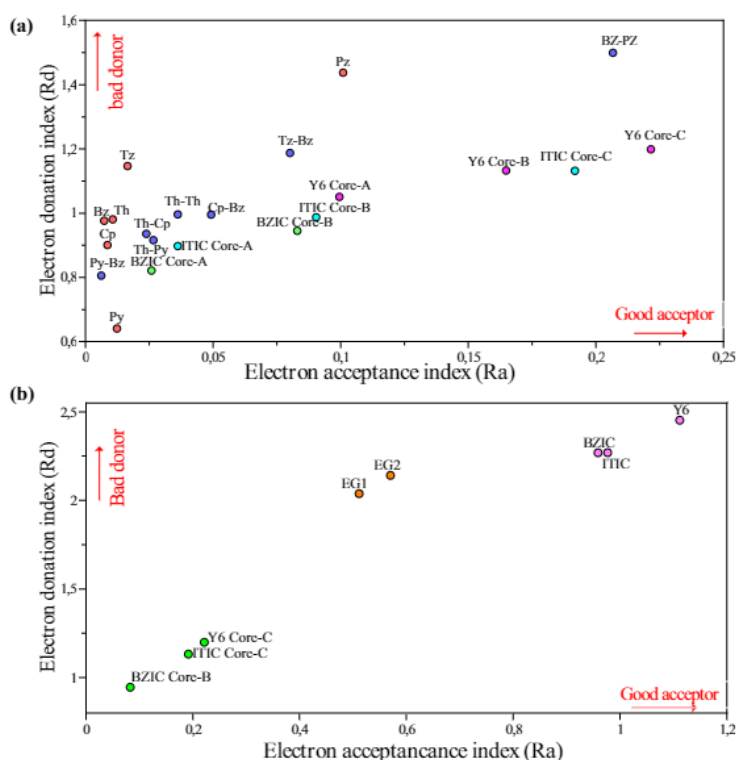
atoms and slight differences in relation to the secondary reactivity on C atoms that connect to the NFA cores.

Lastly, Fig. 11 illustrates the complete structure of the studied NFAs. In particular, for these structures, f^+ and f^- indexes allow us to identify relevant electrons transfer routes, indicating which sites are prone to receive or donate electrons, respectively.

For all the structures it is noticed that the N atom of the EG n branches acts as the dominant electron acceptor center of the molecules, which is compatible with the major contributions of this block on the LUMO of these structures. Such results suggest that the electron insertion in NFA occurs via EG n terminations, indicating that efficient charge D–A transfer processes should take place when donor materials (present into the solar cell active layer) effectively interact with such centers.

The electron donation processes (indicated by f^-) are spread out on the NFA cores, with still a significant contribution of the CN terminal groups of EG n . These centers are relevant to underline the charge transport routes in A domains, involving electrons transfer processes between adjacent NFAs. In this sense, effective electron currents at the acceptor domains of the OSC are supposed to take place in cases where the central regions of NFAs (with high f^-) effectively interact with their terminal CN groups (high f^-). This configuration has been indeed

Figure 12 DAM obtained for **a** isolated rings, considered fused rings, cores (intermediate and complete); **b** complete cores, branches and the selected NFAs.



experimentally observed for Y6 [44, 63, 64], which allows us to understand the high performance of these systems.

In particular, for Y6 it is noticed a relevant role to the center block (Pz) in relation to both descriptors, f^+ and f^- . In relation to f^+ , such an effect suggests the existence of 2 distinct electron acceptance routes, involving not only the acceptor group, but also the central structure, that can result in improved short circuit currents. On the other hand, the high f^- value indicates this center relevance in the charge transportation process inside the acceptors domain present in a BHJ-OSC.

Exciton binding energy

One infamous characteristic of the organic semiconductors are their high exciton binding energy (E_{BE}) compared to the inorganic ones. This problem is usually avoided by focusing on D–A intersection

dissociation of excitons, by cleverly engineering a type II heterojunction [18]. In spite of this, smaller E_{BE} leads to more efficient exciton dissociation inside the D or A material, which may increase the overall PCE. The E_{BE} was studied to verify if there is any kind of evolution as the building blocks grow to a complete NFA.

The E_{BE} was easily estimated as the difference between the electronic bandgap (ΔE_{LH}) and the optical bandgap ($\Delta E_{optical}$) [65]. The ΔE_{LH} is directly calculated from the FMO energies obtained from single point calculations, while $\Delta E_{optical}$ is obtained by calculating the first excited state in a TDDFT framework. Both calculations considered the same basis set and hybrid exchange/correlation functional (B3LYP/6-31G (d,p)). Table 1 presents these results for the EG, NFA-Cores and NFAs. These results for smaller building blocks can be found in Table S1.

Here it is interesting to notice that all the NFA present smaller E_{BE} than their cores, and in fact the energy

Table 1 ΔE_{LH} , $\Delta E_{\text{optical}}$ and E_{BE} for EGs, cores and NFAs

Structure	ΔE_{LH} (eV)	$\Delta E_{\text{optical}}$ (eV)	E_{BE} (eV)
EG1	3.88	3.28	0.60
EG2	3.81	3.33	0.48
BZIC-Core-A	4.26	3.82	0.44
BZIC-Core-B	3.66	3.38	0.28
BZIC	2.17	2.01	0.16
ITIC-Core-A	4.53	4.25	0.28
ITIC-Core-B	3.85	3.62	0.23
ITIC-Core-C	3.34	3.04	0.30
ITIC	2.16	1.96	0.20
Y6-Core-A	3.78	3.20	0.58
Y6-Core-B	3.33	2.83	0.50
Y6-Core-C	3.08	2.65	0.43
Y6	2.08	1.89	0.19

gets smaller as Th units are fused to the cores. The exception is ITIC-Core-C that had a spike in E_{BE} before getting smaller again as the complete NFA. One explanation for this could be the addition of the Bz rings over the structure. This would mean Th and the EGs help reduce the binding energy, while unfused Bz are detrimental to it.

Moreover, this result might suggest the incorporation of more Th units to the core. In fact, a study from Qiu and Zheng [43] suggested a modified Y6 that contains extra Th units. It was studied the modified Y6 with 2 and 4 extra fused Th, 2 bonded Th, and a ThTh fused structure bonded to the core. In accordance with our study, the observed FMO energy does not show great changes. Conversely, these modifications showed enhancement in some key parameters, such as charge transfer rate, electron mobility, UV-vis absorption spectra. The authors, however, have not studied the exciton binding energy for the modified Y6.

Donor acceptor map (DAM)

Figure 12 summarizes the data related to the compound's donation/acceptance capabilities. Generally, high values of R_{a} index define the compounds as good electron acceptors, while low values of R_{d} are associated with good donors.

In general, among the studied isolated rings (red circles in Fig. 12a) we notice a clear order of electron donor capability $\text{Py} > \text{Cp} > \text{Bz} > \text{Th} > \text{Tz} > \text{Pz}$, and very similar electron acceptance properties. Pz, in

particular, presents the highest R_{d} and slight superior R_{a} values, which defines this unit as the worst donor and the best electron acceptor. Py, on the other hand, presents the lowest R_{d} , being defined as the best donor unit. The other rings show similar distributions in the DAM.

Considering the fused rings (blue circles in Fig. 12a), it is noticed that R_{d} tends to assume intermediate values among the constituent rings, with the exception of Pz-Bz and Tz-Bz. The acceptance capability is intensified for the majority of the fused structures, except for Py-Bz.

A linear (positive) shift tendency for R_{d} as a function of R_{a} is observed for more extended structures (cores), showing similar angular coefficients to each other (i.e., similar rate of change of R_{d} as function of R_{a}). Such an effect turns the resulting structures into better acceptors and worse donors than their building blocks. Particularly the Y6 and BZIC cores, which present a similar acceptance capability to Bz-Pz and Bz-Tz, respectively, with the donor capability obtained by the mean value of all the constituent units. Although ITIC does not show units of greater acceptance capability, this structure also shows a significant increase of the R_{a} value in relation to its basic building blocks, which can be assigned to the enhanced conjugation length. Such results suggest that the fusing rings with high R_{d} with symmetric resonant structures such as Bz can lead to NFA cores of great interest.

From Fig. 12b it is clear the drastic effect of adding the acceptor group to the NFA core. Such groups are defined as great acceptors, and their insertion in the core results in structures with optimized acceptance capabilities (the complete NFA molecule).

In particular, it is interesting to note the improved acceptor properties of Y6. Note that, such an improvement is accompanied by a slight reduced electron donation capability of this compound in relation to the others (which could hinder the electron transfer processes in A domains), that can be compensated by the presence of additional electron transfer routes (see Fig. 11) in this NFA.

Conclusions

In this report, we evaluated and compared the electronic and reactivity properties of typical building blocks of NFAs to identify their influence

on the electronic structures of acceptors, such as Y6, BZIC, and ITIC.

Our results demonstrate that the frontier electronic energy levels of NFAs' cores can be estimated through the analysis of FMOs superposition of the building blocks. However, the insertion of EG n led to drastic changes, predominantly affecting the resulting LUMO with some interference in the HOMO.

The studies on local reactivity allowed us to pinpoint the most relevant molecular sites for electron transfer processes. EG n plays a significant role in electron acceptance, particularly through the CN terminal groups. Notably, Y6 presented additional electron acceptance routes that could enhance charge transfer processes.

Donor–acceptor maps validated the observations based on FMOs, highlighting the enhancement of electron acceptance capabilities in extended structures at the expense of donation ones, a trend that is intensified by the addition of EG n .

In summary, these findings enable the identification of significant patterns for designing optimized systems and delineating relevant sites for charge transfer processes. They provide novel insights into the operational mechanisms of NFA-based BHJ-OSCsfig

Acknowledgements

The authors thank the Brazilian National Council for Scientific and Technological Development (CNPq) (Grant 310390/2021-4 (AB-N), 1566-1/2020-PIBIC and 3940-4/2021-PIBIC (AVF)), Pro-rectory for research (PROPe) UNESP (8301-16/2022-ICEx-UNESP (AVF)), the Coordination for the Improvement of Higher Education Personnel (CAPES) (Grants 88887.817533/2022-00 CAPES-Proex and 88887.695844/2022-00 CAPES-PrInt (GGBA)), the Brazilian Financial Agency for Studies and Projects (FINEP) (01.22.0289.00–0034/21 (AB-N)), São Paulo Research Foundation (FAPESP) (Grant 20/12356-8 (AB-N)) and the European Union's Horizon 2020 Research and Innovation program under the Marie Skłodowska-Curie grant agreement N 945416 from for financial support (GMAP). This research was also supported by resources supplied by the Center for Scientific Computing (NCC/Grid-UNESP) of the São Paulo State University (UNESP) and Grand Equipement National de Calcul Intensif—Institute for Development and

Resources in Intensive Scientific Computing (GENCI-IDRIS) (Grant 2022-102485).

Author contributions

AVF: Conceptualization, Formal Analysis, Investigation, Validation, Visualization, Writing—Original Draft; GGBA: Conceptualization, Formal Analysis, Investigation, Validation, Visualization, Writing—Review & Editing; GMAP: Validation, Writing—Review and Editing; WL-H: Validation, Visualization, Writing—Review and Editing; RH: Funding Acquisition, Supervision, Writing—Review and Editing; DB: Funding Acquisition, Resources, Software, Supervision, Validation, Visualization, Writing—Review & Editing; AB-N: Conceptualization, Formal Analysis, Funding Acquisition, Investigation, Methodology, Project Administration, Resources, Software, Supervision, Validation, Visualization, Writing—Original Draft, Writing—Review and Editing. All authors have read and agreed to the published version of the manuscript.

Data availability

The data and software's used here may be provided upon request.

Declarations

Conflict of interest The authors declare that they have no known competing financial interests or personal relationships that could have appeared to influence the work reported in this paper.

Supplementary Information The online version contains supplementary material available at <https://doi.org/10.1007/s10853-024-09811-1>.

References

- [1] Zheng Z, Wang J, Bi P et al (2022) Tandem organic solar cell with 20.2% efficiency. *Joule* 6:171–184. <https://doi.org/10.1016/j.joule.2021.12.017>

- [2] Liu Y, Liu B, Ma C-Q et al (2022) Recent progress in organic solar cells (Part I material science). *Sci China Chem* 65:224–268. <https://doi.org/10.1007/s11426-021-1180-6>
- [3] Wöhrlé D, Meissner D (1991) Organic solar cells. *Adv Mater* 3:129–138. <https://doi.org/10.1002/adma.1991030303>
- [4] Chamberlain GA (1983) Organic solar cells: a review. *Sol Cells* 8:47–83. [https://doi.org/10.1016/0379-6787\(83\)90039-X](https://doi.org/10.1016/0379-6787(83)90039-X)
- [5] Morel DL, Ghosh AK, Feng T et al (1978) High-efficiency organic solar cells. *Appl Phys Lett* 32:495–497. <https://doi.org/10.1063/1.90099>
- [6] Ghosh AK, Feng T (1978) Merocyanine organic solar cells. *J Appl Phys* 49:5982–5989. <https://doi.org/10.1063/1.324566>
- [7] Yu G, Gao J, Hummelen JC et al (1995) Polymer photovoltaic cells: enhanced efficiencies via a network of internal donor-acceptor heterojunctions. *Science* 270:1789–1791. <https://doi.org/10.1126/science.270.5243.1789>
- [8] Hou J, Inganäs O, Friend RH, Gao F (2018) Organic solar cells based on non-fullerene acceptors. *Nat Mater* 17:119–128. <https://doi.org/10.1038/nmat5063>
- [9] Jin K, Deng C, Zhang L et al (2018) A heptacyclic carbon-oxygen-bridged ladder-type building block for A-D-A acceptors. *Mater Chem Front* 2:1716–1719. <https://doi.org/10.1039/C8QM00285A>
- [10] Xiao Z, Liu F, Geng X et al (2017) A carbon-oxygen-bridged ladder-type building block for efficient donor and acceptor materials used in organic solar cells. *Sci Bull* 62:1331–1336. <https://doi.org/10.1016/j.scib.2017.09.017>
- [11] Xiao Z, Yang S, Yang Z et al (2019) Carbon-oxygen-bridged ladder-type building blocks for highly efficient nonfullerene acceptors. *Adv Mater* 31:1804790. <https://doi.org/10.1002/adma.201804790>
- [12] Yan C, Barlow S, Wang Z et al (2018) Non-fullerene acceptors for organic solar cells. *Nat Rev Mater* 3:1–19. <https://doi.org/10.1038/natrevmats.2018.3>
- [13] Lin Y, Wang J, Zhang Z-G et al (2015) An electron acceptor challenging fullerenes for efficient polymer solar cells. *Adv Mater* 27:1170–1174. <https://doi.org/10.1002/adma.201404317>
- [14] Liu Q, Jiang Y, Jin K et al (2020) 18% Efficiency organic solar cells. *Sci Bull* 65:272–275. <https://doi.org/10.1016/j.scib.2020.01.001>
- [15] Li S, Ye L, Zhao W et al (2018) A wide band gap polymer with a deep highest occupied molecular orbital level enables 14.2% efficiency in polymer solar cells. *J Am Chem Soc* 140:7159–7167. <https://doi.org/10.1021/jacs.8b02695>
- [16] Wei Q, Liu W, Leclerc M et al (2020) A-DA'D-A non-fullerene acceptors for high-performance organic solar cells. *Sci China Chem* 63:1352–1366. <https://doi.org/10.1007/s11426-020-9799-4>
- [17] Yuan J, Zhang Y, Zhou L et al (2019) Single-junction organic solar cell with over 15% efficiency using fused-ring acceptor with electron-deficient core. *Joule* 3:1140–1151. <https://doi.org/10.1016/j.joule.2019.01.004>
- [18] Shoaee S, Luong HM, Song J et al (2023) What we have learnt from PM6:Y6. *Adv Mater* 2302005:202302005. <https://doi.org/10.1002/adma.202302005>
- [19] Lu B, Wang J, Zhang Z et al (2021) Recent progress of Y-series electron acceptors for organic solar cells. *Nano Sci* 2:2029–2039. <https://doi.org/10.1002/nano.202100036>
- [20] Feng L, Yuan J, Zhang Z et al (2017) Thieno[3,2-*b*]pyrrolo-fused pentacyclic benzotriazole-based acceptor for efficient organic photovoltaics. *ACS Appl Mater Interfaces* 9:31985–31992. <https://doi.org/10.1021/acsami.7b10995>
- [21] Yuan J, Zou Y (2022) The history and development of Y6. *Org Electron* 102:106436. <https://doi.org/10.1016/j.orgel.2022.106436>
- [22] Hai J, Zhao W, Luo S et al (2021) Vinylene π -bridge: a simple building block for ultra-narrow bandgap nonfullerene acceptors enable 14.2% efficiency in binary organic solar cells. *Dyes Pigm* 188:109171. <https://doi.org/10.1016/j.dyepig.2021.109171>
- [23] Li J, Feng L, Cai F et al (2019) Synthesize non-fullerene acceptors of five fused-ring by modifying side chain. *Sol Energy* 191:566–573. <https://doi.org/10.1016/j.solener.2019.09.013>
- [24] Xiang Y, Xu C, Zheng S (2023) Increasing charge carrier mobility through modifications of terminal groups of Y6: a theoretical study. *Int J Mol Sci* 24:8610. <https://doi.org/10.3390/ijms24108610>
- [25] Hai J, Li L, Song Y et al (2023) Ending group modulation of asymmetric non-fullerene acceptors enables efficient green solvent processed organic solar cells. *Chem Eng J* 462:142178. <https://doi.org/10.1016/j.cej.2023.142178>
- [26] Cai J, Zhang X, Guo C et al (2021) Asymmetric and halogenated fused-ring electron acceptor for efficient organic solar cells. *Adv Funct Mater* 31:2102189. <https://doi.org/10.1002/adfm.202102189>
- [27] Akram SJ, Iqbal J, Ans M et al (2022) Designing of the indacenodithiophene core-based small molecules for optoelectronic applications: a DFT approach. *Sol Energy* 237:108–121. <https://doi.org/10.1016/j.solener.2022.03.072>
- [28] Zhang Z, Li D, Zhang H et al (2022) An asymmetric A-DA'D- π -A type non-fullerene acceptor for

- high-performance organic solar cells. *J Mater Chem C* 10:2792–2799. <https://doi.org/10.1039/D1TC04425G>
- [29] He Y, Alem S, Lu J et al (2023) A new non-fullerene acceptor based on an asymmetric electron-deficient core for indoor organic photovoltaic cells. *Mater Chem Phys* 306:128036. <https://doi.org/10.1016/j.materchemphys.2023.128036>
- [30] Zahid S, Rasool A, Zahid S et al (2022) Designing easily synthesizable non-fused small acceptors for organic solar cells. *Sol Energy* 246:23–35. <https://doi.org/10.1016/j.solener.2022.09.027>
- [31] Galindo LA, Gozzi G, Fugikawa-Santos L et al (2020) Investigation of the polymer-salt interactions in polymeric light emitting electrochemical cells: electronic structure calculations and experimental studies. *Org Electron* 79:105629. <https://doi.org/10.1016/j.orgel.2020.105629>
- [32] Benatto L, Souza JPA, Das Neves MFF et al (2023) Enhancing the chemical stability and photovoltaic properties of highly efficient nonfullerene acceptors by chalcogen substitution: insights from quantum chemical calculations. *ACS Appl Energy Mater* 6:11732–11744. <https://doi.org/10.1021/acsaem.3c02371>
- [33] Collado-Fregoso E, Boufflet P, Fei Z et al (2015) Increased exciton dipole moment translates into charge-transfer excitons in thiophene-fluorinated low-bandgap polymers for organic photovoltaic applications. *Chem Mater* 27:7934–7944. <https://doi.org/10.1021/acs.chemmater.5b02948>
- [34] Schaftenaar G, Noordik JH (2000) Molden: a pre- and post-processing program for molecular and electronic structures. *J Comput Aided Mol Des* 14:123–134
- [35] Hanwell MD, Curtis DE, Lonie DC et al (2012) Avogadro: an advanced semantic chemical editor, visualization, and analysis platform. *J Cheminf* 4:1–7
- [36] Stewart JJP (2007) Optimization of parameters for semiempirical methods V: modification of NDDO approximations and application to 70 elements. *J Mol Model* 13:1173–1213. <https://doi.org/10.1007/s00894-007-0233-4>
- [37] Becke AD (1993) Density-functional thermochemistry. III. The role of exact exchange. *J Chem Phys* 98:5648–5652. <https://doi.org/10.1063/1.464913>
- [38] Lee C, Yang W, Parr RG (1988) Development of the Colle-Salvetti correlation-energy formula into a functional of the electron density. *Phys Rev B* 37:785–789. <https://doi.org/10.1103/PhysRevB.37.785>
- [39] Stephens PJ, Devlin FJ, Chabalowski CF, Frisch MJ (1994) Ab initio calculation of vibrational absorption and circular dichroism spectra using density functional force fields. *J Phys Chem* 98:11623–11627. <https://doi.org/10.1021/j100096a001>
- [40] Vosko SH, Wilk L, Nusair M (1980) Accurate spin-dependent electron liquid correlation energies for local spin density calculations: a critical analysis. *Can J Phys* 58:1200–1211. <https://doi.org/10.1139/p80-159>
- [41] Chai J-D, Head-Gordon M (2008) Long-range corrected hybrid density functionals with damped atom–atom dispersion corrections. *Phys Chem Chem Phys* 10:6615. <https://doi.org/10.1039/b810189b>
- [42] Kuppang G, Chen XK, Brédas JL (2021) Molecular packing of non-fullerene acceptors for organic solar cells: distinctive local morphology in Y6 vs ITIC derivatives. *Mater Today Adv* 11:100154. <https://doi.org/10.1016/j.mtadv.2021.100154>
- [43] Qiu W, Zheng S (2021) Designing and screening high-performance non-fullerene acceptors: a theoretical exploration of modified Y6. *Sol RRL* 5:2100023. <https://doi.org/10.1002/solr.202100023>
- [44] Zhang G, Chen X-K, Xiao J et al (2020) Delocalization of exciton and electron wavefunction in non-fullerene acceptor molecules enables efficient organic solar cells. *Nat Commun* 11:3943. <https://doi.org/10.1038/s41467-020-17867-1>
- [45] Khan MI, Hadia NMA, Iqbal J et al (2023) Novel A- π -D- π -A-type non-fullerene acceptors for solution-processed organic photovoltaic cells: a DFT study. *J Solid State Chem* 317:123714. <https://doi.org/10.1016/j.jssc.2022.123714>
- [46] Hassan T, Sajid I, Ramzan Saeed Ashraf Janjua M et al (2023) Non-fullerene based photovoltaic materials for solar cell applications: DFT-based analysis and interpretation. *Comput Theor Chem* 1224:114128. <https://doi.org/10.1016/j.comptc.2023.114128>
- [47] Barboza BH, Gomes OP, Batagin-Neto A (2021) Polythiophene derivatives as chemical sensors: a DFT study on the influence of side groups. *J Mol Model* 27:17. <https://doi.org/10.1007/s00894-020-04632-w>
- [48] Alves GB, Batagin-Neto A (2023) Local reactivity on carbon quantum dots: the influence of the geometries and chemical doping for chemical sensor applications. *J Phys Chem C* 127:3819–3829. <https://doi.org/10.1021/acs.jpcc.2c08612>
- [49] Frisch MJ, Trucks GW, Schlegel HB, et al (2016) Gaussian 16 Revision A.03
- [50] Yang W, Mortier WJ (1986) The use of global and local molecular parameters for the analysis of the gas-phase basicity of amines. *J Am Chem Soc* 108:5708–5711. <https://doi.org/10.1021/ja00279a008>
- [51] Doat O, Barboza BH, Batagin-Neto A et al (2021) Mini-review: materials and modelling for organic photovoltaic devices. *Polym Int* 6:25. <https://doi.org/10.1002/pi.6280>
- [52] Alves GGB, Lavarda FC, Graeff CFO, Batagin-Neto A (2020) Reactivity of eumelanin building blocks: a DFT study of monomers and dimers. *J Mol Graph Model* 98:107609. <https://doi.org/10.1016/j.jmgm.2020.107609>

- [53] Maia RA, Ventorim G, Batagin-Neto A (2019) Reactivity of lignin subunits: the influence of dehydrogenation and formation of dimeric structures. *J Mol Model* 25:228. <https://doi.org/10.1007/s00894-019-4130-4>
- [54] Galindo LA, Alves GGB, Lavarda FC, Batagin-Neto A (2023) Interaction between components of polymeric light emitting electrochemical cells: a DFT case study for MDMO-PPV/KCF3SO3/PEO system. *Comput Mater Sci* 230:112514. <https://doi.org/10.1016/j.commatsci.2023.112514>
- [55] Cachaneski-Lopes JP, Batagin-Neto A (2021) Effects of mechanical deformation on the optoelectronic properties of fullerenes: a DFT study. *J Nanostruct Chem* 141:157. <https://doi.org/10.1007/s40097-021-00408-7>
- [56] Cachaneski-Lopes JP, Batagin-Neto A (2022) Effects of mechanical deformation on the opto-electronic responses, reactivity, and performance of conjugated polymers: a DFT study. *Polymers* 14:1354. <https://doi.org/10.3390/polym14071354>
- [57] Hirshfeld FL (1977) Bonded-atom fragments for describing molecular charge densities. *Theor Chim Acta* 44:129–138. <https://doi.org/10.1007/BF00549096>
- [58] Roy RK, Pal S, Hirao K (1999) On non-negativity of Fukui function indices. *J Chem Phys* 110:8236–8245. <https://doi.org/10.1063/1.478792>
- [59] De Proft F, Van Alsenoy C, Peeters A et al (2002) Atomic charges, dipole moments, and Fukui functions using the Hirshfeld partitioning of the electron density. *J Comput Chem* 23:1198–1209. <https://doi.org/10.1002/jcc.10067>
- [60] Jmol (2022) Jmol: an open-source Java viewer for chemical structures in 3D. <http://www.jmol.org/>. Accessed 21 Oct 2019
- [61] Chirlian LE, Franci MM (1987) Atomic charges derived from electrostatic potentials: a detailed study. *J Comput Chem* 8:894–905. <https://doi.org/10.1002/jcc.540080616>
- [62] Martínez A, Rodríguez-Gironés MA, Barbosa A, Costas M (2008) Donator acceptor map for carotenoids, melatonin and vitamins. *J Phys Chem A* 112:9037–9042. <https://doi.org/10.1021/jp803218e>
- [63] Zhu L, Zhang M, Zhou G et al (2020) Efficient organic solar cell with 16.88% efficiency enabled by refined acceptor crystallization and morphology with improved charge transfer and transport properties. *Adv Energy Mater* 10:1904234. <https://doi.org/10.1002/aenm.201904234>
- [64] Zhu W, Spencer AP, Mukherjee S et al (2020) Crystallography, morphology, electronic structure, and transport in non-fullerene/non-indacenodithienothiophene polymer:Y6 solar cells. *J Am Chem Soc* 142:14532–14547. <https://doi.org/10.1021/jacs.0c05560>
- [65] Zhu L, Yi Y, Chen L, Shuai Z (2008) Exciton binding energy of electronic polymers: a first principles study. *J Theor Comput Chem* 07:517–530. <https://doi.org/10.1142/S0219633608003939>

Publisher's Note Springer Nature remains neutral with regard to jurisdictional claims in published maps and institutional affiliations.

Springer Nature or its licensor (e.g. a society or other partner) holds exclusive rights to this article under a publishing agreement with the author(s) or other rightsholder(s); author self-archiving of the accepted manuscript version of this article is solely governed by the terms of such publishing agreement and applicable law.

Terms and Conditions

Springer Nature journal content, brought to you courtesy of Springer Nature Customer Service Center GmbH ("Springer Nature").

Springer Nature supports a reasonable amount of sharing of research papers by authors, subscribers and authorised users ("Users"), for small-scale personal, non-commercial use provided that all copyright, trade and service marks and other proprietary notices are maintained. By accessing, sharing, receiving or otherwise using the Springer Nature journal content you agree to these terms of use ("Terms"). For these purposes, Springer Nature considers academic use (by researchers and students) to be non-commercial.

These Terms are supplementary and will apply in addition to any applicable website terms and conditions, a relevant site licence or a personal subscription. These Terms will prevail over any conflict or ambiguity with regards to the relevant terms, a site licence or a personal subscription (to the extent of the conflict or ambiguity only). For Creative Commons-licensed articles, the terms of the Creative Commons license used will apply.

We collect and use personal data to provide access to the Springer Nature journal content. We may also use these personal data internally within ResearchGate and Springer Nature and as agreed share it, in an anonymised way, for purposes of tracking, analysis and reporting. We will not otherwise disclose your personal data outside the ResearchGate or the Springer Nature group of companies unless we have your permission as detailed in the Privacy Policy.

While Users may use the Springer Nature journal content for small scale, personal non-commercial use, it is important to note that Users may not:

1. use such content for the purpose of providing other users with access on a regular or large scale basis or as a means to circumvent access control;
2. use such content where to do so would be considered a criminal or statutory offence in any jurisdiction, or gives rise to civil liability, or is otherwise unlawful;
3. falsely or misleadingly imply or suggest endorsement, approval, sponsorship, or association unless explicitly agreed to by Springer Nature in writing;
4. use bots or other automated methods to access the content or redirect messages
5. override any security feature or exclusionary protocol; or
6. share the content in order to create substitute for Springer Nature products or services or a systematic database of Springer Nature journal content.

In line with the restriction against commercial use, Springer Nature does not permit the creation of a product or service that creates revenue, royalties, rent or income from our content or its inclusion as part of a paid for service or for other commercial gain. Springer Nature journal content cannot be used for inter-library loans and librarians may not upload Springer Nature journal content on a large scale into their, or any other, institutional repository.

These terms of use are reviewed regularly and may be amended at any time. Springer Nature is not obligated to publish any information or content on this website and may remove it or features or functionality at our sole discretion, at any time with or without notice. Springer Nature may revoke this licence to you at any time and remove access to any copies of the Springer Nature journal content which have been saved.

To the fullest extent permitted by law, Springer Nature makes no warranties, representations or guarantees to Users, either express or implied with respect to the Springer nature journal content and all parties disclaim and waive any implied warranties or warranties imposed by law, including merchantability or fitness for any particular purpose.

Please note that these rights do not automatically extend to content, data or other material published by Springer Nature that may be licensed from third parties.

If you would like to use or distribute our Springer Nature journal content to a wider audience or on a regular basis or in any other manner not expressly permitted by these Terms, please contact Springer Nature at

onlineservice@springernature.com

Appendix B

Table B.1 – Detailed experimental and theoretical data (energy given in eV) according to each referenced work for the molecules in Figure 5.2, with the data of reference molecule in *italic*

Compound name	Side chain	n	E_{HOMO}	E_{LUMO}	E_{g}^{HL}	$E_{\text{g}}^{\text{opt}}$	ΔE_{g}	Methods*		Ref.
								HL	$E_{\text{g}}^{\text{opt}}$	
PBnDT-DTBT	R ₁ =3-butylonyl R ₂ =2-ethylhexyl	∞	-5.00	-3.19	2.27	1.77	0.50	CV	UV-vis	[1]
PBDT-DTBT	R ₁ =2-octyldodecyloxy	∞				1.72		CV	UV-vis	[2]
<i>BDT2-T-BT-T</i>	<i>R₁=R₂=H</i>	4	-5.12	-3.15	1.97	1.68	0.29	<i>DFT</i> <i>B3LYP</i> <i>6-311G(d)</i>	<i>TD-DFT</i> <i>B3LYP</i> <i>6-311G(d)</i>	[3]
Average			-5.06	-3.17	2.12	1.72	0.40			
PBnDT-DTffBT	R ₁ =3-butylonyl R ₂ =2-ethylhexyl	∞	-5.54	-3.33	2.21	1.70	0.51	CV	UV-vis	[1]
<i>BDT2-T-ffBT-T</i>	<i>R₁=R₂=H</i>	4	-5.22	-3.32	1.99	1.68	0.31	<i>DFT</i> <i>B3LYP</i> <i>6-311G(d)</i>	<i>TD-DFT</i> <i>B3LYP</i> <i>6-311G(d)</i>	[3]
Average			-5.38	-3.33	2.10	1.69	0.41			
PBnDT-HTAZ	R ₁ =3-butylonyl R ₂ =2-butyloctyl	∞	-5.29	-2.87	2.42	1.98	0.44	CV	UV-vis	[4]
PBDTDTBTz	R ₁ =2-ethylhexoxy R ₂ =octyl	∞	-5.06			1.95		CV	UV-vis	[5]
PBDT-DTBTz	R ₁ =H R ₂ =heptadecan-9-yl	∞	-5.26			1.97		CV	UV-vis	[6]
PBDTTDTBTz	R ₁ =2-ethylhexylthiophene R ₂ =octyl	∞	-4.92	-3.01	1.91	1.78	0.13	CV	UV-vis	[7]
<i>BDT2-T-HTAz-T</i>	<i>R₁=R₂=H</i>	4	-5.02	-2.80	2.22	1.90	0.32	<i>DFT</i> <i>B3LYP</i> <i>6-311G(d)</i>	<i>TD-DFT</i> <i>B3LYP</i> <i>6-311G(d)</i>	[3]
Average			-5.11	-2.89	2.18	1.92	0.30			
BisEH-PFDTBt	R=2-ethylhexyl	∞	-5.50			1.90		CV	UV-vis	[8]
PFDTBt	R=decyl	∞		-3.75		1.92		CV	UV-vis	[9]
PFD _o -DBT	R=dodecyl	∞	-5.44	-3.49	1.95	1.89	0.06	CV	UV-vis	[10]
16	R=methyl	4	-5.08	-2.92	2.16	1.84	0.32	<i>DFT</i> <i>B3LYP</i> <i>6-311G(d)</i>	<i>TD-DFT</i> <i>B3LYP</i> <i>6-311G(d)</i>	[11]
C/CPDP-T-BT-T	R=methyl	4	-4.85	-2.73	2.12	1.80	0.32	<i>DFT</i> <i>B3LYP</i> <i>6-31G(d,p)</i>	<i>TD-DFT</i> <i>B3LYP</i> <i>6-31G(d,p)</i>	[12]
<i>C/CPDP-T-BT-T</i>	<i>R=H</i>	4	-5.04	-2.96	2.09	1.86	0.23	<i>DFT</i> <i>B3LYP</i> <i>6-311G(d)</i>	<i>TD-DFT</i> <i>B3LYP</i> <i>6-311G(d)</i>	[3]
Average			-5.18	-3.17	2.08	1.87	0.23			
PCPDTBT	R=2-ethylhexyl	∞	-5.00	-3.19	1.81	1.44	0.37	CV	UV-vis	[13]
PCPDTBT	R=2-ethylhexyl	∞	-5.30	-3.57	1.73	1.38	0.35	CV	UV-vis	[14]

PCPDTBT	R=2-ethylhexyl	∞	-4.80				1.43		CV	UV-vis	[15]
C/CPDT-BT	R=methyl	4	-4.48	-2.91	1.57	1.34	0.23		DFT B3LYP 6-31G(d,p)	TD-DFT B3LYP 6-31G(d,p)	[12]
17	R=methyl	4	-4.74	-3.12	1.63	1.37	0.26		DFT B3LYP 6-311G(d)	TD-DFT B3LYP 6-311G(d)	[11]
<i>CPT-BT</i>	<i>R=H</i>	4	-4.70	-3.06	1.64	1.39	0.25		DFT B3LYP 6-311G(d)	TD-DFT B3LYP 6-311G(d)	[3]
Average			-4.84	-3.17	1.68	1.39	0.29				
PSiF-DBT	R=octyl	∞					1.82			UV-vis	[16]
PBSDTBT	R=octyl	∞	-5.70	-3.81	1.89	1.85	0.04		CV	UV-vis	[17]
Si/CPDP-T-BT-T	R=methyl	4	-4.85	-2.73	2.13	1.81	0.32		DFT B3LYP 6-31G(d,p)	TD-DFT B3LYP 6-31G(d,p)	[12]
<i>Si/CPDP-T-BT-T</i>	<i>R=H</i>	4	-5.12	-3.05	2.06	1.88	0.18		DFT B3LYP 6-311G(d)	TD-DFT B3LYP 6-311G(d)	[3]
Average			-5.22	-3.20	2.03	1.84	0.18				
PDTSTPD	R ₁ =2-ethylhexoxy R ₂ =octyl	∞	-5.46	-3.15	2.31	1.70	0.61		CV	UV-vis	[18]
PDTSTPD	R ₁ =2-ethylhexoxy R ₂ =octyl	∞	-5.57	-3.88	1.69	1.73	-0.04		CV	UV-vis	[19]
<i>Si/CPT-TPD</i>	<i>R₁=R₂=H</i>	4	-5.28	-3.12	2.16	1.84	0.32		DFT B3LYP 6-311G(d)	TD-DFT B3LYP 6-311G(d)	[3]
Average			-5.44	-3.38	2.05	1.76	0.30				

*Methods for HOMO and LUMO (HL) energies: cyclic voltammetry (CV) and density functional theory (DFT). Methods for E_g^{opt} : ultraviolet-visible spectrometry (UV-vis) and time-dependent DFT (TD-DFT)

Table B.2 – Detailed experimental and theoretical data according to each referenced work for the molecules in Figure 5.4 (energy given in eV)

Compound name	Side chain	n	E_{HOMO}	E_{LUMO}	E_{g}^{HL}	$E_{\text{g}}^{\text{opt}}$	ΔE_{g}	Methods*		Ref
								HL	$E_{\text{g}}^{\text{opt}}$	
PT										
Regio regular PBT	R=butyl	∞				1.70			UV-vis	[20]
P3HT spin-coating	R=hexyl	∞	-4.71			1.93				[21]
P3HT LS	R=hexyl	∞	-4.70			1.92	CV	UV-vis		[21]
P3DT spin-coating	R=decyl	∞	-4.76			1.92				[21]

P3DT LS	R=decyl	∞	-4.77			1.90				[21]
P3HT	R=hexyl	∞	-5.22	-3.68	1.54	1.90	-0.36	CV	UV-vis	[22]
P3HT	R=hexyl	∞	-5.20	-3.53	1.67	1.92	-0.25			[23]
P3OT	R=octyl	∞	-5.25	-3.55	1.70	1.92	-0.22	CV	UV-vis	[23]
P3DDT	R= dodecyl	∞	-5.29	-3.55	1.74	1.93	-0.19			[23]
12T	R=H	12	-6.05	-1.76	4.29	2.23	2.06	DFT LC-PBE0*	TD-DFT LC-PBE0*	[24]
20T	R=H	20	-5.98	-1.86	4.12	2.10	2.02	6-31+G(d)	6-31+G(d)	[24]
20T	R=H	∞	-4.63	-2.50	2.13			NWChem/DFT B3LYP 6-31G(d)		[24]
PT	R=H	∞	-4.61	-2.55	2.06			PBC/DFT B3LYP 6-31G(d)		[24]
P3HT	R=hexyl	∞			2.39	2.00	0.39	Kuhn fit DFT B3LYP-D 6-31G(d)	Kuhn fit TD-DFT B3LYP 6-31G(d)	[25]
P3AT	R=methyl	8	-4.60	-2.10	2.50			DFT B3LYP 6-31G(d)		[26]
Average			-5.05	-2.68	2.51	1.95	0.64			
Mc13										
PBTz	R=2-octyl dodecyl	∞		-3.50		2.10		CV	UV-vis	[26]
P1	R=heptadecan-9-yl	∞	-5.40			2.30		PESA	UV-vis	[27]
PBTz	R=methyl	8	-4.70	-2.30	2.40			DFT B3LYP 6-31G(d)		[26]
13	R=methyl	6	-5.03	-2.41	2.63	2.34	0.29	DFT B3LYP 6-311G(d)	TD-DFT B3LYP 6-311G(d)	[11]
Average			-5.04	-2.74	2.52	2.25	0.29			
Mc1										
H2	R= dodecyl	∞	-5.16	-2.67	2.49	2.13	0.36	CV	UV-vis	[28]
O-PBDT	R=2-ethylhexyl	∞	-5.31	-2.94	2.37	2.21	0.16	CV	UV-vis	[29]
n-OBDT	R=methyl	1				3.63				[30]
n-OBDT	R=methyl	2			3.31	3.07	0.24			[30]
n-OBDT	R=methyl	3			2.95	2.69	0.26	DFT B3LYP 6-31G(d)	TD-DFT B3LYP 6-31G(d)	[30]
n-OBDT	R=methyl	4			2.79	2.50	0.28			[30]
n-OBDT	R=methyl	5			2.68	2.39	0.30			[30]

n-OBDT	R=methyl	6			2.62						[30]
n-OBDT	R=methyl	7			2.59						[30]
n-OBDT	R=methyl	8			2.56	2.24	0.32				[30]
n-OBDT	R=methyl	9			2.54						[30]
n-OBDT	R=methyl	∞			2.30			Line fit			[30]
n-OBDT	R=methyl	∞			2.50			Kuhn fit			[30]
n-OBDT	R=methyl	∞			2.54	2.16	0.38	Meier fit	Meier fit		[30]
n-OBDT	R=methyl	∞			2.45			PBC/DFT B3LYP 6-31G(d)			[30]
O-PBDT	R=methyl	4	-5.11	-2.31	2.80			DFT B3LYP 6-311G(d)	TD-DFT B3LYP 6-311G(d)		[29]
1	R=methyl	6	-5.19	-2.58	2.61	2.30	0.31	DFT B3LYP 6-311G(d)	TD-DFT B3LYP 6-311G(d)		[11]
Average			-5.19	-2.63	2.63	2.53	0.29				
Mc12											
P1 ^S	R _O =2-ethylhexyl R _N =octyl	∞	-5.56	-3.75	1.81	1.80	0.01	CV	UV-vis		[31]
PBDTTPD	R _O =2-ethylhexyl R _N =octyl	∞	-5.35	-3.17	2.18	1.80	0.38	CV	UV-vis		[32]
Pa2	R _O =2-ethylhexyl R _N =H	∞	-4.99		1.83			PBC B3LYP 6-31G(d)			[33]
Pa2	R _O =2-ethylhexyl R _N =H	∞	-5.51		2.52			PBC PBE0 6-31G(d)			[33]
Da2	R _O =methyl R _N =H	2				2.07			TD-DFT O3LYP 6-31G(d)		[33]
12	R=methyl	4	-5.46	-3.10	2.36	2.04	0.32	DFT B3LYP 6-311G(d)	TD-DFT B3LYP 6-311G(d)		[11]
Average			-5.37	-3.34	2.14	1.93	0.24				
CPT-BT											
PCPDTBT	R=2-ethylhexyl	∞	-5.00	-3.19	1.81	1.44	0.37	CV	UV-vis		[13]
PCPDTBT	R=2-ethylhexyl	∞	-5.30	-3.57	1.73	1.38	0.35	CV	UV-vis		[14]
PCPDTBT	R=2-ethylhexyl	∞	-4.80			1.43		CV	UV-vis		[15]
C/CPDT-BT	R=methyl	4	-4.48	-2.91	1.57	1.34	0.23	DFT B3LYP 6-31G(d,p)	TD-DFT B3LYP 6-31G(d,p)		[12]

17	R=methyl	4	-4.74	-3.12	1.63	1.37	0.26	DFT B3LYP 6-311G(d)	TD-DFT B3LYP 6-311G(d)	[11]
CPT-BT	R=H	4	-4.70	-3.06	1.64	1.39	0.25	DFT B3LYP 6-311G(d)	TD-DFT B3LYP 6-311G(d)	[3]
Average			-4.84	-3.17	1.68	1.39	0.29			
PTB7-Th										
PTB7-Th	R=2-ethylhexyl	∞	-5.22			1.58		CV	UV-vis	[34]
PTB7-TH	R=2-ethylhexyl	∞				1.77			UV-vis	[35]
PTB7-TH	R=2-ethylhexyl	∞	-5.20	-3.59	1.61	1.76	-0.15	CV	UV-vis	[36]
PTB7-Th	R=2-ethylhexyl	∞	-5.39	-3.12	2.27	1.78	0.49	CV	UV-vis	[37]
PBDTTT- EF-T	R=2-ethylhexyl	∞	-5.20			1.68		PYS	PYS	[38]
PTB7-Th	R=2-ethylhexyl	∞	-5.02	-3.38	1.64	1.76	-0.12	UPS	UV-vis	[39]
PTB7-Th	R=2-ethylhexyl	∞				1.58			UV-vis	[40]
PTB7-Th	R=H	4				1.75			TD-DFT B3LYP 6-31+G(d)	[35]
PTB7-Th	R=2-ethylhexyl	1	-5.13	-2.23	2.90			DFT B3LYP 6-31+G(d,p)		[34]
Average			-5.19	-3.08	2.11	1.71	0.08			
Mc15										
PCDTBT	R=octyl	∞	-5.45	-3.60	1.85	1.88	-0.03	CV	UV-vis	[41]
PCDTBT	R=decyl	∞				2.17			UV-vis	[42]
PCDTBT	R=octyl	∞	-5.40			1.95		PYS	PYS	[38]
PCDTBT-H	R=methyl	4	-4.98	-2.95	2.02	1.71	0.31	DFT B3LYP 6-311G(d,p)	TD-DFT B3LYP 6-311G(d,p)	[43]
PCDTBT (1)	R=H	3	-4.79	-2.71	2.08	1.77	0.31			[44]
PCDTBT (3)	R=methyl	3	-4.77	-2.70	2.08	1.77	0.31			[44]
PCDTBT (5)	R=ethyl	3	-4.76	-2.69	2.07	1.76	0.31			[44]
PCDTBT (7)	R=propyl	3	-4.76	-2.69	2.07	1.76	0.31	DFT B3LYP 6-31G(d)	TD-DFT B3LYP 6-31G(d)	[44]
PCDTBT (9)	R=butyl	3	-4.75	-2.68	2.07	1.76	0.31			[44]
PCDTBT (13)	R=hexyl	3	-4.75	-2.68	2.07	1.76	0.31			[44]
PCDTBT (17)	R=octyl	3	-4.75	-2.68	2.07	1.76	0.31			[44]

PCDTBT	R=octyl	1	-4.98	-2.57	2.41	1.88	0.53	DFT B3LYP 6-31G(d)	TD-DFT B3LYP 6-31G(d)	[41]
15	R=methyl	4	-5.04	-2.86	2.18	1.86	0.32	DFT B3LYP 6-311G(d)	TD-DFT B3LYP 6-311G(d)	[11]
Average			-4.93	-2.80	2.09	1.83	0.30			
PM6										
PM6	R=2-ethylhexyl	∞	-5.45			1.80		CV	UV-vis	[45]
PM6	R=2-ethylhexyl	∞	-5.56	-3.50	2.06	1.81	0.25	CV	UV-vis	[46]
PM6	R=2-ethylhexyl	∞	-5.50	-3.61	1.89			CV	UV-vis	[47]
PM6	R=2-ethylhexyl	∞	-5.50	-3.61	1.89			CV	UV-vis	[48]
PBDB-TF	R=2-ethylhexyl	∞	-5.54	-3.51	2.03	2.18	-0.15	CV	UV-vis	[49]
PM6	R=2-ethylhexyl	∞	-5.13			1.85		UPS	UV-vis	[50]
PM6	R=methyl	2	-5.00	-2.62	1.63			DFT B3LYP 6-31G(d,p)		[45]
PM6	R=2-ethylhexyl	3	-5.16	-2.77	2.39	1.98	0.41	DFT B3LYP def2-TZVP	TD-DFT B3LYP def2-TZVP	[51]
Average			-5.36	-3.27	1.98	1.92	0.17			

*Methods: cyclic voltammetry (CV), density functional theory (DFT), photoelectron spectroscopy in air (PESA), periodic boundary condition (PBC), photoelectron yield spectroscopy (PYS), ultraviolet photoelectron spectroscopy (UPS), ultraviolet-visible spectrometry (UV-vis) and time-dependent DFT (TD-DFT)

List of Abbreviations

a adiabatic	CdTe cadmium telluride
A electron-acceptor	CIGS copper indium gallium selenide
abs absorption	CO₂ carbon dioxide
APF-D Austin-Frisch-Petersson functional with dispersion	CP critical point
a-Si amorphous silicon	CPDT cyclopentadithiophene
At atomic	CPT cyclopenta[c]dithiophene
B Boltzmann	CT charge-transfer
b exciton binding	CV cyclic voltammetry
B3LYP BLYP hybrid functional	D electron-donor
B88 Becke 88 exchange functional	D~D4 dispersion models
BCP bond CP	DFT density functional theory
BDT benzodithiophene	DHO displaced harmonic oscillator
BIPV building-integrated photovoltaic	disp dispersion
BLA bond length alternation	DoI atomic degree of interaction
BLYP GGA using B88 and LYP	DORI density overlap region indicator
BT benzothiadiazole	e electron
C energy conservation	EA electronic potential
C1 methyl side chain	EDOT 4-ethyldioxythiophene
C4 butyl side chain	em emission
C₆₀ <i>buckminster</i> fullerene	ETL electron transport layer
C6C2 2-ethylhexyl side chain	eV electron-Volt
cat cation	ext external
	fund fundamental

GD3(BJ) D3 version of Grimme's dispersion with Becke-Johnson damping	ML machine learning
GGA generalized gradient approximation	MO molecular orbital
GHG greenhouse gas	MO5-2X Zhao-Schultz-Truhlar hybrid meta exchange-correlation functional
GIXD grazing incidence X-ray diffraction	n nuclei
HF Hartree-Fock	NCI noncovalent interaction
HK Hohenberg-Kohn	NIR near-infrared region
HL HOMO-LUMO	NREL National Renewable Energy Laboratory
HOMO highest occupied molecular orbital	opt optical
HTL hole transport layer	OPV organic photovoltaic
IBSI intrinsic bond strength index	OSC organic solar cell
id second chain identical (no rotation)	P product
IGM independent gradient model	P3AT poly(3-alkylthiophene)
IGMH IGM method based on the Hirshfeld partition of molecular density	P3HT poly(3-hexylthiophene)
IP ionization potential	PBE Perdew-Burke-Ernzerhof GGA functional
IPES inverse photoelectron spectroscopy	PBE0 PBE hybrid
IRI interaction region indicator	PCE power of conversion efficiency
ITO indium-tin oxide	PEDOT:PSS poly(3,4-ethylenedioxythiophene) polystyrene sulfonate
KS Kohn-Sham	PET poly(ethylene terephthalate)
LCA life cycle assessment	PSC polymer solar cell
LDA local density approximation	PTB7 TT/benzodithiophene polymer
LUMO lowest unoccupied molecular orbital	
LYP Lee-Yang-Parr correlation functional	
MEP molecular electrostatic potential	

PTB7-Th poly([2,6'-4,8-di(5-ethylhexylthienyl)benzo[1,2-b;3,3-b]dithiophene){3-fluoro-2[(2-ethylhexyl)carbonyl]thieno[3,4-b]thiophenediyl})	vdW van der Waals
PV photovoltaic	Vis-NIR visible and near-infrared region
QTAM quantum theory of atom in molecules	VMD Visual Molecular Dynamics software
R reactant	X exchange
RDG reduced density gradient	XC exchange-correlation
rx second chain rotated in turn of axis x	XRD X-ray diffraction
ry second chain rotated in turn of axis y	ZnO₂ zinc oxide
rz second chain rotated in turn of axis z	ωB97X-D Head-Gordon and coworkers' functional with empirical dispersion
SBT dithieno-silole	6-31G Pople's double-ξ gaussian basis set
S_k k-th state	6-311G Pople's triple-ξ gaussian basis set
SnO₂ tin oxide	6-31G(d) or 6-31G* Pople's double-ξ gaussian basis set with polarization functions for all atoms except hydrogen
SVWN Slater-Vosko-Wilk-Nusair functional	6-311G(d) or 6-311G* Pople's triple-ξ gaussian basis set with polarization functions for all atoms except hydrogen
T thiophene block	6-31G(d,p) or 6-31G** Pople's double-ξ gaussian basis set with polarization functions for all atoms
TD-DFT time-dependent DFT	6-311G(d,p) or 6-311G** Pople's triple-ξ gaussian basis set with polarization functions for all atoms
TF Thomas-Fermi	6-311++G(d,p) Pople's triple-ξ gaussian basis set with polarization functions for all atoms, with supplementary diffuse s and p functions
TFSCs thin film solar cells	
TiO₂ titanium oxide	
TT thieno[3,4b]thiophene	
UPS ultraviolet photoelectron spectroscopy	
UV-Vis ultraviolet and visible	
v vertical	



ABSTRACT

Organic photovoltaic (OPV) cells are technologies that use semiconductor materials to generate photocurrent from incident light on the device. The first process in the photovoltaic effect is light absorption, when photons of light interact with electrons of molecules in the active layer. So, it is suitable to work with materials that have light absorption in the range of the highest intensity solar irradiance, such as conjugated systems, which aromatic rings create overlaps of π -orbitals, facilitating the delocalization of electrons along the polymer backbone.

Ab initio modeling is a powerful technique to design materials at the atomistic level and predict electronic properties such as optical and electronic gaps, electronic affinity and ionization potential, that are strongly related to the OPV performance. The correlation between method and accurately estimation of these properties is well known. Designing a novel molecule from computational investigation requires a deeply understanding about parameters of the polymer structure, combining blocks with different chemical functions to tune optoelectronic properties.

In this work, we present a theoretical study targeting trends of such properties from a benchmarking, for a series of compounds: PM6, PTBT-Th, P3HT, C/CPCT-T-BT-T, CPT-BT, Si/CPT-TPD, BDT2-T-ffBT-T, BDT2-T-BT-T, BDT2-T-HTAZ-T, Si/CPDP-T-BT-T, and other polymers based on fused-aromatic rings such as oxybenzodithiophenes, benzotriazoles, piazthiolebenzothiadiazole and N-isopropylcarbazole. The calculations based on density functional theory (DFT) and time-dependent DFT (TD-DFT) were carried out using Gaussian16, B3LYP functional and a 6-31G(d) basis set. This thesis counted with intense explanations about optical and electronic properties and demonstrations of correlated parameters, clarifying terminologies vastly used to materials for photovoltaic applications. Other approaches based on electron density were also considered to give support to visualization analysis of noncovalent interactions.

We have found, through optimisations carried out on self-assembled molecular systems, that the interactions of π systems between neighbouring molecules have a greater impact on the optoelectronic properties than the side chains attached to them. We have thus shown that it is possible to replace long branched side chains with methyl groups, reducing the computational



cost without any major change in the results. The post-computational treatment of the set of interactions was carried out using the independent gradient model (IGM) and showed that it is possible to distinguish the key interactions responsible for stabilising self-assembled (macro)molecular systems as they must exist in the conducting polymer of OPV devices.

This thesis has mainly enabled us to establish how the molecular structure of aggregates affects the electronic properties of a system. With this work, we presented the main assumptions of how molecular structure can affect the electronic properties, then to guide researchers on designing a new material with a high light absorption.



RÉSUMÉ

Les cellules photovoltaïques organiques (OPV) sont des dispositifs qui utilisent des matériaux semi-conducteurs pour générer un photocourant à partir de la lumière incidente qui frappe le dispositif. Le premier processus en jeu dans l'effet photovoltaïque est l'absorption de lumière, soit l'interaction entre les photons incidents et les électrons des molécules de la couche active du dispositif. Il apparaît donc évident qu'il convient d'employer des matériaux présentant une absorption maximale dans la gamme de la plus forte irradiance solaire. Les systèmes conjugués, dont les anneaux aromatiques créent des recouvrements d'orbitales π , sont des candidats idéaux puisqu'ils facilitent la délocalisation des électrons le long de l'ossature polymère.

La modélisation *ab initio* est un outil puissant pour qui cherche à concevoir ces nouveaux matériaux, puisqu'elle permet de prédire avec une grande fiabilité des propriétés électroniques telles que les gaps optiques et électroniques, l'affinité électronique ou encore le potentiel d'ionisation, auxquelles les performances des dispositifs OPV sont fortement corrélées. Concevoir une nouvelle molécule à l'appui des calculs théoriques nécessite une compréhension approfondie de la structure du polymère, le jeu consistant à combiner des blocs porteurs de fonctions chimiques différentes afin d'ajuster les propriétés optoélectroniques.

Le travail présente une étude théorique descriptive (benchmark) des propriétés électroniques évoquées ci-avant, calculées pour une série de composés de type PM6, PTBT-Th, P3HT, C/CPCT-T-BT-T, CPT-BT, Si/CPT-TPD, BDT2-T-ffBT-T, BDT2-T-BT-T, BDT2-T-HTAZ-T, Si/CPDP-T-BT-T, et pour une autre série molécules de cœur π de type oxybenzodithiophènes, benzotriazoles, piazthiolebenzothiadiazole et N-isopropylcarbazole. Les calculs réalisés sont de type DFT (théorie de la fonctionnelle de la densité) et TD-DFT (théorie de la fonctionnelle de la densité dépendante du temps), et ont été réalisés via Gaussian16, en employant la fonctionnelle B3LYP et un ensemble de bases 6-31G(d). Cette thèse vise à fournir une compréhension approfondie des propriétés optiques et électroniques des matériaux, en regard de ces mêmes paramètres pour les matériaux couramment employés dans les dispositifs OPV. D'autres approches basées sur la densité électronique ont également été considérées pour soutenir l'analyse des interactions non covalentes.



Nous avons constaté, via les optimisations réalisées sur les systèmes moléculaires auto-assemblés, que les interactions des systèmes π entre molécules voisines, ont un impact plus important sur les propriétés optoélectroniques que les chaînes latérales qui y sont attachées. Nous avons ainsi montré qu'il est possible de remplacer les longues chaînes latérales ramifiées par des groupes méthyles réduit le coût computationnel sans changement majeur dans les résultats. Le traitement post-calculatoire de l'ensemble des interactions a été réalisé à l'aide du modèle de gradient indépendant (IGM) et a montré qu'il est possible de distinguer les interactions clés responsables de la stabilisation des systèmes (macro)moléculaires auto-assemblés telles qu'elles doivent exister dans le polymère conducteur des dispositifs OPV.

Cette thèse nous a principalement permis d'établir la manière dont la structure moléculaire des agrégats affecte les propriétés électroniques d'un système. Notre travail pose également les bases d'un guide théorique pouvant servir de fil rouge à la conception de nouveaux matériaux présentant une absorption de lumière optimale pour un emploi dans les dispositifs OPV.

Ecole doctorale sciences exactes et leurs applications

ED SEA 211

Institut des Sciences Analytiques et de Physico-Chimie pour l'Environnement et les Matériaux

IPREM

